NUMERICAL ANALYSIS OF PUNCHING FAILURE IN REINFORCED CONCRETE STRUCTURES

THÈSE N^{O} 1279 (1994)

PRÉSENTÉE AU DÉPARTEMENT DE GÉNIE CIVIL

ÉCOLE POLYTECHNIQUE FÉDÉRALE DE LAUSANNE

POUR L'OBTENTION DU GRADE DE DOCTEUR ÈS SCIENCES TECHNIQUES

PAR

PHILIPPE MENETREY
Ingénieur civil diplômé EPF, Master of Science University of Colorado, Boulder
originaire du Mont-sur-Lausanne (VD)

acceptée sur proposition du jury:

Prof. R. Walther, rapporteur
Prof. P. Regan, corapporteur
Prof. K.J. Willam, corapporteur
Dr Th. Zimmermann, corapporteur

Lausanne, EPFL
1994

Abstract

Reinforced concrete slabs supported on columns fail by punching when a conical plug of concrete perforates the slab above the column. This failure has been mostly investigated experimentally, so what can numerical simulation contribute to understand this phenomenon?

To answer this question, a computational simulation tool based on the finite element method is developed. This numerical model is implemented into a computer code in applying the object-oriented programming concept. The requirements that the numerical model should fulfill are derived from a review of the experimental results published in the literature and obtained in our laboratory.

The numerical model reproduces the non-linear material behavior characterizing reinforced concrete structures by decoupling the actions of steel reinforcement and concrete. The steel reinforcement is represented by uniaxial truss elements which follow a bi-linear stress-strain response. The concrete is modelled with continuum elements which are described at the constitutive level within the framework of the incremental flow theory of plasticity. The concrete triaxial strength is delimitated with a new failure criterion. A plastic flow rule is derived so as to reproduce the evolution of the plastic strain observed experimentally. Cracking induces strain-softening which refers to a gradual decrease in tensile strength with increasing deformations. The reduction of the tensile strength is controlled by an isotropic decohesion process which is monitored by constant fracture energy. The stiffness degradation due to cracking is reproduced with an isotropic elastic damage model. A perfect bond between concrete and steel is assumed.

The capabilities of the numerical model are illustrated by simulating the localized shear failure in soil under a footing, the uniaxial tensile, and the confined compressive tests in plain and reinforced concrete specimens.

The simulation of punching failure is investigated for three circular reinforced concrete slabs. The comparison with experimental results indicates that: (1) the punching failure mechanism—characterized by a localized inclined punching crack—is generated, (2) the value of the punching load is predicted, (3) the cracking sequence is reproduced, (4) the global response is slightly too stiff. For slabs with orthogonal reinforcement, the perfect bond hypothesis does not allow to capture the punching failure mechanism and the numerical model is improved by relaxing this hypothesis.

The developed computational simulation tool reproduces the punching failure observed experimentally and is consequently used to investigate the failure mechanism. First, it is shown that the punching crack results from a crack coalescence phenomenon at the top of the slab followed by a crack propagation in the direction of the corner slab-column. Second, a condition for punching failure to occur is determined. Third, it is illustrated that the size-effect observed experimentally is reproduced and is reflected by a modification of the tensile stress distribution along the punching crack. Finally, a parametric study of the punching failure is performed revealing that punching failure is governed by the tensile strength of concrete. It is also shown that increasing the percentage of reinforcement raises the punching load and reduces the ductility of failure. Lastly, the computational simulation tool allows to demonstrate that in a circular slab, the applied bending moment is not determinant for the value of the punching load.

Résumé

Une dalle en béton armé appuyée sur une colonne se rompt par poinçonnement lorsque la colonne passe brusquement au travers de la dalle par extrusion d'un cône de béton. L'analyse de cette rupture est couramment effectuée par des essais en laboratoire, mais qu'en est-il des possibilités de simulations numériques?

Pour répondre à cette question, un modèle de simulation numérique basé sur la méthode des éléments finis a été développé. Ce modèle est programmé dans un logiciel selon le concept de programmation orientée objet. Les exigences que le modèle numérique doit satisfaire ont été déterminées sur la base de résultats expérimentaux publiés dans la littérature scientifique et obtenus à notre laboratoire.

Le modèle numérique reproduit le comportement non linéaire du béton armé en dissociant le béton et l'armature. L'armature est modélisée par des éléments finis de barre satisfaisant une loi contrainte-déformation bilinéaire. Le béton est modélisé par des éléments finis de volume. Le comportement rhéologique du béton est décrit sur la base de la théorie de la plasticité. La réponse triaxialle du béton est délimité par un nouveau critère de rupture. Une loi d'écoulement plastique reproduisant l'évolution de la déformation due à la fissuration observée expérimentalement est développée. La fissuration est modélisée selon un adoucissement isotrope contrôlé par une énergie de rupture constante. De plus, la fissuration engendre une dégradation de la rigidité du béton qui est reproduite par un modèle d'endommagement élastique isotrope.

Les capacités du modèle numérique ont été démontrées par les simulations suivantes: rupture par cisaillement d'un sol sous une semelle de fondation, essais de traction et de compression confinée sur des éprouvettes en béton et béton armé.

La rupture par poinçonnement a été simulée numériquement pour trois dalles circulaires. La comparaison avec les résultats expérimentaux indique que: (1) le mécanisme de ruine caractérisé par une fissure de poinçonnement inclinée est reproduit, (2) la charge de ruine est déterminée, (3) la séquence de fissuration est reproduite, (4) la réponse obtenue avec le modèle numérique est légèrement trop rigide. Pour une dalle constituée d'armature orthogonale, l'hypothèse d'adhérence parfaite entre le béton et l'armature ne permet pas d'obtenir le mécanisme de ruine et le modèle numérique a été amélioré en écartant cette hypothèse.

Le modèle de simulation numérique permet de reproduire la rupture par poinçonnement observée expérimentalement. Il est donc utilisé pour analyser ce phénomène de rupture. Premièrement, il est montré que la fissure de poinçonnement est due à un regroupement de fissures dans la partie supérieure de la dalle, suivi d'une propagation de fissure en direction du coin colonne-dalle. Deuxièmement, une condition pour la rupture par poinçonnement est déterminée. Troisièmement, il est démontré que l'effet de la taille de la structure, observé expérimentalement, est reproduit par le modèle et qu'il est illustré par une modification de la distribution des contraintes de traction le long de la fissure de poinçonnement. Finalement, une étude paramétrique a révélé que la rupture par poinçonnement est contrôlée par la résistance à la traction du béton. Il est également démontré qu'en augmentant le pourcentage d'armature de flexion la charge de poinçonnement augmente mais la ductilité de la réponse diminue. Le modèle de simulation numérique a en plus permis de montrer que pour une dalle circulaire, le moment de flexion influence peu la charge de poinçonnement.

Contents

List of Figures

List of Tables

Preface

Punching failure is one of the most complex forms of rupture observed in reinforced concrete structures. This type of failure which still occurs nowadays, is potentially very dangerous as it happens without any preliminary warning.

This problem was extensively analyzed experimentally during this century, on footings (Talbot 1913 or Richard 1948) and on thin slabs (Graf 1938, Elstner and Hognestad 1956, Kinnunen and Nylander 1960, Marti et al. 1977). So far, however, it was not possible to understand correctly the failure mechanisms. Based on these experimental investigations, many empirical or mechanical models were proposed (Kinnunen and Nylander 1960 or Pralong 1982), however, none of these models could adequately predict the rupture.

Mr Menétrey has pursued a different approach, developing a numerical model to analyze punching failure in reinforced concrete structures. Even though such an approach is rather complex, the method chosen appears to be promising.

To begin with, Mr Menétrey studied the punching failure based on experimental results and tests performed at our laboratory. During the course of this study, the requirements that the numerical model should fulfill were determined. A computational simulation tool based on the finite element method was then developed. It reproduces the particular behavior of reinforced concrete such as cracking, influence of confinement, dilatancy and yielding of reinforcement. The numerical model was tested by simulating the shear failure in soil and standard tensile and compressive tests in plain and reinforced concrete specimens. Finally, the punching failure in reinforced concrete was simulated. A parametric study was furthermore performed, revealing that punching failure is mostly influenced by the tensile strength of concrete.

It was gratifying to ascertain that the analysis performed by Mr Menétrey did indeed lead to convincing results. To my knowledge, it was the first time that all the influencing parameters were correctly apprehended. A computational simulation tool is now available to investigate the punching failure mechanism. The development of new design methods for standard is now possible. Even though the model may still be improved and more analysis should be performed, this thesis has opened new horizons in the understanding of the failure behavior in reinforced concrete structures.

Lausanne, October 1994 Prof. Dr. R. Walther

Foreword

This research was performed in Switzerland at the "Institut de béton armé et précontraint" at the "Ecole Polytechnique fédérale de Lausanne" under the guidance of Professor R. Walther. I am very grateful to Professor R. Walther for giving me the opportunity to undertake this research as well as for his guidance, encouragement, and patience. Part of the financial support which is acknowledged with gratitude was provided by "La fondation pour la recherche scientifique et systématique dans les domaines de la construction en béton et béton armé de la Société suisse des fabricants de ciment, chaux et gypse".

I would like to express my special thanks to Dr Th. Zimmermann, who made this research possible by many fruitful comments, discussions and suggestions. I also want to thank Professor P.E. Regan and Professor K.J. Willam for their guidance and support as well as Professor R. Rivier for presiding the examinations.

I would like to acknowledge the conversations I had with Professors R. Favre, F. Frey, and S. Kinnunen. The discussions with Professor Ch. Huet, Dr S. Hazanov and Dr P. Navi at the "Club de Rhéologie" as well as with Dr E. Frochaud at the Mathematical Department, are also acknowledged.

I would also like to thank all my colleagues, among others I. Cecco (for her help and for proofreading the first draft), D. Amsler, C. Broquet, Dr J. Carbajal, L. Chevalier, R. Gisler (for the experimental tests), R. Gunn (for proofreading the manuscript), Dr J.-F. Klein, M. Mielbradt, A. Oribasi, J.-C. Reymond (for drawing most of the figures), F. Séverin (for the last figure), J. Treleani, D. Weber, A. Wohnlich, B. Farra, M. Hassan, B. Gardel (for the first figure), Dr J.P. Jaccoud, P. Bomme, A. Barry (for numerous discussions), Dr Y. Dubois-Pèlerin (for the original object-oriented code), Dr A. Ibrahimbegovic, and Y. Li (for numerous discussions). Not only did they help me with their suggestions and comments, but they also made my years of research more enjoyable.

At our computer center (SIC), I would like to thank P. Lemeur for several developments concerning the post-processor, A. Brossard for the maintenance of the Sun Work-Stations, A. Possoz at the finite element work group, and A. de Brossin.

Finally, I want to thank you Karin for your support, patience, understanding, and encouragement all along this research. I also want to express my gratitude to all my family and friends.

Notations

The notations used in this thesis are presented in the following:
Latin capital letters:

A	cross sectional area
A_f, B_f, C_f	parameters of the generalized failure criterion
A_g, B_g, C_g	parameters of the concrete plastic potential
$\boldsymbol{B}$	strain displacement matrix
$\overline{\boldsymbol{B}}$	improved strain displacement matrix
$\boldsymbol{C}$	elastic constitutive tensor
$\boldsymbol{Cep}$	elastic-plastic constitutive tensor
$\boldsymbol{D}$	elastic constitutive matrix
$\boldsymbol{Dep}$	elastic-plastic constitutive matrix
D	flexural rigidity of a slab
E	Young's modulus, residual energy
$\boldsymbol{F}$	force vector
$\boldsymbol{Fext}, \boldsymbol{Fint}$	external and internal force vector
F	component of a force
G	shear modulus
G_f	fracture energy
H	hardening modulus for the steel model
$\boldsymbol{I}$	fourth order identity tensor
I_1, I_2, I_3	first, second and third invariants of the stress tensor
$\boldsymbol{J}$	Jacobian matrix
J_2, J_3	second and third invariants of the deviatoric stress tensor
$\boldsymbol{K}$	stiffness matrix
K	bulk modulus
L	length
$\boldsymbol{N}$	matrix of the shape functions, normal vector to a force or discontinuity
N	fictitious number of cracks
$\boldsymbol{Q}$	elastic acoustic tensor/matrix
$\boldsymbol{Qep}$	elastic-plastic acoustic tensor/matrix
P	concentrated load
P_{crack}	load corresponding to the appearance of the first crack
P_{yield}	load corresponding to the yielding of the reinforcement
P_{flex}	ultimate flexural load computed with the yield-line theory
P_{punch}	punching load
S	surface of a body
$\boldsymbol{T}$	rotation matrix
U	second order work
V	volume of a body
W	strain energy function
$Wext, Wint$	external and internal virtual works
$\boldsymbol{X}$	position vector of the initial configuration
$\mathbf{1}$	second order identity tensor

Latin lower-case letters:

a	steepness parameter of the softening formulation
a_{ϕ}	material characteristic of the Drucker-Prager yield surface
a_{ψ}	material characteristic of the Drucker-Prager plastic potential
$\boldsymbol{b}$	vector of body force per unit volume
b	number of fictitious cracks in uniaxial compression
c	cohesion
$\boldsymbol{d}$	nodal displacement vector
d	total differential, effective depth of a slab
e	out-of-roundness parameter
$\boldsymbol{f}$	stress vector
f	yield surface or failure criterion, function
f_c	uniaxial compressive strength of concrete
f_{bc}	biaxial compressive strength concrete
f_t	uniaxial tensile strength of concrete
f_y	uniaxial tensile and compressive strength of steel
g	plastic potential
$\boldsymbol{h}$	operator describing the hardening/softening rule
h	overall depth of a slab, distance
k	material characteristic of the Drucker-Prager yield surface
l	length
l_T	transmission length over which slip between steel and concrete occurs
l_F	fastening length between concrete and reinforcement
$\boldsymbol{m}$	plastic flow direction vector
m	bending moment per unit length
$\boldsymbol{n}$	gradient of the yield surface
n	number of time step, number of integration point
$\boldsymbol{p}$	load per unit area, weighing factor for Gauss point integration
$\boldsymbol{q}$	internal variables vector describing material with memory
r	radius in cylindrical coordinate
$r(\theta, e)$	elliptic function
$\boldsymbol{s}$	deviatoric stress tensor
s	reinforcement spacing, crack spacing
$\boldsymbol{t}$	vector of force per unit surface
t	thickness
$\boldsymbol{u}$	displacement vector
u	perimeter of control section, axial displacement in a truss
w	crack opening, vertical displacement of a slab
$\boldsymbol{x}$	position vector of the current configuration
x, y, z	Cartesian coordinates

Calligraphic letters:

$\mathcal{A}$	the finite element assembly operator
$\mathcal{L}$	operator to construct the strain displacement matrix
$\mathcal{N}$	general non-linear operator
$\mathcal{O}$	order of polynomial

Greek letters:

α	inclination, cone opening angle
β	relative size
Γ	finite element surface
γ	plastic multiplier
Δ	increment
δ	symbol of Kronecker, virtual value, plastic degradation variable
ϵ	strain tensor
σ	stress tensor
Θ	general tensor
κ	internal variable monitoring the amount of steel plastic strain
λ, μ	Lamé constants
ν	Poisson's ratio
ξ, η, μ	natural coordinates of isoparametric element
ξ, ρ, θ	hydrostatic, deviatoric invariants, and polar angle of Haigh-Westergaard
φ	polar coordinate angle
ϕ	friction parameter, diameter
τ	shear stress
ψ	dilatancy angle
ρ	percentage of reinforcement
∇	gradient operator
Ω	finite element volume
ω	elastic damage parameter

Superscripts:

$\_^{dev}, \_^{vol}, \_^{dil}$	deviatoric, volumetric, and dilatational part
$\_^{e}$	value of the e-th finite element
$\_^{i}, \_^{k}$	iteration
$\_^{S}$	symmetric part
$\_^{trial}$	trial value
$\_^{T}$	transpose operator

Subscripts:

$-_c, -_s$	concrete, steel contribution
$-_{i,j,k,l}$	tensorial indices
$-_e, -_p$	elastic, plastic part
$-_f, -_g$	value related to the yield function, plastic potential
$-_{mc}$	refer to Mohr-Coulomb criterion
$-_N, -_T$	normal, tangential component
$-_n$	load step, nominal value
$-_0$	initial or undamaged value
$-_r$	value at the rupture
$-_t$	at time t, tensile part, related to tensile force
$-_u$	related to the displacement
$-_{\phi,r,z}$	polar coordinate components
$-_{1,2,3}$	principal values

Chapter 1

Introduction

1.1 Description of the punching failure

The *punching failure*[1] in reinforced concrete structures was defined by Richart in 1948 [116] for a square slab as a pyramidal plug of concrete perforating through the slab beneath the column. This failure is sketched in figure 1.1 for a circular column illustrating that the *punching cone* is separated from the slab by the *punching crack.*

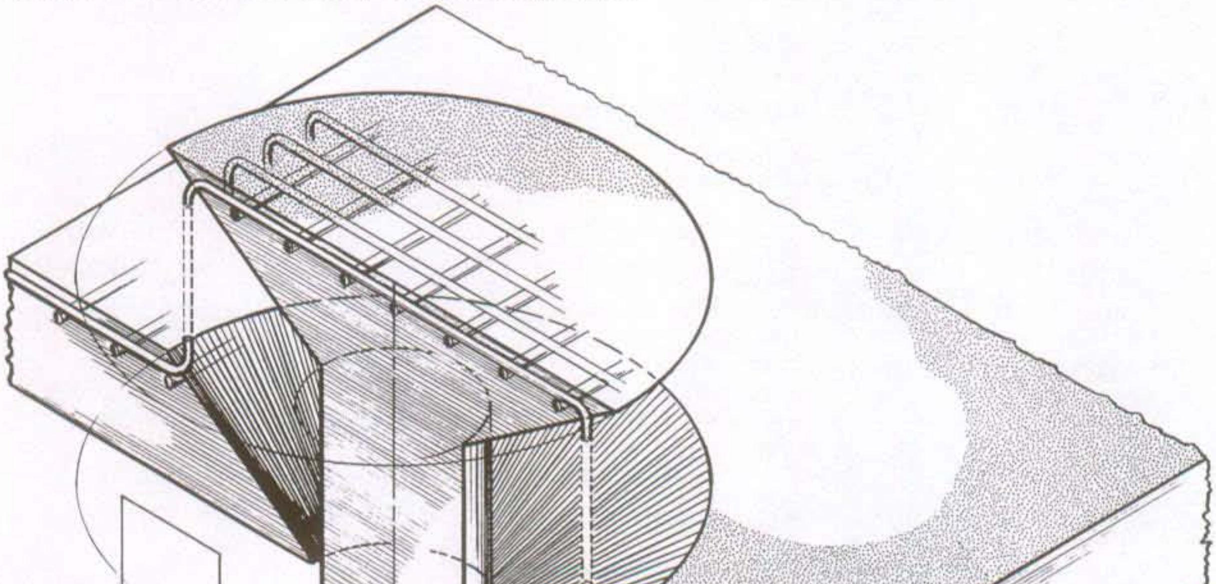

Figure 1.1: Sketch of punching failure in reinforced concrete

---

[1] All the terms that are defined in this research are given in italic for clarity purposes.

Various definitions which will be used in this research are presented in figure 1.2 for a circular slab of constant thickness h: the polar coordinates (r, φ, z), the tangential bending moment m_φ, the radial bending moment m_r, the radial and tangential cracks.

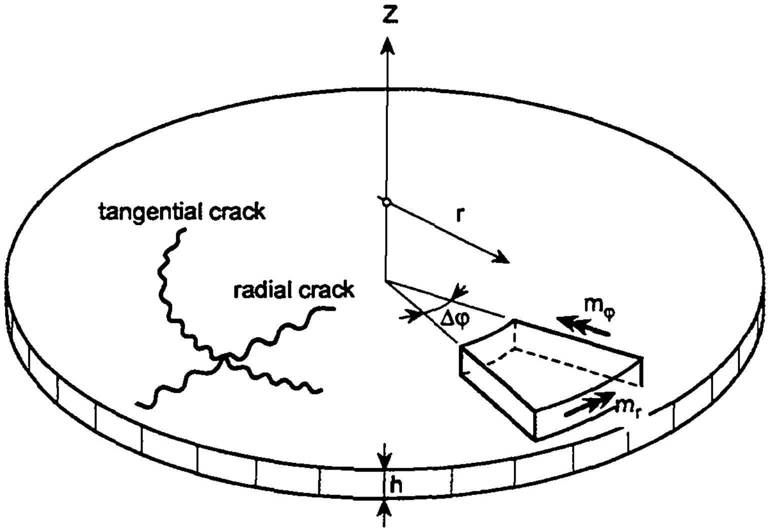

Figure 1.2: Polar coordinates, internal forces, and cracks observed in a circular slab

1.2 Failure prediction methods

1.2.1 Experimental methods

Experimental methods are commonly used to analyze punching failure in reinforced concrete structures. Even though punching failure experiments are determinant to understand the phenomenon they are characterized by the following drawbacks:

- experimental investigations are expensive,
- it is very difficult to obtain information such as strains, stresses, and cracks through the slab thickness without modifying the response of the slab,
- punching failure experiments are very sensitive with regard to the defects in concrete material, resulting in a large dispersion of the results.

More detail on the results of experimental investigations are presented in chapter 2.

1.2.2 Analytical methods

Control surface model

In 1913 Talbot [135] proposed a model to determine the shear strength of slabs. This model is based on the definition of the *nominal shear stress* which is calculated by dividing the punching load by the area of a cylindrical control surface which is normal to the plane of the slab. The strength of the slab is determined by comparing this nominal shear stress with a reference or admissible shear strength defined as a concrete characteristic. Based on Talbot's model, various models were proposed in which the control surface, the considered depth of the slab, and the distribution of the shear stress over the thickness were different. These derived models are included in the so-called *control surface model* as defined by Regan and Braestrup [114].

A commonly used version of this model is based on the control surface defined as the product of the effective depth d of the slab and the perimeter u at a distance $d/2$ from the column. The resulting nominal shear stress is:

$$\tau_n = \frac{P}{ud} = \frac{P}{\pi(2r + d)d}. \tag{1.1}$$

This version of the model is based on the assumption of a constant nominal shear stress over the slab thickness. The basic ingredients of this model (the control surface and the shear stress distribution) are shown in figure 1.3.

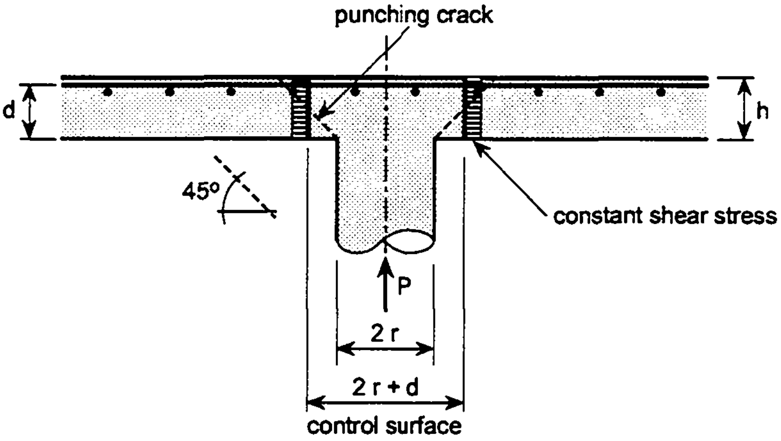

Figure 1.3: Control surface model

This model can be further extended by introducing empirical factors which depend on the amount of flexural reinforcement, the size of the slab, the shape of the column and so on. The resulting model is used by most code recommendations around the world (for example the SIA 162 [131]). The main disadvantage of this model is that for particular cases, such as large slabs or high percentage of reinforcement or tendons, the obtained levels of safety are inconsistent.

Mechanical model of Kinnunen and Nylander

The model developed by Kinnunen and Nylander [68] is derived from mechanical observations resulting from punching failure experiments of circular slabs. The mechanical model is shown in figure 1.4 and is composed of:

- rigid segments located outside the punching cone; each segment is bounded by two radial cracks, by the punching crack, and by the circumference of the slab; the rigid segments behave like rigid bodies,
- a compressed truncated conical shell that extends from the column to the root of the punching crack.

The compressed truncated conical shell is assumed to carry the segmental parts. The forces are determined based on equilibrium equations of the segmental parts. The criterion of failure is expressed in terms of a limitation of the inclined radial compressive stress and a limitation of the tangential compressive concrete strain at the shear crack. This model was originally developed for axisymmetric reinforcement. However, it was extended to take into account orthogonal reinforcement and dowel forces by Kinnunen [66].

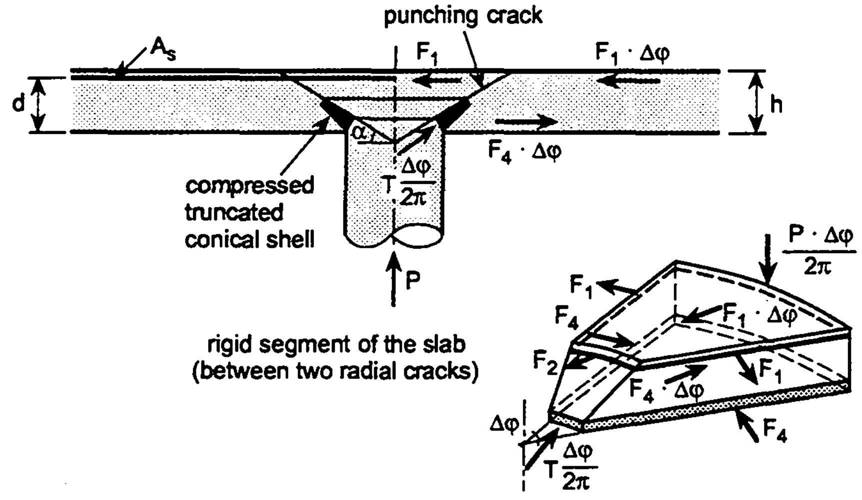

Figure 1.4: Mechanical model; (Kinnunen and Nylander 1960)

Comments

An upper bound value[2] for the punching load of reinforced concrete slabs was derived by Braestrup et al. [13] [14]. A failure mechanism was assumed so that the deformation are concentrated in a rotationally symmetric surface representing the punching crack. The concrete punch is assumed to be perpendicular to the slab. By equating the rate of external work done by the applied load with the rate of internal work dissipated by the failure, an analytical expression is derived for the punching load. It can be noted that this method does not take into account the flexural reinforcement.

Others interesting analytical models were developed, among others: the models developed by Hognestad [55], Andrä [1], or Pralong [106]. These models are not further described here.

Even though analytical methods are used worldwide, the only value that can be relied upon is the punching load. Displacements, strains and stresses, although necessary to understand such a complex phenomenon cannot be computed. The geometry is another important limitation of the analytical methods because only structures with simple geometry can be considered (symmetry, no hole or stiffening). Similarly, the effect of stirrups, prestressed cables or shear-heads is not adequately taken into account with analytical models.

1.2.3 Numerical methods

The development of numerical methods are a recent and active field of research. This is due to the development of computer technology and also to the progress in the area of finite element method applied to non-linear behavior. Some numerical simulations of punching failure in reinforced concrete structures are summarized below. It should be noted that all the simulations of punching failure were performed at the macro-level and that the micro-mechanics approach as recently summarized by Huet [57] was never applied to punching failure simulation.

Nilsson [100] examined the impact problem of a steel rod on a circular reinforced concrete slab (low impact velocity). Concrete was first assumed isotropic and then, due to crack formation, anisotropy was introduced by brittle failure. Reinforcement was treated as an elastic-viscoplastic material. The discretization in space (two-dimensional) and in time of the

---

[2] Upper bound load is a load at which an ideal structure will fail if a path of failure exists. This value is based on limit theorems as presented by Chen [19].

continuum equations was performed by the finite elements and finite difference techniques respectively. Yielding occurred in a wide region all around the punching pattern and no strain localization of the deformation was observed.

Zimmermann and Rodriguez [155] analyzed the non-linear response of a reactor building under an airplane impact loading. The concrete model considered isotropic hardening, multi-axial cracking and crushing in concrete. An elastic-plastic stress-strain relation coupled with kinematic hardening was used for steel reinforcement. The space discretization was done with three-dimensional isoparametric membrane elements for concrete and truss elements for steel. Time discretization used an implicit Newmark algorithm. The simulation of the impact of the Phantom type of aircraft leads to a punching failure. Figure 1.5 shows that, the steel yielding and concrete cracking and crushing points are diffusing at 45^0 under the load application area, similarly to the punching crack.

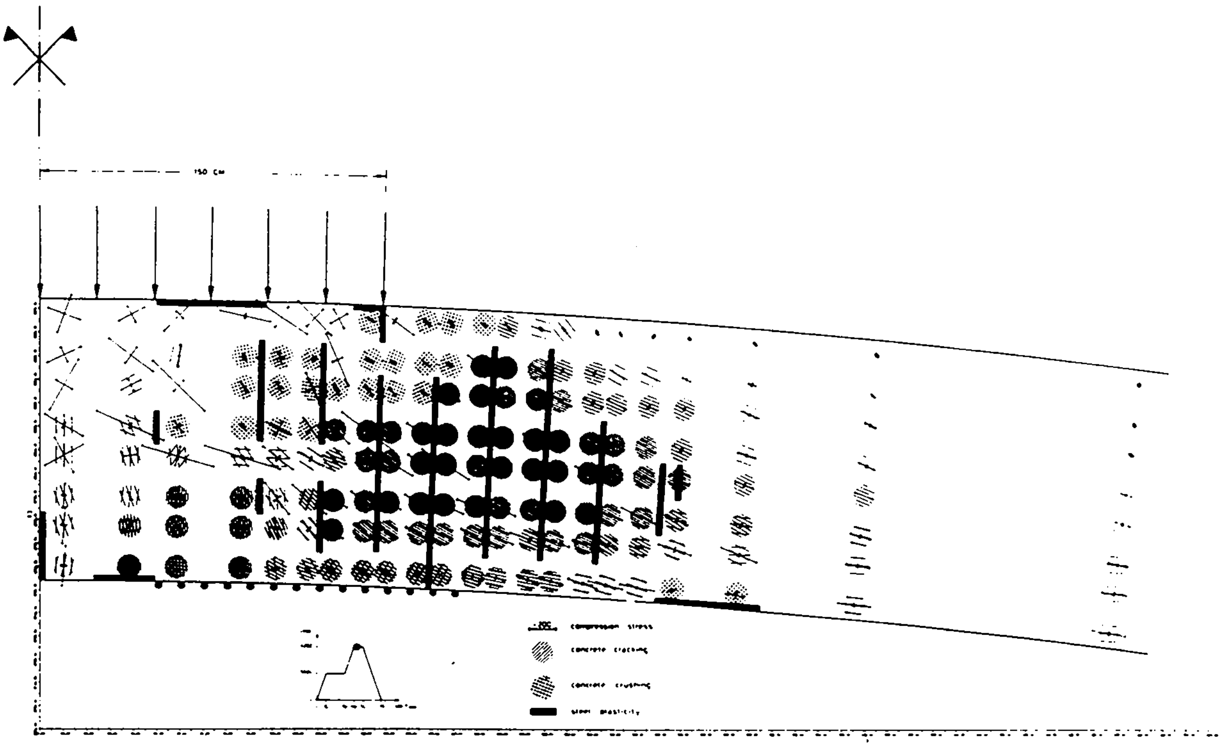

Figure 1.5: Simulation of a phantom impact on a reactor building; (Zimmermann and Rodriguez 1982)

Loseth et al. [78] showed that a finite element program developed for non-linear analysis of concrete structures can be used for the analysis of punching failure. However, they observed some numerical instabilities due to a tension cut-off[3] condition when stress reaches the uniaxial tensile strength of concrete. They also confirmed that the triaxial strength of the concrete model should take into account the influence of the confinement pressure.

Andrä [1] analyzed numerically the punching failure using the ADINA program. He compared the numerical prediction with the experimental results showing satisfactory agreement. Tangential and radial cracks were distinguished. However, the punching failure mechanism was not observed.

De Borst and Nauta [11] applied a model for handling non-orthogonal cracks. Deformations

---

[3] The tension cut-off condition limits the maximal normal stress to the uniaxial tensile strength. This condition is also known as the Rankine criterion as presented on page 45.

in concrete and cracks were decoupled allowing the algorithm to satisfy the yield surface and the fracture function. Punching of an axisymmetric slab was simulated with eight-node plane stress elements and discrete reinforcement. The predicted response was close to experimental results concluding that the smeared crack approach is capable of predicting diagonal cracks which occur in punching failures. The predicted crack pattern was close to the experimental results as shown in figure 1.6. At the ultimate load step no strain localization was observed as the punching crack spreads over various elements.

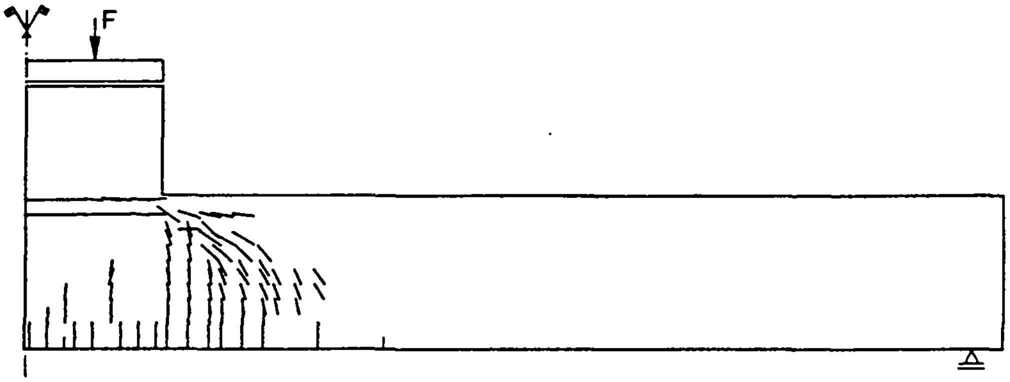

Figure 1.6: Tangential cracks in an axisymmetric slab simulation; (De Borst and Nauta 1985)

González-Vidoza, Kotsovos, and Pavlović [47] proposed a two-dimensional non-linear finite element analysis of symmetrical punching failure in reinforced concrete slabs. A modified Newton-Raphson method is used to follow the equilibrium path. The constitutive law for concrete is based on the decomposition of the elastic and plastic strains. The generalized triaxial conditions are expressed in terms of a smooth yield surface in the deviatoric plane. The concrete-steel interaction is governed by the assumption of perfect bond. The uniaxial steel behavior is modeled with a trilinear stress-strain law. Numerical predictions showed good agreement with the experimental ultimate load and displacement. Flexural and shear failures were distinguished. Again, no localized crack pattern was observed.

Dyngeland et al. [36] investigated the capabilities of various material models available in the DIANA program to simulate a shell exposed to punching. Even though it is mentioned that a strong indication of punching failure was obtained, the failure mechanism was not generated. It can be noted that the simulated response was stiffer than the one obtained experimentally.

The numerical simulation of punching failure in reinforced concrete structures seems to be promising. However, the localized punching failure mechanism was never clearly generated. Furthermore, the influence of the size—known as the size-effect—was not considered.

1.3 The purpose of this research

In 1953, Hognestad [55] wrote:

> *At present, it is hardly possible to evaluate the shearing strength of a slab through a rational theory based on fundamental principles, since they are not fully understood. The alternative is an approach of empirical nature which recognizes all the important known facts.*

But, the numerical simulation gives us the tool required to understand the fundamental principles governing punching failure. Along these lines, in 1985, Regan and Braestrup [23] mentioned that:

> *The treatment of punching by fracture mechanics is promising but will be extremely complex, requiring elaborate numerical procedures.*

The numerical simulation of punching failure is promising and therefore, the purpose of this research is:

the numerical analysis of punching failure in reinforced concrete structures.

Our capability to predict structural behavior should be improved in order to build more economic, safe, and aesthetic structures. The development of computational simulation tools will improve our ability to predict the performance of reinforced concrete structures.

1.4 Scope and organization

The development of the computational simulation tool is initiated with a description of punching failure in chapter 2. Different experimental reports are presented and discussed in order to establish the requirements and hypothesis that the numerical model must fulfill.

The development of the numerical model is described in two chapters. In chapter 3, the numerical model is formulated at the constitutive level whereas in chapter 4 the numerical model is described at the structural level. Once the numerical model is developed, it is tested and its capabilities and limitations are examined. The model is first tested using the shear failure of a footing. This simulation is followed by the simulation of simple tests on plain and reinforced concrete specimens: uniaxial traction and confined compression.

The simulation of punching failure of circular slabs is presented in chapter 6. This simulation should reveal the capabilities and limitations of the numerical model to predict the punching failure in reinforced concrete. This research ends with chapter 7 in which the punching failure is analyzed. The condition for punching failure to occur is established. Additionally, a parametric study of the punching failure phenomenon is realized.

A conclusion summarizes and assembles the results obtained during this research. Some suggestions for further work are given.

For conciseness purposes, five appendices are given: appendix A defines some mathematical notations, appendix B presents some notes on the flexural analysis of circular slabs, appendix C gives the gradients of the concrete model, appendix D describes the numerical models that are used for soil analysis, and appendix E depicts the implementation of the numerical model.

Chapter 2

Punching failure experiments in reinforced concrete structures

2.1 Introductory remarks

The punching failure in reinforced concrete structures is described in this chapter based on experimental results. The failure process is introduced with four typical experiments: Graf [48], Elstner and Hognestad [37], Kinnunen and Nylander [68], and Pralong, Marti, Brändli, and Thürlimann [84] [107] which were chosen to exemplify most of the phenomenons connected to punching failure. A discussion of the failure phenomenon is presented by adding to the description of these four experiments others complementary experimental results. Based on this discussion, the requirements that the numerical model should fulfill to predict the punching failure in reinforced concrete structures are derived.

2.2 Description of typical experiments

2.2.1 The experiment of Graf

In 1938, Graf [48] investigated the strength of thick reinforced concrete slabs submitted to concentrated loading. To exemplify this, four slabs 300 and 500 mm thick, composed of straight or bent reinforcement as shown in figures 2.1 and 2.2 are considered.

It is reported that punching failure is characterized by a distinctive cracking sequence. The first crack appears at the bottom of the slab along the perimeter of the column. As the load increases so does the number of cracks and they expend through the slab thickness. At the outermost part of the slab, only radial cracks are observed. The punching failure takes place suddenly at the load called the *punching load.*

The punching crack across the slab thickness for slabs with straight reinforcement is shown in figure 2.1. This crack is depicted along the direction of the reinforcement and is characterized by an inclination which varies from 31^0 to 53^0. This inclination increases with increasing slab thickness, as for the thin slab, the punching crack has a lower inclination than for the thick one. However, this remark is not rigorous as for the thick slab, the punching crack is also influenced by the boundary conditions (punching crack reaches the supports). Another parameter which influences the inclination of the punching crack is the direction of the steel layer. The inclination of the shear crack along the bottom layer of reinforcement is always lower than the one along the top layer. The position of the steel layer is characterized by the effective depth of the slab and the previous observation can thus be restated as: the inclination of the punching crack is reduced when the effective depth is increased.

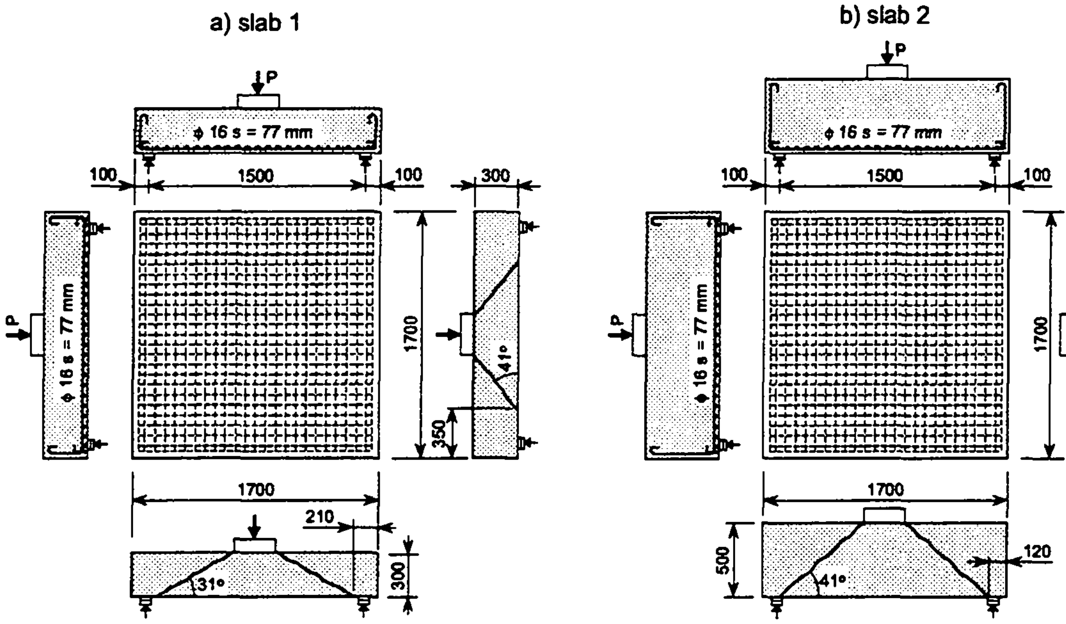

Figure 2.1: Setup and punching cracks of slabs with straight reinforcement: (a) 300 mm, (b) 500 mm thick slab; (Graf 1938)

The type of reinforcement also influences the shape of the punching crack as illustrated by comparing figures 2.1 and 2.2. For slabs with straight reinforcement, one punching crack which is practically linear is observed whereas for slabs with bent reinforcement the punching crack is curved and various opened shear cracks are observed. For slabs with straight reinforcement, prior to failure, no crack could be seen on the top of the slab, whereas for slabs with bent reinforcement, the punching crack at the top of the slab could be observed.

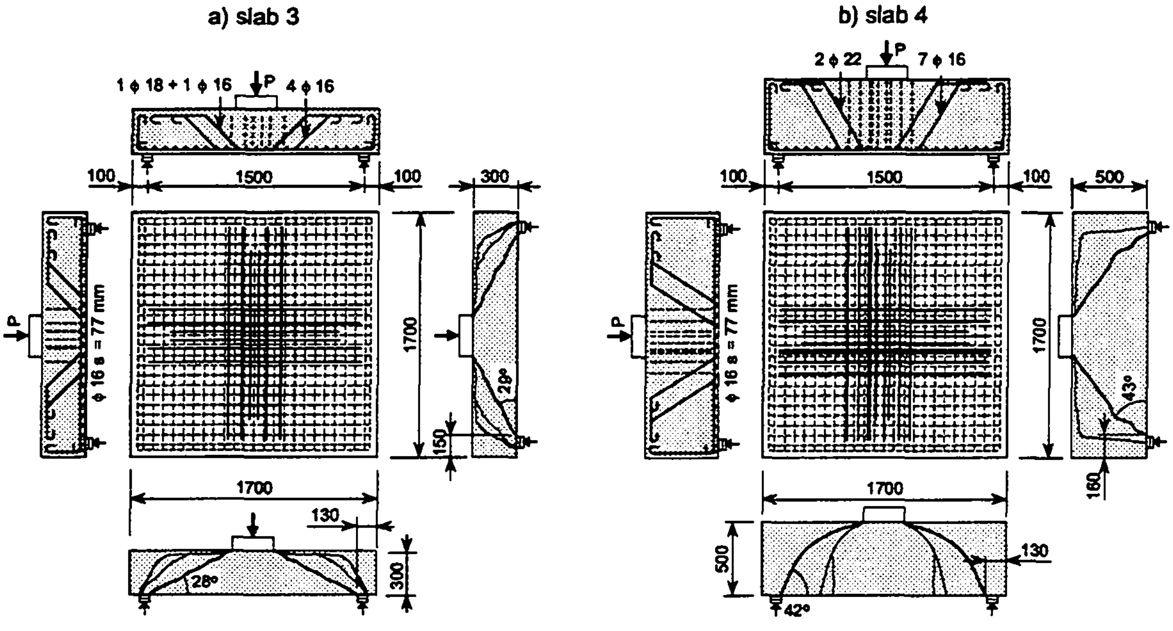

Figure 2.2: Setup and punching cracks of slabs with bent reinforcement: (a) 300 mm, (b) 500 mm thick slab; (Graf 1938)

The load-displacement curves of these four slabs are presented in figure 2.3. Slabs 1 and 2 which are made of straight reinforcement but different thickness behave in a similar way even though slab 2 is much stiffer than slab 1. The same analogy is valid for slabs with bent reinforcement. The main difference between slab made with bent reinforcement and slab made with straight reinforcement is that the first one sustains larger displacement and higher load. Therefore, the shape of the bars influences the slab response. Nevertheless, the behavior of slabs with bent reinforcement is also improved because the shape of the reinforcement increases the bond between steel and concrete. This increase of bond is particularly important for this experiment as bars without ribs were used.

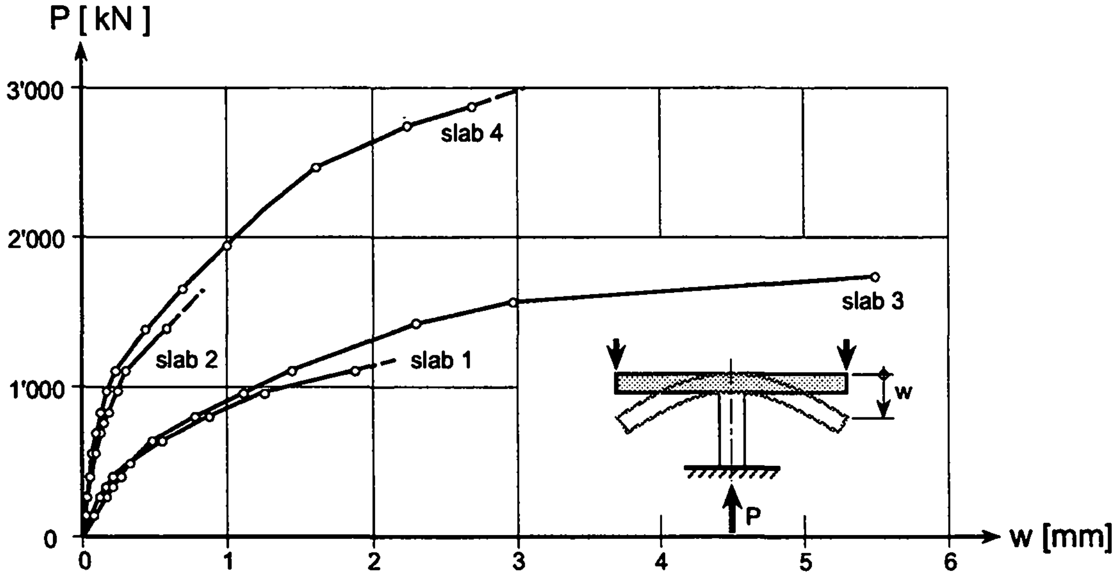

Figure 2.3: Responses of tested slabs; (Graf 1938)

An attempt to illustrate the influence of the slab thickness is presented. The nominal shear stress as defined in equation 1.1 is computed for the slabs made of straight reinforcement. The 300 mm thick slab is characterized by a nominal shear stress of 3.3 N/mm^2 which reduces to 2.8 N/mm^2 for the 500 mm thick slab. Therefore, the nominal shear stress decreases as the slab thickness increases. The same observation is made for slabs with bent reinforcement. This influence of the size—known as the size-effect—observed here is further discussed in section 2.3.4.

2.2.2 The experiment of Elstner and Hognestad

In 1956, Elstner and Hognestad [37] investigated extensively the behavior of reinforced concrete slabs. But, contrary to most of the tests performed at that time, they investigated the strength of relatively thin slabs. They tested 1830 mm square slabs supported at the four edges and loaded up to failure through a centrally located column stub as presented in figure 2.4.

The influence of the percentage of flexural reinforcement is illustrated in figure 2.5(a) where the response curves of similar slabs except for the percentage of flexural reinforcement of ($0.5\% \leq \rho \leq 3.0\%$) are presented. In addition, along these response curves are indicated the load value for which the first yielding of the reinforcement P_{yield} is measured on strain gages. It is observed that slabs with a high percentage of reinforcement fail in a brittle[1] way whereas

---

[1] A brittle failure is characterized by little deformation before the occurrence of a sudden failure.

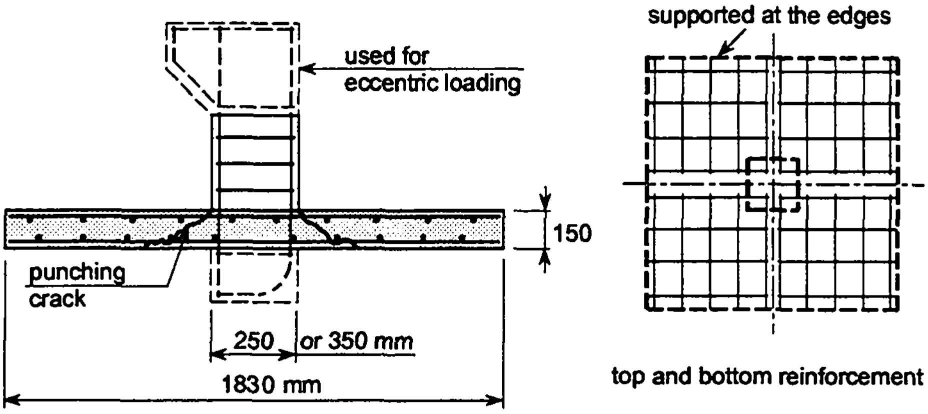

Figure 2.4: Setup of punching experiment; (Elstner and Hognestad 1956)

slabs with a low reinforcement percentage fail in a ductile[2] manner. This leads to the definition of two types of failure:

- *the flexural failure* which is characterized by a rapid increase of the deflection for a small increase of load,
- *the punching failure* which is a characterized by a sudden failure along an inclined crack.

This failure distinction is further studied in section 2.3.1.

The influence of the concrete strength on the slab behavior has been examined by varying systematically the compressive strength of concrete. In figure 2.5(b) the response of similar slabs, except for the concrete compressive strength ($12.7\leq f_c \leq 34.5$ N/mm^2) are reproduced. The punching load increases (355 to 546 kN) with increasing concrete strength and the stiffness of the response is also increased. For slab made of low compressive strength concrete, it is not possible to observe any yielding of the reinforcement because the punching failure occurs first.

2.2.3 The experiment of Kinnunen and Nylander

Kinnunen and Nylander [68] tested circular 150 mm thick slabs, 1840 mm in diameter supported along the circumference and loaded on a column stub at the center.

The influence of the arrangement of the reinforcement is demonstrated with the two slabs shown on the top of figure 2.6. One of them is made with ring reinforcement and the other is made with orthogonal reinforcement. The overall behavior of these two slabs are similar except for little differences as presented in the following.

The shape of the punching crack through the slab thickness is shown in figure 2.6(c). It is observed that the punching crack is more inclined for the slab with ring reinforcement than for the slab with orthogonal reinforcement. The type of reinforcement is not the only difference between these two slabs as the percentage of reinforcement is not similar. Considering these two dissimilarities between the tested slabs, it is inferred that the inclination of the punching crack is influenced by the type and the percentage of reinforcement.

The crack pattern at the top of the slab is shown in figure 2.6(d). In slab with ring reinforcement the tangential and the radial cracks can be clearly distinguished, whereas in the slab with orthogonal reinforcement, the crack pattern does not follow the radial and tangential geometry but is more like a net, especially inside the punching cone. The difference between the crack pattern of these two slabs is explained by the fact that the state of stress in slab with ring

---

[2] A ductile type of failure is preceded by large deformation.

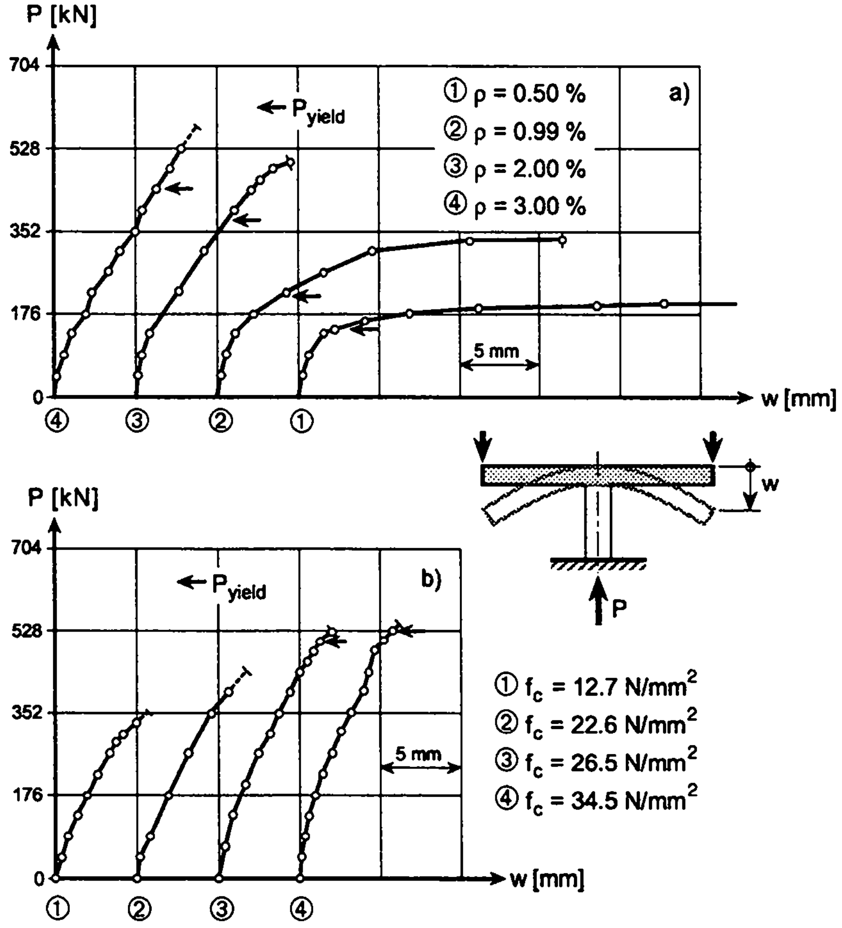

Figure 2.5: Responses for slabs made of: (a) different percentages of reinforcement, (b) different concrete strength; (Elstner and Hognestad 1956)

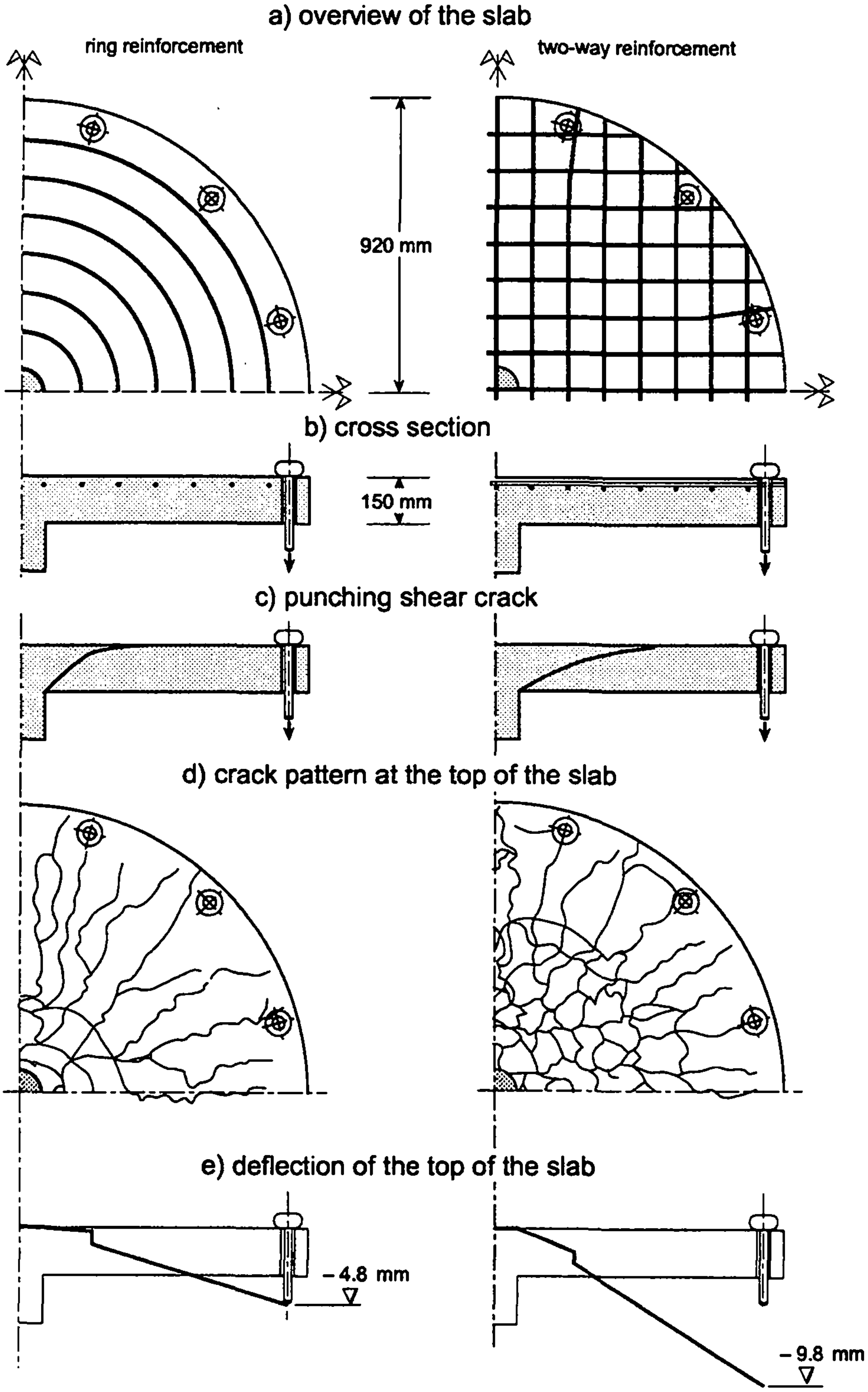

Figure 2.6: Comparison of slabs with ring and orthogonal reinforcement; (Kinnunen and Nylander 1960)

reinforcement is polar-symmetrical. However, in the slab with orthogonal reinforcement the state of stress is oriented toward the direction of the reinforcement, resulting in a bi-directional state of stress.

The deflection of the top of the slab is also different between these two slabs as shown in figure 2.6(e). For slab with ring reinforcement little deflection is observed in the portion of the slab inside the punching crack. However, for slab with orthogonal reinforcement, this deflection is important. This illustrates that ring reinforcement inside the punching cone is stiffer than orthogonal reinforcement. For slab with orthogonal reinforcement, the sustained deflection at failure is much larger than for slab with ring reinforcement. This difference is due to the *dowel action*[3] of the reinforcement cutting across the punching crack. For a slab made of orthogonal reinforcement, the punching crack intersects several reinforcement bars, whereas for the slab made of ring reinforcement the punching crack intersects no bars.

The steel strain at the top of the slab made of ring reinforcement is shown in figure 2.7. The extreme value of the steel strain is located in the region of the punching crack. At the exterior of the punching crack, the strain in the flexural reinforcement decreases with increasing radius. For the reinforcement located between the column and the punching crack, the steel strain decreases as the load increases. This decrease is only observed for the slab with ring reinforcement because for the slab with orthogonal reinforcement each bar located inside the punching cone crosses the punching crack and never unloads except during the post-failure response.

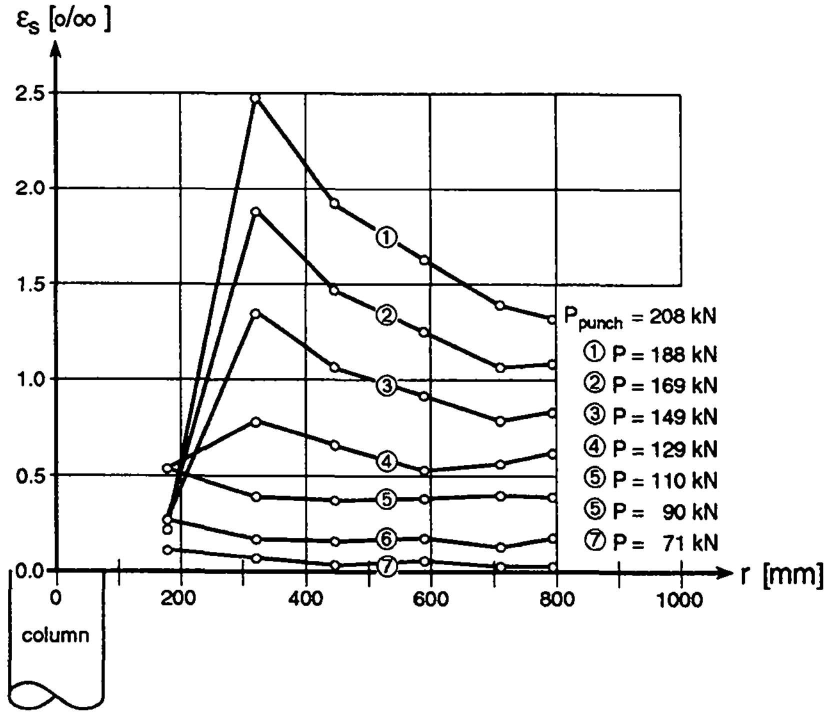

Figure 2.7: Tangential steel strains at the top of slab with ring reinforcement; (Kinnunen and Nylander 1960)

---

[3] The dowel action is defined as a shear transfer mechanism between concrete and reinforcement where a highly localized state of stress is observed as defined by Chen [19].

2.2.4 Experiments performed at ETHZ

At the ETH in Zürich two series of test were performed and reported by Marti et al. [84] and Pralong et al. [107] on the same octagonal slab supported at the center by a circular column and loaded at the edges.

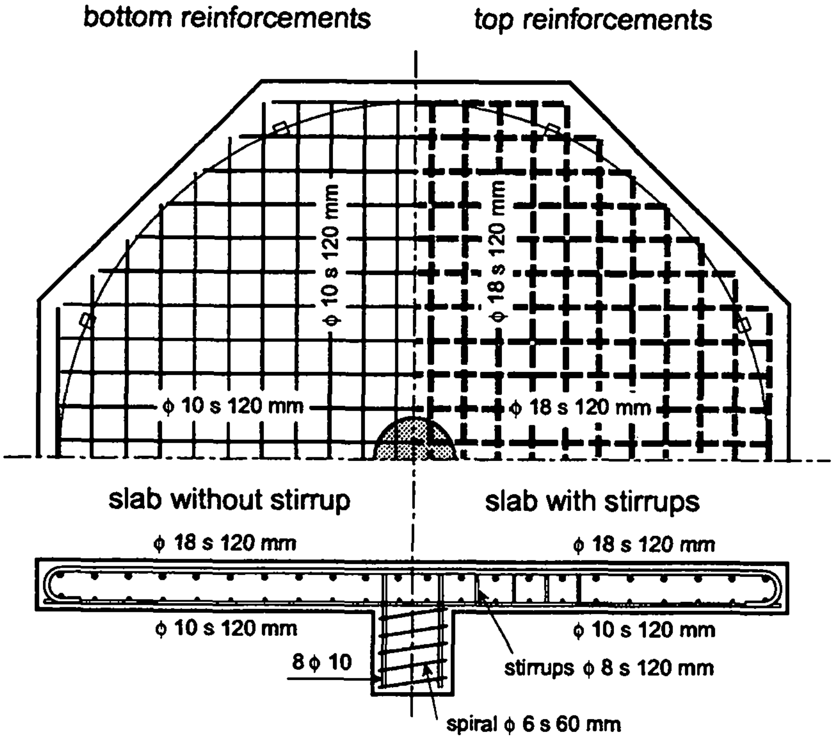

Figure 2.8: Setup of punching experiment; (Marti et al. 1977)

The influence of the shear reinforcement is examined with the two slabs shown in figure 2.8 which are made of the same flexural reinforcement but vertical stirrups are set in only one slab. The response of these two slabs is reproduced in figure 2.9. It is observed that already for low load level, the stiffness of the slab with stirrup is higher than the one of the slab without stirrup. This indicates that cracking occurs for low load level as the stirrup are active only when cracking is initiated. By comparing the response curves, it can be observed that the stirrups mainly increase the maximal displacement that the slab can sustain. It can also be noted that the punching load of the slab with stirrups is slightly higher than the one observed in slab without stirrup. Slab without stirrup fails under very little deformation characterizing a brittle type of failure. On the other hand, the slab with stirrups fails in a ductile way as large strains due to yielding of the stirrups close to the extremity of the column are observed.

Pralong et al. [107] tested a similar slab than the one shown in figure 2.8 (without stirrup) but with ring reinforcement at the top layer. For this slab, the evolution of the concrete strain is shown in figure 2.10. The radial and tangential strains are presented at the top and bottom of the slab, for different load steps. It is observed that the tangential and radial strains at the top of the slab are maximum in the vicinity of the punching crack. The variation of the radial strain along the radius is more important than the variation of the tangential strain. The compressive strain at the bottom of the slab exhibits less variation along the radius than the tensile strain at the top. It can be noted that, close to the column stub, the compressive strain in a radial direction decreases as the load approaches its ultimate value. This is probably due to a change of response of the slab which approaches an arch type of response where the points located outside the arch unload.

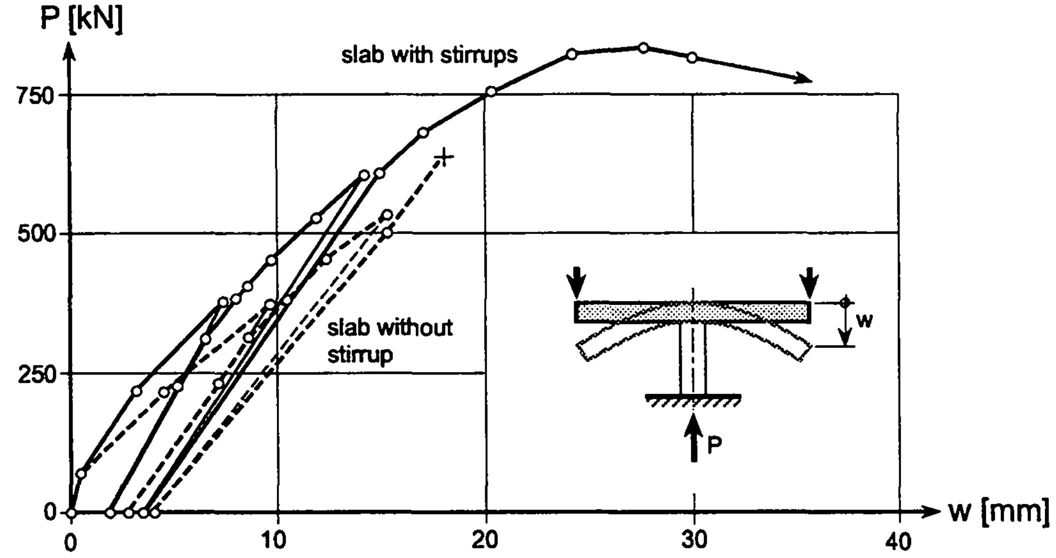

Figure 2.9: Influence of stirrups on the response; (Marti et al. 1977)

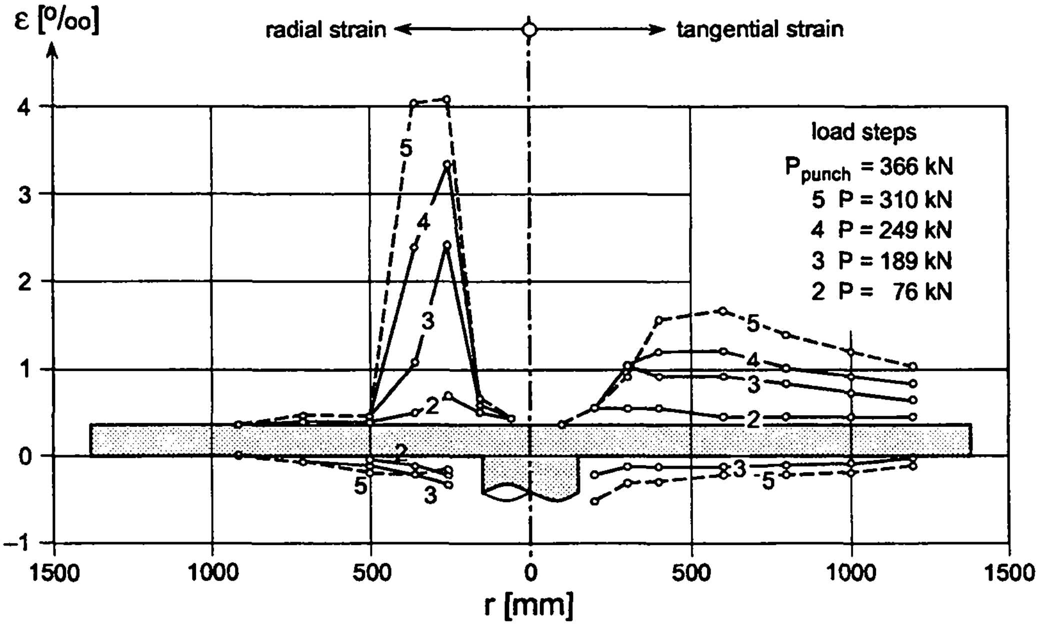

Figure 2.10: Evolution of concrete strains during punching experiment; (Pralong et al. 1979)

2.3 Discussion of the experimental results

2.3.1 Distinction between different failure modes

Two different failure modes were already illustrated in section 2.2.2 which are the flexural and punching failure modes. A classification of these failure modes is established as suggested by Moe [95]. The *ultimate flexural load*=P_{flex} of a slab is the load at which a flexural failure is observed. This value is computed with the yield-line theory as developed in appendix B.2. The *punching load*=P_{punch} is measured experimentally and is the load at which the punching failure occurs. Based on these two definitions the distinction between the flexural and punching failure are summarized in table 2.1. Practically, this distinction between failure modes is not clearly defined as other factors such as boundary conditions, layout of reinforcement, dispersion of concrete quality influence the failure.

$P_{punch}/P_{flex} > 1$	flexural failure
$P_{punch}/P_{flex} < 1$	punching failure

Table 2.1: Condition for flexural or punching failure

Even though flexural and punching failures could be differentiated, the flexural and shear strength interact. This interaction is partly due to the fact that the maximum flexural moment and the maximum shear force are located in the same section of the slab, that is in the perimeter of the support. This interaction is clearly demonstrated by the test performed by Elstner and Hognestad [37]. For different slabs with very close compressive strength the punching load and the ultimate flexural load are summarized in table 2.2. It is observed that for increasing flexural strength the punching load increases. Therefore, the flexural and shear strength interact in the punching failure phenomenon as suggested by Moe [95].

Slab type	f_c [N/mm^2]	P_{flex} [kN]	P_{punch} [kN]
B-1	14.2	156.6	176.4
A-1a	14.7	357.3	299.2
A-2a	13.7	576.4	330
A-3a	12.8	649.4	352

Table 2.2: Ultimate flexural loads and punching loads for slabs with close compressive strength; (Elstner and Hognestad 1956)

Richart [116] considering reinforced concrete column footings, distinguished in addition to flexural and punching failures a bond failure. A *bond failure* is characterized by a slip of the reinforcement and is due to a lack of bond between steel and concrete. This failure is circumvented by using reinforcement with inclined ribs. Even though some of the footings failed initially due to yielding in steel, or excessive bond slip, the final collapse was mostly due to punching failure.

2.3.2 Decomposition of the punching phenomenon into phases

The punching failure phenomenon can be decomposed into distinct phases according to many authors. Prior to delimiting these phases, different results are examined.

Walther et al. [144] investigated the punching failure of slabs reinforced with stiff shear-heads. They tested 300 mm slab supported at the center on a circular column of 300 mm diameter and loaded on the side. The shear-head was stiff enough so that the failure occurs outside the shear-head. The punching crack across the slab is shown in figure 2.11. It can be observed that for a slab with a stiff shear-head and a high percentage of reinforcement (ρ=0.78%) several inclined cracks are formed across the slab thickness but the failure mechanism is localized only along one inclined crack. It can be noted that at the top of the slab, the punching crack expands horizontally between the reinforcement layers up to the support.

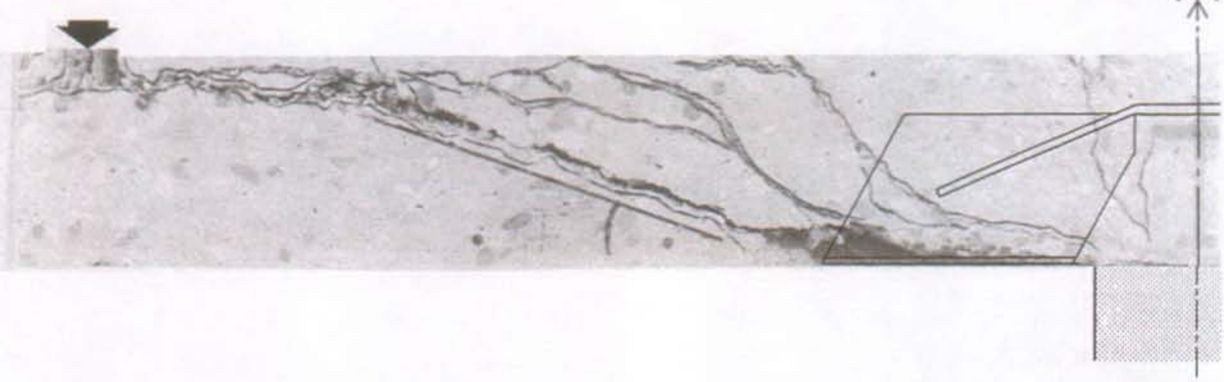

Figure 2.11: Punching crack in a slab reinforced with a shear-head; (Walther et al. 1994)

During the same investigation, a reference slab was tested without shear-head and the cracking sequence at the top of the slab is shown in figure 2.12. It is observed that the radial cracks are formed in the very early loading stage and they quickly expand toward the support. In the opposite, the tangential cracks are concentrated in the vicinity of the column. The top of the punching crack is shown in the last picture of figure 2.12. Even though the test was carefully operated, the punching crack is not axially symmetrical. This indicates that the shape of the punching crack is very sensitive.

Elstner and Hognestad [37] reported that prior to punching failure, it is impossible to predict the location of the punching crack which seems to be completely independent of the cracks formed beforehand. This confirms that punching failure is a sudden phenomenon.

Regan [113] showed that punching failure is preceded by cracking across the slab thickness. This is determined by measuring the concrete strains across the slab thickness during loading as reproduced in figure 2.13. It is observed that the strain increases linearly up to the cracking load. Under further increase of the load, the strain increases faster than during the linear phase, revealing non-linear deformations characterizing micro-cracking. This micro-cracking across the slab thickness is appearing at half of the punching load. Under further increase of the load the increase of concrete strain is stabilized to a constant rate (constant slope) identifying a stable behavior. These observations illustrate that micro-cracks are already formed across the slab thickness before failure occurs. It is conceivable that failure occurs by coalescence of these micro-cracks into one single punching crack. It has to be noted that these experiments were realized for thin slabs.

Moe [95] tested square slabs with holes near the face of the column. These particular slabs provided the opportunity to study the internal failure mechanism. He observed through these holes the formation of inclined cracks. These cracks develop at 60% of the punching load. They usually start from bending cracks and extend up to the neutral axis. For increasing load these cracks develop toward the top of the slab. The observed crack width evolution is smooth indicating that the cracks formation prior to failure may not be as sudden as it is generally assumed. It should be noted that the holes influence the slab response as reported by Müller et al. [92] especially for slab without shear reinforcement.

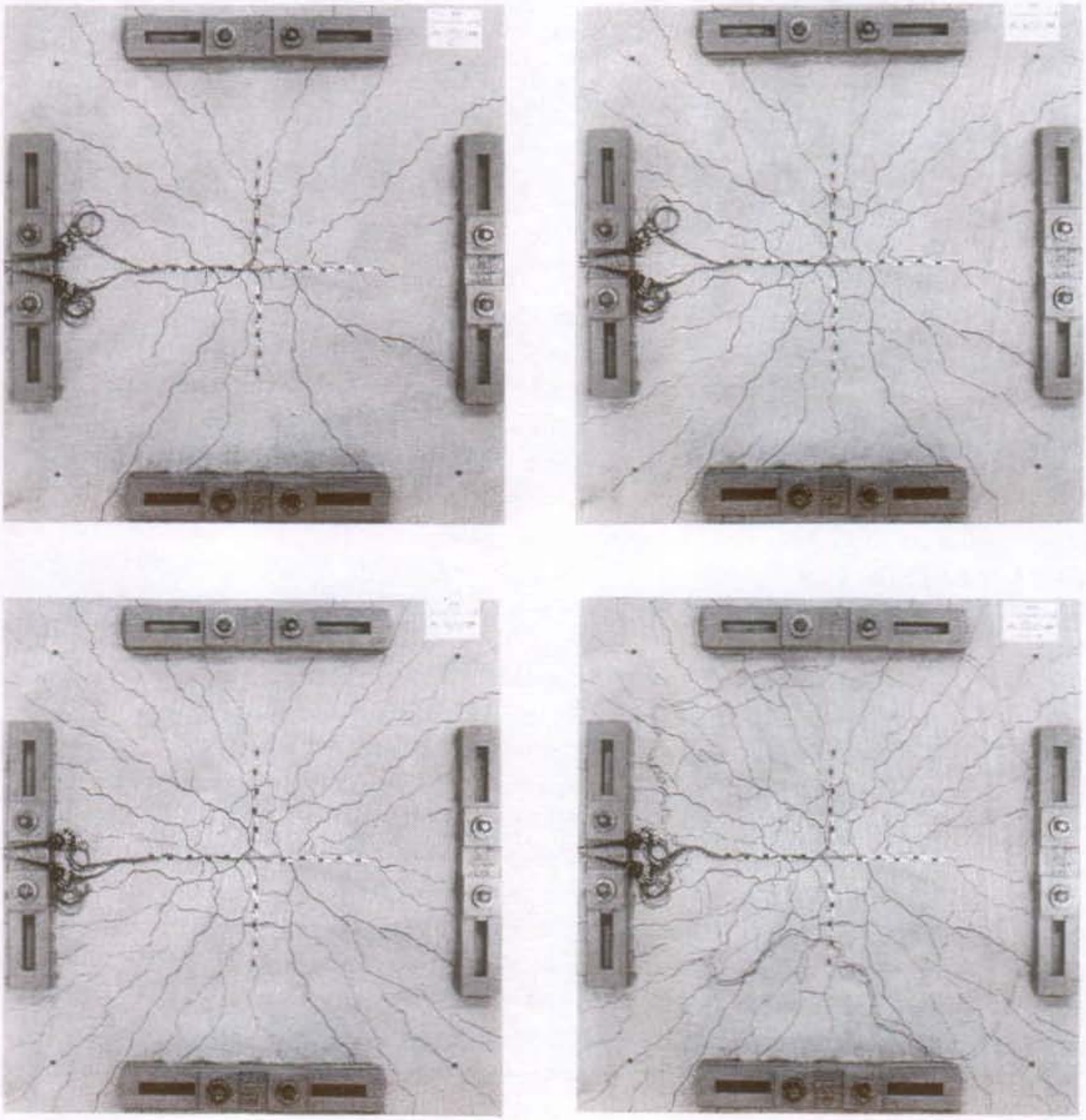

Figure 2.12: Cracking sequence at the top of a slab for P=480, 720, 1000, and 1200 kN; (Walther et al. 1994)

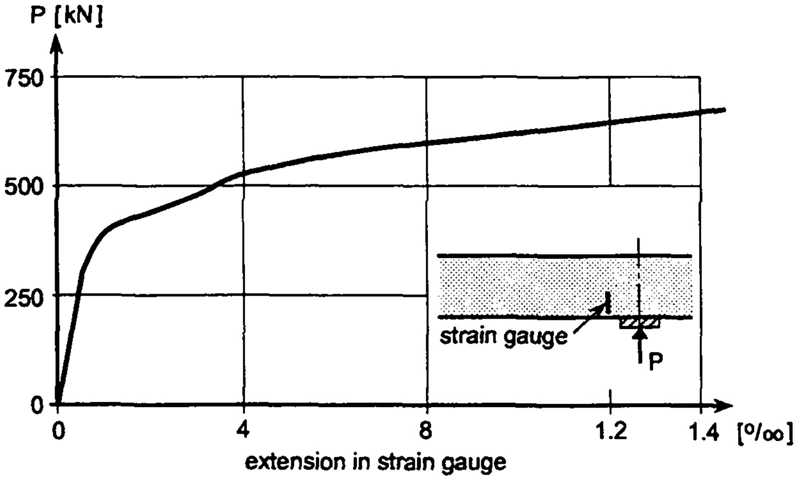

Figure 2.13: Evolution of the concrete strain across the slab thickness; (Regan 1983)

Cracking being the most important non-linear phenomenon occurring during the punching process, it will be used to delimitate the different phases of punching failure. Considering all the descriptions presented here, the punching failure mechanisms in reinforced concrete structures is best decomposed into four phases.

1. *The linear elastic phase:* where both the concrete and steel behave in a linear and elastic manner so that no cracking or yielding are observed. The slab response during this phase can be analyzed with the elastic bending theory as summarized in appendix B.1. This phase is completed when the first crack arises which corresponds to the *cracking load*=P_{crack}.

2. *The phase of flexural response:* this phase is initiated when the first flexural crack appears. This crack is a tangential crack located on the top surface along the circumference of the column. Under increasing load, radial cracks begin to form at the perimeter of the column and spread out toward the extremity of the slab. This phase is completed once the first tangential crack is a stress-free crack.

3. *The phase of shear resistance:* once the first tangential crack is a stress free crack, the behavior of the slab changes and shear resistance is mobilized. This shear behavior is characterized by inclined cracks across the slab thickness. The shear resistance is not only influenced by the concrete strength but also by the shear reinforcement and the dowel action. During this phase, few new flexural cracks form. However, existing cracks open and sudden coalescence into a single inclined crack which is the punching crack occurs. This is the end of the shear resistance phase.

4. *The post-punching failure phase:* the slab is separated into two parts connected by reinforcement. This phase depends considerably on the presence of shear reinforcement as shown in section 2.3.6.

These four phases are distinguished in all punching experiments even though the transition between the phase of flexural response and the phase of shear resistance is not clearly observed.

2.3.3 The influence of the geometry and the boundary conditions

Geometry

Different types of structures fail by punching such as: footings, slabs or shells. Footings were mainly tested at the beginning of the century: Talbot [135] and Richart [116] tested footing walls rested on a bed of springs to approximate the soil pressure. Later, the punching of slabs was investigated in laboratory and are nowadays the most tested structures. Recently, the punching of shell structures is investigated. For these three kinds of structures, punching failure can be concocted with little differences in the overall behavior.

The influence of the curvature of the shell is reported by McLean et al. [86]. They tested reinforced and prestressed lightweight concrete slabs and shells, representing the exterior walls of offshore structures. They clearly showed that due to the curvature of the shell, the shear strength increases. This effect is due to the dome action.

In flat slabs, the presence of *capitals* (flare the top of the column), *drop panels* (increasing thickness around the column), beam-supported slab and holes are of great importance. Skew slabs behave differently than rectangular slabs as shown by Regan [113]. Rectangular slabs are stiffer than skew slabs and the corresponding punching load is also higher.

The span-depth ratio of square flat slabs influences the punching failure as presented by Lovrovich and McLean [79] for axisymmetric slabs with a constant thickness and a varying support diameter. The punching strength increases as the span-depth ratio decreases below the value of six. This increase of strength is due to the development of compressive struts for low span-depth ratio.

The boundary conditions

The influence of the boundary conditions was introduced in section 2.2.1 as Graf [48] reported that for a thick slab, the punching crack reaches the support. Elstner and Hognestad [37] tested similar slabs supported either at the entire perimeter or on only two opposite edges. The resulting crack pattern is different for each slab. The slab supported at the whole perimeter shows a stiffer behavior than the other one and the failure load is also higher.

The influence of the horizontal restraints presented by Taylor and Hayes [136] was determined by testing pairs of slabs; one is simply supported and the other is simply supported but confined within a surrounding steel frame. For slabs with a low percentage of reinforcement, the increase in punching strength due to lateral restraint is 24% to 60%, whereas for a slabs with a high percentage reinforcement, the increase due to the lateral restraints varies from zero to 16%. The presence of the frame reduces the ductility of the section and results in a failure process which is similar to a brittle type of failure.

Regan [113] tested slabs subjected to in-plane loading which was provided by prestressing the slab prior to testing. The influence of the in-plane compression on the crack pattern is illustrated in figure 2.14. The in-plane compression closes the cracks perpendicularly to the axis of the in-plane loading. The punching load of the slab with in-plane compression is increased by 10%.

The influence of the shape of the support (column) has been reviewed by the committee ASCE-ACI [2]. In general, slabs loaded through circular areas are stronger than those loaded through square or rectangular areas.

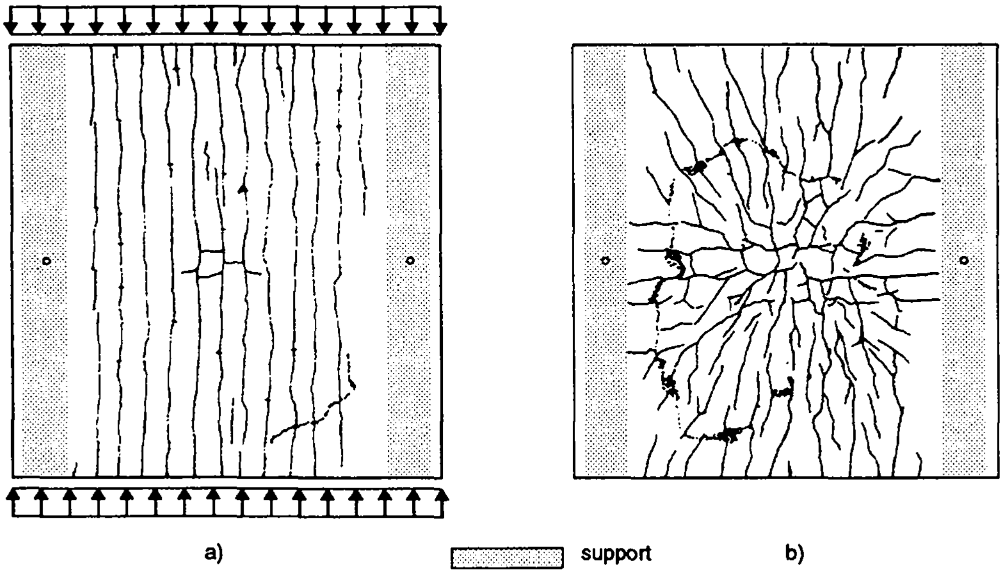

Figure 2.14: Crack pattern at the top of slabs: (a) with, (b) without in-plane compression; (Regan 1983)

2.3.4 The size-effect

The size-effect in punching failure was introduced in section 2.2.1 where it is shown that the nominal shear stress of a thin slab is higher than the one of a thick slab.

Kinnunen et al. [69] investigated the influence of slab thickness and the effect of shear reinforcement on the punching strength of rectangular slabs. Thick slabs of 730 mm and 550 mm were tested and compared to small scale slabs. It is observed that the size-effect exists as the nominal shear stress decreases with increasing the effective depth of the slab. In addition, it is reported that the size-effect decreases if the slab is made with shear reinforcement.

Tolf [141] tested circular slabs supported on circular columns. Two different slabs scaled with a factor two for the geometry, the aggregate sizes, the diameters of the reinforcing bars and the testing arrangement were tested. It is reported that the size-effect is obvious for slabs without shear reinforcement and that it is more pronounced for higher percentage of reinforcement.

Bažant and Cao [10] further verified the size-effect characterizing punching failure. They tested circular reinforced concrete slabs with different scales. The response curves of these slabs are presented in figure 2.15. The shape of the response curves and especially the shape of the post-peak response are influenced by the slab thickness. A thick slab exhibits an important softening response after the peak, whereas a thin slab shows little softening after the peak. The response curve of a thick slab is quite similar to the response curve of a direct tension test. The response curve of a thin slab is similar to an elastic perfectly plastic behavior. They concluded that the behavior of a thick slab being brittle is related to linear elastic fracture mechanics, whereas the behavior of thin slab is close to plasticity theory. It has to be noted that the slabs tested by Bažant and Cao are very thin and not comparable to slabs built in reality.

2.3.5 The influence of concrete strength

The influence of the concrete compressive strength was examined by Elstner and Hognestad [37] as introduced in section 2.2.2. Except for this investigation, few tests were performed

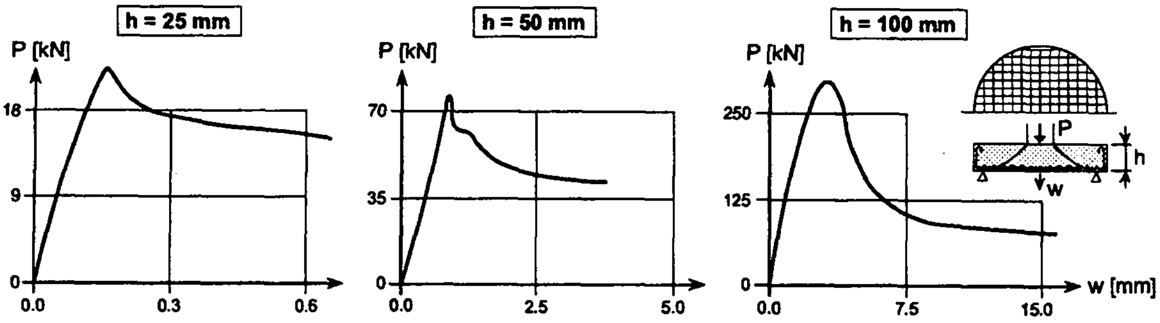

Figure 2.15: Responses for slabs with different thickness; (Bažant and Cao 1987)

on the influence of the concrete strength on punching failure as mentioned by Regan [112]. Furthermore, the uniaxial compressive strength was the only investigated parameter.

Recently, Hallgren and Kinnunen [50] performed some tests on punching of high strength concrete slabs. For concrete with a compressive strength of 110 N/mm^2, the load capacity of punched slabs is 60% to 70% higher than the one for slabs made of normal concrete. The capacity of angular rotation is also increased by 45% with the use of high strength concrete.

2.3.6 The influence of reinforcement

Influence of the flexural reinforcement

The influence of the flexural reinforcement was examined by Elstner and Hognestad [37] as already presented in section 2.2.2. They further investigated the influence of the reinforcement in showing that the degree of yielding at failure ranged from none for slabs with a high percentage of reinforcement to practically full yielding for slabs with a low percentage. Another observation showed that the ultimate capacity of slabs does not depend on compressive reinforcement. The arrangement of the reinforcement is also important as shown in section 2.2.3, when considering the difference between orthogonal and ring reinforcement. Likewise, the influence of skew reinforcement is important as reported by Regan [113]. Two skew slabs, one with skew reinforcement and one with orthogonal reinforcement were tested. The slab with skew reinforcement is softer than the slab with orthogonal reinforcement, but the punching load is similar for both slabs.

Influence of shear reinforcement

Shear reinforcement can be divided into three basic types: shear-head reinforcement, bent reinforcement, and stirrup. Shear-head reinforcement is not examined in this research because failure always occurs outside the shear-head leading to a standard punching failure as shown by Walther et al. [144]. The influence of bent reinforcement was already investigated in section 2.2.1. The influence of stirrups was introduced in section 2.2.4 and is further examined.

Dilger and Ghali [30] showed that stirrups have a significant effect on the ductility. The response curves of three different slabs are reproduced in figure 2.16: one slab without stirrup and two slabs with stirrups (one failing outside and one through the stirrups). The slab without and the slab with stirrups but failing at the outside of the shear reinforcement are characterized by a brittle failure, even though the slab with stirrups failed at a punching load which is higher. The slab failing through the shear reinforcement behaves in a more ductile way due to yielding of all the stirrups before the punching load is reached. Slabs with stirrups demonstrate that they sustain more loads and displacements.

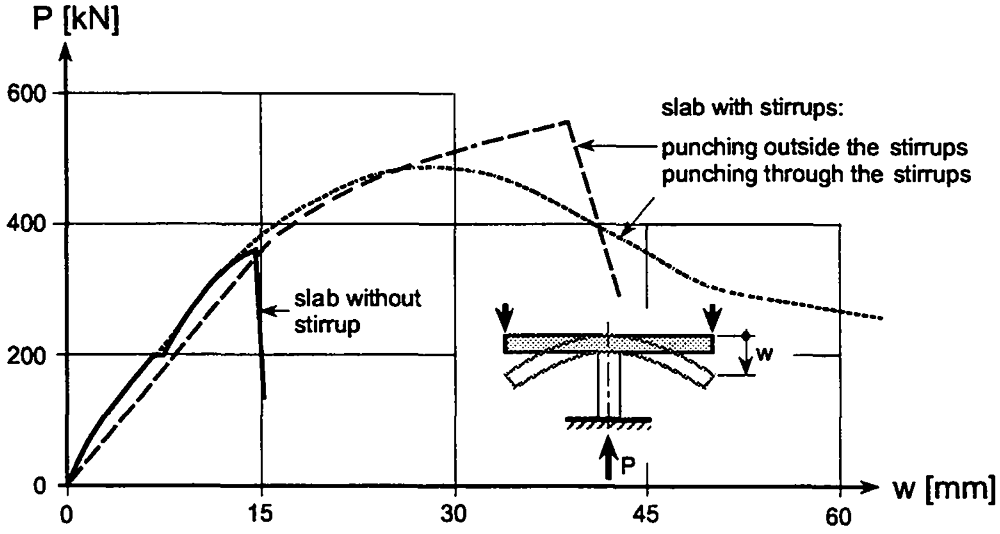

Figure 2.16: Influence of stirrups on the response; (Dilger and Ghali 1981)

It has to be noted that most of the failure observed in slabs with stirrups takes place outside of the shear reinforcement, but if the failure occurs through the stirrups the failure is more likely to be ductile.

2.4 Requirements for the numerical model

To conclude this investigation of punching failure experiments, the requirements that the numerical model should fulfill for the analysis of punching failure are derived as follows:

1. Punching failure crucially depends on the geometry and boundary conditions. Consequently, the finite element method which accounts for general geometry and arbitrary boundary conditions is well adapted.
2. The punching failure involves tangential cracks as well as radial cracks. Consequently the model should treat multiple cracks.
3. Shear and flexural effects interact and cannot be considered separately. Consequently, a continuum model should be developed as opposed to a structural one.
4. Punching failure is localized along the punching crack and is not a diffused failure. Therefore, the numerical model should include localization limiters.
5. Size-effect influences the punching failure. Therefore, fracture mechanics concept should be included in the numerical model.
6. The influence of the flexural and shear reinforcements is important. Therefore, an explicit formulation of the reinforcement as opposed to an embedded one should be considered so that yielding and debounding can be simulated.

The assumptions made for the development of the numerical model are the following:

1. Punching failure is a three-dimensional failure phenomenon which can be simplified in considering the axisymmetry of the problem. The difference between axisymmetric and orthogonal reinforcement as presented in section 2.2.3 on page 12 should be kept in mind.

2. The bond between concrete and steel is reported to be important only in the case of bond failure. Consequently, this effect is considered to be secondary to start with. It will be shown latter however, in section 6.4.2 on page 122, that bond behavior can be important for the simulation of punching failure.

3. It was shown that the dowel action influences the response of slab with orthogonal reinforcement, but this effect is neglected in a first approach. However, it will be shown in section 6.4.3 on page 122 that dowel action influences the punching load for slab with orthogonal reinforcement.

Now that the requirements of the numerical model are established, its development is presented in the following two chapters.

Chapter 3

Constitutive model

3.1 Introductory remarks

The purpose of this chapter is to formulate the reinforced concrete model at the constitutive level. The general constitutive relations are introduced, followed by the description of the incremental flow theory of plasticity. The reinforced concrete model uncouples the actions of steel reinforcement (described in section 3.4) and concrete (described in section 3.5). A perfect bond between concrete and steel is assumed. Mathematical preliminaries are given in appendix A.

3.2 Constitutive mechanics

3.2.1 Continuum displacement and deformation

A continuum is defined as a body for which to any configuration there corresponds a region R in three-dimensional space so that all points of the region are occupied by a particle (material point) of the body. The continuum shown in figure 3.1 is characterized by an initial or reference configuration R_0 and a configuration at time t denoted by R_t. The position vector from the fixed origin O to the considered particle in the initial configuration R_0 is denoted by $\boldsymbol{X}$, whereas the position vector from the fixed origin O to the considered particle in the current

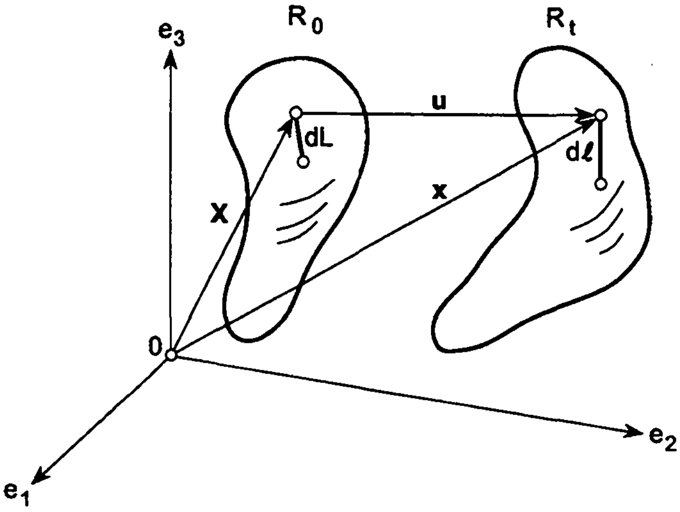

Figure 3.1: Displacement of a continuum

configuration R_t is denoted by $\boldsymbol{x}$. The displacement vector $\boldsymbol{u}(\boldsymbol{X}, t)$ is regarded as a mapping from R_0 to R_t which defines the motion between the two configurations in terms of: $\boldsymbol{u} = \boldsymbol{x} - \boldsymbol{X}$. This displacement is composed of translations and rotations.

The Lagrangian or referential description of a physical phenomenon associated with the deformation of a body involves fields defined over R_0, while the Eulerian or spatial description involves fields defined over R_t. The Lagrangian description is convenient in continuum analysis because the initial configuration is always known. *Therefore, the Lagrangian description is considered here.*

The distance between every pair of points in a continuum remains constant during a rigid motion. But when the relative position of any two points in a continuum is changed, then the continuum is said to undergo deformation. The deformation is measured with the infinitesimal strain tensor[1]

$$\epsilon_{ij} = \frac{1}{2}\left(\frac{\partial u_i}{\partial X_j} + \frac{\partial u_j}{\partial X_i}\right) \text{ or } \boldsymbol{\epsilon} = \nabla^S \boldsymbol{u} = \frac{1}{2}(\nabla \boldsymbol{u} + (\nabla \boldsymbol{u})^T), \tag{3.1}$$

which is symmetric. The infinitesimal strain tensor is decomposed into

$$\epsilon_{ij} = \epsilon_{ij}^{vol} + \epsilon_{ij}^{dev} = \frac{1}{3}\epsilon_{kk}\delta_{ij} + \epsilon_{ij}^{dev}, \tag{3.2}$$

where ϵ_{ij}^{dev} are the components of the deviatoric strain tensor describing shear distortion and ϵ_{kk} is the volumetric strain measuring dilatation. The incompressibility, that is the inability of a continuum to change its volume is expressed as

$$\epsilon_{kk} = \nabla \cdot \boldsymbol{u} = 0. \tag{3.3}$$

Since the strain tensor $\boldsymbol{\epsilon}$ is symmetric, it has three mutually orthogonal characteristic vectors which are the principal axes of strain. The corresponding principal strains are known as the eigenvalues of the strain tensor so that

$$\det(\boldsymbol{\epsilon} - \epsilon \mathbf{1}) = -\epsilon^3 + I_1^\epsilon \epsilon^2 - I_2^\epsilon \epsilon + I_3^\epsilon = 0. \tag{3.4}$$

The principal strains satisfying this equation are denoted by: $\epsilon_1, \epsilon_2, \epsilon_3$, which leads to the following expression of the strain tensor

$$\boldsymbol{\epsilon} = \begin{pmatrix} \epsilon_1 & 0 & 0 \\ 0 & \epsilon_2 & 0 \\ 0 & 0 & \epsilon_3 \end{pmatrix}. \tag{3.5}$$

The corresponding three invariants of the strain tensor are

$$\begin{aligned} I_1^\epsilon &= \epsilon_1 + \epsilon_2 + \epsilon_3 \\ I_2^\epsilon &= \epsilon_1\epsilon_2 + \epsilon_2\epsilon_3 + \epsilon_3\epsilon_1 \\ I_3^\epsilon &= \epsilon_1\epsilon_2\epsilon_3. \end{aligned} \tag{3.6}$$

Now that the displacement and deformation of a continuum has been described, the effect of forces is considered in analyzing the stress tensor.

---

[1] The infinitesimal strain tensor is an approximation of the Green strain tensor expressed as:

$$E_{ij} = \frac{1}{2}(\frac{\partial u_i}{\partial X_j} + \frac{\partial u_j}{\partial X_i} + \frac{\partial u_k}{\partial X_i}\frac{\partial u_k}{\partial X_j}),$$

as described by Fung [44]. This approximation of the Green strain tensor is admissible only if both the deformation and rotation are infinitesimal.

3.2.2 Stress tensor

According to Cauchy, the concept of stress vector $\boldsymbol{f}$ results from a limiting process of the force $\boldsymbol{F}$ acting on an area defined by its normal $\boldsymbol{N}$ so that

$$\boldsymbol{f} = \frac{d\boldsymbol{F}}{dS}. \tag{3.7}$$

Cauchy's theorem states that there exists a second-order tensor field $\boldsymbol{\sigma}$ independent of $\boldsymbol{N}$ so that

$$f_i = \sigma_{ij} N_j. \tag{3.8}$$

Often referred as Cauchy's formula this relation as stated by Fung [44] assures that the nine components of the Cauchy stresses tensor σ_{ij} are necessary and sufficient to define the traction across any surface element in a body. Hence, the stress state in a body is characterized completely by the set of nine quantities σ_{ij}. The Cauchy stress tensor is symmetric[2] if no couple stresses are active

$$\sigma_{ij} = \sigma_{ji}. \tag{3.9}$$

The stress tensor is decomposed in a similar way as the strain tensor so that

$$\sigma_{ij} = \sigma_{ij}^{vol} + \sigma_{ij}^{dev} = \frac{1}{3}\sigma_{kk}\delta_{ij} + s_{ij}, \tag{3.10}$$

where s_{ij} are the components of the deviatoric stress tensor and σ_{kk} is the volumetric stress.

Since the stress tensor $\boldsymbol{\sigma}$ is symmetric, it has three mutually orthogonal characteristic vectors which are the principal axes of stress. The corresponding principal stresses are known as the eigenvalues of the stress tensor so that

$$\det(\boldsymbol{\sigma} - \sigma\mathbf{1}) = -\sigma^3 + I_1^\sigma \sigma^2 - I_2^\sigma \sigma + I_3^\sigma = 0. \tag{3.11}$$

The principal stresses satisfying this equation are denoted by: $\sigma_1, \sigma_2, \sigma_3$, which leads to the following expression of the stress tensor

$$\boldsymbol{\sigma} = \begin{pmatrix} \sigma_1 & 0 & 0 \\ 0 & \sigma_2 & 0 \\ 0 & 0 & \sigma_3 \end{pmatrix}. \tag{3.12}$$

The corresponding three invariants of the stress tensor are:

$$\begin{aligned} I_1^\sigma &= \sigma_1 + \sigma_2 + \sigma_3 \\ I_2^\sigma &= \sigma_1\sigma_2 + \sigma_2\sigma_3 + \sigma_3\sigma_1 \\ I_3^\sigma &= \sigma_1\sigma_2\sigma_3. \end{aligned} \tag{3.13}$$

Another set of invariants which leads to an attractive geometric interpretation is the Haigh-Westergaard coordinates (Chen and Han [21]) often used to define strength criteria (applied in section 3.5.2). These invariants are: the hydrostatic stress invariant ξ, the deviatoric stress invariant ρ, and the deviatoric polar angle θ (Lode angle):

$$\xi = \frac{1}{\sqrt{3}} I_1 \quad \text{where} \quad I_1 = \sigma_{ii} \tag{3.14}$$

$$\rho = \sqrt{2J_2} \quad \text{where} \quad J_2 = \frac{1}{2} s_{ij} s_{ji} \tag{3.15}$$

$$\cos 3\theta = \frac{3\sqrt{3}}{2} \frac{J_3}{J_2^{\frac{3}{2}}} \quad \text{where} \quad J_3 = \frac{1}{3} s_{ij} s_{jk} s_{ki}. \tag{3.16}$$

---

[2] The demonstration of the symmetry of the stress tensor which dates back to Boltzmann is detailed by Fung in [44] p. 123-124.

It can be shown that the Haigh-Westergaard coordinates span a cylindrical coordinate system of the stress space. These invariants are related to the principal stresses (as shown by Malvern [82]) as follows:

$$\begin{Bmatrix} \sigma_1 \\ \sigma_2 \\ \sigma_3 \end{Bmatrix} = \frac{1}{\sqrt{3}} \begin{Bmatrix} \xi \\ \xi \\ \xi \end{Bmatrix} + \sqrt{\frac{2}{3}}\rho \begin{Bmatrix} \cos\theta \\ \cos(\theta - \frac{2\pi}{3}) \\ \cos(\theta + \frac{2\pi}{3}) \end{Bmatrix}, \tag{3.17}$$

where $0 \leq \theta \leq \frac{\pi}{3}$ and consequently $\sigma_1 \geq \sigma_2 \geq \sigma_3$. The relation between the strain and the stress tensor is described in the following section for the case of linear elastic behavior.

3.2.3 Elastic constitutive relation

The dependence of the stress-strain relation on the thermodynamics, chemical, hydraulic and all other processes is ignored so that $\sigma = \sigma(\epsilon)$. The stress-strain relation can be expressed in terms of the strain energy function[3] $W(\epsilon)$ in the absence of internal constraints as:

$$\sigma = \frac{\partial W}{\partial \epsilon}. \tag{3.18}$$

This strain energy function was introduced by Green and such materials are called hyperelastic material in opposition to hypo-elastic or Cauchy elastic materials where no strain energy function is assumed. *Hyperelasticity is considered here* and is expressed in terms of the classical constitutive equations called the generalized Hooke's law:

$$\sigma_{ij} = C_{ijkl}\epsilon_{kl}, \tag{3.19}$$

where C_{ijkl} are the elastic components of a fourth order tensor called the elastic constitutive tensor. As shown in equation 3.9 the stress tensor is symmetric implying that $C_{ijkl} = C_{jikl}$. Furthermore, as the strain tensor is symmetric the elastic constitutive tensor must satisfy $C_{ijkl} = C_{ijlk}$. As there exists a strain energy function W so that

$$C_{ijkl} = \frac{\partial^2 W}{\partial \epsilon_{ij}\epsilon_{kl}}, \tag{3.20}$$

the symmetry $C_{ijkl} = C_{klij}$ must hold. Furthermore, *isotropic material behavior is assumed.* The hypothesis of isotropy states that the elastic constants are independent of the orientation of the coordinate axis, and this implies that there are only two independent elastic constants. The isotropic elastic constitutive tensor has the following representation:

$$C_{ijkl} = \lambda\delta_{ij}\delta_{kl} + \mu(\delta_{ik}\delta_{jl} + \delta_{il}\delta_{jk}) \text{ or } \boldsymbol{C} = \lambda\mathbf{1}\otimes\mathbf{1} + 2\mu\boldsymbol{I}, \tag{3.21}$$

where λ, μ are the Lamé constants. The Lamé constants can be expressed in terms of Young's modulus E and Poisson's ratio ν as:

$$\mu = G = \frac{E}{2(1+\nu)} \text{ and } \lambda = \frac{\nu E}{(1+\nu)(1-2\nu)}. \tag{3.22}$$

Associated with the shear modulus G, the bulk modulus is defined as:

$$K = \frac{E}{3(1-2\nu)}. \tag{3.23}$$

---

[3] The strain energy function is equivalent to the internal energy density or the free energy density when the thermal state are ignored as further described by Lubliner [80] p 46.

The isotropic linear elastic stress-strain relation can be rephrased based on the Lamé constants so that:

$$\sigma_{ij} = \lambda\delta_{ij}\epsilon_{kk} + 2\mu\epsilon_{ij}. \tag{3.24}$$

The elastic constitutive tensor is transformed into a matrix form so that

$$D_{IJ} = C_{ijkl}, \tag{3.25}$$

as proposed by Hughes [59]. For a general three dimensional format with the strain written in a vector form so that $\epsilon^T = (\epsilon_{xx}; \epsilon_{yy}; \epsilon_{zz}; 2\epsilon_{yz}; 2\epsilon_{xz}; 2\epsilon_{xy})$, the elastic constitutive matrix is given as:

$$\boldsymbol{D} = \frac{E}{(1+\nu)(1-2\nu)} \begin{bmatrix} 1-\nu & \nu & \nu & 0 & 0 & 0 \\ \nu & 1-\nu & \nu & 0 & 0 & 0 \\ \nu & \nu & 1-\nu & 0 & 0 & 0 \\ 0 & 0 & 0 & \frac{1}{2}(1-2\nu) & 0 & 0 \\ 0 & 0 & 0 & 0 & \frac{1}{2}(1-2\nu) & 0 \\ 0 & 0 & 0 & 0 & 0 & \frac{1}{2}(1-2\nu) \end{bmatrix}. \tag{3.26}$$

The corresponding compliance matrix is:

$$\boldsymbol{D}^{-1} = \frac{1}{E} \begin{bmatrix} 1 & -\nu & -\nu & 0 & 0 & 0 \\ -\nu & 1 & -\nu & 0 & 0 & 0 \\ -\nu & -\nu & 1 & 0 & 0 & 0 \\ 0 & 0 & 0 & 2(1+\nu) & 0 & 0 \\ 0 & 0 & 0 & 0 & 2(1+\nu) & 0 \\ 0 & 0 & 0 & 0 & 0 & 2(1+\nu) \end{bmatrix}. \tag{3.27}$$

Now that linear elasticity has been described, the incremental flow theory of plasticity is introduced as it will be the framework for the implementation of the steel and the concrete model.

3.3 Incremental flow theory of plasticity

3.3.1 Three basic assumptions

The incremental flow theory of plasticity is based on three basic assumptions: additive decomposition of strain increment, the yield criterion, and the plastic flow rule which is normally based on the plastic potential.

1. The first assumption states that the elastic and plastic strains increments are uncoupled so that:

   $$\dot{\epsilon} = \dot{\epsilon}_e + \dot{\epsilon}_p. \tag{3.28}$$

   The subscripts e and p stand for elastic and plastic parts respectively.

2. The second assumption states that the elastic domain is delimited by a surface f defined as the yield surface or strength condition or even failure criterion. It should be emphasized that a yield surface formulated in stress space, does not necessarily limit the accompanying deformations except for the elastic strains in the enclosed region. In the case of the dual formulation of an elastic strain constraint, such as the St. Venant

criterion[4] of maximum strain, the corresponding strength envelope involves the elastic material properties with an explicit dependence on Poisson's ratio. Therefore, the strain-based or energy-based failure descriptions do involve elastic material properties, while the failure description in stress space constrains the stress state independently of the underlying material description. As a consequence, a stress-based failure criterion infers that the strength of concrete is independent of its stiffness, thus there is no correlation between the elastic modulus and the uniaxial compressive strength. In contrast the strain- and energy-based limit models introduce strong correlation between stiffness and strength.

Material behavior generally depends on the past history. These materials known as materials with memory are described through an array of independent variables defined as the internal variables $\boldsymbol{q}$. The resulting yield surface is

$$f(\boldsymbol{\sigma}, \boldsymbol{q}) \leq 0. \tag{3.29}$$

For isotropic conditions, the yield surface must remain invariant with regard to observer transformation[5] $\bar{f}(T_{ik}\sigma_{kl}T_{lj}) = f(\sigma_{ij}) = 0$. Thus isotropic yield surfaces depend on the set of three independent scalar invariants, for example in the form of the three principal stresses, $f(\sigma_{ij}) = f(\sigma_1, \sigma_2, \sigma_3) = 0$, or the three stress invariants, $f(\sigma_{ij}) = f(I_1, I_2, I_3) = 0$, as demonstrated by Ogden [101].

3. The third assumption is known as the flow rule and it is a material law which describes the evolution of the plastic deformation. It describes the evolution of the plastic strain rate when the material undergoes plastic deformation. This evolution of the plastic strain is function of the plastic potential g, which depends on the stress tensor and the internal variables so that $g(\boldsymbol{\sigma}, \boldsymbol{q})$. The flow rule takes the following form:

$$\dot{\epsilon}_p = \dot{\gamma}\frac{\partial g(\boldsymbol{\sigma}, \boldsymbol{q})}{\partial \boldsymbol{\sigma}} = \dot{\gamma}\boldsymbol{m}(\boldsymbol{\sigma}, \boldsymbol{q}), \tag{3.30}$$

   where $\boldsymbol{m}(\boldsymbol{\sigma}, \boldsymbol{q})$ describes the direction of the plastic flow, and $\dot{\gamma}$ is a positive scalar factor called the plastic multiplier. The value of $\dot{\gamma}$ is positive only when plastic deformations occur. If the plastic potential is equivalent to the yield surface, this leads to the so-called associated plasticity. The plastic strain is governed by the rate equation 3.30 which defines the incremental flow theory of plasticity[6].

The presence of internal variables requires additional constitutive equations known as the equations of evolution of the internal variables expressed in a general form as:

$$\dot{\boldsymbol{q}} = \dot{\gamma}\boldsymbol{h}(\boldsymbol{\sigma}, \boldsymbol{q}), \tag{3.31}$$

where $\boldsymbol{h}$ is an operator which defines the dependence of the yield surface on the internal variables. This operator expresses the hardening (expansion of the yield surface) or softening (contraction of the yield surface) properties of the material. A stationary yield surface describes a perfectly plastic behavior. The evolution of the yield surface is classified into three

---

[4] The Saint-Venant criterion or maximum strain theory states that yielding will occur when the maximum value of the principal strain equals the value of the yield strain in simple tension as stated by Mendelson [87].

[5] Observer transformations are characterized by a proper orthogonal matrix $\mathbf{T}$ which satisfies $\det\mathbf{T} = +1$ and $\mathbf{T}\mathbf{T}^T = \mathbf{T}^T\mathbf{T} = 1$, and whose coefficients T_{ij} are the direction cosines.

[6] The incremental flow theory of plasticity is different from the deformation theory of plasticity developed by Hencky where the total plastic strain tensor is assumed to be determined by the stress tensor.

types of hardening/softening rules. First, the isotropic hardening/softening rule which is characterized by an isotropic expansion or contraction of the yield surface in all the directions. The isotropic rule is characterized by only one scalar-value parameter. Two standard isotropic hardening/softening rules have been proposed: the work-hardening/softening evolution: $\dot{q}_w = tr(\sigma \dot{\epsilon}_p) = \dot{\gamma} tr(\sigma m)$ and the strain-hardening/softening evolution: $\dot{q}_\epsilon = tr(\dot{\epsilon}_p^2)^{\frac{1}{2}} = \dot{\gamma}\|m\|$. The second rule is the kinematic rule which is characterized by a rigid translation of the loading surface whereby the elastic domain does not change. The third rule is a combination of the two preceding ones called the mixed hardening/softening rule.

3.3.2 Loading-unloading conditions

The increment of the plastic multiplier $\dot{\gamma}$ and the yield condition $f = 0$ satisfy the Kuhn-Tucker conditions of optimization theory:

$$\dot{\gamma} f = 0, \; \dot{\gamma} \geq 0, \; f \leq 0. \tag{3.32}$$

In addition, they must satisfy the requirement:

$$\dot{\gamma} \dot{f} = 0. \tag{3.33}$$

From these conditions, different loading cases are differentiated. First if $f(\sigma, q) < 0$, then $\dot{\gamma} f = 0$ inferred that $\dot{\gamma} = 0$. And if $\dot{\gamma} = 0$ this implies that $\dot{\epsilon}_p = 0$ and $\dot{q} = 0$. This case correspond to the elastic loading case. The second case to be considered is when the stress path has reached the yield condition $f(\sigma, q) = 0$. Two sub-case can be differentiated: $\dot{f}(\sigma, q) < 0$ and $\dot{f}(\sigma, q) = 0$. First, if $\dot{f}(\sigma, q) < 0$, infers that $\dot{\gamma} = 0$, implying that $\dot{\epsilon}_p = 0$, which corresponds to the elastic unloading. The other sub-case $\dot{f}(\sigma, q) = 0$, defines the differential form of plastic consistency condition which satisfies equation 3.33. If $\dot{\gamma} > 0$, then $\dot{\epsilon}_p \neq 0$ and $\dot{q} \neq 0$, refers to plastic loading. If $\dot{\gamma} = 0$ neutral loading is obtained. These loading-unloading conditions are summarized in table 3.1.

$f < 0$	$\Longrightarrow$	$\dot{\gamma} = 0$ Elastic loading			
$f = 0$	$\Longrightarrow$	$\dot{f} < 0$	$\Longrightarrow$	$\dot{\gamma} = 0$	Elastic unloading
		$\dot{f} = 0$	and	$\dot{\gamma} = 0$	Neutral loading
		$\dot{f} = 0$	and	$\dot{\gamma} > 0$	Plastic loading

Table 3.1: Loading-unloading conditions

3.3.3 Elastic-plastic operator split

General observations

The basic problem of elastic-plastic computations is stated as follows: given the initial values σ, ϵ, q at time t^i and a variation of strain $\dot{\epsilon}$, find the new internal state defined as: (σ^{i+1}, q^{i+1}). To solve that problem, the operator split methodology is applied as suggested by Simo and Hughes [127]:

$$\begin{pmatrix} \dot{\epsilon} & = & \nabla^S \dot{u} \\ \dot{\epsilon}_p & = & 0 \\ \dot{q} & = & 0 \end{pmatrix} + \begin{pmatrix} \dot{\epsilon} & = & 0 \\ \dot{\epsilon}_p & = & \dot{\gamma} m(\sigma, q) \\ \dot{q} & = & \dot{\gamma} h(\sigma, q) \end{pmatrix} = \begin{pmatrix} \dot{\epsilon} & = & \nabla^S \dot{u} \\ \dot{\epsilon}_p & = & \dot{\gamma} m(\sigma, q) \\ \dot{q} & = & \dot{\gamma} h(\sigma, q) \end{pmatrix}. \tag{3.34}$$

The elastic-predictor step is obtained based on the previous converged step so that $\epsilon^{i+1} = \epsilon^i + \dot{\epsilon}$. This leads to the definition of the trial stress tensor so that:

$$\sigma^{trial} = \sigma^i + C : \dot{\epsilon}. \tag{3.35}$$

If the trial stress is outside the yield surface, the plastic-corrector step takes place in considering the trial stress as initial condition so that:

$$\sigma^{i+1} = \sigma^{trial} - \dot{\sigma}_p = \sigma^{trial} - \dot{\gamma} C : \boldsymbol{m}. \tag{3.36}$$

The purpose of the second step is to restore consistency by returning the trial stress to the yield surface. An important issue in plasticity computations is the evaluation of the plastic stress rate $\dot{\sigma}_p$. Two conditions have to be satisfied simultaneously:

- the stress tensor must be on the loading surface,
- the evolution of the internal variables must satisfy equation 3.31.

The most common approach to evaluate the new stress tensor is the linearized consistency condition. This approach is described in the next section. Another approach, called the full consistency condition will be presented later.

Linearized consistency condition

The linearized consistency condition is derived by expanding the yield condition given in equation 3.29 into a first order truncated Taylor series around the previous converged state. Assuming that $f^i = 0$ is satisfied, the classical linearized consistency condition is written as:

$$\begin{aligned} f^{i+1} \simeq f^i + \dot{f} = \dot{f} &= \frac{\partial f}{\partial \sigma} : \dot{\sigma} + \frac{\partial f}{\partial q} \cdot \dot{q} \\ &= \boldsymbol{n} : C : [\dot{\epsilon} - \dot{\epsilon}_p] + \frac{\partial f}{\partial q} \cdot \dot{q} \\ &= \boldsymbol{n} : C : \dot{\epsilon} - \dot{\gamma}\, \boldsymbol{n} : C : \boldsymbol{m} + \dot{\gamma} \frac{\partial f}{\partial q} \cdot \boldsymbol{h} = 0. \end{aligned} \tag{3.37}$$

The plastic multiplier can be expressed in an explicit form as:

$$\dot{\gamma} = \frac{\boldsymbol{n} : C : \dot{\epsilon}}{-\frac{\partial f}{\partial q} \cdot \boldsymbol{h} + \boldsymbol{n} : C : \boldsymbol{m}}. \tag{3.38}$$

Up to this point it was assumed that the stress σ^i has reached the yield surface and that the gradient $\boldsymbol{n}$ was evaluated at the stress σ^i. However, if the stress tensor σ^i is inside the loading surface, then the contact stress has to be estimated. To avoid the computation of the contact stress, the truncated Taylor series can be expanded around the trial stress σ^{trial}.

$$f^{i+1} = f^{trial} + \frac{\partial f^{trial}}{\partial \sigma} : \dot{\sigma} + \frac{\partial f^{trial}}{\partial q} \cdot \dot{q} = 0. \tag{3.39}$$

This leads to an other explicit form of the plastic multiplier:

$$\dot{\gamma} = \frac{f^{trial}}{-\frac{\partial f}{\partial q} \cdot \boldsymbol{h} + \boldsymbol{n} : C : \boldsymbol{m}}. \tag{3.40}$$

This equation is more convenient than equation 3.38 as the location of the contact stress is not necessary. It can be noted that the denominator must remain positive.

Full consistency condition

The full consistency condition is expressed as:

$$f^{i+1} = f(\sigma^{i+1}, q^{i+1}) = f(\sigma^i + \dot{\sigma}, q^i + \dot{q}) = 0. \tag{3.41}$$

The full consistency condition is different from the linearized consistency condition except for simple formulations such as linear yield condition and hardening/softening rule. The full consistency condition can be expressed in terms of equations 3.36 and 3.31 which leads to an implicit equation:

$$f^{i+1}(\dot{\gamma}) = 0, \tag{3.42}$$

where the plastic multiplier $\dot{\gamma}$ is the only unknown. For some special cases as for example J_2 plasticity with an isotropic hardening/softening rule this equation is explicit since the backward projection results in the radial return method. But usually equation 3.42 is an implicit relation.

One way of satisfying the full consistency condition expressed in equation 3.42 is by Newton's method. However, divergence is observed if the initial guess is not close enough from the converged solution. An accurate initial guess is obtained with the explicit equation 3.38 or 3.40 derived from linearized consistency condition.

Two others families of algorithm—as described by Ortiz and Popov [103]—can be used to satisfy the full consistency condition: the generalized trapezoidal rule and the generalized midpoint rule. These two algorithms differ mainly on the location where the gradients of the yield surface and the plastic potential are evaluated. These algorithms require the computation of the second derivative of the yield criterion which can be a complicated task.

Another method used to satisfy the full consistency condition is the cutting plane algorithm developed by Ortiz and Simo [104]. This algorithm is an explicit procedure which involves only function evaluations. As mentioned by Simo and Hughes [127] this algorithm is only conditionally stable.

3.3.4 Elastic-plastic constitutive tensor

The elastic-plastic constitutive tensor[7] is defined as follows based on the differential format

$$\dot{\sigma} = \boldsymbol{Cep} : \dot{\epsilon}. \tag{3.43}$$

Using the definition of the flow rule this leads to $\dot{\sigma} = \boldsymbol{Cep} : (\dot{\epsilon}_e - \dot{\gamma}\boldsymbol{m})$, and inserting the linearized consistency condition given in equation 3.38 leads to:

$$\boldsymbol{Cep} = \boldsymbol{C} - \frac{\boldsymbol{C} : \boldsymbol{m} \otimes \boldsymbol{n} : \boldsymbol{C}}{-\frac{\partial f}{\partial \boldsymbol{q}} \cdot \boldsymbol{h} + \boldsymbol{n} : \boldsymbol{C} : \boldsymbol{m}}. \tag{3.44}$$

The modification of the fourth order elastic constitutive tensor is a rank-one modification and therefore, the elastic-plastic constitutive tensor $\boldsymbol{Cep}$ has no complex conjugate roots. The denominator of equation 3.44 must remain positive. It can be mentioned that for non-associated plasticity ($\boldsymbol{m} \neq \boldsymbol{n}$), the elastic-plastic constitutive tensor $\boldsymbol{Cep}$ is non-symmetric.

---

[7] The elastic-plastic constitutive tensor also called the tangential elastic-plastic operator is different from the algorithmic tangent operator developed by Simo and Taylor [129].

3.3.5 Material stability

The material stability is defined by the positive value of the second order work as proposed by Hill [51]. A stable rate-independent elastic-plastic material satisfies:

$$d^2U = \dot{\sigma} : \dot{\epsilon} = \dot{\epsilon} : \boldsymbol{Cep} : \dot{\epsilon} > 0. \tag{3.45}$$

*This limit provides the criterion for diffuse failure. For non-associated flow rules, the elastic-*plastic constitutive tensor is non-symmetric. The stability criterion $d^2U = 0$ leads to premature[8] diagnosis of material failure compared to ($\det \boldsymbol{Cep} = 0$) as only the symmetric part of the elastic-plastic operator is activated. This premature failure assessment was illustrated by Willam and Etse [148].

3.4 The steel model for reinforcement

The steel model is a direct application of the incremental flow theory of plasticity justifying its presentation before that of the concrete model. Steel reinforcement is mainly one-dimensional in reinforced concrete structures. It is therefore not necessary to introduce complex multiaxial formulation and a uniaxial constitutive model is considered. This steel model is characterized by: (1) a bi-linear stress-strain response, (2) identical response behavior under traction and compression. These assumptions provide close agreement with experimental results according to Chen [19].

The uniaxial steel model satisfies linear isotropic hardening. The resulting yield surface is expressed as

$$f = \mid \sigma \mid -(f_y + H\kappa), \tag{3.46}$$

where f_y is the uniaxial yield strength, κ is the internal variable monitoring the amount of plastic strain, $\Delta\kappa = \Delta\gamma$, and K is the hardening modulus. The corresponding uniaxial stress-strain curve is shown in figure 3.2. Using the full consistency condition $f^{i+1} = 0$ the plastic multiplier is obtained so that

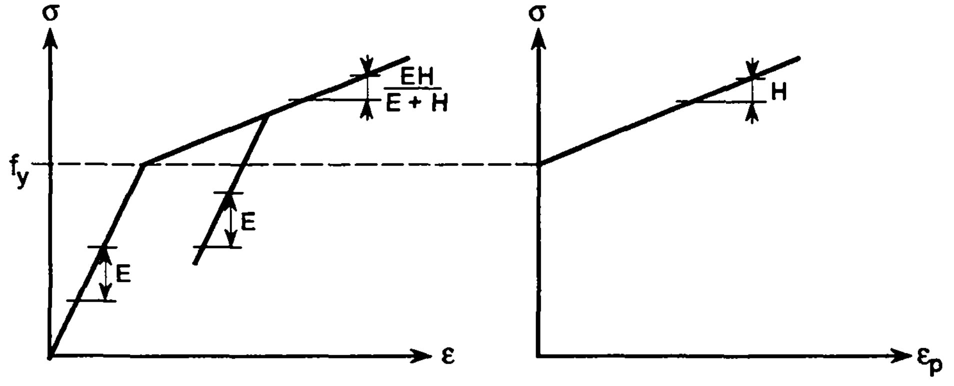

Figure 3.2: Uniaxial elastic-plastic constitutive model for steel

$$\Delta\gamma = \frac{f^{trial}}{E+H}, \tag{3.47}$$

---

[8] The failure is premature because the eigenvalues of a symmetrized operator embeds that of the non-symmetric operator as stated by Bromwich [15] .

where E is the Young's modulus of steel. The algorithmic elastic-plastic constitutive coefficient is obtained explicitly in computing $\partial\sigma^{trial}/\partial\epsilon$ which leads to

$$Dep = \frac{E\,H}{E+H}. \tag{3.48}$$

Assuming that the state at time t^i is completely defined, and supposing that an increment of strain is given, the solution at time t^{i+1} is computed with the stress integration algorithm presented in table 3.2. Now that the steel model has been formulated, the concrete model is described so to complete the description of the reinforced concrete numerical model.

```
1. Compute elastic trial stress,
   $\sigma^{trial} = \sigma^i + E\Delta\epsilon$.
2. Compute the trial yield value,
   $f^{trial} = |\sigma^{trial}| - (f_y + H\kappa^i)$.
3. Check the yield condition; if ($f^{trial} \leq 0$) then:
   $\sigma^{i+1} = \sigma^{trial}$,
   $\kappa^{i+1} = \kappa^i \rightarrow$ GO TO STEP 6.
4. Compute the plastic corrector:
   $\Delta\gamma = \frac{f^{trial}}{E+H}$,
   $\sigma_p = \Delta\gamma\,E$.
5. Update the stress and the internal variable:
   $\sigma^{i+1} = \sigma^{trial} - \sigma_p$,
   $\kappa^{i+1} = \kappa^i + \Delta\gamma$.
6. Compute the elastic-plastic constitutive matrix,
   $Dep = \begin{cases} \frac{EH}{E+H} & \text{if } \Delta\gamma > 0 \\ E & \text{if } \Delta\gamma = 0. \end{cases}$
```

Table 3.2: Stress integration algorithm for the uniaxial steel model

3.5 The plain concrete model

3.5.1 Preliminaries

The plain concrete model is described in four sections: triaxial concrete failure criterion, concrete flow rule, cracking simulation, and numerical implementation. This concrete model will be used to simulate punching failure in reinforced concrete structures. Consequently, it must take into account only the principal characteristics of plain concrete behavior so to be efficient but not too complex. Special attention was given to the development a simple failure criterion which captures the principal features of triaxial concrete strength, and which includes standard strength hypotheses for a variety of engineering materials. This failure criterion was published by Menétrey and Willam [89] and it is presented in the following section.

3.5.2 Triaxial concrete failure criterion

Introduction

Considering concrete as a cement-aggregate composite, the failure hypothesis for concrete must combine the cohesive strength of the cement paste with the frictional adhesion of aggregate interaction. Thus the failure criterion of the concrete composite must encompass pressure sensitivity on one hand, and tensile strength limiters on the other hand. Moreover, triaxial experiments on concrete cylinders clearly demonstrate the substantial difference of shear strength in conventional triaxial compression ($\sigma_1 = \sigma_2 \geq \sigma_3$) and triaxial extension testing ($\sigma_1 \geq \sigma_2 = \sigma_3$) which diminishes with increasing confinement. As a result, the failure criterion should be sensitive with regard to the intermediate principal stress and this influence should increase with triaxial confinement.

The proposed failure criterion combines the simplicity of Mohr's strength envelope with the complexity of a three invariant formulation. The resulting strength criterion provides a fair representation of the tensile/cohesive strength of cement materials, and a reasonable description of shear strength of frictional materials. In extent of the traditional formulation of tensile strength along the line of the Rankine criterion (maximum tensile stress hypothesis expressed in footnote page 45), and shear strength along the line of the Mohr envelope criterion (Coulomb shear strength hypothesis), the proposed formulation incorporates the effect of all three principal stresses including that of the intermediate one.

The proposed failure criterion is expressed with the Haigh-Westergaard coordinates (defined on page 29) which span a cylindrical coordinate system of the stress space. The circular trace of the deviatoric polar radius $\rho(\theta)$ is transformed into a triple symmetric ellipse through the elliptic function $r(\theta, e)$ which was developed by Klisinski [70] based on the 5-parameter model by Willam and Warnke [151]:

$$r(\theta, e) = \frac{4\,(1-e^2)\cos^2\theta + (2e-1)^2}{2\,(1-e^2)\cos\theta + (2e-1)\,[4\,(1-e^2)\cos^2\theta + 5e^2 - 4e]^{1/2}}. \tag{3.49}$$

The parameter e describes the out-of-roundness of the deviatoric trace as illustrated in figure 3.3. Along the tensile ($\theta = 0$) and the compressive meridian the elliptic function takes the following values:

$$\begin{aligned} r(\theta = 0, e) &= 1/e \quad \text{tensile meridian} \\ r(\theta = \tfrac{\pi}{3}, e) &= 1 \quad\;\;\, \text{compressive meridian} \end{aligned}$$

Although the elliptic function is only defined in the sector $0 \leq \theta \leq \frac{\pi}{3}$, the polar radius $r(\theta, e)$ extends to all polar directions $0 \leq \theta \leq 2\pi$ using the three-fold symmetry, as shown in figure 3.3.

Convexity and smoothness of the elliptic function requires that $0.5 < e \leq 1$. At the upper limit $e = 1$ leads to $r(\theta, 1) = 1$ which describes a circle as shown in figure 3.3. At the lower limit $e = 0.5$ leads to $r(\theta, 0.5) = 2\cos(\theta)$, which forms a triangle in the deviatoric plane as shown in figure 3.3. This triangle violates the smoothness condition and introduces loss of unique gradients at the three corners which justifies exclusion of the out-of-roundness parameter $e = 0.5$ when corners and loss of uniqueness are to be avoided.

Development of the concrete failure criterion

The proposed concrete failure criterion is based on the empirical strength criterion which was proposed by Hoek and Brown [54] for rock masses:

$$f(\sigma_1, \sigma_3) = \left[\frac{\sigma_1 - \sigma_3}{f_c}\right]^2 + \phi\frac{\sigma_1}{f_c} - c = 0. \tag{3.50}$$

The material parameters c and ϕ are measures of cohesive and frictional strength, and f_c designates the uniaxial compressive strength. This relatively simple failure criterion was originally developed for rock masses and is attractive because of the continuous combination of the

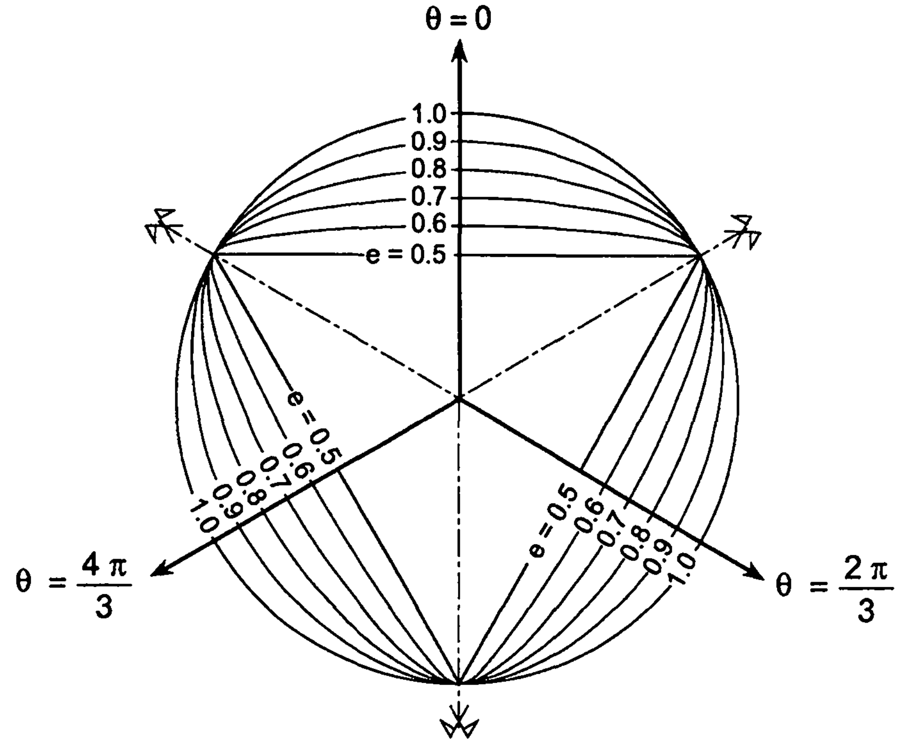

Figure 3.3: Elliptic function $0.5 \geq r(\theta, e) \geq 1$

maximum tensile stress condition of Rankine (expressed in footnote page 45) and the Mohr-Coulomb friction law (expressed in footnote page 45) of limited shear strength. The Hoek and Brown criterion was used by Willam et al. [149] to characterize the triaxial test data of medium strength concrete and was subsequently extended by Pramono and Willam [108] to formulate an elastic-plastic constitutive model for hardening/softening behavior of concrete when subjected to arbitrary triaxial loading. The principal stresses representation does not account for the intermediate principal stress and also leads to numerical difficulties at the corners in the deviatoric plane. To overcome these deficiencies, the principal stress criterion was transformed into an invariant formulation using the interrelationship between the principal stresses and the Haigh-Westergaard coordinates given in equation 3.17. Inserting the principal stresses σ_1 and σ_3 into the Hoek and Brown criterion in equation 3.50 leads to:

$$f(\xi, \rho, \theta) = \left[\sqrt{2}\frac{\rho}{f_c}\sin(\theta + \frac{\pi}{3})\right]^2 + \phi\left[\sqrt{\frac{2}{3}}\frac{\rho}{f_c}\cos\theta + \frac{\xi}{\sqrt{3}f_c}\right] - c = 0. \tag{3.51}$$

This format was extended by Weihe [145] to generate a continuous failure surface which does not exhibit corners in the deviatoric plane:

$$f(\xi, \rho, \theta) = \left[\sqrt{1.5}\frac{\rho}{f_c}r(\theta, e)\right]^2 + \phi\left[\frac{\rho}{\sqrt{6}f_c}r(\theta, e) + \frac{\xi}{\sqrt{3}f_c}\right] - c = 0. \tag{3.52}$$

This failure criterion was called the modified Leon-Pramono model because of its analogy to the parabolic failure model by Leon [75] (given in footnote page 46) for modeling the triaxial strength of concrete. This failure criterion was subsequently incorporated by Etse [38] in a comprehensive elastic-plastic hardening/softening formulation under the name of the extended Leon model. It was enlarged for three dimensional computations by Menétrey [88] and applied to finite element studies of concrete structures. The shape of the triple symmetric deviatoric sections remains affine if the out-of-roundness parameter is constant. This contrasts many experimental observations on concrete, as the deviatoric section has a triangular shape at low confinement and a circular one at high confinement. Therefore, the out-of-roundness parameter was expressed in terms of the hydrostatic stress for reasonable approximation of the experimental data which further complicates the extended Leon model, see Etse and Willam [39].

A slightly different extension of the Hoek and Brown criterion (equation 3.51) which leads also to a smooth criterion is obtained if one assumes:

$$\begin{aligned}\sqrt{2}\sin(\theta+\tfrac{\pi}{3}) &\approx \sqrt{1.5}\\ \sqrt{\tfrac{2}{3}}\cos(\theta) &\approx \tfrac{1}{\sqrt{6}}r(\theta,e).\end{aligned}$$

The resulting approximation is illustrated in figure 3.4 for different values of the out-of-roundness parameter. This approximation reproduces the tensile ($\theta = 0$) and compressive meridians ($\theta = \pi/3$) of the Hoek and Brown criterion in equation 3.50 if $e = 0.5$.

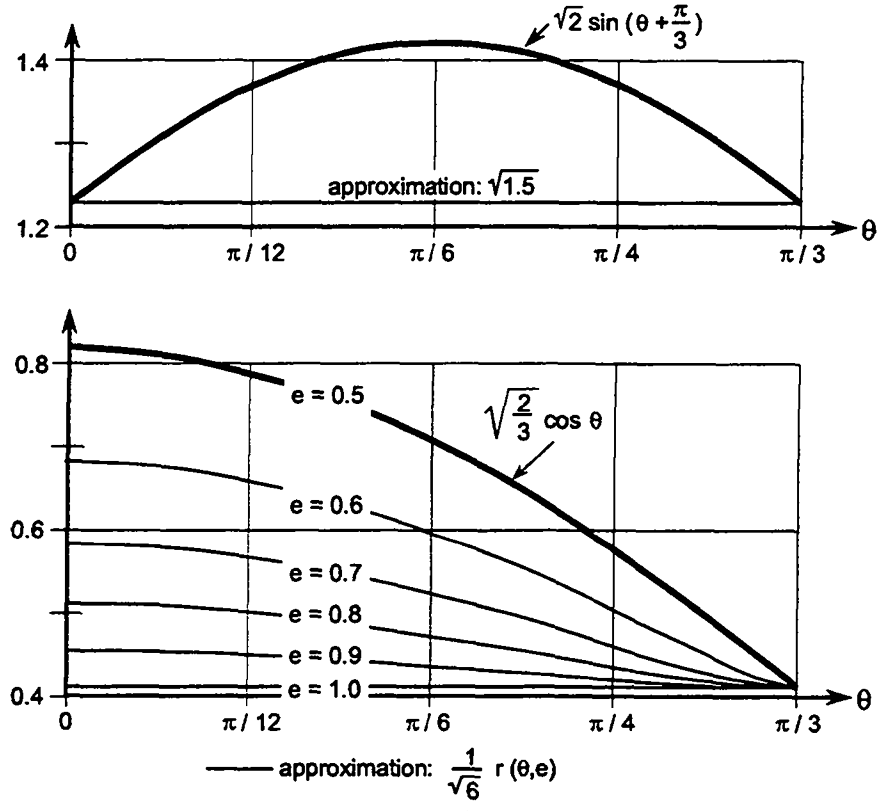

Figure 3.4: Approximation of trigonometric functions for the concrete failure criterion

The resulting triaxial strength criterion, which will be named the "concrete failure criterion", is expressed as:

$$f(\xi,\rho,\theta) = \left[\sqrt{1.5}\frac{\rho}{f_c}\right]^2 + \phi\left[\frac{\rho}{\sqrt{6}f_c}r(\theta,e) + \frac{\xi}{\sqrt{3}f_c}\right] - c = 0. \tag{3.53}$$

In contrast to the Hoek and Brown criterion (equation 3.50) the intermediate principal stress σ_2 is accounted for as the concrete failure criterion is expressed in terms of the three Haigh-Westergaard coordinates. Another advantage of this criterion is that the shape of the deviatoric section tends to a circular form with increasing confining pressure due to the circular deviatoric shape of the ρ^2 contribution.

The meridians of this criterion are parabolic and intersect the hydrostatic axis only at the point of equi-triaxial extension. At this point a discontinuity of the gradient is observed defining a vertex. However, except for that particular point, the concrete failure criterion describes a smooth and convex surface.

The structure of the concrete failure criterion is characteristic of an isotropic loading functions, where the limit function may be written as $f(\sigma) = \bar{f}(\sigma) - c = 0$. In other terms, the cohesive strength c is decoupled from the stress function. This expression may be readily used to describe isotropic loss of cohesive strength, when $c \rightarrow 0$. The friction parameter ϕ is also uncoupled and may be adjusted to control frictional hardening/softening when so desired. For convenience the cohesion and friction parameters are expressed below in terms of the uniaxial strength data in compression and tension.

$$\begin{cases} c &= 1 \\ \phi &= 3\frac{f_c^2-f_t^2}{f_c f_t}\frac{e}{e+1}. \end{cases}$$

Thus the concrete failure surface passes through the points of uniaxial compressive and tensile strength when the cohesion and the friction parameters are so specified.

The out-of-roundness parameter

The concrete failure criterion (equation 3.53) is characterized by three parameters: f_c, f_t and e. Identification of the uniaxial strength parameters f_c and f_t is well established in the concrete literature, which includes the on-going controversy on the tensile strength of concrete and appropriate experiments to measure this elusive property. In contrast, the out-of-roundness parameter e is less known, thus its effect on the triaxial failure surface deserves further discussion.

The influence of the out-of-roundness parameter e is illustrated in figure 3.5 showing the trace of the failure surface in three deviatoric sections for two out-of-roundness parameters $e = 0.5$ and $e = 0.6$. The three levels of hydrostatic pressure correspond to the values in uniaxial tension, $\xi = \frac{f_t}{\sqrt{3}}$, uniaxial compression, $\xi = -\frac{f_c}{\sqrt{3}}$, and triaxial compression, $\xi = -\sqrt{3}f_c$. Comparing the deviatoric sections of the failure surface generated by the two out-of-roundness parameters, it can be seen that the shape is more rounded for $e = 0.6$ as compared to $e = 0.5$. Furthermore, for $e = 0.5$ the shape is no longer smooth because of the corners which appear along the three compressive meridians, whereas for $e = 0.6$ the shape of the deviatoric section remains smooth. It can also be noted that for both out-of-roundness parameters, the shape of the deviatoric section changes from an almost triangular to an almost circular form with increasing confinement.

The influence of the out-of-roundness parameter e is also illustrated for plane stress when the failure surface intersects the $\sigma_3 = 0$ plane. The trace of the concrete failure criterion is shown in figure 3.6 for the uniaxial strength ratio $f_c = 10.35\, f_t$ and for different values of the out-of-roundness parameter $0.5 \leq e \leq 1.0$. It can be seen that the out-of-roundness parameter hardly influences the failure description in biaxial tension and in tension-compression. However, it strongly affects the biaxial compression region. The lower limit of the out-of-roundness parameter, $e = 0.5$, leads to an equi-biaxial compressive strength of $f_{bc} = f_c$, whereas the upper limit, $e = 1$, increases dramatically the equi-biaxial compressive strength to $f_{bc} = 5.31\, f_c$.

Turning the argument around, one may ask what out-of-roundness parameter should be used to obtain a prescribed equi-biaxial compressive strength. Figure 3.7 plots the relationship between the equi-biaxial compressive strength f_{bc} and the out-of-roundness parameter e.

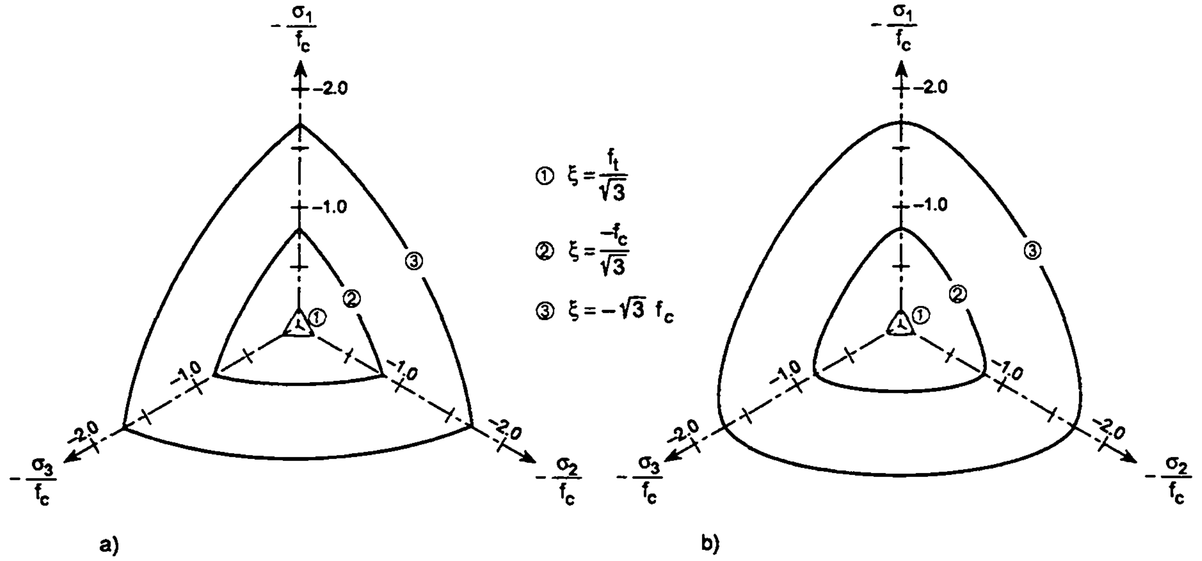

Figure 3.5: Three deviatoric sections of the concrete failure criterion for out-of-roundness parameter: (a) $e = 0.5$, (b) $e = 0.6$

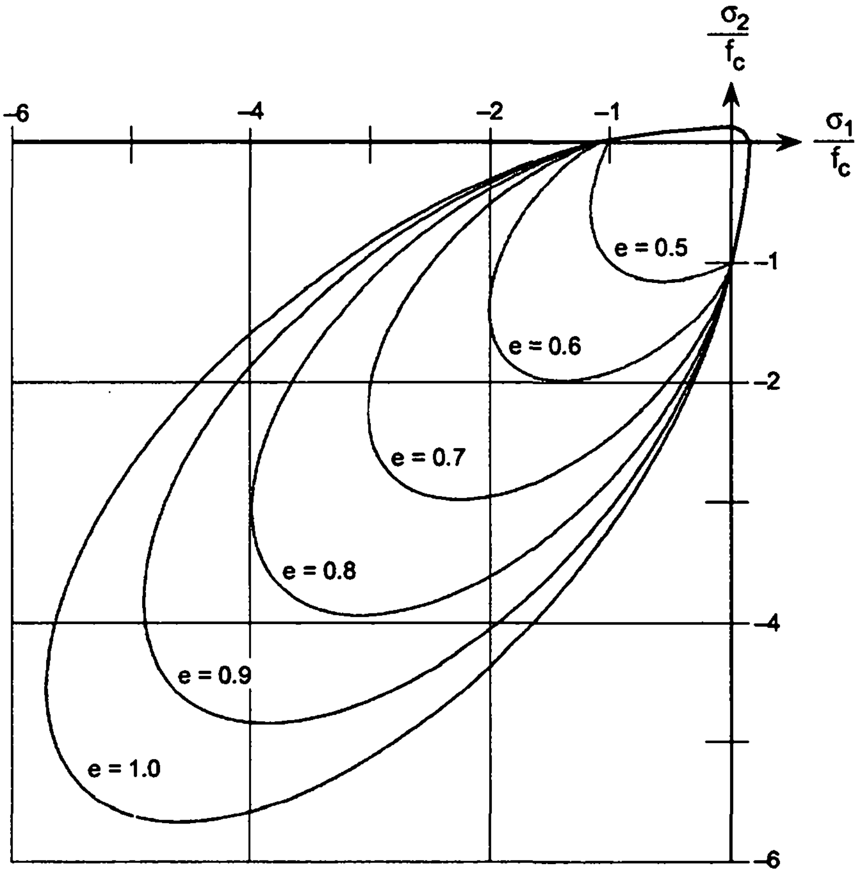

Figure 3.6: Influence of the out-of-roundness parameter on the plane stress section of the concrete failure criterion

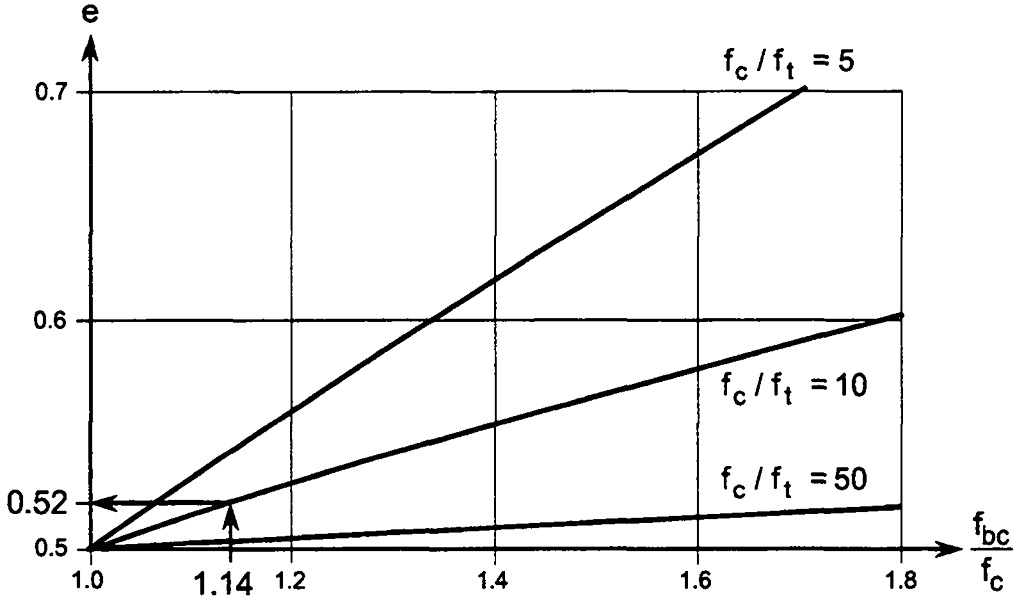

Figure 3.7: Relation between out-of-roundness parameter e and biaxial compressive strength f_{bc}

Comparison with experimental strength data

After showing the influence of the calibration parameters which characterize the triaxial strength criterion, the predictive value of the failure surface is assessed with particular test data in plane stress and triaxial compression.

The strength prediction of the concrete failure criterion is compared in figure 3.8 with the plane stress experiments by Kupfer, Hilsdorf and Rüsch [72]. The particular concrete is calibrated by the three model parameters: $f_c = 32.1$ N/mm^2, $f_t = 3.1$ N/mm^2, and[9] $e = 0.52$. The resulting trace of the concrete failure criterion provides very close agreement with the experimental data.

Comparison of the concrete failure criterion with the triaxial strength data by Chinn and Zimmerman [22] and Mills and Zimmerman [94] is shown in figure 3.9 along the tensile and compressive meridians. The calibration of the three model parameters is based on the uniaxial strength ratio $f_c/f_t = 10$ and on the out-of-roundness parameter $e = 0.6$. Again, the concrete failure criterion provides close agreement with the experimental data.

From the test data summarized by the CEB [23] it can be inferred that for concrete, the out-of-roundness parameter should be so that $0.5 < e \leq 0.6$, and that the value $e = 0.52$ provides an excellent biaxial strength envelope for low and medium strength concrete.

Generalized failure criterion

The concrete failure criterion (equation 3.53) may be generalized to include other strength criteria, such as the Huber-Mises, the Drucker-Prager, the Rankine, the Mohr-Coulomb, and the parabolic Leon. The main advantage of such a generalization is that these well-known engineering criteria for failure are readily recovered once the generalized criterion has been implemented into a computer code. The generalized failure criterion is expressed as:

$$f(\xi, \rho, \theta) = [A_f \rho]^2 + \phi\,[B_f \rho r(\theta, e) + C_f \xi] - c = 0. \tag{3.54}$$

---

[9] The value of the out-of-roundness parameter is obtained with the help of figure 3.7 with $f_{bc} = 1.14 f_c$.

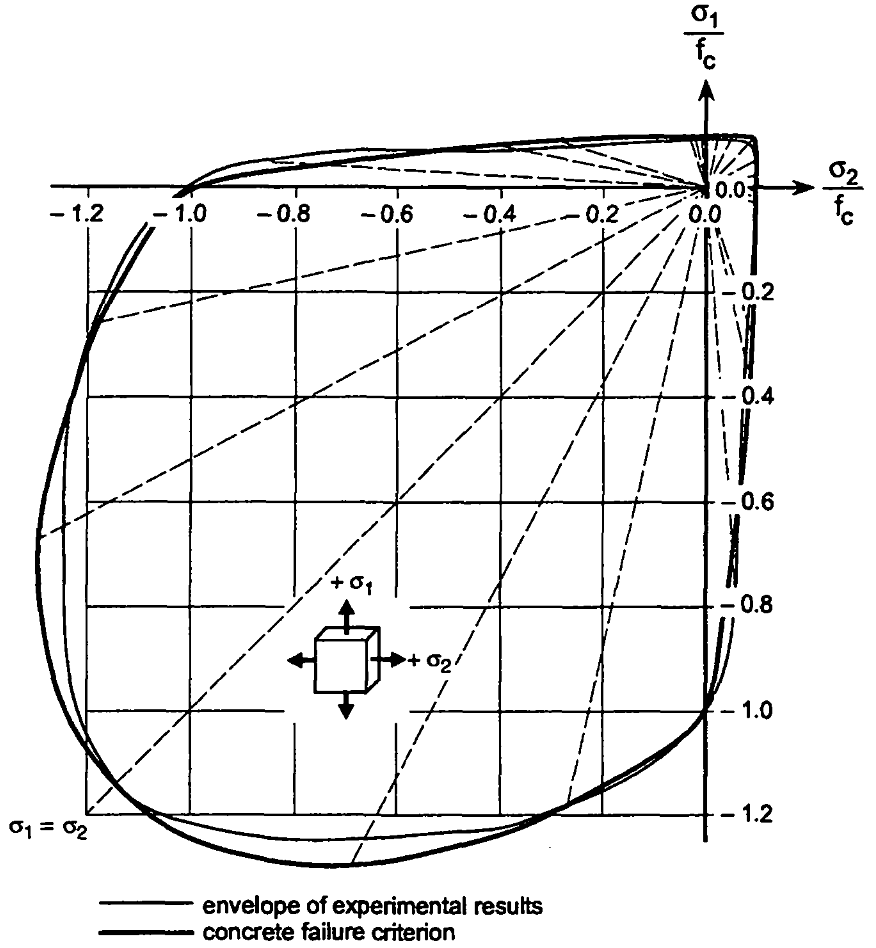

Figure 3.8: Comparison of the concrete failure criterion with biaxial test data; (Kupfer, Hilsdorf and Rüsch 1969)

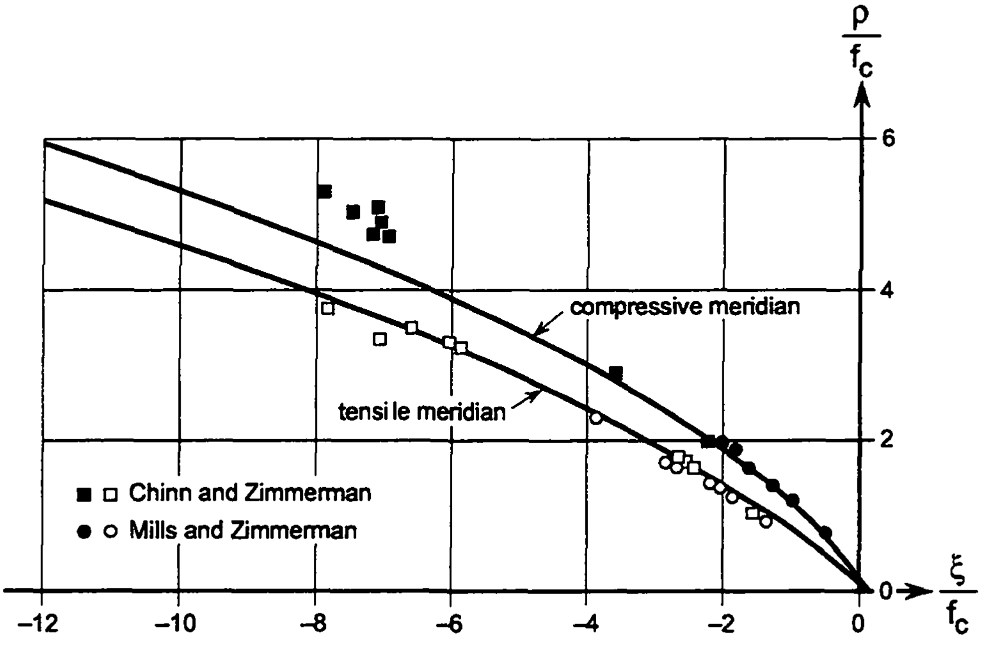

Figure 3.9: Comparison of the concrete failure criterion with triaxial test data; (Chinn and Zimmerman 1965) and (Mills and Zimmerman 1970)

This generalized form leads to a smooth and convex surface for $0.5 < e \leq 1$ except along the hydrostatic axis where a vertex is located at the point of equi-triaxial extension:

$$\sigma_{apex} = \frac{c}{\sqrt{3}\phi C_f}\mathbf{1}. \tag{3.55}$$

This generalized criterion uncouples the cohesion parameter $c = 1$ from the friction parameter ϕ and lends itself to hardening/softening descriptions. The gradient of the generalized concrete failure criterion are given in appendix C. The parameters A_f, B_f and C_f are used to reduce the general failure criterion to a specific format and to calibrate the strength parameters in terms of the uniaxial tensile and compressive strength and the out-of-roundness parameter.

(a) **The Huber-Mises criterion** delimits the deviatoric stress for example by the uniaxial compressive strength in the form:

$$f(\rho) = \rho - \sqrt{\frac{2}{3}}f_c = 0. \tag{3.56}$$

This one parameter criterion infers that $f_c = f_t$ because of lack of pressure sensitivity. The reduction of the generalized failure criterion to the Huber-Mises condition is achieved by letting: $A_f = 0, B_f = \sqrt{\frac{3}{2}}\frac{1}{f_c}, C_f = 0, \phi = 1,$ and $e = 1$.

(b) **The Drucker-Prager criterion** [32] delimits the deviatoric stress by a linear combination of the cohesive and frictional strength in the form:

$$f(\rho, \xi) = \rho + \sqrt{6}a_\phi\xi - \sqrt{2}k = 0, \tag{3.57}$$

where a_ϕ and k denote the two free material parameters as defined in appendix D.3. Reduction of the generalized failure criterion to the Drucker-Prager condition is achieved by letting: $A_f = 0, B_f = \frac{1}{\sqrt{2}k}, C_f = \sqrt{3}\frac{a_\phi}{k}, \phi = 1,$ and $e = 1$. These parameters are further expressed in terms of f_c and f_t, so that: $B_f = \sqrt{\frac{3}{8}}\frac{f_c+f_t}{f_c f_t}$ and $C_f = \frac{3}{2}\frac{f_c-f_t}{f_c f_t}$.

(c) **The Rankine criterion**[10] for tensile cracking delimits the maximum tensile stress in the form:

$$f(\rho, \xi, \theta) = \sqrt{2}\rho\cos\theta + \xi - \sqrt{3}f_t = 0. \tag{3.58}$$

Reduction of the generalized failure criterion to the Rankine condition is achieved by letting: $A_f = 0, B_f = \frac{1}{\sqrt{6}f_t}, C_f = \frac{1}{\sqrt{3}f_t}, \phi = 1,$ and $e = \frac{1}{2}$.

(d) **The Mohr-Coulomb criterion** [11] for shear slip may be recast in terms of the invariants (Chen and Han [21]) as:

$$f(\rho, \xi, \theta) = \sqrt{2}\xi\sin(\phi_{mc}) + \sqrt{3}\rho\sin(\theta + \frac{\pi}{3}) + \rho\cos(\theta + \frac{\pi}{3})\sin\phi_{mc} - \sqrt{6}c_{mc}\cos\phi_{mc} = 0, \tag{3.59}$$

where c_{mc} denotes the cohesive strength and ϕ_{mc} the angle of internal friction. Full reduction of the general failure criterion to the Mohr-Coulomb condition cannot be achieved because the Mohr-Coulomb criterion is characterized by a hexagonal section in the deviatoric plane. The generalized failure criterion may be calibrated so that the tensile and the compressive meridians match exactly when the out-of-roundness parameter is determined by

$$e = \frac{3 - \sin(\phi_{mc})}{3 + \sin(\phi_{mc})}. \tag{3.60}$$

---

[10] The original form of the Rankine criterion states that the maximum normal stress is bounded by the uniaxial tensile strength $\sigma_1 \leq f_t$.

[11] The original format of the Mohr-Coulomb criterion states that the shear stress at the critical slip plane is restricted by the linear combination of frictional resistance and cohesive strength: $\mid \tau \mid \leq -\sigma\tan\phi_{mc} + c_{mc}$.

The other parameters are obtained by letting: $A_f = 0, B_f = \frac{3-\sin(\phi_{mc})}{\sqrt{24}c_{mc}\cos(\phi_{mc})}, C_f = \frac{1}{\sqrt{3}c_{mc}}\tan(\phi_{mc})$ and $\phi = 1$. These parameters can be further expressed in terms of: f_c and f_t, so that: $B_f = \frac{1}{\sqrt{6}}\frac{f_c+2f_t}{f_cf_t}, C_f = \frac{1}{\sqrt{3}}\frac{f_c-f_t}{f_cf_t}$, and $e = \frac{f_c+2f_t}{2f_c+f_t}$.

(e) **The parabolic Leon criterion** is a simplification of the original concrete strength criterion by Leon [75] [12] and further described by Romano [119]. In terms of the principal stresses that criterion may be written as:

$$f(\sigma_1, \sigma_3) = \left[\frac{\sigma_1 - \sigma_3}{f_c}\right]^2 + \phi_{leon}\frac{\sigma_1 + \sigma_3}{f_c} - c_{leon} = 0. \tag{3.61}$$

Transforming σ_1 and σ_3 into the Haigh-Westergaard coordinates according to equation 3.17 leads to:

$$f(\xi, \rho, \theta) = \left[\sqrt{2}\frac{\rho}{f_c}\sin(\theta + \frac{\pi}{3})\right]^2 + \phi_{leon}\left[\sqrt{\frac{2}{3}}\frac{\rho}{f_c}\cos(\theta + \frac{\pi}{3}) + \frac{2}{\sqrt{3}}\frac{\xi}{f_c}\right] - c_{leon} = 0. \tag{3.62}$$

Introducing the following approximations:

$$\begin{array}{lcl} \sqrt{2}\sin(\theta + \frac{\pi}{3}) & \approx & \sqrt{1.5} \\ \cos(\theta + \frac{\pi}{3}) & \approx & 0, \end{array}$$

leads to the parabolic Leon criterion below with a circular section in the deviatoric plane:

$$f(\xi, \rho) = \left[\sqrt{1.5}\frac{\rho}{f_c}\right]^2 + \phi_{leon}\frac{2}{\sqrt{3}}\frac{\xi}{f_c} - c_{leon} = 0. \tag{3.63}$$

The cohesion and the friction parameters are calibrated from the uniaxial tensile and compressive strength so that: $c_{leon} = \frac{f_cf_t+(f_t)^2}{f_cf_t+(f_c)^2}$ and $\phi_{leon} = \frac{3}{2}\frac{(f_c)^2-(f_t)^2}{f_cf_t+(f_c)^2}$. The reduction of the generalized failure criterion is achieved letting: $A_f = \sqrt{\frac{1.5}{f_cf_t}}, B_f = 0, C_f = \sqrt{3}\frac{f_c-f_t}{f_cf_t}$, and $\phi = 1$. It should be noted that this approximation of the original Leon criterion is independent of θ and corresponds to a parabolic generalization of the Drucker-Prager failure criterion. In fact, it falls into the format of rotationally symmetric failure hypotheses which were originally proposed by Schleicher [125] and Burzynski [16] in the 1920's.

The most significant examples of the generalized failure criterion are summarized in table 3.3. Some examples of the calibration are illustrated in figure 3.10 along the meridian plane where the Huber-Mises criterion is calibrated by the uniaxial compressive strength, while the Drucker-Prager, the circular approximation of the original Leon criterion and the proposed concrete failure criterion with a circular deviatoric section ($e = 1.0$) pass through both data points of uniaxial tension and uniaxial compression.

Concluding remarks

The proposed concrete failure criterion has the following characteristics:

1. It is a function of the three stress invariants and has been formulated in terms of the Haigh-Westergaard coordinates for easy geometric interpretation.

2. It is a three parameter model which has been calibrated in terms of the uniaxial tensile and compressive strength f_c, f_t and the out-of-roundness parameter e.

---

[12] The original form of the Leon criterion states that the shear stress at the critical slip plane is restricted by the parabolic relation: $\tau^2 \leq C_1\sigma + C_2$, where C_1 and C_2 are combinations of the friction and cohesion parameters.

Generalized criterion	A_f	B_f	C_f	ϕ	e
Huber-Mises	0	$\sqrt{\frac{3}{2}\frac{1}{f_c}}$	0	1	1
Drucker-Prager	0	$\sqrt{\frac{3}{8}\frac{f_c+f_t}{f_c f_t}}$	$\frac{3}{2}\frac{f_c-f_t}{f_c f_t}$	1	1
Rankine	0	$\frac{1}{\sqrt{6}f_t}$	$\frac{1}{\sqrt{3}f_t}$	1	$\frac{1}{2}$
Mohr-Coulomb	0	$\frac{1}{\sqrt{6}}\frac{f_c+2f_t}{f_c f_t}$	$\frac{1}{\sqrt{3}}\frac{f_c-f_t}{f_c f_t}$	1	$\frac{f_c+2f_t}{2f_c+f_t}$
Parabolic Leon	$\sqrt{\frac{1.5}{f_c f_t}}$	0	$\sqrt{3}\frac{f_c-f_t}{f_c f_t}$	1	no e
concrete failure	$\frac{\sqrt{1.5}}{f_c}$	$\frac{1}{\sqrt{6}f_c}$	$\frac{1}{\sqrt{3}f_c}$	$3\frac{f_c^2-f_t^2}{f_c f_t}\frac{e}{e+1}$	e

Table 3.3: Reduction of the generalized failure criterion to specific criteria

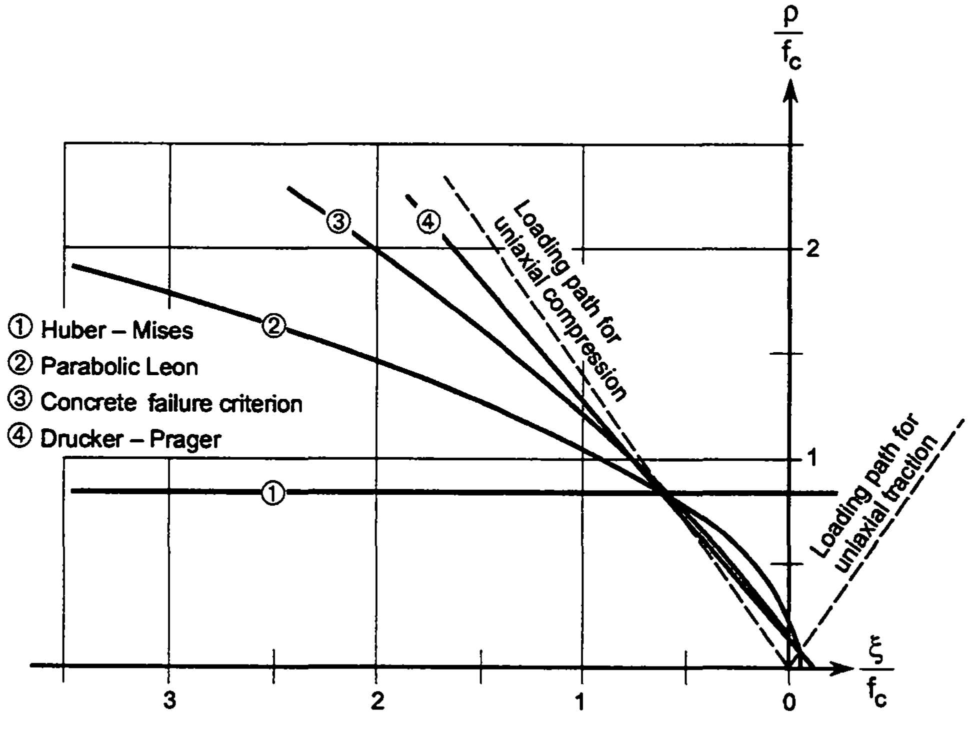

Figure 3.10: Calibration of the generalized failure criterion to Huber-Mises, Drucker-Prager, parabolic Leon and concrete failure criteria in the meridian plane

3. It describes a smooth and convex surface in stress space (parabolic meridians) as long as $0.5 < e \leq 1$, except for the vertex at equi-triaxial extension.
4. Its cohesion and frictional parameters are uncoupled in order to provide direct control for hardening/softening extensions.
5. Its deviatoric sections tends to a circular shape with increasing confinement.

The validity of the concrete failure criterion has been demonstrated with different strength data for plain concrete. It is shown that both biaxial as well as triaxial test data can be captured by the proposed failure criterion.

The concrete failure criterion may be readily generalized to a format which includes the Huber-Mises, the Drucker-Prager, and the Rankine criteria. The generalized failure envelope also degenerates to the tensile and compressive meridians of the linear Mohr-Coulomb criterion. In addition, it reduces to the parabolic two invariant approximation of Leon criterion. The advantage of the unified formulation is that it encompasses a large number of well-known failure criteria as special cases.

3.5.3 Concrete flow rule

Preliminaries

The flow rule controlling the evolution of the concrete plastic deformation is described in this section. As presented in the previous section, the dependance of the concrete failure criterion on the first invariant is justified. But, if the plastic potential coincides with the failure criterion (normality principle or associated plasticity), the prediction of volume expansion is considerable. Therefore, the constitutive relation based on the normality principle cannot be applied for concrete as mentioned by many authors, among others Chen [21] and Lubliner [80].

Experimentally, *dilatancy* is defined as a volume increase resulting from the formation and growth of cracks which are parallel to the direction of the compressive stress. Dilatancy is characterized by the dilatancy angle ψ, defined as the angle between the normal of the plastic potential and the vertical axis. This angle represents the ratio of the increment of plastic volumetric strain over plastic shear strain. In figure 3.11 duplicated from Smith [130], the plastic strain vectors obtained experimentally for conventional triaxial compression tests are reproduced along with the stress paths. This figure illustrates that concrete is characterized by a non-associated flow rule as the angle between the plastic strain vectors and the normal to the failure envelope are not similar. For increasing confinement pressure the non-associated direction increases which corresponds to a reduction of the plastic volumetric strain and therefore a reduction of the dilatancy angle.

Different type of flow rules

The plastic potential monitoring the flow rule is expressed with the same equation as the one describing the generalized failure criterion in equation 3.54. This expression has the advantage that many different types of surface can be calibrated. However, contrary to the failure criterion, the plastic potential is assumed to be independent of the deviatoric polar angle, and is consequently not expressed in terms of the elliptic function which gives

$$g(\rho, \xi) = (A_g \rho)^2 + B_g \rho + C_g \xi, \tag{3.64}$$

where A_g, B_g and C_g are parameters characterizing the plastic potential. The assumption that the plastic potential is independent of the deviatoric polar angle is convenient because

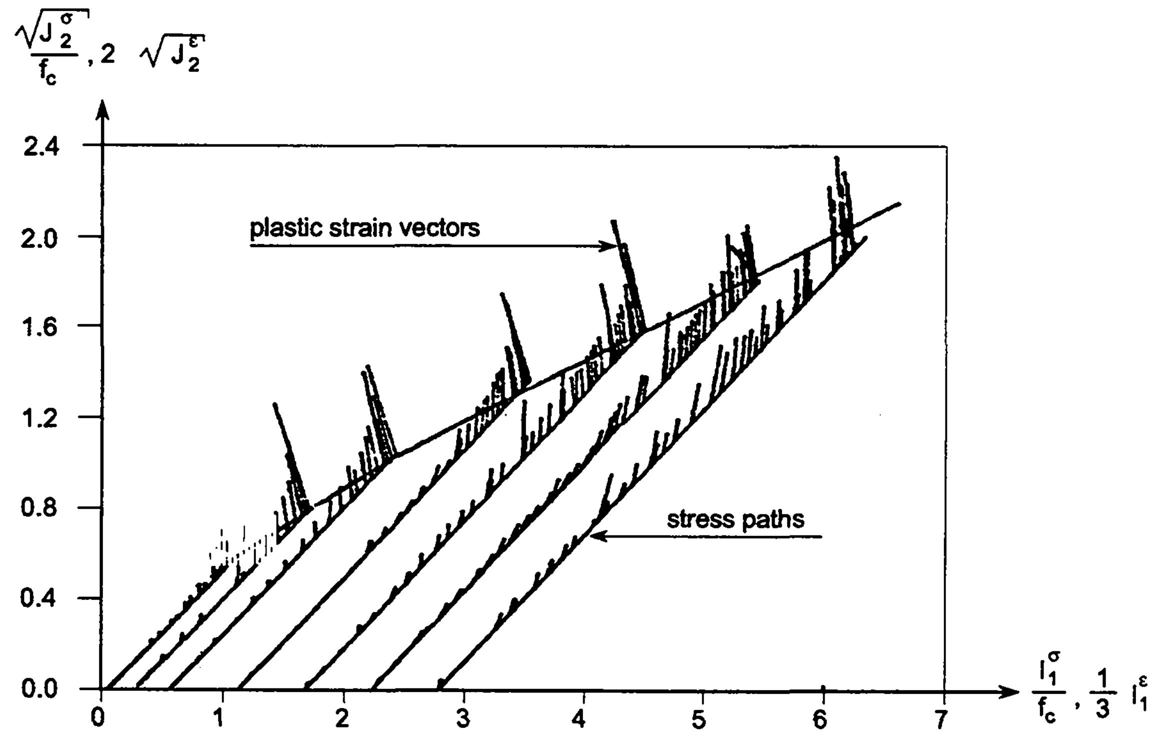

Figure 3.11: Plastic strain rate vectors and stress paths for conventional triaxial compression test; (Smith 1987)

it simplifies the formulation, and the stress integration algorithm presented in section 3.5.5 is consequently facilitated. The shape of the flow rule is circular in the deviatoric plane as shown in figure 3.12 similarly to the radial return originally developed by Wilkins [146]. The failure criterion and the plastic potential are different in the deviatoric plane (if $e \neq 1$). This difference induces a non-associated flow rule in the deviatoric plane as the failure criterion is elliptic and the plastic potential is circular. It can be argued that this assumption is neither in contradiction nor reproducing experimental results as very few are available. The gradients of the plastic potential are given in appendix C. From equation 3.64, the flow direction is expressed as

$$\frac{\partial g}{\partial \sigma_{ij}} = m_{ij} = \left(2A_g^2 + B_g\frac{1}{\rho}\right)s_{ij} + \frac{C_g}{\sqrt{3}}\delta_{ij}. \qquad (3.65)$$

It can be observed that the flow direction depends of the deviatoric stress tensor and has a constant volumetric component.

In the meridian plane, the type of plastic potential that should be used to simulate concrete behavior is not well defined even though some experimental data are available as presented in figure 3.11. In order to determine the most appropriate flow rule, four different types are investigated:

1. The deviatoric flow rule; is derived from a Huber-Mises plastic potential which is adjusted as presented in table 3.3. This flow rule exhibits a constant volumetric plastic strain (equivalent to the incompressibility condition expressed in equation 3.3). This flow rule is relevant for concrete behavior at high confinement pressure as shown in figure 3.11. The condition of incompressibility of the plastic flow generates some locking behavior as mentioned by Nagtegaal et al. [98]. This problem is treated in section 4.4.2 where the $\bar{\boldsymbol{B}}$ method is presented.

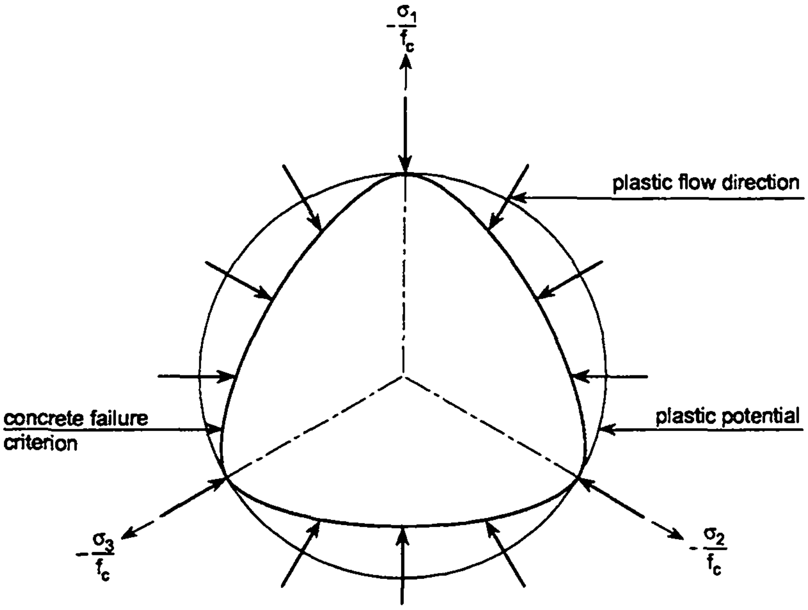

Figure 3.12: Plastic flow direction in the deviatoric plane for the concrete model

2. The tensile meridian flow rule; is derived from a plastic potential generated by the tensile meridian of the concrete criterion. This plastic potential is obtained with: $A_g = A_f$, $B_g = \phi B_f 1/e$, and $C_g = \phi C_f$.

3. The parabolic flow rule; is obtained from a plastic potential which is similar to the parabolic Leon criterion and adjusted as presented in table 3.3. This flow rule generates no apex at the point of equi-triaxial extension.

4. The concrete flow rule; is derived from a plastic potential which satisfies the evolution of the plastic strain observed experimentally so that the following two conditions are fulfill: (1) for the uniaxial tensile test, the plastic strain follows the loading path for uniaxial traction, (2) at the uniaxial ultimate compressive strength, the flow rule is given by the dilatancy angle ψ_c introducing a new material parameter.

   The first condition is satisfied if the slope of the loading path for uniaxial traction equals the flow direction at the ultimate uniaxial tensile strength point ($\xi = f_t/\sqrt{3}, \rho = \sqrt{2/3}f_t, \theta = 0$). The slope of the loading path for uniaxial traction is: $\xi/\rho = 1/\sqrt{2}$. The slope of the plastic potential is derived from equation 3.65 by expressing the invariants of the flow rule: $\xi(m) = C_g$ and $\rho(m) = 2A_g^2\rho + B_g$. The slope of the plastic flow direction equals the slope of the loading path for uniaxial traction imposing that

$$\frac{\xi}{\rho} = \frac{C_g}{2A_g^2\rho + B_g} = \frac{1}{\sqrt{2}}. \tag{3.66}$$

   This equation must be valid at the uniaxial tensile strength point leading to

$$\frac{2}{\sqrt{3}}f_t A_g^2 + \frac{1}{\sqrt{2}}B_g = C_g. \tag{3.67}$$

   The second condition states that at the uniaxial ultimate compressive strength point, ($\xi = -f_c/\sqrt{3}, \rho = \sqrt{2/3}f_c, \theta = \pi/3$), the flow rule is given by the dilatancy angle ψ_c.

This condition can be expressed as $\tan\psi_c = \xi/\rho$, and introducing the invariants of the flow rule leads to

$$\frac{2\sqrt{2}}{\sqrt{3}}\tan\psi_c f_c A_g^2 + \tan\psi_c B_g = C_g. \tag{3.68}$$

Combining these two equations and assuming that $A_g = 1$ leads to

$$B_g = \frac{2(\sqrt{2}\tan\psi_c f_c - f_t)}{\sqrt{3}(1/\sqrt{2} - \tan\psi_c)} \tag{3.69}$$

$$C_g = \frac{1}{\sqrt{2}}B_g + \frac{2}{\sqrt{3}}f_t. \tag{3.70}$$

The parameter B_g must remain positive which implies that:

$$\arctan\frac{f_t}{\sqrt{2}f_c} < \psi_c < \arctan\frac{1}{\sqrt{2}} \approx 35.3^0, \tag{3.71}$$

for $f_c/f_t = 10$ this condition reads: $4^0 < \psi_c < 35.3^0$. The influence of this parameter is examined in chapter 5.

The failure criterion, the plastic potential, and the plastic flow vectors are represented in figure 3.13 in the meridian plane for the concrete flow rule. It can be checked that the concrete flow rule follows the loading path for uniaxial traction and is characterized by a dilatancy angle ψ_c for the ultimate uniaxial compressive strength point.

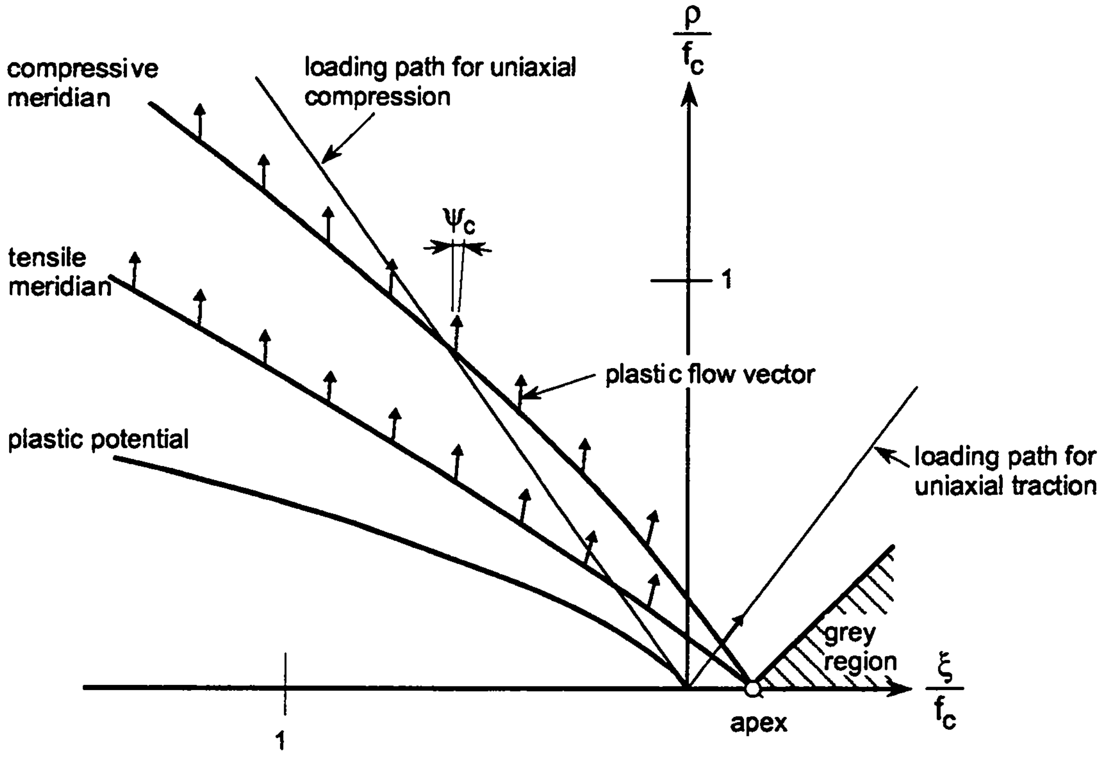

Figure 3.13: Failure criterion, plastic potential, plastic flow vectors, and grey region for the concrete model in the meridian plane

Treatment of the apex

A non-smooth failure criterion is characterized by the existence of singular points or apexes. The general failure criterion depicted in equation 3.54 is continuous and smooth except for one singular apex along the hydrostatic axis if $C_f > 0$. The coordinates of this apex are: $(\xi = c/(\phi C_f), \rho = 0)$. This apex implies the existence of a *grey region* which is a region in the stress space where the stress return algorithm is not defined. The grey region as shown in figure 3.13 also depends on the plastic flow direction and for the general failure criterion given in equation 3.54 and the plastic potential given in equation 3.64 the grey region is delimited by

$$\xi \leq \rho \frac{C_g}{B_g} + \frac{c}{\phi C_f}. \tag{3.72}$$

An apex is a particular point of interest and its numerical treatment is described in section 3.5.5.

3.5.4 Cracking simulation

Preliminaries

According to fundamental concepts of fracture mechanics, three basic crack or fracture modes are differentiated: the fundamental mode I which is a tensile opening mode, mode II which is an in-plane shear mode, and mode III which is an out-of-plane shear mode as illustrated in figure 3.14.

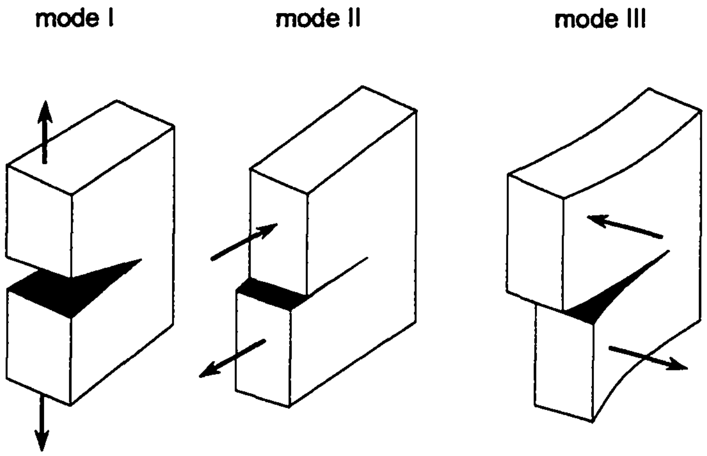

Figure 3.14: Basic fracture modes: I-tensile opening, II-in-plane shear, and III-out-of-plane shear; (Broek 1974)

Cracking in concrete is simulated with the fictitious crack model developed by Hillerborg et al. [53]. This fictitious crack model is illustrated in figure 3.15 for mode I fracture. The term fictitious crack is used as no well defined crack tip is identified due to micro-cracking, but rather a fracture zone is delimited, within which stress decreases as the deformation increases. The fictitious crack is bounded by the following two extreme points:

- the point where the maximal tensile stress reaches f_t,
- the point where the tensile stress transfer ends and the crack opening reaches w_r defined as the *crack rupture opening*; this point is the beginning of the stress-free crack.

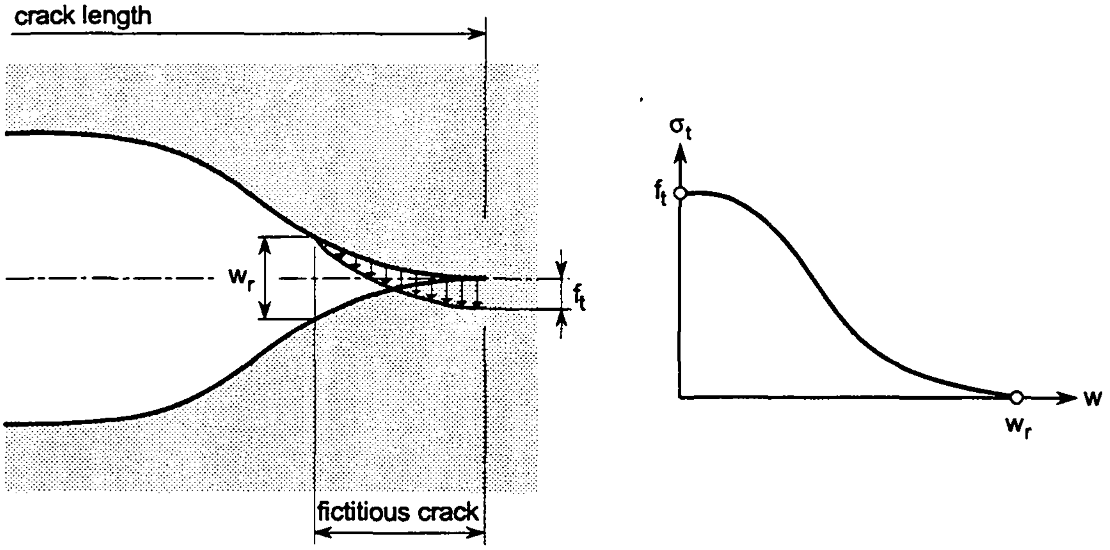

Figure 3.15: Fictitious crack model; (Hillerborg et al. 1974)

In between these points, the tensile stress is controlled by the *crack opening* w. The amount of energy absorbed per unit area in opening the crack from zero to the crack rupture opening w_r is

$$G_f = \int_0^{w_r} \sigma_t dw, \tag{3.73}$$

which defines the fracture energy. This energy is a material property and is specified as the energy required to propagate a tensile crack of unit area (N·m/m2).

In assuming a constant fracture energy which depends on both the fracture length and the cracked zone, Bažant [7] derived a size-effect law which is expressed as

$$\sigma_n = C_0(1+\beta)^{-\frac{1}{2}}, \tag{3.74}$$

where σ_n is the nominal stress, β is the relative size, and C_0 a constant. This law has been shown to describe brittle failure of concrete structures as summarized by Bažant in [9], and particularly the diagonal shear failure of beams, punching failure of slabs, pullout of bars and anchors. Experimentally, the size-effect influences the punching failure as described in section 2.3.4. Therefore, to reproduce the size-effect, the use of fracture mechanics is justified.

Decohesion process

The crack formation is described with a *strain-softening* model which refers to a gradual decrease in tensile strength with additional deformation. This reduction of tensile strength may be thought as a decrease of the cohesion defined as

$$c = \frac{\sigma_t}{f_t}, \tag{3.75}$$

where σ_t is the degrading tensile stress. The concrete failure criterion given in equation 3.53 can be written so that the cohesive strength is decoupled: $\bar{f}(\sigma, q) - c = 0$. This form results in an isotropic loss of strength due to reduction of the cohesion.

The strain-softening response is initiated, when the concrete starts cracking and the material cannot be assumed intact any longer. This mechanism is controlled by the degradation of the cohesion parameter $1 \leq c \leq 0$. For $c = 1$, the material is intact, and for $c = 0$, the material is considered to be completely fractured and it only exhibits a residual frictional strength similar to granular cohesion-less materials.

Complete loss of cohesion results in the residual concrete failure criterion shown in figure 3.16. This surface is plotted in the plane $\sigma_1 = \sigma_3$ for different value of the out-of-roundness parameter. It can be observed that for $e > 0.5$, some parasitic tensile stresses are accepted.

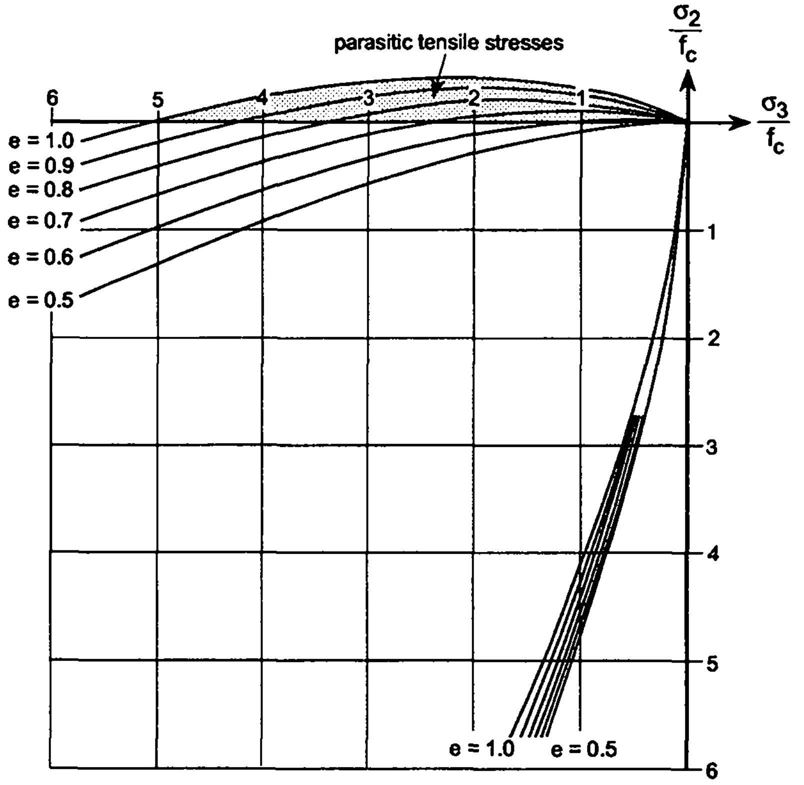

Figure 3.16: Residual concrete failure criterion for complete decohesion in the $\sigma_1 = \sigma_3$ plane

However, for $e = 0.5$ the failure criterion is strictly located in the compressive region. Consequently, to avoid these parasitic tensile stresses the value of the out-of-roundness parameter should not be too far from the value $e = 0.5$ which is in agreement with experimental results as: $0.5 < e \leq 0.6$, for plain concrete as described on page 43. The consequence of these parasitic tensile stresses is studied in section 5.2.2 for the Drucker-Prager yield surface applied to the footing problem.

The hardening behavior of concrete is of secondary importance compared to fracture and consequently it is not considered here. This implies that softening exists even for high levels of confinement and that no transition point between brittle and ductile response as suggested by Willam et al [147] is considered. This is not in agreement with experimental results. However this assumption simplifies the numerical model and does not affect the numerical prediction dramatically as shown in section 5.4.3 when the confined compressive test is simulated.

The decohesion function is expressed with an exponential in order to fit the tensile experimental data which dominates the post-peak response of concrete. This exponential softening decay is expressed as

$$c = \exp\left\{-a\frac{w}{w_r}\right\}, \tag{3.76}$$

where w is the crack opening, w_r is the crack rupture opening, and a the steepness parameter. A graphic representation of this decohesion function is shown in figure 3.17. This function is

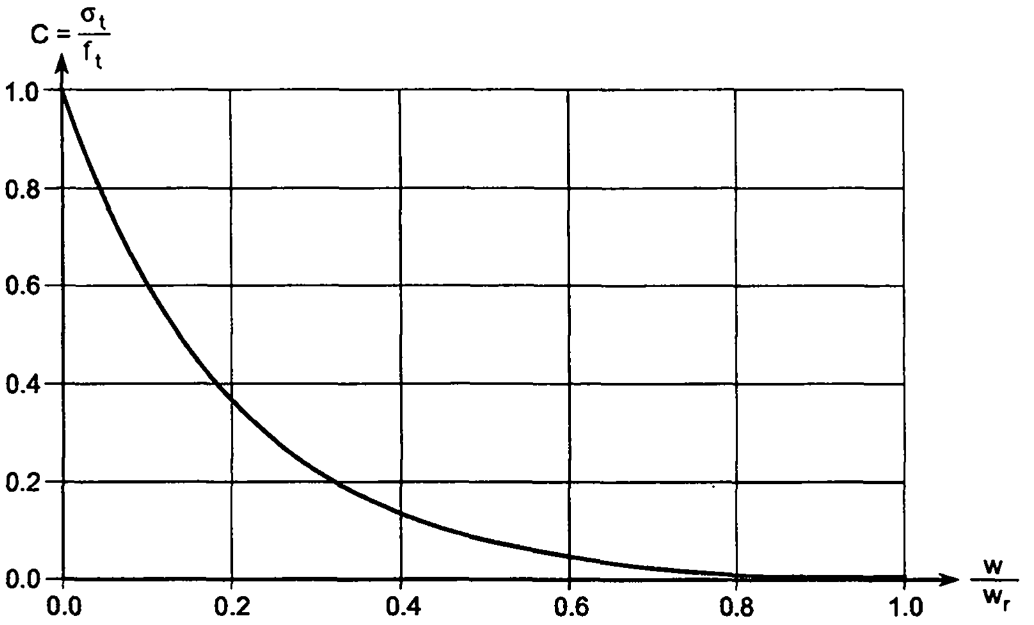

Figure 3.17: Decohesion function

plotted for a convenient value $a = 5$, leading to a residual cohesion of 0.007 for $w = w_r$.

Fracture model in traction

During a tensile test, the energy absorbed in the fracture zone to complete separation of the specimen is defined in equation 3.73. Using equation 3.75 and 3.76 the fracture energy can be expressed as

$$G_f = \int_0^{w_r} \sigma_t dw = \int_0^{w_r} f_t \exp\left\{-a\frac{w}{w_r}\right\} dw = \frac{f_t w_r}{a}(1 - \exp(-a)) \approx \frac{f_t w_r}{a}. \tag{3.77}$$

The fracture energy G_f is considered as a material property (see Rots et al. [121]) implying that it must be invariant with the element size. Therefore, the mapping between the crack opening w used for the definition of the constant fracture energy, and the strain ϵ used at the constitutive level leads to the definition of the height of the element h^e normal to the crack band so that

$$w = h^e \epsilon. \tag{3.78}$$

This height depends on the size of the finite element and its computation is presented in section 4.4. This dependance on the element dimension was originally proposed by Pietruszczak and Mróz [105]. Introducing the finite element size in the softening formulation implies that a crack in a small or large finite element dissipates the same fracture energy. Localization of the failure requires this dependance on the finite element size which is one form of localization limiters.

The strain-softening is controlled with one internal variable which is the positive norm of the plastic strain or fracture strain. The evolution of the internal variable given in equation 3.31 is rewritten in an incremental form as:

$$\Delta q = ||\langle \Delta \epsilon_p \rangle|| = \Delta\gamma ||\langle \boldsymbol{m} \rangle|| = \Delta\gamma \boldsymbol{h}, \tag{3.79}$$

where $\langle\rangle$ are the Macauley brackets which extract the tensile components of the plastic strain so that $\langle \boldsymbol{x} \rangle = \sqrt{0.5(x_i + \mid x_i \mid) x_i}$. The positive norm of the fracture strain governs the crack opening as follows

$$\Delta w = h^e \Delta q = h^e \|\langle \Delta \epsilon_p \rangle\| = h^e \Delta\gamma \|\langle m \rangle\|. \tag{3.80}$$

Now that the fracture model for traction is defined, it is extended to a general state of stress.

General fracture model

From experiments, it is known that tensile splitting in compression as well as shear is due to distributed micro-cracking. Hence, a general crack model can be interpreted as a multiple tensile crack model. Consequently, the fracture model for traction is extended to capture general fracture based on the definition of the fictitious number of cracks N which is formed in a specimen under a given state of stress. The resulting amount of fracture energy which can be dissipated in a specimen is $N \cdot G_f$.

The fictitious number of cracks in a specimen depends on the state of stress. In order to determine an analytical expression of the fictitious number of cracks some elementary experimental results are reviewed. The uniaxial tensile test is characterized by one crack, as with the triaxial extension test. The uniaxial compressive test is characterized by "b" cracks. A biaxial compressive test is characterized by one crack. For punching failure, the state of stress in the corner slab-column is close to a biaxial state of stress with traction acting perpendicularly to the plane of biaxial compression justifying that this experiment is considered here. This review of elementary plain concrete experiments is summarized in table 3.4 along with the corresponding invariants of the stress tensor. An analytical expression of the fictitious number of cracks must reproduce all these elementary plain concrete results. To achieve that, the deviatoric polar angle is included to distinguish between localized failure along the tensile meridian and distributed failure along the compressive meridian. The ratio ξ/ρ is preferred over the value ξ because during proportional unloading, this ratio is not modified. The fictitious number of cracks is expressed as follows:

test	ξ	ρ	θ	N
triaxial extension	$\sqrt{3}f_t$	0	0	1
uniaxial traction	$f_t/\sqrt{3}$	$\sqrt{2/3}f_t$	0	1
uniaxial compression	$-f_c/\sqrt{3}$	$\sqrt{2/3}f_c$	$\pi/3$	b
biaxial compression	$-2\ f_{bc}/\sqrt{3}$	$\sqrt{2/3}f_{bc}$	0	1

Table 3.4: Number of cracks observed in different plain concrete tests

$$N = \begin{cases} \sqrt{2}(-\frac{\xi}{\rho} + 1/\sqrt{2})(1-\cos\theta)(b-1)+1 & \frac{\xi}{\rho} < 1/\sqrt{2} \\ 1 & \frac{\xi}{\rho} \geq 1/\sqrt{2}. \end{cases} \tag{3.81}$$

A graphical representation of this function is given in figure 3.18 for $b = 10$ (the influence of this parameter is presented in section 5.4) and for three different ratios ξ/ρ which corresponds to the traction, compression and pure shear state of loading. It can be checked that for $\theta = 0$ (uniaxial tensile test or the biaxial compressive test) only one crack is induced. For $\theta = 60^0$ and $\xi/\rho = -1/\sqrt{2}$ which corresponds to the uniaxial compressive test, the number of fictitious cracks is $b = 10$.

Using this development of the fictitious number of crack, the increment of crack opening given in equation 3.80 is restated for the general fracture model as

$$\Delta w = h^e \Delta q \frac{1}{N} = h^e \Delta\gamma \|\langle m \rangle\| \frac{1}{N}. \tag{3.82}$$

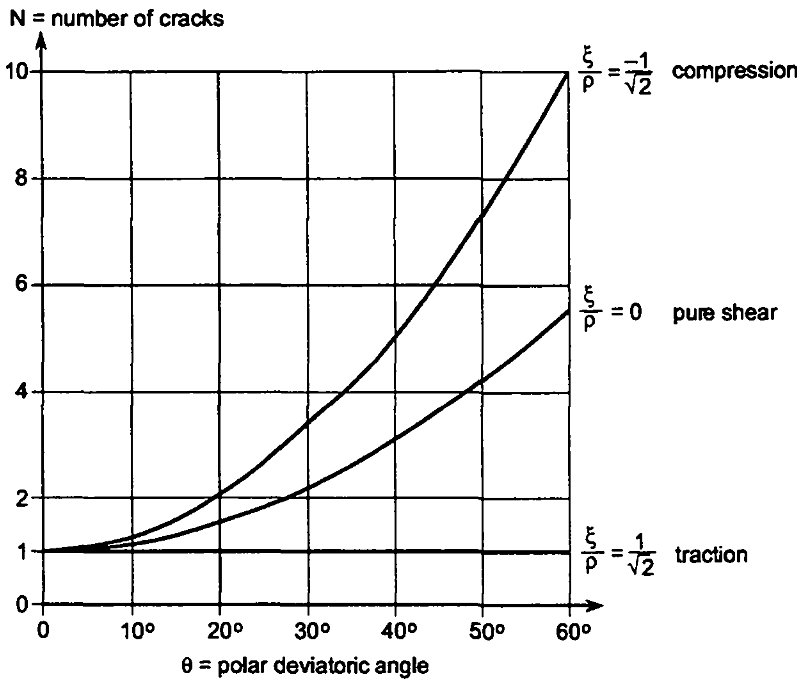

Figure 3.18: Variation of the fictitious number of cracks in terms of the stress invariants

The gradients of the failure criterion with respect to the softening parameters are given in appendix C.

Crack indicators

The formation of weak discontinuities[13] such as Lüder's band in metal as described by Nadai [97] or cracking in concrete can be monitored with the localization condition described by Rice [115], Ortiz et al. [102] and Rudnicki and Rice [122]. This localization condition in elastic-plastic material across a shear band is characterized by the acoustic[14] tensor

$$\boldsymbol{Qep} = \boldsymbol{NDepN}. \tag{3.83}$$

For localization of the deformation to occur along a discontinuity normal to the direction $\boldsymbol{N}$, the acoustic tensor $\boldsymbol{Qep}$ has to have at least one zero eigenvalue which gives the localization condition

$$\det(\boldsymbol{Qep}) = 0. \tag{3.84}$$

This condition is also called the condition of loss of ellipticity because it corresponds to the change of the static equilibrium equation from elliptic to hyperbolic type. For the 2-D case, the normal to a discontinuity is defined as:

$$\boldsymbol{N} = \begin{pmatrix} \cos\alpha \\ \sin\alpha \\ 0 \end{pmatrix}. \tag{3.85}$$

---

[13] Weak discontinuities indicate the formation of jumps in the strain fields, whereas strong discontinuities result in jumps not only in the strain but also in the displacement field as distinguished by Willam et al. [150].

[14] The analysis of discontinuity leads to the same format and relations as the propagation condition for plane acoustic waves in solids, see Hill [52] explaining the origin of the name acoustic tensor.

The determinant of the acoustic matrix is expanded following the work presented by Ortiz et al. [102] but this time extended to non-symmetric elastic-plastic constitutive matrix.

$$\det(\boldsymbol{Q}\,\boldsymbol{ep}) = a_0 \sin^4\alpha + a_1 \sin^3\alpha\cos\alpha + a_2\sin^2\alpha\cos\alpha^2 + a_3\sin\alpha\cos\alpha^3 + a_4\cos^4\alpha, \quad (3.86)$$

where:

$$\begin{aligned}
a_0 &= Dep_{33}Dep_{22} - Dep_{32}Dep_{23}\\
a_1 &= Dep_{13}Dep_{22} + Dep_{31}Dep_{22} - Dep_{12}Dep_{23} - Dep_{32}Dep_{21}\\
a_2 &= Dep_{11}Dep_{22} + Dep_{13}Dep_{32} + Dep_{31}Dep_{23} - Dep_{12}Dep_{21} - Dep_{12}Dep_{33} - Dep_{33}Dep_{21}\\
a_3 &= Dep_{11}Dep_{23} + Dep_{11}Dep_{32} - Dep_{13}Dep_{21} - Dep_{12}Dep_{31}\\
a_4 &= Dep_{11}Dep_{33} - Dep_{13}Dep_{31}.
\end{aligned}$$

The determinant of the acoustic tensor is an explicit expression for α. The critical orientation for which the determinant of the acoustic tensor is minimal is determined numerically. For graphical representation, the value of the determinant of the acoustic tensor is scaled with the determinant of the elastic acoustic tensor expressed as:

$$\det \boldsymbol{Q} = \mu(\lambda + 2\mu). \quad (3.87)$$

It can be checked that the determinant of the elastic acoustic tensor is independent of the orientation of the discontinuity.

Stiffness degradation

The cracking phenomenon is also responsible for stiffness degradation which is reproduced with damage models as presented by Lemaitre and Chaboche [74]. The general format of the stiffness degradation can be described through the dependence of the elastic constitutive matrix $\boldsymbol{D}$ on two sets of scalar internal variables: the elastic and the plastic degradation variables which are denoted by ω_i and δ_i:

$$\boldsymbol{\sigma} = \boldsymbol{C}(\omega_1, ...; \delta_1 ...) : (\boldsymbol{\epsilon} - \boldsymbol{\epsilon}_p). \quad (3.88)$$

This general format includes the model developed by Kachanov, Dougill [31] and Simo and Ju [128]. A simplified model which is appropriate for plastic degradation of concrete strength has been described by Lubliner et al. [81]. It is based on the assumption that elastic degradation occurs only in the softening range and that the stiffness is then proportional to the cohesion. This elastic damage model is considered here. The isotropic modification of the elastic constitutive matrix is

$$\boldsymbol{C} = (1 - \omega)\boldsymbol{C}_0, \quad (3.89)$$

where the indices zero indicate the undamaged values. Using the Lamé constants λ and μ defined in equation 3.22 the damaged elastic constitutive tensor is expressed as:

$$\boldsymbol{C} = \lambda \mathbf{1} \otimes \mathbf{1} + 2\mu \boldsymbol{I}. \quad (3.90)$$

Three damage types are differentiated as suggested by Rizzi [118]:

1. E-damage: is obtained by degradation of Young's modulus so that: $E = (1 - \omega)E_0$. Poisson's ratio is not modified with this approach.

2. Shear damage: is obtained by degradation of the shear modulus which results in:

$$C = \lambda_0 \mathbf{1} \otimes \mathbf{1} + 2\mu_o(1-\omega)\boldsymbol{I}. \tag{3.91}$$

A system of two equations is obtained by matching the terms $\mathbf{1} \otimes \mathbf{1}$ and also the terms $\boldsymbol{I}$ of equations 3.90 and 3.91 which gives:

$$E = \frac{(1-\omega)E_0[(1-\omega)(1-2\nu_0)+3\nu_0]}{(1+\nu_0)[(1-\omega)(1-2\nu_0)+2\nu_0]} \tag{3.92}$$

$$\nu = \frac{\nu_0}{(1-\omega)(1-2\nu_0)+2\nu_0}. \tag{3.93}$$

A complete degradation leads to Young's modulus equals to zero and to Poisson's ratio equals to 0.5 (incompressibility).

3. Bulk damage: is obtained by degradation of the bulk properties which can be expressed as:

$$C = (1-\omega)\lambda_0 \mathbf{1} \otimes \mathbf{1} + 2\mu_o\boldsymbol{I}. \tag{3.94}$$

A similar system of equation to the one obtained previously can be solved which leads to

$$E = \frac{E_0[1+\nu_0-3\nu_0\omega]}{(1+\nu_0)(1-2\nu_0\omega)} \tag{3.95}$$

$$\nu = \frac{\nu_0(1-\omega)}{1-2\omega\nu_0}. \tag{3.96}$$

A complete degradation leads to Young's modulus equals to $E = \frac{E_0}{1+\nu_0}$ and Poisson's ratio equals to zero.

The effects of these types of damage on Young's modulus and Poisson's ratio are illustrated in figure 3.19.

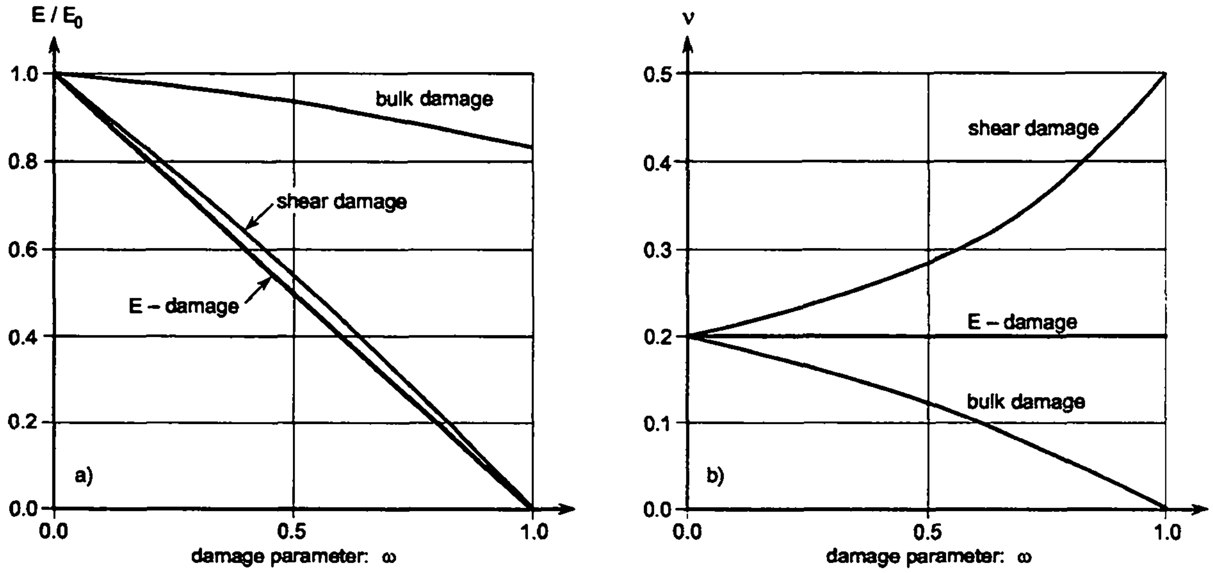

Figure 3.19: Effects of the types of damage on: (a) Young's modulus, (b) Poisson's ratio

The damaged elastic constitutive tensor given in equation 3.90 can be expressed in a matrix form for two dimensional analysis as follows

$$\boldsymbol{D} = \begin{bmatrix} \lambda + 2\mu & \lambda & \lambda & 0 \\ \lambda & \lambda + 2\mu & \lambda & 0 \\ \lambda & \lambda & \lambda + 2\mu & 0 \\ 0 & 0 & 0 & \mu \end{bmatrix}. \tag{3.97}$$

From this matrix expression, it can be clearly observed that under a complete degradation of the shear modulus μ, the damaged elastic constitutive matrix has one zero diagonal term. This zero diagonal term is not obtained for a degradation of the bulk property. However, for a degradation of Young's modulus it can be observed from equation 3.26 that all terms of the damaged elastic constitutive matrix are zero. The consequence of these zero terms of the damaged elastic constitutive matrix will be examined in section 6.2.5 when simulating punching failure.

The elastic-plastic constitutive tensor given in equation 3.44 is modified to take into account the elastic damaged model so that the damage elastic-plastic constitutive matrix is:

$$\boldsymbol{Dep} = \boldsymbol{D}_n - \frac{(\boldsymbol{D}_n \boldsymbol{m})(\boldsymbol{D}_n \boldsymbol{n})^T}{-\frac{\partial f}{\partial \boldsymbol{q}} \boldsymbol{h} + \boldsymbol{n}^T \boldsymbol{D}_n \boldsymbol{m}}, \tag{3.98}$$

where $\boldsymbol{D}_n$ is the damaged elastic constitutive matrix expressed at load step n (load step in the sense of chapter 4). The damaged elastic constitutive matrix at the previous converged load step and not at the previous iteration is considered. This results in a constant damaged elastic constitutive matrix during a load step which has the advantage that no coupling between elastic degradation and plastic softening has to be considered for the computation of the damaged elastic-plastic constitutive matrix.

The denominator of the damaged elastic-plastic constitutive matrix must remain strictly positive thus the plastic softening modulus is delimitated by:

$$-\frac{\partial f}{\partial \boldsymbol{q}} \boldsymbol{h} > \boldsymbol{n}^T \boldsymbol{D}_n \boldsymbol{m}. \tag{3.99}$$

This condition expresses a limit of the softening slope. If this condition is not satisfied the simulation is stopped. It can be noted that this condition is equivalent to the positive definiteness of the denominator of the plastic multiplier given in equation 3.40.

3.5.5 Numerical implementation

The general stress integration algorithm used for the concrete model is expressed in table 3.5. *This algorithm is based on the elastic predictor, plastic corrector strategy. A state variable* "state" is defined to control the state of stress and its treatment. Along the yield surface a fictitious band of a thickness "tol" is defined to control neutral loading. This distinction increases the numerical stability avoiding oscillations due to the computation of the $\boldsymbol{D}$ and $\boldsymbol{Dep}$ matrices. If the stress point is located at the apex, then the damaged elastic constitutive matrix is considered instead of the elastic-plastic constitutive matrix.

In order to evaluate the plastic corrector step, the cutting plane algorithm developed by Ortiz and Simo [104] is used. This algorithm is modified due to the exponential softening. This is due to the fact that along the softening branch, the slope at a converged point is always steeper than the secant one, implying that the stress point is returned inside the elastic

```
1. Compute trial values:
   $\sigma^{trial} = \sigma^i + \boldsymbol{D}\Delta\epsilon$    trial stress,
   $f^{trial} = f(\sigma^{trial}, q_n)$    trial failure criterion.
2. Check the failure criterion:
   $state^i \leq 0$    $f^{trial} \leq 0$              $state^{i+1} = state^i$    elastic or unloading,
                       $f^{trial} > 0$                 $state^{i+1}$              plastic,
   $state^i > 0$       $f^{trial} \leq -tol$           $state^{i+1}$              unloading,
                       $-tol < f^{trial} \leq 0$       $state^{i+1}$              neutral,
                       $f^{trial} > 0$                 $state^{i+1}$              plastic.
3. Compute the stress and internal variable:
   $state^{i+1}$ not plastic:,    $\sigma^{i+1} = \sigma^{trial}$ and $q^{i+1} = q_n$,
   $state^{i+1}$ = plastic    $(\sigma^{i+1}, q^{i+1})$ computed via plastic corrector algorithm table 3.6.
4. Compute the elastic-plastic constitutive matrix:
   $state^{i+1}$ = elastic    $\boldsymbol{Dep} = \boldsymbol{D}_n$                damaged elastic constitutive matrix,
   $state^{i+1}$ = plastic    $\boldsymbol{Dep}$                                   elastic-plastic constitutive matrix: equation 3.98,
   $state^{i+1}$ = neutral    $\boldsymbol{Dep}^{i+1} = \boldsymbol{Dep}^i$        constitutive matrix of previous iteration,
   $state^{i+1}$ = apex       $\boldsymbol{Dep} = \boldsymbol{D}_n$                damaged elastic constitutive matrix.
```

Table 3.5: Stress integration algorithm for the concrete model

domain. Therefore, a relaxation method has to be coupled with the cutting plane algorithm in order to reduce the value of the plastic multiplier. This algorithm is presented in table 3.6.

The algorithm considered here to treat the apex is the following: if the trial stress is in the grey region it is corrected using one iteration of the standard plastic corrector algorithm. Then, if the stress state is still in the grey region, it is directly returned to the apex of the failure criterion which is

$$\sigma_{apex} = \frac{c^{k+1}}{\sqrt{3}\phi C_f}\mathbf{1}. \tag{3.100}$$

This procedure has the advantage that it allows decohesion to take place even though the stress point is located in the vertex.

The following parameters were used: the adopted "Tolerance" = 10^{-5}, the maximum iterations is fixed to 20, and the relaxation factor $r = 0.9$ was observed to give the best results.

```
1.  Initiate the number of stress integration iterations $k = 0$.
2.  Trial values:
        $\boldsymbol{\sigma}^k = \boldsymbol{\sigma}^{trial}$   trial stress,
        $\boldsymbol{q}^k = \boldsymbol{q}_n$   internal variables at previous step (see chap. 4),
        $f^k = f^{trial}$   trial yield value.
3.  WHILE: ($f^k >$ Tolerance) and ($k \leq$ max iteration) : new iteration $k = k + 1$.
4.      Compute the linearized plastic multiplier:
        $\Delta\gamma = \frac{f^k}{-\frac{\partial f}{\partial q^k}||\langle \boldsymbol{m}^k \rangle|| + \boldsymbol{n}^k \boldsymbol{D} \boldsymbol{m}^k}$, increment of plastic multiplier,
        and initiate the number of relaxation iterations $r = 0$.
5.      Update the stress:
        $\boldsymbol{\sigma}^{k+1} = \boldsymbol{\sigma}^k - \Delta\gamma \boldsymbol{D}\, \boldsymbol{m}^k$,
        compute invariants: $\xi^{k+1}, \rho^{k+1}, \theta^{k+1}$.
6.      Update internal variables:
        $\Delta q = \Delta\gamma ||\langle \boldsymbol{m}^k \rangle||$, internal variable (equation 3.79),
        $N^{k+1} = \sqrt{2}(-\frac{\xi^{k+1}}{\rho^{k+1}} + 1/\sqrt{2})(1 - \cos\theta^{k+1})(b-1) + 1$, if $\frac{\xi^{k+1}}{\rho^{k+1}} < 1/\sqrt{2}$ (equation 3.81),
                $= 1$, if $\frac{\xi^{k+1}}{\rho^{k+1}} \geq 1/\sqrt{2}$,
        $w^{k+1} = w^k + h^e \Delta q \frac{1}{N^{k+1}}$, (equation 3.82),
        $c^{k+1} = \exp\left\{-a\frac{w^{k+1}}{w_r}\right\}$, (equation 3.76).
7.      Treat the apex:
        if $\left(\xi^{k+1} \geq \rho^{k+1}\frac{C_g}{B_g} + \frac{c^{k+1}}{\phi C_f}\right)$,
        then: $\boldsymbol{\sigma}^{k+1} = \frac{c^{k+1}}{\sqrt{3\phi C_f}}\mathbf{1}$,   new stress,
              state$^{k+1} =$ apex,   update control state loading.
8.      Compute the yield value: $f^{k+1} = f(\boldsymbol{\sigma}^{k+1}, \boldsymbol{q}^{k+1})$.
9.      Perform relaxation process if: ($f^{k+1} < -$ Tolerance:)
            $r = r + 1$; if ($r >$ max iteration) $\rightarrow$ STOP,
            $\Delta\gamma = R \cdot \Delta\gamma \rightarrow$ GO TO STEP 5.
10. END WHILE;
    return: $\boldsymbol{\sigma}^{i+1} = \boldsymbol{\sigma}^{k+1}$ and $\boldsymbol{q}^{i+1} = \boldsymbol{q}^{k+1}$.
```

Table 3.6: Plastic corrector algorithm for the concrete model

Chapter 4

Structural model

4.1 Introductory remarks

The numerical model reproduces the behavior of reinforced concrete structures by decoupling the actions of steel reinforcement and concrete. This dissociation is valid at the constitutive level as presented in the previous chapter, but it is also applied at the structural level as the steel reinforcement is represented with uniaxial truss elements and the concrete is modelled with continuum elements.

The purpose of this chapter is to formulate the numerical model at the structural level. The point of departure of this description is continuum mechanics. The basic equations of equilibrium are presented. The incremental form and the discretization of these equations are derived. The finite element method is then described and the solution algorithm used to follow the non-linear behavior is established.

4.2 Boundary value problem

4.2.1 Preliminaries

The standard boundary value problem in solid mechanics may be phrased as: find the displacement field $\boldsymbol{u}$ and the stress field $\boldsymbol{\sigma}$ in the volume V so that the applied forces and the boundary conditions are satisfied. In order to solve the boundary value problem, the field equations, and the boundary conditions are defined in the strong form, transformed into the weak form and then discretized.

4.2.2 Field equations and boundary conditions

The field equations are composed of the balance of mass or continuity principle, and the equations of motion also called Euler's equations of motion which are composed of the balance of linear momentum and the balance of angular momentum. It is assumed that the initial and the current configuration are similar, which implies that the continuity equation[1] is always satisfied. The derivation of both equations of motion are detailed in the books by Fung [44], Malvern [82] and Ogden [101].

A boundary value problem must not only satisfy the field equations, but also the boundary conditions. For generality, mixed boundary conditions are considered which are expressed as:

---

[1] The continuity equation or continuity of the mass as described by Ogden [101] is always satisfied for constant configuration.

- prescribed boundary displacements: $\overline{u}$ on S_u,
- prescribed boundary traction: $\overline{t}$ on S_t,

where the following conditions must hold: $S_u \cup S_t = S$ and $S_u \cap S_t = \emptyset$. The field equations and the boundary conditions for the static behavior are expressed as:

$$\begin{cases} \sigma_{ij,j} + b_i = 0 & \text{in } V \\ \sigma_{ij} = \sigma_{ji} & \text{in } V \\ u_i = \overline{u}_i & \text{on } S_u \\ \sigma_{ij} n_j = \overline{t}_i & \text{on } S_t, \end{cases} \tag{4.1}$$

where b_i is the body force per unit volume. The constitutive equations derived in the previous chapter complete these set of equations leading to the strong form of the boundary value problem.

4.2.3 Principle of virtual displacement

The principle of virtual displacement is presented in this section. An infinitesimal virtual displacement δu is applied to each point of a body in an equilibrium configuration. The virtual displacement field δu must be kinematically admissible, that is it must satisfy any prescribed displacement boundary conditions and possess continuous first partial derivatives in the interior of the body. Figure 4.1 illustrates an admissible virtual displacement. For such a motion, no additional virtual displacement δu is permitted where the boundary condition fixes the value of $\overline{u}$. The displacement boundary conditions are therefore automatically satisfied. Given a set of traction forces, body forces, and a virtual displacement field δu the principle of virtual displacement is expressed as:

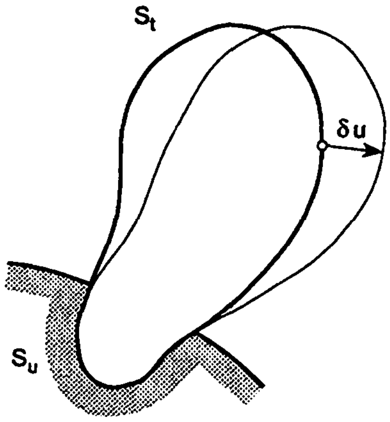

Figure 4.1: Admissible virtual displacement field

$$\delta W_{int} = \int_V \delta\epsilon_{ij}\sigma_{ij} dV = \int_V \delta u_i b_i dV + \int_S \delta u_i t_i dS = \delta W_{ext}. \tag{4.2}$$

Adding to this equation the constitutive relations that were developed in the previous chapter leads to the weak form of the boundary value problem. The following comments can be expressed:

- as shown by Malvern [82] p. 239, also the virtual displacements are infinitesimal, no restrictions are placed on the magnitudes of the real displacements,

- also mentioned by Malvern [82] p. 240, the principle of virtual displacement is independent of constitutive relations and can be applied when mechanical energy is not conserved, for example in plastic deformation.
- Segel [126] demonstrated the uniqueness of the elasticity problem using the principle of virtual displacement,
- a solution of the strong form is a solution of the weak form and vice versa.

The weak form of the boundary value problem being presented, the discretization of this form is undertaken.

4.2.4 Discretization

From now on, the matrix notation is used instead of indicial notation. The principle of virtual displacement expressed in equation 4.2 is restated as:

$$\int_V \delta\epsilon^T \sigma dV = \int_V \delta\boldsymbol{u}^T \boldsymbol{b} dV + \int_S \delta\boldsymbol{u}^T \boldsymbol{t} dS. \tag{4.3}$$

The principle of virtual displacement represents an integral-equation which must be solved numerically by approximated algebraic equations. This is accomplished by means of a spatial discretization of the continuum. The displacement based finite element method—being the most commonly used dicretization method—is considered. The displacement field is given by:

$$\boldsymbol{u} = \boldsymbol{N}\boldsymbol{d}, \tag{4.4}$$

where the vector field $\boldsymbol{u}$ is the displacement field at every points of the element domain, $\boldsymbol{d}$ denotes the nodal displacement vector, and $\boldsymbol{N}$ is a matrix composed of the shape functions, which defines the fundamental variation of the displacement field in the element domain. Further detail of the discretization method are given for example by Hughes [59] and Zienkiewicz and Taylor [153]. From this discretization, the strain tensor is obtained by applying a suitable differential operator $\boldsymbol{\mathcal{L}}$ on the displacement field leading to:

$$\epsilon = \boldsymbol{\mathcal{L}}\boldsymbol{u} = \boldsymbol{\mathcal{L}}\boldsymbol{N}\boldsymbol{d} = \boldsymbol{B}\boldsymbol{d}. \tag{4.5}$$

The $\boldsymbol{B}$ matrix is defined as the strain displacement matrix: $\boldsymbol{B} = \boldsymbol{\mathcal{L}}\boldsymbol{N}$. The virtual displacement field is discretized in the same way as the displacement:

$$\delta\boldsymbol{u} = \boldsymbol{N}\delta\boldsymbol{d}. \tag{4.6}$$

This virtual strain which is valid only in the case of linear kinematics is expressed as:

$$\delta\epsilon = \boldsymbol{\mathcal{L}}\delta\boldsymbol{u} = \boldsymbol{\mathcal{L}}\boldsymbol{N}\delta\boldsymbol{d} = \boldsymbol{B}\delta\boldsymbol{d}. \tag{4.7}$$

The stress tensor is written as a general non-linear function of the displacement: $\sigma = \sigma(\boldsymbol{d})$. Based on this notation and inserting equations 4.4, 4.5, 4.6, and 4.7 into the matrix form of the principle of virtual displacement expressed in equation 4.3 gives:

$$\int_V \delta\boldsymbol{d}^T \boldsymbol{B}^T \sigma(\boldsymbol{d})\, dV = \int_V \delta\boldsymbol{d}^T \boldsymbol{N}^T \boldsymbol{b} dV + \int_S \delta\boldsymbol{d}^T \boldsymbol{N}^T \boldsymbol{t} dS$$

The principle of virtual displacement is independent of the virtual displacement, which is canceled, leading to:

$$\int_V \boldsymbol{B}^T \sigma(\boldsymbol{d}) dV = \int_V \boldsymbol{N}^T \boldsymbol{b} dV + \int_S \boldsymbol{N}^T \boldsymbol{t} dS. \tag{4.8}$$

The left term corresponds to the internal force vector which is a non-linear function of the displacement. The right term is the external force vector. Therefore, this equation can be restated as[2]:

$$\boldsymbol{Fint} = \boldsymbol{Fext} \text{ with } \boldsymbol{Fint} = \mathcal{N}(\boldsymbol{d}). \tag{4.9}$$

This equation is a non-linear equilibrium equation in which $\mathcal{N}$ is a general non-linear operator.

4.3 Solution of the boundary value problem

4.3.1 Preliminaries

The solution of a boundary value problem is performed in considering the discretized form of the principle of virtual displacement expressed in equation 4.9. This equilibrium equation is a highly non-linear expression and can be solved only for particular cases. Therefore, an incremental procedure is developed in order to follow the response of the structure along the equilibrium path.

4.3.2 Increment

The solution of the boundary value problem is decomposed into incremental steps which has the following advantages as enumerated by Felippa [42]: (1) helping convergence, (2) avoiding extraneous roots, (3) giving an overview of the structural behavior, (4) limiting the surprise of unforeseen particular points, (5) allowing path dependent problem.

The non-linear equilibrium equation 4.9 is rewritten for convenience:

$$\mathcal{N}(\boldsymbol{d}) = \boldsymbol{Fext}. \tag{4.10}$$

To solve the non-linear algebraic problem, a reduction to the linear algebraic problem by way of incremental-iterative strategy is performed. The first order of Taylor series at time t_n reads:

$$\mathcal{N}(\boldsymbol{d}_n) + \frac{\partial \mathcal{N}(\boldsymbol{d}_n)}{\partial \boldsymbol{d}} \Delta \boldsymbol{d} = \boldsymbol{Fext}. \tag{4.11}$$

The first term corresponds to the internal force vector at time t_n.

$$\mathcal{N}(\boldsymbol{d}_n) = \boldsymbol{Fint}_n = \int_V \boldsymbol{B}^T \sigma(\boldsymbol{d}_n) dV. \tag{4.12}$$

The partial derivative term of the first order Taylor series is:

$$\frac{\partial \mathcal{N}(\boldsymbol{d}_n)}{\partial \boldsymbol{d}} = \frac{\partial}{\partial \boldsymbol{d}} \int_V \boldsymbol{B}^T \sigma(\boldsymbol{d}_n)\, dV = \int_V \boldsymbol{B}^T \frac{\partial \sigma}{\partial \epsilon} \boldsymbol{B}\, dV = \boldsymbol{K}_T, \tag{4.13}$$

which is the definition of the tangent stiffness matrix. For the constitutive model developed in chapter 3, the term $\partial\sigma/\partial\epsilon = \boldsymbol{Dep}$ is given in table 3.2 for the steel model and in table 3.5 for the concrete model. Using the stiffness matrix definition as well as the definition of the internal force vector, the first order Taylor series is rewritten as:

$$\boldsymbol{Fint}_n + \boldsymbol{K}_T \Delta \boldsymbol{d} = \boldsymbol{Fext}, \tag{4.14}$$

which can be expressed as:

$$\boldsymbol{K}_T \Delta \boldsymbol{d} = \boldsymbol{Fext} - \boldsymbol{Fint}_n = \Delta \boldsymbol{F}. \tag{4.15}$$

This expression is the incremental equilibrium equation.

---

[2] This form was suggested by Hughes [60] for the formulation and solution of non-linear problems.

4.3.3 Assembly

The entire structure is replaced by a mesh of finite elements. Each element is considered individually before being assembled with the assembly operator $\mathcal{A}$. Each element is characterized by its volume Ω and its surface Γ. Applying these concepts to the incremental equilibrium equation 4.15 leads to:

$$\mathcal{A}\{\boldsymbol{K}_T^e\}\,\Delta\boldsymbol{d} = \mathcal{A}\{\Delta\boldsymbol{F}^e\} = \mathcal{A}\{\boldsymbol{Fext}^e - \boldsymbol{Fint}^e\} \tag{4.16}$$

The computation of each of these terms is detailed in the following. The tangent stiffness matrix is formed by assembling each element contribution using the assembly operator $\mathcal{A}$. The tangent stiffness matrix at the element level $\boldsymbol{K}_T^e$ is:

$$\boldsymbol{K}_T^e = \int_\Omega \boldsymbol{B}^T \boldsymbol{Dep}\boldsymbol{B} d\Omega, \tag{4.17}$$

where $\boldsymbol{Dep}$ is the elastic-plastic constitutive matrix obtained from table 3.2 for the steel model and from table 3.5 for the concrete model.

The incremental force vector is formed by assembling each forces contribution using the assembly operator $\mathcal{A}$. The incremental external force vector is composed of the body force, the nodal forces denoted by $\boldsymbol{F}_{nodal}$, and forces due to imposed displacements $\bar{\boldsymbol{d}}$ so that:

$$\boldsymbol{Fext}^e = \boldsymbol{F}_{nodal} + \int_\Omega \boldsymbol{N}^T \boldsymbol{b} d\Omega - \sum \boldsymbol{K}_T^e \bar{\boldsymbol{d}}. \tag{4.18}$$

The internal force is given by:

$$\boldsymbol{Fint}^e = \int_\Omega \boldsymbol{B}^T \sigma d\Omega. \tag{4.19}$$

The incremental equilibrium equations given in equation 4.16 is completely determined. The remaining ingredient required to follow the equilibrium path is the algorithm.

4.3.4 The modified Newton-Raphson algorithm

Preliminaries

The statement of the problem is: "assuming that an equilibrium configuration has been reached at the time t_n find a new equilibrium configuration at time t_{n+1}". This new equilibrium configuration must satisfy the incremental equilibrium equation 4.16. The solution of this problem is performed with the modified Newton-Raphson algorithm[3]. The modified Newton-Raphson algorithm is decomposed into a predictor step, followed by a corrector step where iterations are performed until the criterion of convergence is reached.

Predictor step

The predictor step is of two types. The first type of predictor implements the tangent stiffness matrix at the previous converged step $\boldsymbol{K}_T$. Another predictor step is implemented in applying $\boldsymbol{Kel}$ (elastic stiffness matrix). This matrix is accurate for elements that remain elastic or unload. Consequently, elastic unloading is facilitated which leads to an interesting step especially when localization of the failure is desired as unloading is encouraged in elements around the localization surface. The drawback of this predictor step is its poor prediction when the plastic process is significant.

---

[3] The modified Newton-Raphson algorithm applied to non-linear finite element procedures is described by Bathe [6]. This algorithm is powerful because the rate of convergence is quadratic. The drawback of this algorithm is the lack of convergence for initial guess far from the solution and when the higher-order derivative terms are important.

Corrector step

Following the predictor step, the modified Newton-Raphson method generates a sequence of iterations known as the corrector step up to convergence. Different strategies are considered based on the applied stiffness matrix as enumerated below:

1. The strategy is obtained when applying the elastic stiffness matrix $\boldsymbol{Kel}$ in the incremental equilibrium equation. This method is known as the initial load method or pseudo-force method. This strategy is the most stable one, but it is characterized by the lowest rate of convergence.
2. An other strategy is obtained when applying for all iterations the same tangent stiffness matrix $\boldsymbol{K_T}$ obtained at the previous converged load step.
3. The conventional strategy is obtained when updating at every "j" iterations the tangent stiffness matrix. If $j = 1$ the full Newton-Raphson algorithm is obtained.
4. An interesting strategy for localization analysis is obtained when requiring that the "l" first iterations are performed with $\boldsymbol{Kel}$.
5. Also oriented toward localization analysis, the strategy requiring "l" converging iterations with $\boldsymbol{Kel}$ is implemented.
6. An improvement of the previous strategy is obtained when requiring "f(l)" converging iterations with $\boldsymbol{Kel}$ at the beginning of the load step and as soon as divergence is detected. The number of required converging iterations increases with the current iteration number in order to avoid cycle so that: $f(l) = l +$ current iteration/10.

The performance of these strategies will be investigated in section 5.3.3. However, it can be expected that a strategy combining the elastic stiffness matrix and the tangent stiffness matrix should be the most efficient one to capture localized failure. This is due to the fact these two matrices reproduce different phenomenons which are observed during failure localization: (1) the elastic stiffness matrix facilitates unloading, (2) the tangent stiffness matrix capture the failure mechanism. The numerical implementation of these strategies is described in appendix E and summarized in table E.2.

Convergence and divergence limiters

The convergence of the modified Newton-Raphson algorithm is monitored with two values: the norm of the out-of-balance force $||\Delta \boldsymbol{F}||$ and the residual energy $\Delta E = \Delta \boldsymbol{F}^T \Delta \boldsymbol{d}$. These threshold criteria are complementary. The dependance of these values on physical units is undesirable, and it is therefore more convenient to work out with ratios. The convergence condition on the norm of the out-of-balance force (RHS) reads:

$$\frac{||\Delta \boldsymbol{F}^{i+1}||}{||\Delta \boldsymbol{F}^{1}||} < \text{tol(RHS)},$$

where tol(RHS) varies from 10^{-2} to 10^{-5}. The convergence condition on the residual energy reads:

$$\frac{\Delta E^{i+1}}{\Delta E^{1}} < \text{tol(Energy)},$$

where tol(Energy) varies from 10^{-1} to 10^{-4}. It was often observed that the convergence condition on the residual energy is more severe than the one on the norm of the out-of-balance force.

This justifies the following relation between the two tolerances: tol(Energy)=10·tol(RHS) for simplicity.

In order to avoid numerical problems at the first iteration, the convergence is satisfied if the norm of the out-of-balance force or the residual energy is sufficiently small, that is:

$$\|\Delta \boldsymbol{F}^1\| < \text{tol} \ \text{ or } \ \Delta E^1 < \text{tol},$$

where the value tol=10^{-8}. It should be noted that both convergence criteria are monitoring a mean value of the out-of-balance force and the energy. These convergence criteria can fail to detect a local out-of-equilibrium force or energy. Another more restrictive approach is to monitor the out-of-equilibrium force and residual energy locally, which is not considered here.

The modified Newton-Raphson algorithm is not guaranteed to converge. Therefore divergence detections which will cause the iteration to be interrupted are implemented. The divergence is diagnosed if either of the following inequalities occur:

$$\frac{\|\Delta \boldsymbol{F}^{i+1}\|}{\|\Delta \boldsymbol{F}^1\|} > \text{tol(divergence)} \ \text{ or } \ \frac{\Delta E^{i+1}}{\Delta E^1} > \text{tol(divergence)}\ ,$$

where tol(divergence) is 1000 for example as suggested by Felippa [42].

Description of the algorithm

The modified Newton-Raphson algorithm proceeds as shown in table 4.1. The full Newton-Raphson algorithm is illustrated in figure 4.2 for one degree of freedom and for one load step composed of three iterations.

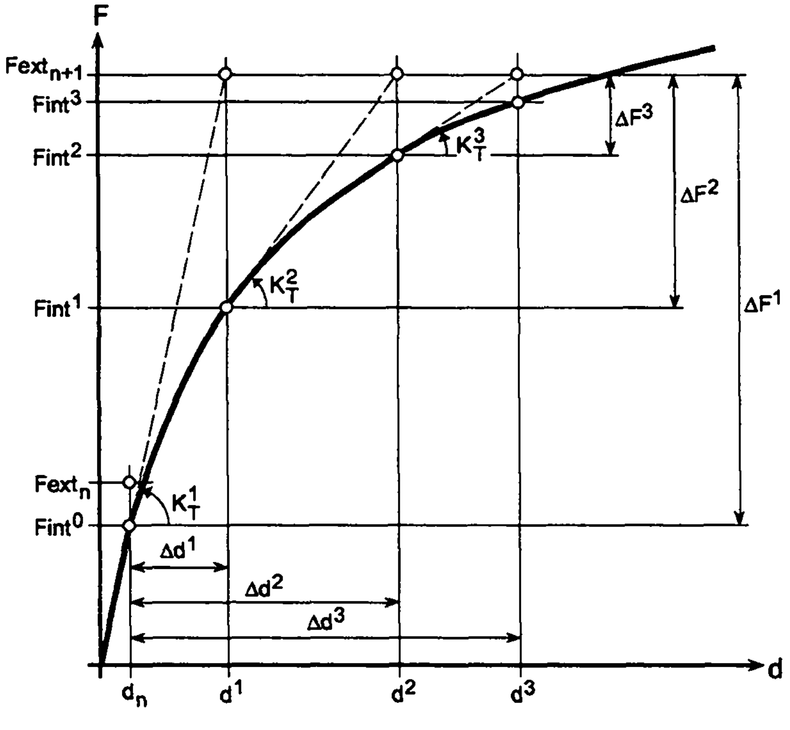

Figure 4.2: Illustration of the Newton-Raphson algorithm for one degree of freedom

```
1. Load step loop: $n = 1$; $n \leq$ Number of load steps; $n = n + 1$.
2. Compute external force:
   $\boldsymbol{Fext}_{n+1} = \boldsymbol{Fext}_n + \Delta \boldsymbol{F}_{nodal} + \boldsymbol{\mathcal{A}}\left\{\int \boldsymbol{N}^T \Delta \boldsymbol{b} d\Omega\right\}$.
3. Iteration loop: $i = 1$; $i \leq$ Max(Iteration)s; $i = i + 1$.
4. Form the left hand side:
   $\boldsymbol{K}_T = \boldsymbol{\mathcal{A}}\left\{\int \boldsymbol{B}^T \boldsymbol{Dep}^i \boldsymbol{B} d\Omega\right\}$.
5. Form the right hand side:
   $\Delta \boldsymbol{F} = \boldsymbol{Fext}_{n+1} - \boldsymbol{Fint}^i$,
   if $(i = 1)$ $\Delta \boldsymbol{F} - = \boldsymbol{\mathcal{A}}\{\sum \boldsymbol{K}_T^e \Delta \overline{\boldsymbol{d}}\}$.
6. Solve the system for the displacement:
   $\boldsymbol{K}_T \Delta \boldsymbol{d} = \Delta \boldsymbol{F}$,
   $\Delta \boldsymbol{d}^{i+1} = \Delta \boldsymbol{d}^i + \Delta \boldsymbol{d}$; $\boldsymbol{d}^{i+1} = \boldsymbol{d}^i + \Delta \boldsymbol{d}$.
7. Check the convergence of the iteration:
   $\|\Delta \boldsymbol{F}^{i+1}\| = \sqrt{\Delta \boldsymbol{F}^{i+1} (\Delta \boldsymbol{F}^{i+1})^T}$ with $\Delta \boldsymbol{F}^{i+1} = \boldsymbol{Fext}_{n+1} - \boldsymbol{Fint}^{i+1}$,
   $\Delta E^{i+1} = (\Delta \boldsymbol{F}^{i+1})^T \Delta \boldsymbol{d}^{i+1}$,
   $\boldsymbol{Fint}^{i+1} = \boldsymbol{\mathcal{A}}\{\int \boldsymbol{B}^T \boldsymbol{\sigma}^{i+1} d\Omega\}$,
   $\boldsymbol{\sigma}^{i+1}$; $\boldsymbol{q}^{i+1}$ computed via stress integration algorithm (table 3.2 or 3.5),
   $\boldsymbol{\epsilon}^{i+1} = \boldsymbol{\epsilon}_n + \Delta \boldsymbol{\epsilon}^{i+1}$; $\Delta \boldsymbol{\epsilon}^{i+1} = \boldsymbol{B} \Delta \boldsymbol{d}^{i+1}$,
   if $\left(\|\Delta \boldsymbol{F}^1\| < \text{tol or } \Delta E^1 < \text{tol}\right) \leadsto$ converged
   if $\left(\frac{\|\Delta \boldsymbol{F}^{i+1}\|}{\|\Delta \boldsymbol{F}^1\|} \text{ or } \frac{\Delta E^{i+1}}{\Delta E^1} > \text{tol(divergence)}\right) \leadsto$ diverging iteration $\Rightarrow$ STOP
   if $\left(\frac{\|\Delta \boldsymbol{F}^{i+1}\|}{\|\Delta \boldsymbol{F}^1\|} < \text{tol(RHS) and } \frac{\Delta E^{i+1}}{\Delta E^1} < \text{tol(Energy)}\right) \leadsto$ converged
8. Terminate iteration:
   $\boldsymbol{d}^i = \boldsymbol{d}^{i+1}$; $\boldsymbol{d}^{i+1} = \emptyset$,
   $\boldsymbol{Fint}^i = \boldsymbol{Fint}^{i+1}$; $\boldsymbol{Fint}^{i+1} = \emptyset$,
   if (algorithm request new tangent stiffness)
     $\boldsymbol{K}_T = \emptyset$,
     $\boldsymbol{Dep}^{i+1}$ computed at material level (table 3.2 or 3.5),
   else $\boldsymbol{Dep}^{i+1} = \boldsymbol{D}_n$,
   if (not converged) $\boldsymbol{\epsilon}^{i+1} = \boldsymbol{\sigma}^{i+1} = \boldsymbol{q}^{i+1} = \emptyset$,
  if (Load step has converged) $\Rightarrow$ BREAK
9. Terminate the current load step:
   if $(| d_{n+1} - d_n | < \text{tol})$ $\boldsymbol{D}_{n+1}$ and $\boldsymbol{Dep}^{i+1}$ reevaluated due to concrete damage,
   $\boldsymbol{d}_n = \boldsymbol{d}^i$; $\boldsymbol{d}^i = \emptyset$,
   $\boldsymbol{Fext}_n = \boldsymbol{Fext}_{n+1}$; $\boldsymbol{Fext}_{n+1} = \emptyset$,
   $\boldsymbol{\epsilon}_n = \boldsymbol{\epsilon}^{i+1}$; $\boldsymbol{\sigma}_n = \boldsymbol{\sigma}^{i+1}$; $\boldsymbol{q}_n = \boldsymbol{q}^{i+1}$.
```

Table 4.1: The modified Newton-Raphson algorithm

4.3.5 The solution of the linear system of equations

The equation $\boldsymbol{K}_T \Delta \boldsymbol{d} = \Delta \boldsymbol{F}$ is a system of n linear equations with n unknowns where n is the number of degrees of freedom of the structural system. This linear set of equations is characterized by:

- a large number of equations requiring the use of an efficient solver such as a variant of Gauss elimination known as the Crout decomposition[4],
- a tangent stiffness matrix which is a band matrix where skyline storage is necessary in order to minimize the memory space,
- a tangent stiffness matrix which can be non-symmetric requiring factorization of non-symmetric matrices.

The solution of a non-symmetric system of equations allow to use the modified Newton-Raphson algorithm.

4.4 The finite elements

4.4.1 Preliminaries

The last step of the development of the structural model to analyze reinforced concrete structures is the definition of the finite elements. The concrete is modelled with continuum elements, and as axially symmetric structures are considered, only one continuum element is described, which is the quad-axi element. The steel reinforcement is represented with truss elements. These two types of elements are described in the following.

4.4.2 The bilinear axisymmetric quadrilateral element (quad-axi)

Isoparametric description

The isoparametric description interpolates both the element geometry and the displacement with the same shape functions. The isoparametric definition of a three dimensional geometry is:

$$x = x_i \boldsymbol{N}_i^e \; ; \quad y = y_i \boldsymbol{N}_i^e \; ; \quad z = z_i \boldsymbol{N}_i^e .$$

The isoparametric definition of the displacement is:

$$d = d_i \boldsymbol{N}_i^e . \tag{4.20}$$

---

[4] Crout decomposition is described by Hughes [59] p.633-643. The solution of a system of linear equation written in the form $\mathbf{Ax} = \mathbf{b}$ is obtained in four steps as described by Golub and Van Loan [46] p.134 using an $\mathbf{LDM}^T$ decomposition where $\mathbf{D}$ is a diagonal matrix and $\mathbf{L}$ and $\mathbf{M}$ are unit lower triangular matrices.

1. The factorization: $\mathbf{A} = \mathbf{LDM}^T$
2. The forward reduction: $\mathbf{Lz} = \mathbf{b}$
3. The diagonal scaling: $\mathbf{Dy} = \mathbf{z}$
4. The back substitution: $\mathbf{M}^T\mathbf{x} = \mathbf{y}$

The implementation of that solution process with the object-oriented programming concept is described by Dubois-Pèlerin [33].

These definitions can be combined in a matrix form as:

$$\begin{Bmatrix} 1 \\ x \\ \vdots \\ d_x \\ \vdots \end{Bmatrix} = \begin{bmatrix} 1 & 1 & \cdots & 1 \\ x_1 & x_2 & \cdots & x_n \\ \vdots & \vdots & \cdots & \vdots \\ d_{x_1} & d_{x_2} & \cdots & d_{x_n} \\ \vdots & \vdots & \cdots & \vdots \end{bmatrix} \begin{Bmatrix} N_1^e \\ N_2^e \\ \vdots \\ N_n^e \end{Bmatrix}, \tag{4.21}$$

where n is the number of nodes.

The partial derivatives of the shape functions are required for the strain computations. *Since the shape functions are not expressed in terms of x, y, and z but in terms of the natural* coordinates (ξ, η, μ), their derivatives are computed with the chain rule of differentiation so that:

$$\begin{aligned} \frac{\partial N_i^e}{\partial x} &= \frac{\partial N_i^e}{\partial \xi}\frac{\partial \xi}{\partial x} + \frac{\partial N_i^e}{\partial \eta}\frac{\partial \eta}{\partial x} + \frac{\partial N_i^e}{\partial \mu}\frac{\partial \mu}{\partial x} \\ \frac{\partial N_i^e}{\partial y} &= \frac{\partial N_i^e}{\partial \xi}\frac{\partial \xi}{\partial y} + \frac{\partial N_i^e}{\partial \eta}\frac{\partial \eta}{\partial y} + \frac{\partial N_i^e}{\partial \mu}\frac{\partial \mu}{\partial y} \\ \frac{\partial N_i^e}{\partial z} &= \frac{\partial N_i^e}{\partial \xi}\frac{\partial \xi}{\partial z} + \frac{\partial N_i^e}{\partial \eta}\frac{\partial \eta}{\partial z} + \frac{\partial N_i^e}{\partial \mu}\frac{\partial \mu}{\partial z}. \end{aligned} \tag{4.22}$$

The Jacobian matrix of that coordinate transformation is defined as:

$$J = \frac{\partial(x, y, z)}{\partial(\xi, \eta, \mu)}. \tag{4.23}$$

Therefore, the partial derivatives of the shape functions expressed in equation 4.22 can be restated as:

$$\begin{Bmatrix} \frac{\partial N_i^e}{\partial x} \\ \frac{\partial N_i^e}{\partial y} \\ \frac{\partial N_i^e}{\partial z} \end{Bmatrix} = J^{-1} \begin{Bmatrix} \frac{\partial N_i^e}{\partial \xi} \\ \frac{\partial N_i^e}{\partial \eta} \\ \frac{\partial N_i^e}{\partial \mu} \end{Bmatrix}. \tag{4.24}$$

Numerical integration

The finite element computation requires the computation of integrals as seen in the previous section. The evaluation of these integrals over isoparametric elements is based on numerical integration. This numerical integration for one dimension is expressed as:

$$\int_{-1}^{1} f(x) \approx \sum_{1}^{n} p_i f(x_i), \tag{4.25}$$

where n is the number of integration points, x_i is the coordinate and p_i is the weight of the ith integration point. Many numerical integration methods are available, but the Gaussian quadrature rule is preferred which is given as follows:

$$\text{For } n = 2, \ \ \pm x_i = \frac{1}{\sqrt{3}}, \ \ p_i = 1.$$

The corresponding integration points are called Gauss points.

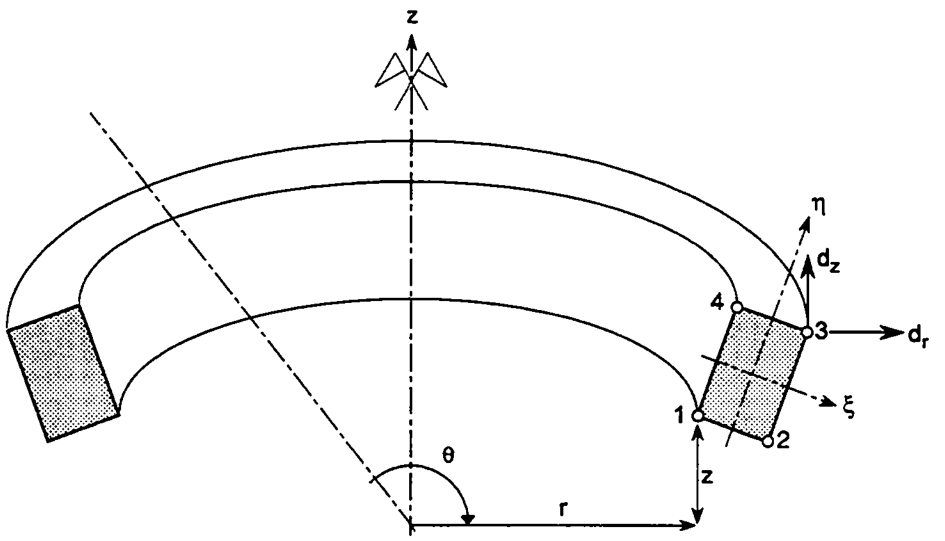

Figure 4.3: Axisymmetric quad element (quad-axi)

The quad-axi formulation

The quad-axi element used to model concrete is represented in figure 4.3. It is composed of 4 nodes, each of them are endowed with two displacements: d_r, d_z.
The linear isoparametric shape functions are:

$$\begin{aligned} N_1^e &= \tfrac{1}{4}(1-\xi)(1-\eta) \\ N_2^e &= \tfrac{1}{4}(1+\xi)(1-\eta) \\ N_3^e &= \tfrac{1}{4}(1+\xi)(1+\eta) \\ N_4^e &= \tfrac{1}{4}(1-\xi)(1+\eta). \end{aligned} \tag{4.26}$$

The Jacobian matrix takes the form:

$$\boldsymbol{J} = \begin{bmatrix} x_i \frac{\partial N_i^e}{\partial \xi} & y_i \frac{\partial N_i^e}{\partial \xi} \\ x_i \frac{\partial N_i^e}{\partial \eta} & y_i \frac{\partial N_i^e}{\partial \eta} \end{bmatrix}. \tag{4.27}$$

Defining the strain vector as $\boldsymbol{\epsilon}^T = (\epsilon_{rr}; \epsilon_{zz}; \epsilon_{\theta\theta}; 2\epsilon_{rz})$, the strain-displacement matrix takes the form:

$$\boldsymbol{B} = \boldsymbol{\mathcal{L}}\boldsymbol{N} = \begin{bmatrix} \frac{\partial}{\partial r} & 0 \\ 0 & \frac{\partial}{\partial z} \\ \frac{1}{r} & 0 \\ \frac{\partial}{\partial z} & \frac{\partial}{\partial r} \end{bmatrix} \begin{bmatrix} \boldsymbol{N} & 0 \\ 0 & \boldsymbol{N} \end{bmatrix} = \begin{bmatrix} \boldsymbol{N}_{,r} & 0 \\ 0 & \boldsymbol{N}_{,z} \\ \frac{\boldsymbol{N}}{r} & 0 \\ \boldsymbol{N}_{,z} & \boldsymbol{N}_{,r} \end{bmatrix}, \tag{4.28}$$

where $\boldsymbol{N} = [N_1^e ... N_4^e]$. The vectors $\boldsymbol{N}_{,r}$ and $\boldsymbol{N}_{,z}$ are the partial derivative of the shape function with respect to r and z respectively.

The dimension of the stiffness matrix is 8 (4 nodes times 2 degrees of freedom at each node). The quad-axi has 1 rigid body mode (1 translation). Consequently, the stiffness matrix of the quad-axi element has a rank of 7. The ***Dep*** matrix has a rank of 3 implying that each integration point adds at most 3 independent deformation modes to the stiffness matrix. Due to isotropy conditions (no preferred direction), all faces must have the same number of integration points. The corresponding lower number of integration points is 2 in order to avoid rank deficiency. The tangent stiffness matrix is determined based on equation 4.17 so that:

$$\boldsymbol{K}_T^e = \sum_{i=1}^{2}\sum_{j=1}^{2} p_i p_j B_{ij}^T \boldsymbol{Dep} B_{ij} J_{ij} r_{ij}, \tag{4.29}$$

where the $\boldsymbol{Dep}$ matrix is obtained as described in table 3.5.
The volume of the finite element is computed using Gauss quadrature so that:

$$\Omega = 2\pi \sum_{i=1}^{2} \sum_{j=1}^{2} p_i p_j J_{ij} r_{ij}, \tag{4.30}$$

where the radius is:

$$r(\xi_k, \eta_l) = \sum_{i=1}^{4} r_i N_i(\xi_k, \eta_l). \tag{4.31}$$

The 2π term in the volume computation is suppressed in the implementation as it appears on both sides of the equilibrium equation. However, concentrated forces acting along the z axis do not involve volume computation. Therefore, the 2π term should divide such forces.

The size of the quad-axi included in the softening formulation is computed as:

$$h^e = \sqrt{\sum_{i=1}^{2} \sum_{j=1}^{2} p_i p_j J_{ij}}, \tag{4.32}$$

which is the square root of the cross section area. In this expression, the radial direction is not included. This implies that a constant crack spacing along the perimeter is simulated. This choice is justified because the constant crack spacing in the tangential direction is observed experimentally in punching failure as shown in figure 2.12.

The external force vector acting on the quad-axi element includes nodal, body, and boundary forces. The computation of the internal force vector is obtained by adding the product $\boldsymbol{B}^T \boldsymbol{\sigma}$, of each Gauss point contribution.

$$\boldsymbol{Fint}^e = \sum_{i=1}^{2} \sum_{j=1}^{2} p_i p_j B_{ij}^T \sigma_{ij} J_{ij} r_{ij}. \tag{4.33}$$

As shown by Taylor et al. [137] the four-node element exhibits parasitic shear when the element is subjected to pure bending. This is due to its inability to represent stress gradients associated with bending.

The treatment of incompressibility

Mesh locking occurs as a result of near incompressibility as presented by Nagtegaal et al. [98]. For the concrete model developed in section 3.5, the flow rule often allows for little volume change, so if plastic strains become large, the response becomes nearly incompressible. This difficulty can be overcome by the treatment of incompressibility as developed by Hughes [58] and presented here. The $\boldsymbol{B}$ matrix expressed in equation 4.28 is rewritten in the form:

$$\boldsymbol{B} = \begin{bmatrix} B_1 & 0 \\ 0 & B_2 \\ B_0 & 0 \\ B_2 & B_1 \end{bmatrix}. \tag{4.34}$$

The $\boldsymbol{B}$ matrix is decomposed into a deviatoric and a dilatational part so that:

$$\boldsymbol{B} = \boldsymbol{B}^{dev} + \boldsymbol{B}^{dil}. \tag{4.35}$$

The $\boldsymbol{B}^{dil}$ matrix is replaced by and "improved" dilatational contribution the $\overline{\boldsymbol{B}}^{dil}$ matrix. The resulting $\overline{\boldsymbol{B}}$ matrix is expressed as:

$$\overline{\boldsymbol{B}} = \begin{bmatrix} B_{12} & B_6 \\ B_{10} & B_7 \\ B_{11} & B_6 \\ B_2 & B_1 \end{bmatrix}, \tag{4.36}$$

where:

$$\begin{aligned} B_0 &= \frac{N}{r} \\ B_6 &= \frac{\overline{B}_2 - B_2}{3} \\ B_7 &= B_2 + B_6 \\ B_{10} &= B_4 + \frac{\overline{B}_0 - B_0}{3} \\ B_{11} &= B_0 + B_{10} \\ B_{12} &= B_1 + B_{10}. \end{aligned} \tag{4.37}$$

The definitions of the $\overline{B}_i$'s are a generalization of the mean-dilatation formulation of Nagtegaal et al. [98] so that

$$\overline{B}_i = \frac{\int_{\Omega^e} B_i d\Omega}{\int_{\Omega^e} d\Omega}. \tag{4.38}$$

Now that the finite element used for concrete is described, the one modeling steel reinforcement are considered.

4.4.3 Truss elements

Rotation matrix

Finite elements are expressed in the global coordinate system. But, the development of truss elements is performed in the local coordinate system where ξ is the natural coordinate along the axis of the truss. Consequently, the truss element must be rotated from the local to the global coordinate system. The stiffness matrix in the global coordinate is obtained so that $\boldsymbol{K}^e_{global} = \boldsymbol{T}^T \boldsymbol{K}^e_{local} \boldsymbol{T}$. The internal force vector computed in the local coordinate system as $\boldsymbol{Fint}_{local} = \sigma A$, must also be rotated into the global axis so that $\boldsymbol{Fint}_{global} = \boldsymbol{T}\boldsymbol{Fint}_{local}$.

The axisymmetric truss element (truss-axi)

The axisymmetric truss element presented in figure 4.4 is characterized by a constant deformation and stress along the length of the element. Each of these two node is characterized by two displacement components: d_r, d_z. The truss-axi resists only along its longitudinal dimension, through the axial displacement u. The axial displacement between node 1 and 2 is interpolated linearly as:

$$u = \begin{bmatrix} d_1 & d_2 \end{bmatrix} \begin{Bmatrix} N_1^e \\ N_2^e \end{Bmatrix}. \tag{4.39}$$

Using the natural coordinate $\xi = 2x/L$, the shape functions are expressed as:

$$N_1^e = \frac{1}{2}(1 - \xi) \; ; \; N_2^e = \frac{1}{2}(1 + \xi).$$

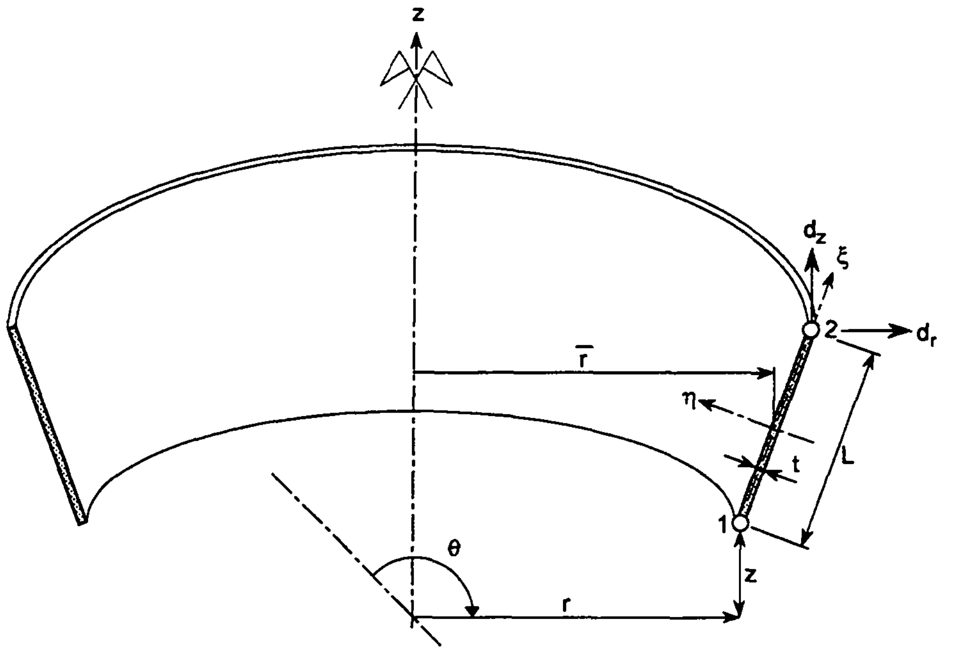

Figure 4.4: Axisymmetric truss element (truss-axi)

The axial strain is defined as $\epsilon = du/dx$, which leads to the expression of the $\boldsymbol{B}$ matrix as:

$$\boldsymbol{B} = \frac{1}{L}[-1 \quad 1]. \tag{4.40}$$

The Jacobian, relating an element length in the global coordinate system to an element length in the natural coordinate system is $J = L/2$. The tangent stiffness matrix is computed using equation 4.17 with one integration point which gives:

$$\boldsymbol{K}_T^e = \frac{Dep\, A}{L}\begin{bmatrix} 1 & -1 \\ -1 & 1 \end{bmatrix}, \tag{4.41}$$

where the Dep term is obtained from table 3.2. The rotation matrix is expressed as:

$$\boldsymbol{T} = \begin{bmatrix} \cos\alpha & \sin\alpha & 0 & 0 \\ 0 & 0 & -\sin\alpha & \cos\alpha \end{bmatrix}, \tag{4.42}$$

where α is the angle between the local and the global coordinate axis.

The volume computation involves the computation of the mean radius $\bar{r} = 0.5(r_1 + r_2)$. This leads to the following expression of the volume of the element: $V = L\ t\ \bar{r}$ where t is the thickness of the truss (the 2π term is dropped out as for the quad-axi computation).

The ring element

The ring element is a one node element characterized by the axisymmetric geometry depicted in figure 4.5. The displacement is not interpolated as it is exactly computed at the node. The tangential strain is $\epsilon_\theta = d_r/r$, which leads to the following expression of the $\boldsymbol{B}$ matrix:

$$\boldsymbol{B} = \frac{1}{r}[-1 \quad 0]. \tag{4.43}$$

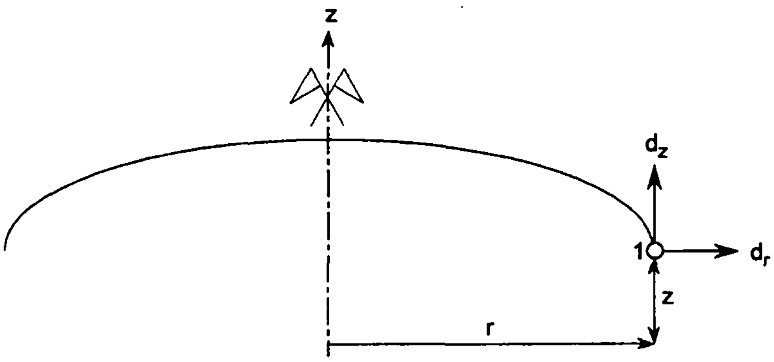

Figure 4.5: Ring element

The volume of the element is: $dV = 2\pi\ A\ r$. The 2π term drops as for the quad-axi computation. The tangent stiffness matrix is computed using equation 4.17 leading to:

$$\boldsymbol{K}^e = \frac{Dep\,A}{r}, \tag{4.44}$$

where the Dep term is obtained from table 3.2. The ring element is similar in the local and global coordinate system.

Chapter 5

Tests of the numerical model

5.1 Introductory remarks

The purpose of this chapter is to examine the capabilities of the numerical model developed in chapters 3 and 4. These capabilities are first simulated with the simulation of the shear failure in footings so to investigate a known shear failure phenomenon which is comparable to punching failure. The capabilities of the reinforced concrete model are examined by simulating standard tests in plain and reinforced concrete. The plain concrete model is tested with the simulations of the uniaxial tensile test, and the confined compressive test. The reinforced concrete model is investigated with the simulations of the uniaxial tensile test to examine the axial contribution of the reinforcement and with the confined compressive test to check the confinement effect created by spiral reinforcement. The consequences for the simulation of punching failure are discussed at the end of this chapter.

5.2 Shear failure of footing

5.2.1 Preliminaries

This section is devoted to the discussion of the bearing capacity of circular footings along the line of the work presented by Menétrey and Zimmermann [91]. A circular footing submitted to an increasing load usually generates a shear failure inside the soil. This problem known as the footing problem has already been discussed by many authors using analytical methods: Terzaghi [138], Cox et al. [26], Lambe and Whitman [73], Chen [18], Vesić [142], and Salençon and Matar [85] and [123]. Three different modes of failure are distinguished for the footing problem: the global, the local and the punching shear failure. The global shear failure is characterized by a continuous failure mechanism developed between the perimeter of the footing and the ground surface as shown in figure 5.1(a); it is a sudden phenomenon as shown in the response curve presented in figure 5.1(d). In the opposite, local shear failure is characterized by a local failure mechanism which does not reach the ground surface as shown in figure 5.1(b) and it is a progressive phenomenon. The punching shear failure is also characterized by a progressive settlement but this settlement is generated by shearing in the vertical direction around the perimeter of the footing as shown in figure 5.1(c).

Numerical analysis of such failure mechanism were already performed by many authors, among others: Chen [18], Desai and Siriwarde [29], Chen and Baladi [20], Prevost and Hughes [109], and De Borst and Vermeer [12]. The approach adopted here is similar to previous analyses, however the yield condition, the plastic flow rule, the treatment of incompressibility and

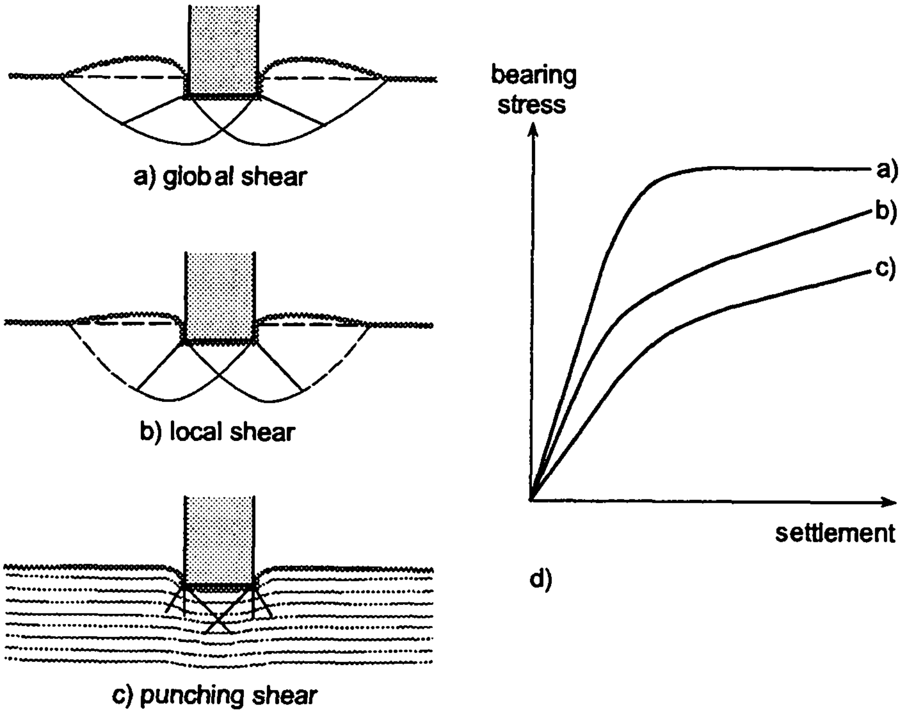

Figure 5.1: Different shear failure mechanisms observed in the footing problem: (a) global, (b) local, (c) and punching shear failure, (d) corresponding responses; (Vesić 1975)

the non-linear algorithm are slightly different. Two material models based on the incremental flow theory of plasticity are investigated, the Drucker-Prager and a smooth Mohr-Coulomb. A complete description of these models is presented in appendix D where the yield condition, the plastic potential, the treatment of the apex, and the calibration of soil characteristics are given. A close look at the standard calibration of the Drucker-Prager yield surface is presented and a new calibration is proposed.

The role of the yield surface on the ultimate bearing capacity and on the failure mechanism is investigated. After that the influence of the flow rule is examined and the difference between local and global shear failure is brought to evidence.

5.2.2 Role of the yield condition

On the bearing capacity

The role of the shape and the size of the yield surface is investigated by comparing the ultimate bearing capacity predicted numerically using different yield surfaces with the one obtained analytically. In order to perform that task, a typical footing problem presented in figure 5.2 is considered. It is composed of a concrete footing modeled with 9 quad-axi elements layered on a soil medium modeled with 72 quad-axi elements and characterized by: Young's modulus E=3000 kN/m^2, Poisson's ratio $\nu = 0.38$, cohesion c_{mc}=1 kN/m^2 and dilatancy angle $\psi = 0^0$. The simulation is performed by controlling the displacement to increase the numerical stability in the vicinity of limit loads. The value of the friction angle varies from 20^0 to 45^0 in order to cover most of the types of soil. The predicted ultimate bearing loads are presented in figure 5.3 for three different yield surfaces: the smooth Mohr-Coulomb, the internal and the external Drucker-Prager. These numerical predictions are compared with the analytical results given

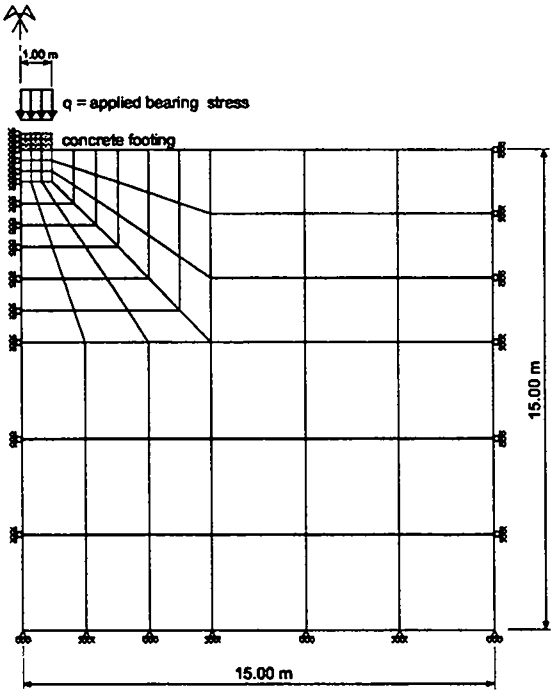

Figure 5.2: Geometry of the footing problem

by three different methods. Two of these methods are based on the limit analysis, that is Terzaghi's method adjusted by Vesić [142] for circular footings and the method developed by Salençon and Matar [85] and [123]. The third analytical method is based on the slip-line method and was developed by Cox et al. [26]. All the results are presented in figure 5.3 for comparison. It can be seen that all the theoretical and numerical methods predict the same increase of the ultimate bearing stress with increasing friction angle. However, that increase varies depending on the considered method and is not only observed for the numerical methods but also for the analytical ones illustrating the sensitivity of the problem. From figure 5.3 it can be seen that the ultimate bearing stress is bounded by the values obtained with the Drucker-Prager material calibrated to the two extreme values. For a friction angle greater than 36.8^0 no clear failure could be obtained with the external Drucker-Prager material as illustrated by the vertical asymptote. This limitation is further studied in section 5.2.2. It can also be observed that the bearing stress predicted with the smooth Mohr-Coulomb surface and the one obtained with the method developed by Salençon and Matar are in very close agreement. Furthermore, this agreement is improved for increasing friction angle. This is due to the fact that the smooth Mohr-Coulomb condition approximates the original Mohr-Coulomb one (used by Salençon and Matar) more closely for high values of the friction angle as illustrated in figure D.2.

On the failure mechanism

The role of the yield surface is further investigated in analyzing the footing problem with the external Drucker-Prager model for a criterion which extends into the tensile region (as described in appendix D.3), that is for $\phi_{mc} > 36.8^0$. In order to perform that, the footing problem is analyzed in more detail for $\phi_{mc} = 40^0$, and $\psi = 0^0$. Two different computations are performed, one using the external Drucker-Prager model and the other, using the smooth Mohr-Coulomb model in order to have a reference prediction. The response of these two computations is shown

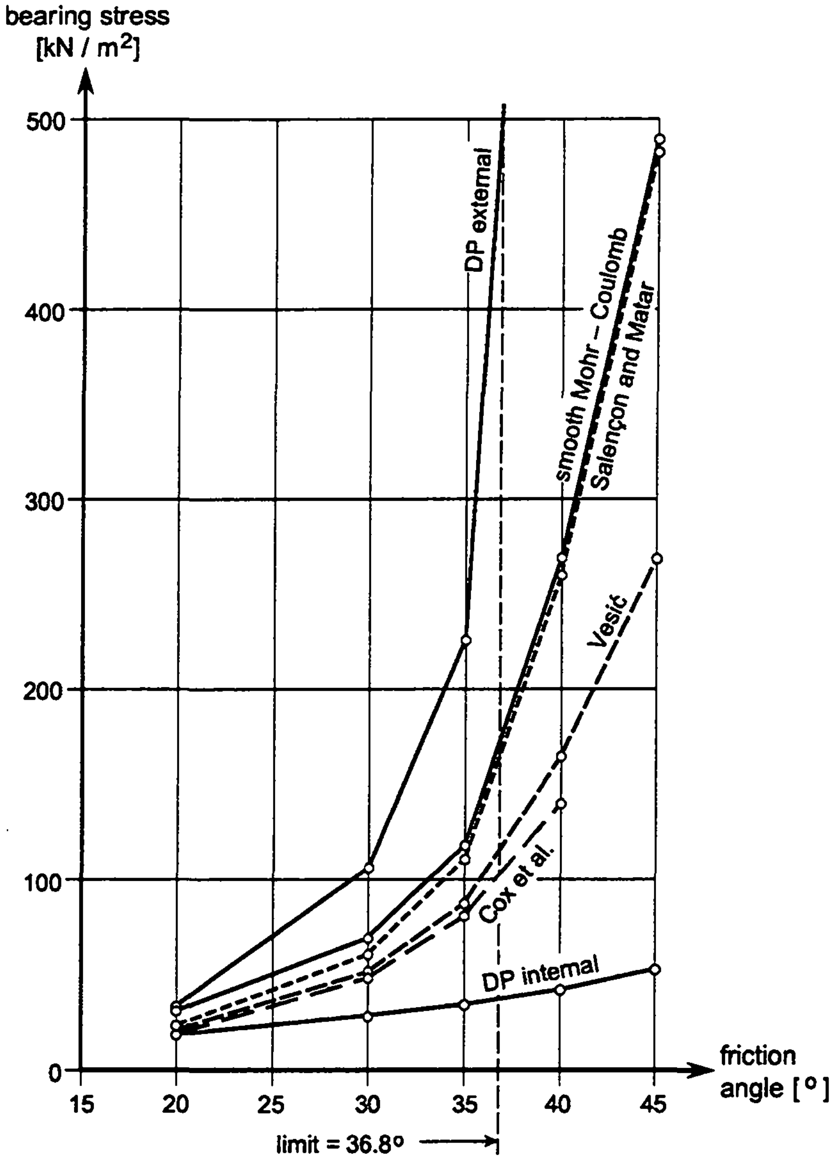

Figure 5.3: Comparison of the computed ultimate bearing stress for the footing problem

in figure 5.4. It can be seen that the smooth Mohr-Coulomb model leads to a clear failure as

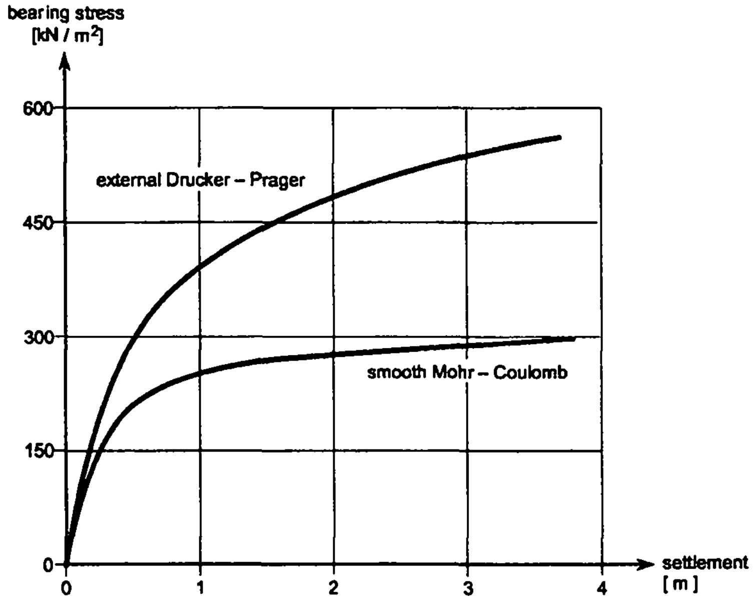

Figure 5.4: Responses obtained with the external Drucker-Prager and the smooth Mohr-Coulomb models for the footing problem ($\phi_{mc} = 40^0, \psi = 0^0$)

the slope of the response curve becomes close to horizontal, characterizing global shear failure. On the contrary, the Drucker-Prager model does not lead to a sharp failure as the load always increases for rising displacement.

Additional insight is provided in figure 5.5 where the deformed mesh, the velocity field, and the tensile stresses are presented for both simulations. All these plots correspond to the same settlement of 1.8 meters, which corresponds to a value close to the ultimate bearing stress of the Mohr-Coulomb simulation. For this settlement, the small deformation hypothesis is no longer valid. However, similar qualitative behavior was observed by Davidson and Chen [28] for small and large deformation simulations and large friction angles. Consequently, the results of figure 5.5 can be considered as a tendency of behavior. The deformed meshes illustrate that the behavior of the soil around the footing is different for both simulations. The smooth Mohr-Coulomb model predicts that the soil around the footing lifts up similarly to the mechanism of Hill (as described by Chen in [18]). However, the external Drucker-Prager model predicts that the soil around the footing settles characterizing punching shear failure. These two different mechanisms are corroborated by the plots of the velocity field. Furthermore, the tensile stresses shown at the bottom of figure 5.5 are different for both simulations, especially in the vicinity of the footing as only the external Drucker-Prager model predicts tensile stresses at 45^0 which contributes to stability. These tensile stresses resist to the settlement and consequently modify the failure mechanism. It can be concluded that a Drucker-Prager surface not strictly located in the compressive region and allowing parasitic tensile stresses generates a trend toward a punching shear failure mechanism.

5.2.3 Influence of the plastic flow rule

The influence of the plastic flow rule is studied in this section. In order to perform that task, the footing problem presented in figure 5.2 is considered and the soil is simulated with the smooth Mohr-Coulomb model. The material characteristics are the same as previously except

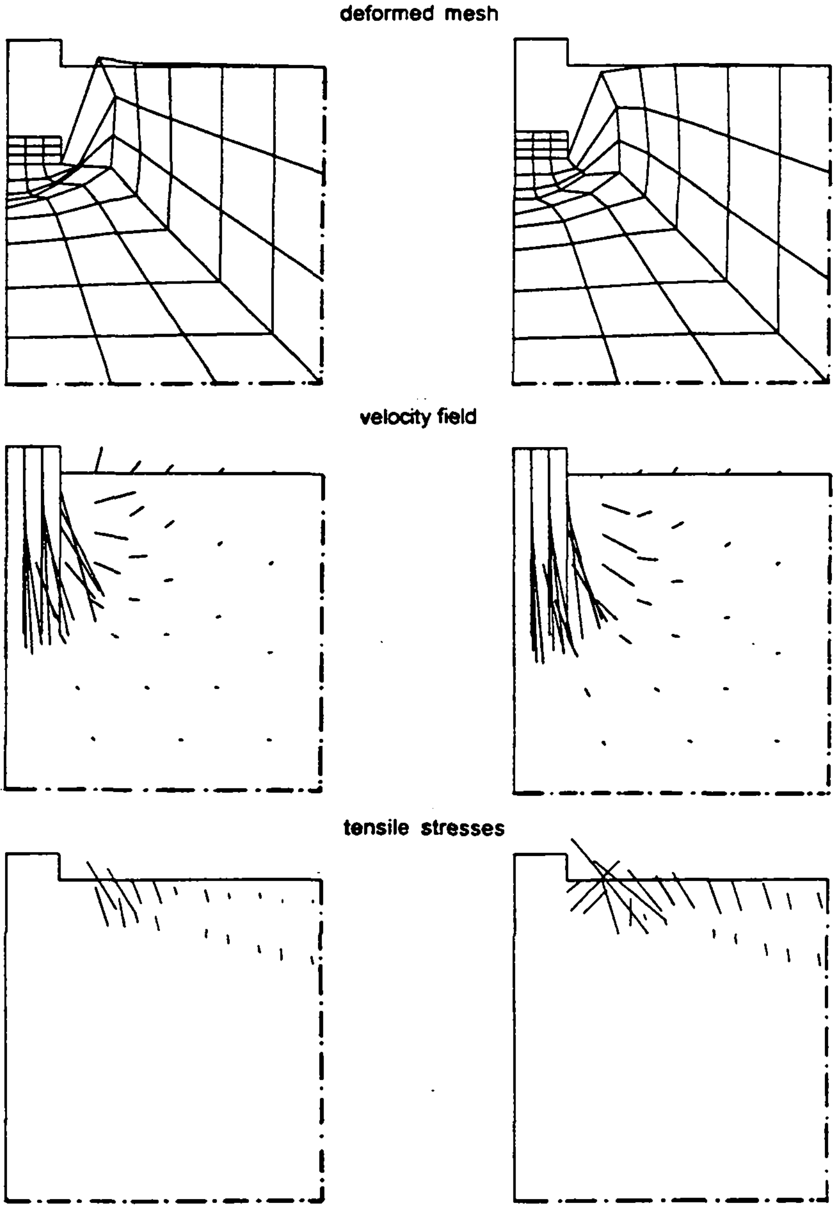

Figure 5.5: Comparison of the simulated mechanism with the smooth Mohr-Coulomb model (left) and the external Drucker-Prager one (right) for the footing problem

that the dilatancy angle varies from $\psi = 0^0$, which corresponds to the deviatoric flow rule, to $\psi = \phi_{mc}$, which corresponds to associated flow rule along the tensile meridian plane (internal calibration given in equation D.12).

The responses of the numerical simulation are presented in figure 5.6 for two different friction angles: $\phi_{mc} = 20^0$, and $\phi_{mc} = 40^0$. It can be seen that for both friction angles, the response is comparable. A sharp failure characterizing global shear failure is only observed with a deviatoric flow rule (incompressible plastic strain). For increasing value of the dilatancy angle (compressible plastic strain) the bearing stress increases and no clear failure can be obtained as the load increases continuously with rising displacement. This type of failure is characteristic of the local shear failure. Therefore, the flow rule does not only influence the value of the ultimate bearing stress but also the type of failure mechanism. This result is different from the one reported by De Borst and Vermeer [12] who stated that the limit load is practically insensitive to the adopted flow rule.

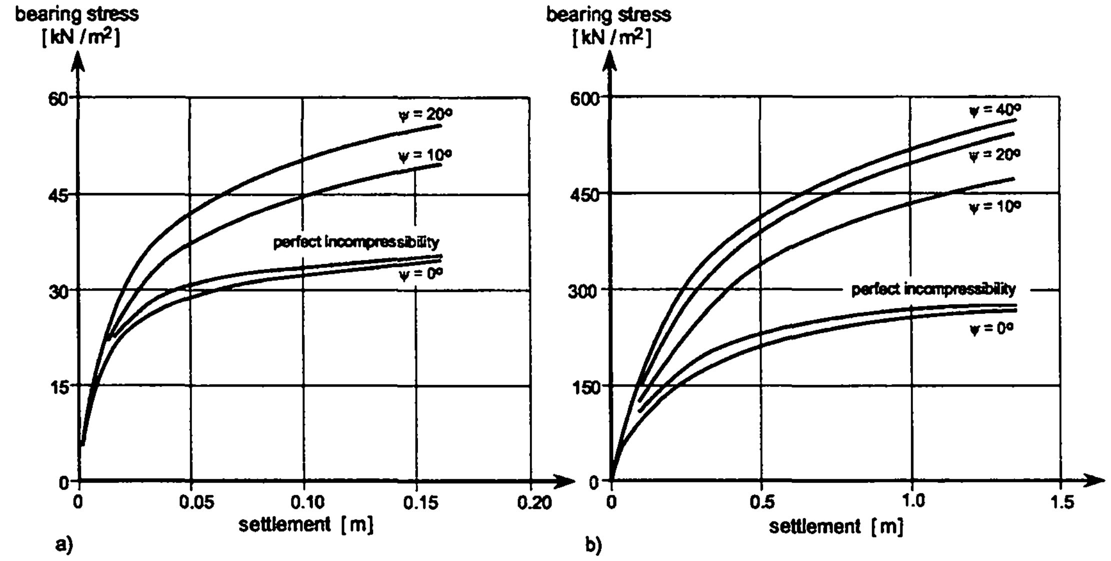

Figure 5.6: Influence of the plastic flow rule on the response of the footing problem for: (a) $\phi_{mc} = 20^0$, (b) $\phi_{mc} = 40^0$

The failure mode depends on the compressibility of soil as stated by Vesić [142]. In elastic-plastic analysis, the compressibility depends on Poisson's ratio and on the plastic flow rule. As the influence of the flow rule has just been presented, the influence of Poisson's ratio is now analyzed. The two limiting values of Poisson's ratio are considered $\nu = 0$ and $\nu = 0.5$ approximated by $\nu = 0.49999$. The standard footing problem is analyzed for $\phi_{mc} = 20^0, \psi = 0^0$ and the response curves are presented in figure 5.7. It is shown that Poisson's ratio equal to 0.5 leads again to a sharper failure identification than the one simulated with Poisson's ratio equal to zero. However, both failures are apparently global shear failures. From figure 5.6 and 5.7 it can be concluded that:

- incompressibility of the plastic strain is an essential condition to generate a global shear failure,

- incompressibility of the elastic strain is not required to observe a global shear failure, but it will result in a sharper failure identification,

- compressibility of the plastic strain leads to a local shear failure.

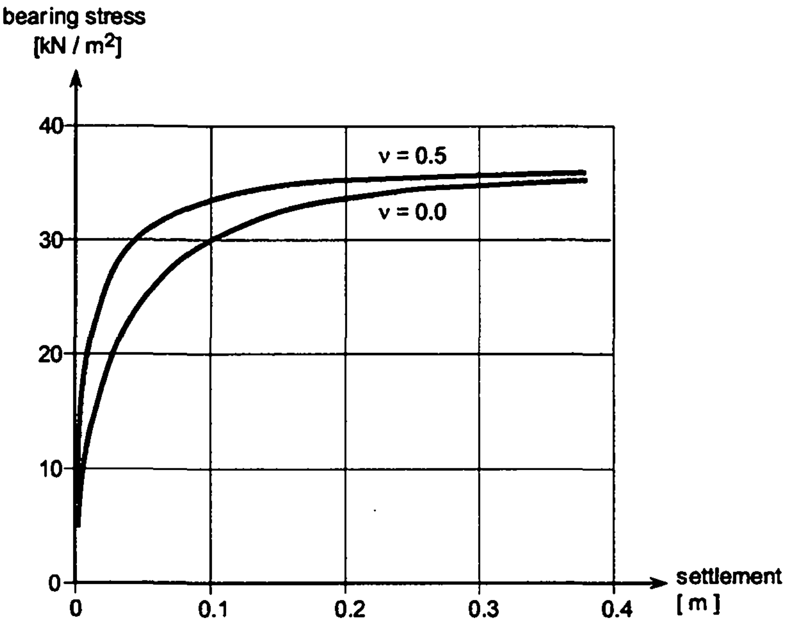

Figure 5.7: Influence of Poisson's ratio on the response of the footing ($\phi_{mc} = 20^0, \psi = 0^0$)

Although in elastic-plastic computations the plastic strain is larger than the elastic one the influence of elastic strains should not be neglected to distinguish failure mechanism. In the case of deviatoric flow rule ($\psi = 0^0$), only the plastic strain is incompressible and the elastic part depends on Poisson's ratio. This can lead to numerical problems as the plastic part deforms at constant volume but not the elastic one. Therefore, a special treatment—called perfectly incompressible—is performed such that if the flow rule is incompressible then Poisson's ratio is modified so that the elastic part is also incompressible. The results of these simulations are reported in figure 5.6 where it can be seen that the failure is again sharper than the one observed without elastic incompressibility.

5.2.4 Concluding remarks

The role of the yield condition is examined in analyzing a standard footing problem for different yield conditions and in comparing with analytical solutions. A large dispersion of the ultimate bearing stress prediction is observed in which the solution is bounded by the internal and external Drucker-Prager models. The results obtained with a smooth Mohr-Coulomb model are close to the one given by Salençon and Matar and about half way between the internal and external Drucker-Prager predictions. A new calibration which matches results obtained with a smooth Mohr-Coulomb criterion is proposed in appendix D for axisymmetric computations.

The external Drucker-Prager model exhibits no clear ultimate bearing stress even for large settlements when the friction angle is larger than the limit for the yield surface to be strictly located in the compressive region for zero cohesion. It is shown when comparing two similar computations for $\phi_{mc} = 40^0$, one with the smooth Mohr-Coulomb and one with the external Drucker-Prager, that the resulting failure mechanism is different. The failure mechanism observed with the smooth Mohr-Coulomb is similar to the one proposed by Hill. However, the one observed with the external Drucker-Prager is a punching failure.

The influence of the plastic potential is investigated in analyzing the standard footing problem for different dilatancy angles. It is shown that the dilatancy angle does not only influence the ultimate bearing stress but also the type of failure as only a deviatoric flow rule leads to a global shear failure. Furthermore, it is shown that the plastic strain (governed by the dilatancy angle) is more important than the elastic strain (Poisson's ratio) for the prediction of the failure type. However, incompressibility of the elastic and plastic strain leads to the sharpest failure.

The results obtained with the Drucker-Prager material model were compared and shown to be the same as the ones obtained with program ZSOIL [152]. The numerical model proves its capabilities for the analysis of shear failure in soil as the failure mechanisms are generated. This model can therefore be used to analyze shear failures in reinforced concrete, but previously, the reinforced concrete model is examined.

5.3 Tensile test of plain concrete

5.3.1 Description of the test

The tensile test performed at the University of Colorado at Boulder by Hurlbut [61] illustrates the tensile behavior of plain concrete. Un-notched cylindrical concrete specimens 108 mm high and 54 mm diameter as shown in figure 5.8(a) are tested. The test is performed under displacement control, in order to follow the descending branch of the response curve shown in figure 5.8(c). Up to the peak load the response is nearly linear. At peak, the axial tensile force decreases sharply without the noticeable formation of a crack. Upon close inspection, a single transverse hairline crack appeared around the periphery of the sample when the residual tensile strength diminished to near zero load level. Upon increasing displacement further opening of the crack is observed. At the end of the test, the specimen has separated into two distinct parts.

The capabilities of the numerical model to simulate the response of plain concrete in traction are examined. A sensitivity analysis of the numerical model is presented in order to adjust the parameters. This sensitivity analysis is followed by the simulation of the experimental test.

5.3.2 Sensitivity of the model in traction

Preliminaries

The sensitivity of the numerical model with regard to the flow rule and the softening parameters is examined. In order to perform that task, the tensile test is modeled with one quad-axi element as shown in figure 5.8(b). The concrete specimen is characterized by the following parameters E=19300 N/mm^2, ν=0.2, f_c=19.3 N/mm^2, and f_t=2.8 N/mm^2.

Influence of the flow rule

The influence of the flow rule is examined in simulating the tensile test for two different concrete flow rules: the parabolic and the concrete flow rules (described in section 3.5.3). The results of these simulations are shown in figure 5.9 where the response curves in the radial and axial directions are presented. It can be observed that the response curves predicted by the two different flow rules are affine. However, the parabolic flow rule predicts a large value of radial displacement which increases when the axial force decreases. Experimentally this is not observed as once cracking occurs, elastic unloading in the radial direction is measured. This phenomenon of elastic unloading of the radial displacement is only simulated with the concrete flow rule which results from the choice of the direction of the concrete flow rule. This direction satisfies the loading path for uniaxial traction as presented in section 3.5.3. The result of the simulation with the concrete flow rule is independent of the value of ψ_c illustrating that the flow

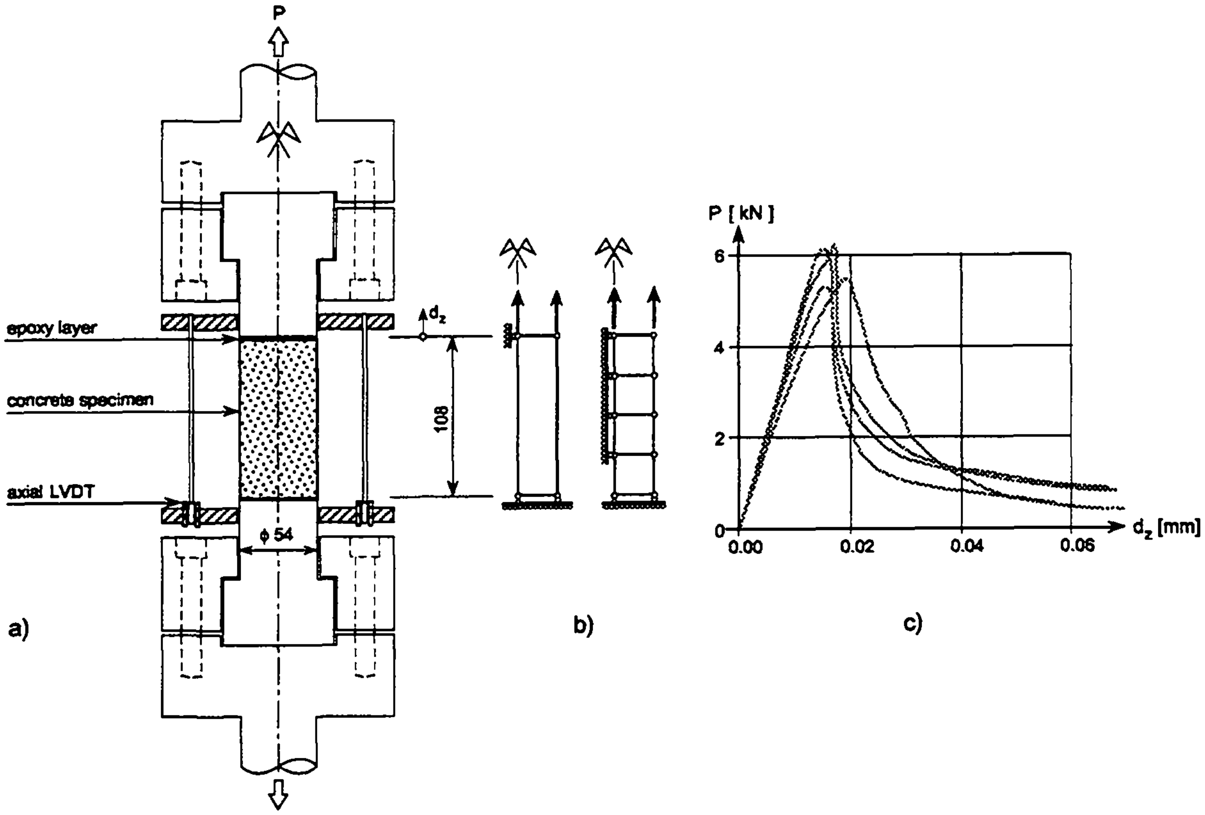

Figure 5.8: Tensile test in plain concrete: (a) setup, (b) finite element mesh, (c) experimental response; (Hurlbut 1983)

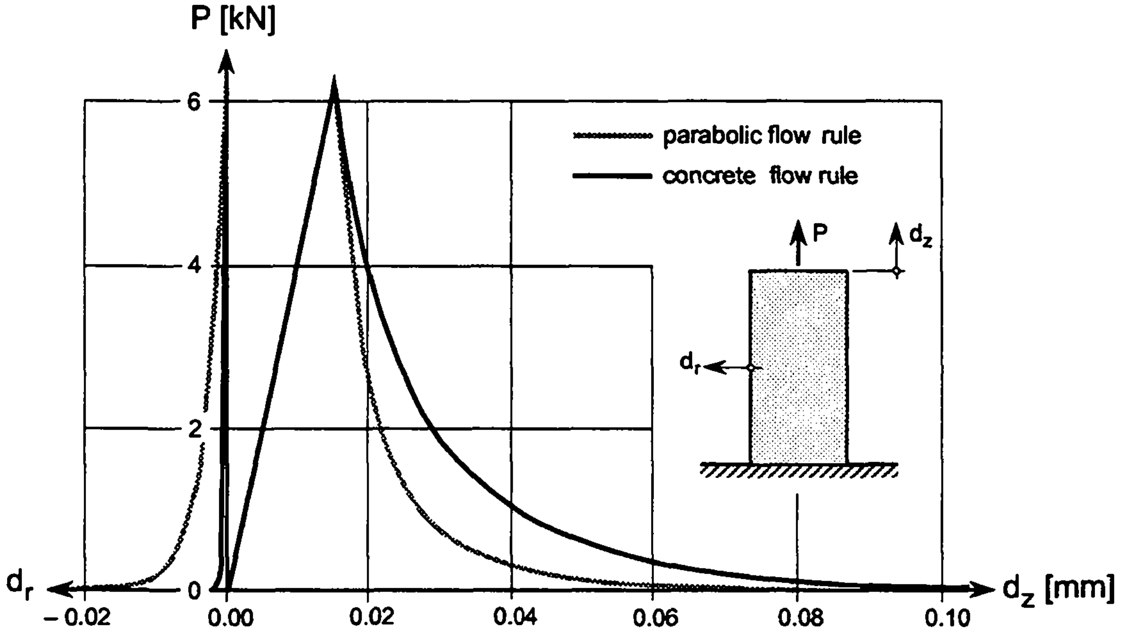

Figure 5.9: Influence of the flow rule on the response of the tensile test in plain concrete

direction along the loading path for uniaxial traction exclusively influences the response. It can be concluded that for tensile tests, the concrete flow rule gives a better prediction compared with the parabolic flow rule.

Influence of the softening parameters

The influence of two softening parameters is examined: the fracture energy G_f and the steepness parameter a (described in section 3.5.4). The influence of these parameters is investigated for the concrete flow rule. The corresponding response curves are presented in figure 5.10. It can be observed that the fracture energy controls the area under the softening branch since by increasing the value of the fracture energy, the area under the response curve increases. The steepness parameter controls the slope of the softening branch as shown in figure 5.10(b) for a constant value of the crack opening displacement (variable value of fracture energy). The higher the steepness parameter, the steeper is the softening branch.

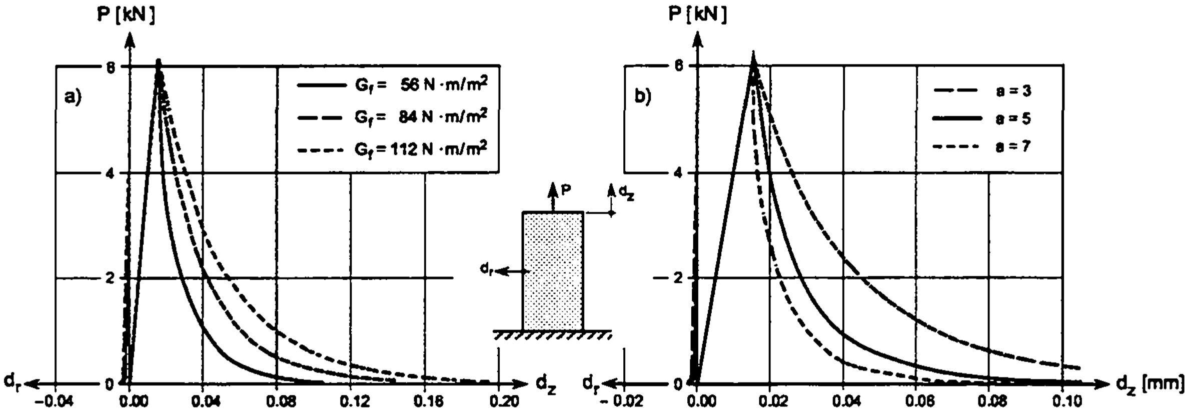

Figure 5.10: Influence of: (a) the fracture energy, (b) the steepness parameter, on the response of the tensile test in plain concrete

5.3.3 Prediction of the experimental results

Simulation with one quad-axi element

The tensile test of Hurlbut is first simulated with one quad-axi element as shown in figure 5.8(b). The concrete is characterized by a concrete flow rule (described in section 3.5.3), no damage implementation, and the softening parameters G_f=56 N·m/m^2 and a=5. The response curve obtained with a displacement control simulation is reproduced in figure 5.11 along with the experimental response curves. It can be observed that the predicted ultimate force is similar to the one obtained experimentally. Additionally, the simulated softening branch is bounded by the experimental ones. This demonstrates that the numerical model is capable of simulating the tensile test in plain concrete.

For this simulation, the material stability condition of Hill [51] stated in equation 3.45 is not satisfied as soon as the softening response is reached. This condition indicates that a diffused failure is occurring.

The indications given by the acoustic tensor are also investigated. For convenience, the scaled ratio of the determinant of the acoustic tensor is plotted versus the angle α (normal to the discontinuity) in figure 5.12. It can be inferred that as soon as the plastic response is activated, that is for the load step d_z=0.015 mm, the determinant of the acoustic tensor

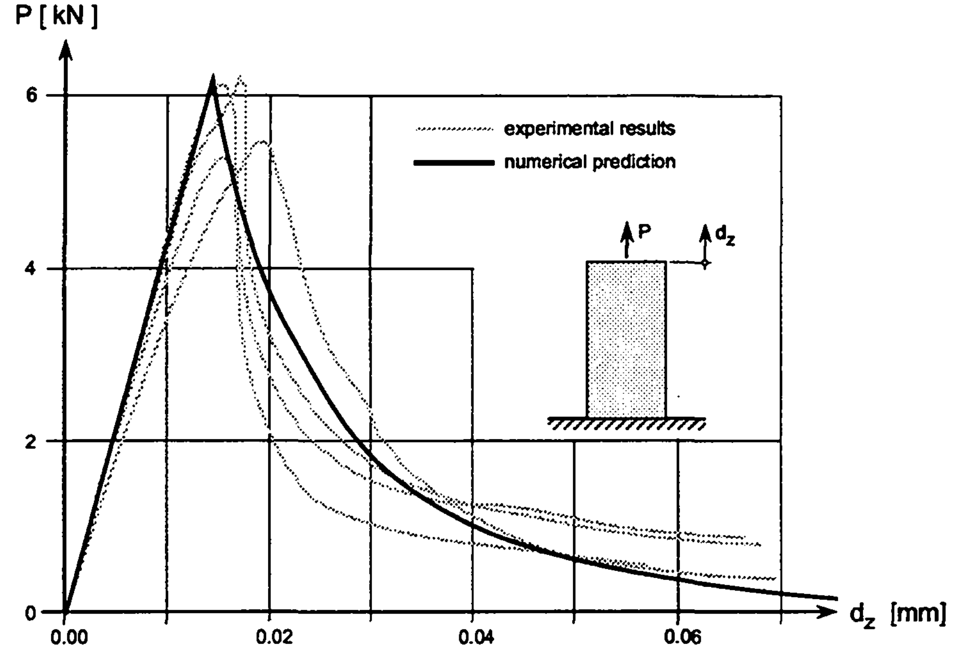

Figure 5.11: Experimental and numerical responses of the tensile test in plain concrete

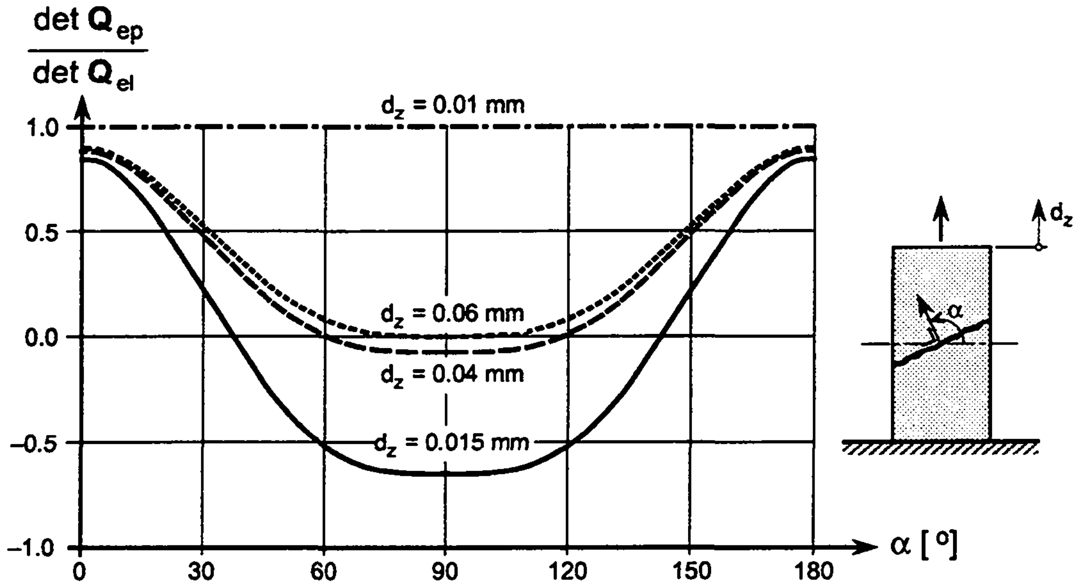

Figure 5.12: Analysis of the acoustic tensor for the tensile test in plain concrete

varies with the angle α. For certain inclination, the acoustic tensor is negative indicating a weak discontinuity (defined in footnote page 57). The lowest value of the determinant of the acoustic tensor is observed for $\alpha = 90^0$. This corresponds exactly to the orientation of the tensile crack. Therefore, the acoustic tensor notifies the presence of tensile cracks. It can be noted that with increasing load step, the sector where the determinant of the acoustic tensor is negative decreases.

Simulation with four quad-axi elements

The tensile test is also simulated with 4 quad-axi elements as shown in figure 5.8(b). The simulation is first performed with the same material characteristics in all the four elements. The obtained response curve is similar to the one resulting from a one quad-axi element simulation. This demonstrates that the numerical response is independent of the mesh size (for the uniaxial tensile test). This mesh insensitivity results from the introduction of the finite element size in the softening formulation as presented in section 3.5.4.

Another simulation with 4 quad-axi elements is performed in order to examine the localization condition of the deformation in only one element. This strain localization can be obtained by selecting a different tensile strength in each element. The desired localization is achieved only if the trial tensile stress is larger than the strength in the element where cracking is desired and lower than the strength in the other un-cracked elements. This method is not used for this simulation but it will be used in section 5.5 for the simulation of the tensile test in reinforced concrete.

Another method used to trigger failure localization is to modify the softening slope of some elements so as to force a non-uniform solution. This method was used by Li and Zimmermann [77] for non-linear fracture model. The application of this method is obtained by assuming the same tensile strength and fracture energy in all the elements (this is justified because both are material characteristics), but assuming in one element, a steeper softening slope that is a higher value of the softening parameter a (described in section 3.5.4).

The simulation is performed with the six strategies defined on page 68. It is observed that the first and second strategies lead to a localization of the failure in many iterations. The third strategy which is a full Newton-Raphson algorithm, induces no localization of the failure. The fourth strategy which implements an elastic stiffness matrix for an initial number of iterations reveals a localized failure only for a high number of elastic iteration. The strategies five and six lead to a localized failure and they will be further considered.

The response curve of the simulation for which strain localization is generated, is shown in figure 5.13 along with the response predicted with one quad-axi simulation. It can be observed that the prediction with four quad-axi elements leads to a residual load carrying capacity similar to the one observed experimentally. This remaining load is due to a non-uniform state of stress. The deflection and the crack pattern obtained with the simulation for which strain localization is generated are presented in figure 5.14. The strain localization phenomenon can be checked as the deflection and tensile cracks are concentrated in one element and the three other elements unload. The element where cracking occurs is characterized by the highest steepness parameter.

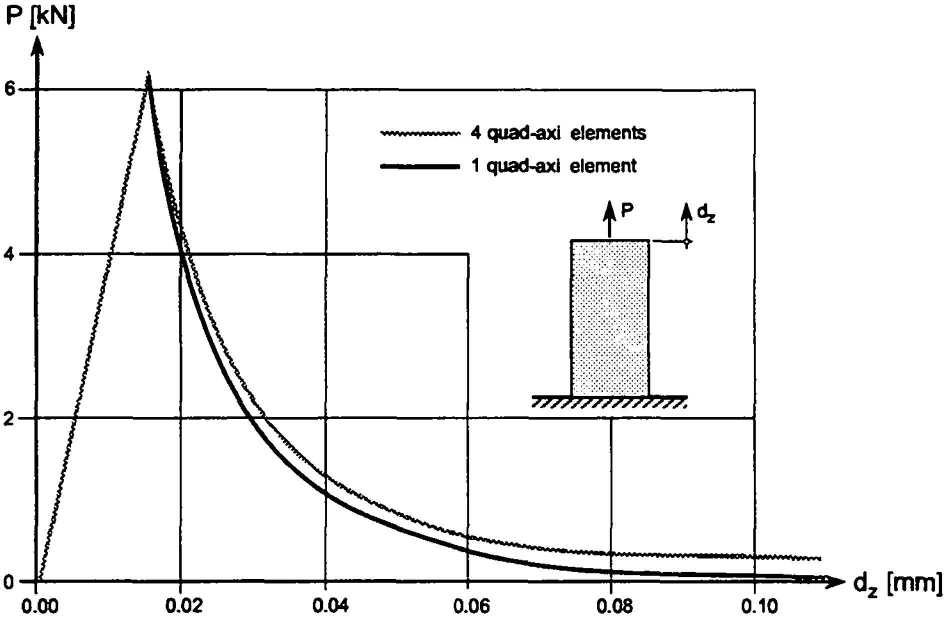

Figure 5.13: Response of tensile test in plain concrete discretized with one and four quad-axi elements (localized response)

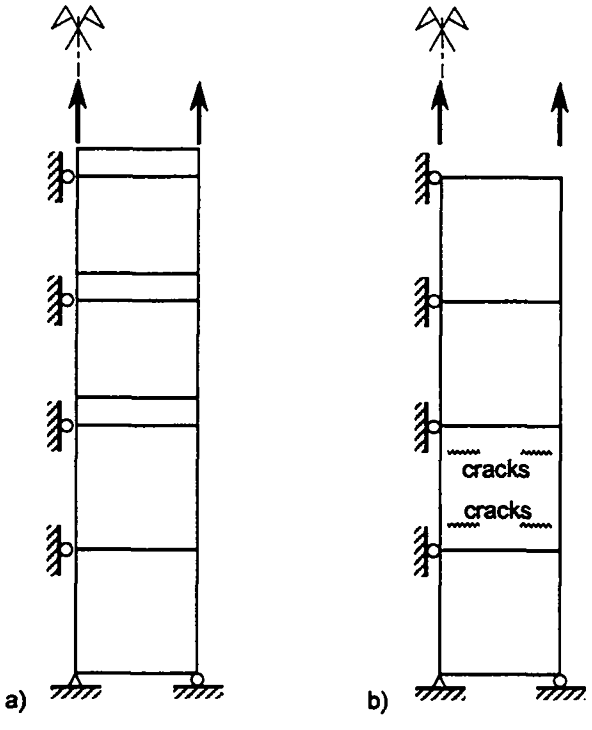

Figure 5.14: Localized deflection and crack pattern for the tensile test in plain concrete (4 quad-axi elements simulation)

5.4 Confined compressive test of plain concrete

5.4.1 Description of the test

Smith [130] performed a series of confined compressive tests on concrete cylinders 108 mm high and 54 mm diameter as shown in figure 5.15(a). The vertical load is transmitted to the concrete specimen from the load frame to steel ram. No friction-reducing material is used between the steel-concrete interface, thus the interface conditions are rigid. The resulting state of stress is non-uniform and only an average strength can be considered as described by Van Mier [93]. The confining pressure is applied by means of fluid pressure on a flexible membrane.

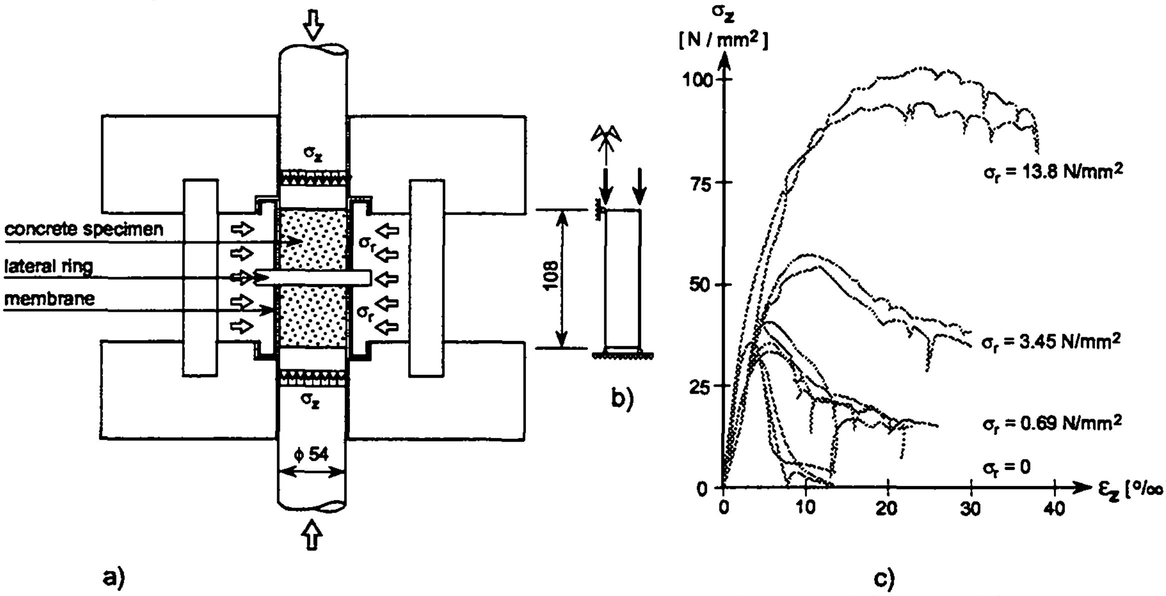

Figure 5.15: Confined compressive test in plain concrete: (a) setup, (b) mesh, (c) experimental responses; (Smith 1987)

From figure 5.15(c) it can be observed that the unconfined compressive test ($\sigma_r = 0$) is characterized by a linear elastic behavior, followed by a gradual increase of deformation due to internal micro-cracking (hardening regime). The failure occurs suddenly and is followed by a steep softening branch with zero residual stress. In figure 5.15(c) the influence of the confinement pressure is also presented. It can be observed that the ultimate stress increases when the confining pressure raises. The confining pressure also influences the softening response, as the softening slope decreases and the residual stress increases when the confinement pressure raises.

The capabilities of the numerical model to simulate the concrete behavior under uniaxial compression as well as confined compression are examined. A sensitivity analysis of the numerical model is presented first in order to adjust the parameters. This sensitivity analysis is followed by the simulation of the experimental test.

5.4.2 Sensitivity of the model in compression

Preliminaries

The unconfined compressive test is preferred over the confined compressive test for the sensitivity analysis as it is more brittle. The influence of the flow rule and the softening parameters are examined. This analysis is performed with one quad-axi element as shown in figure 5.15(b).

The concrete characteristics are: E=35000 N/mm^2, ν=0.2, f_c=35.2 N/mm^2, f_t=3.1 N/mm^2, and G_f=62 N·m/m^2.

Influence of the flow rule

The influence of the flow rule on the simulation of the unconfined compressive test is investigated with three different flow rules: the deviatoric, the concrete, and the parabolic (described in section 3.5.3). The stress-strain curves of these three simulations are presented in figure 5.16. It can be observed that the flow rule has no influence on the prediction of the peak strength but it affects the post-peak behavior. The concrete flow rule predicts the steepest response.

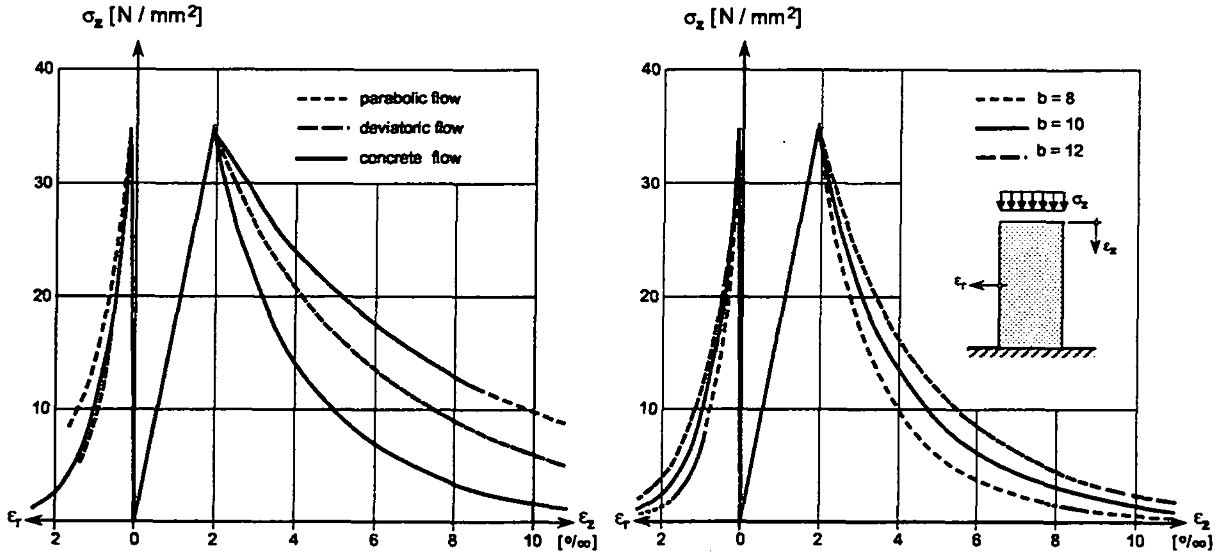

Figure 5.16: Influence of the flow rule and the softening parameter "b" on the response of the unconfined compressive test in plain concrete

Influence of the softening parameters

The influence of the softening parameters was already studied in section 5.3.2 except for the parameter "b" (number of cracks in uniaxial compressive test as defined in section 3.5.4). The influence of this parameter is investigated for the concrete flow rule and the stress-strain curves obtained for three different values of "b" are presented in figure 5.16. It can be observed that the lower the parameter "b" the steeper the softening branch for the axial and the radial strains.

5.4.3 Prediction of the experimental results

Simulation of the unconfined compressive test

Smith's unconfined compressive test is simulated with one quad-axi element as shown in figure 5.15(b). The concrete is modeled as described in section 5.4.2 along with a concrete flow rule, no damage implementation, and the softening parameter b=10. The stress-strain curve obtained with a displacement control simulation is reproduced in figure 5.17 along with the experimental results. It can be observed that the simulated pre-peak branch is slightly different from the experimental one as a linear branch is numerically predicted and a non-linear

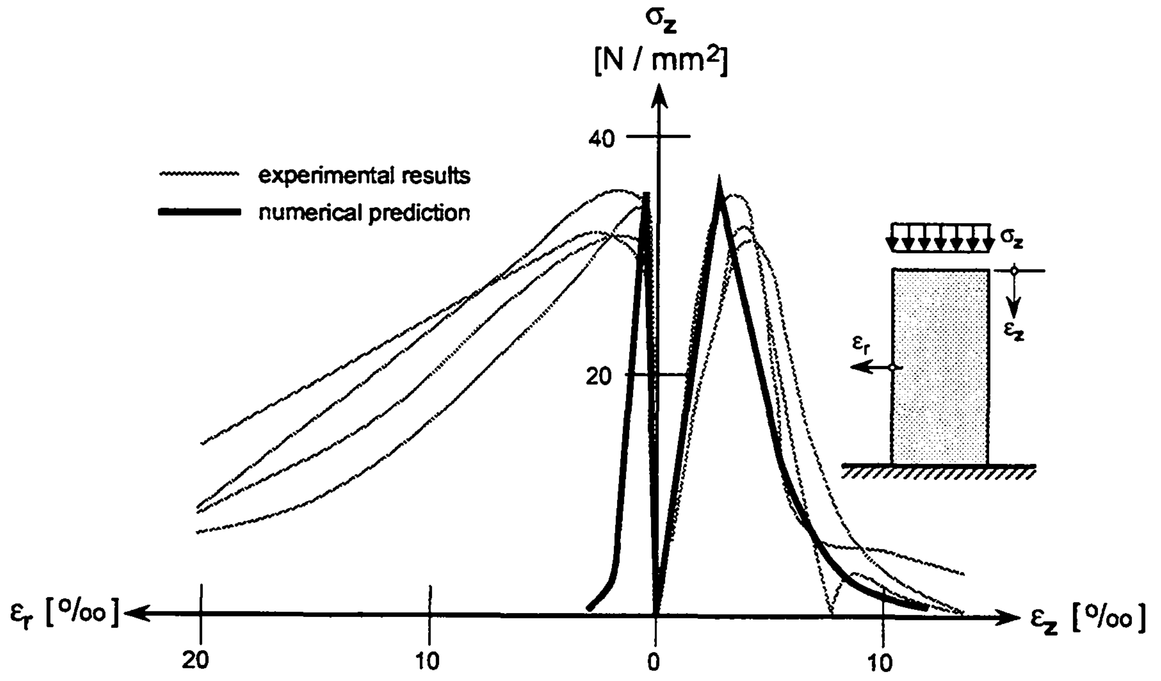

Figure 5.17: Experimental and numerical responses of the unconfined compressive test in plain concrete

hardening behavior is observed experimentally. However, the prediction of the maximum load is accurate. The predicted softening branch of the axial strain is close to the experimental one. However, the softening branch of the radial strain is different from the one observed experimentally. This is due to the fact that the test is modeled with one quad-axi element resulting in a constant radial deformation over the height of the element. In the experimental test, the radial deformation is not constant and the one which is reported is the maximum deformation located in the middle of the specimen measured with the lateral ring shown in figure 5.15(a).

Hill's material stability condition [51] stated in equation 3.45 is not satisfied as soon as the softening response is reached. This condition indicates that a diffuse failure is occurring.

The indications given by the acoustic tensor are also investigated. The scaled ratio of the determinant of the acoustic tensor is plotted versus the angle α (normal to the discontinuity) in figure 5.18 for three different flow rules: deviatoric, parabolic, and the concrete flow rule (described in section 3.5.3). It can be observed that the three flow rules predict the same variation of the acoustic tensor. However, the critical orientation for which the determinant of the acoustic tensor is minimal depends on the flow rule as α=36.9^0 for a deviatoric flow rule, α=34.8^0 for a parabolic flow rule, and α=30.5^0 for a concrete flow rule. It can be noted that Kupfer [71] reported experimentally a mean inclination of the shear band of 30^0 which confirms the results obtained with the numerical simulation. The determinant of the acoustic tensor for this test is not negative in the softening regime as reported for example by Pramono [108] for the Leon model. This is due to the axially symmetric assumption as the same test performed under plain strain condition reveals a negative determinant of the acoustic tensor.

For the simulation of the unconfined compressive test, it is also observed that the acoustic tensor is not influenced by the damage of the constitutive matrix. It is also observed that the influence of the out-of-roundness parameter (e=0.52, 0.55, and 0.6) is negligible on the determinant of the acoustic tensor (for the unconfined compressive test).

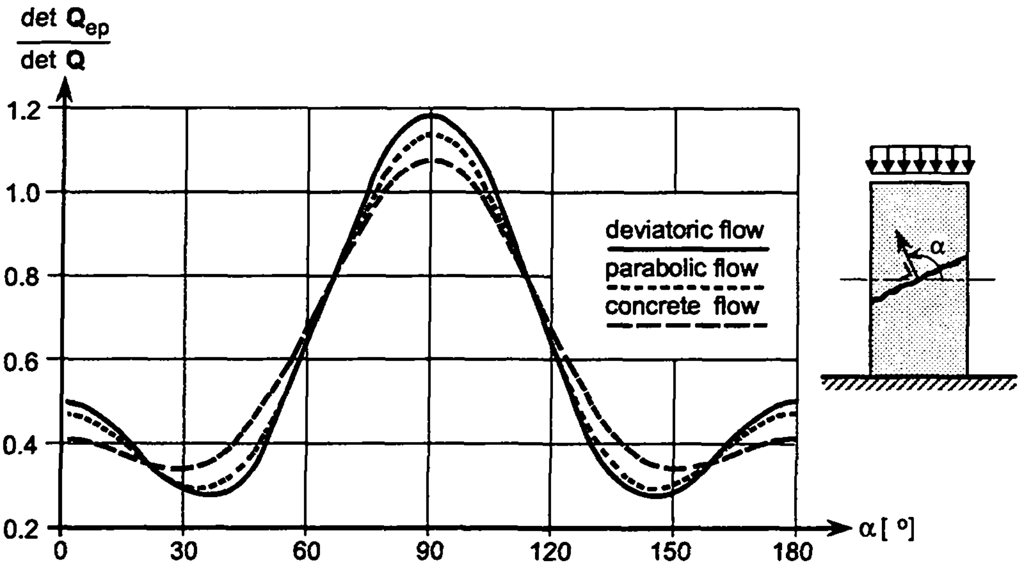

Figure 5.18: Influence of the flow rule on the acoustic tensor for the unconfined compressive test in plain concrete

Simulation of the confined compressive test

The influence of the confinement pressure is investigated in simulating the confined compressive test for three different confinement pressures: 0.69, 3.45, and 13.8 N/mm^2. The experimental stress-strain curves and the predicted ones are shown in figure 5.19. It can be observed that the overall prediction of the three stress-strain curves matches the experimental results. The increase of the ultimate stress with increasing confinement pressure is reproduced and the value of that ultimate stress is close to the experimental one. The softening branch is also reproduced and the residual stress is predicted. It can be noted that the hardening behavior observed experimentally is not reproduced by the numerical simulation (one of the simplification assumption as mentioned on page 54). By neglecting the hardening behavior, the numerical prediction is stiffer specially for high confinement pressure. Another consequence of the lack of hardening behavior is that the constitutive model does not consider transition point between brittle and ductile response. This explains the small softening branch which is predicted even for high confinement pressure.

5.5 Tensile test of reinforced concrete

5.5.1 Description of the test

The numerical simulation of reinforced concrete structures is first investigated with a reinforced concrete specimen subjected to a tensile force which is parallel to the reinforcement. The experiment performed by Jaccoud et al. [62] [63] is considered. Large size specimens of 2.5 m long and characterized by a rectangular cross section are tested. The tensile force is transmitted from the testing machine to the specimen through steel anchors. The measuring zone of 1.2 m located in the middle of the specimen is characterized by a uniaxial state of stress. The test B-13 is considered and the setup is illustrated in figure 5.20(a). The response curve of this particular specimen is presented in figure 5.20(c). It is bounded by two states of stress defined by the CEB [24]: *state I* during which concrete and steel are active both in tension and compression and *state II-naked* during which the reinforcement is effective in traction

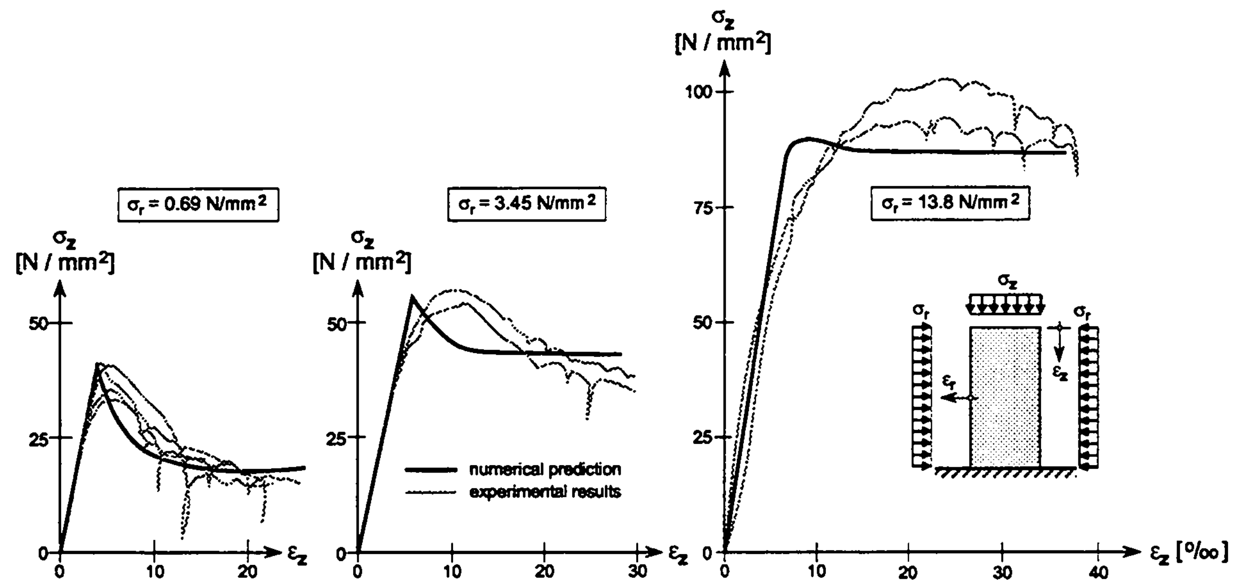

Figure 5.19: Experimental and numerical responses of the confined compressive test in plain concrete

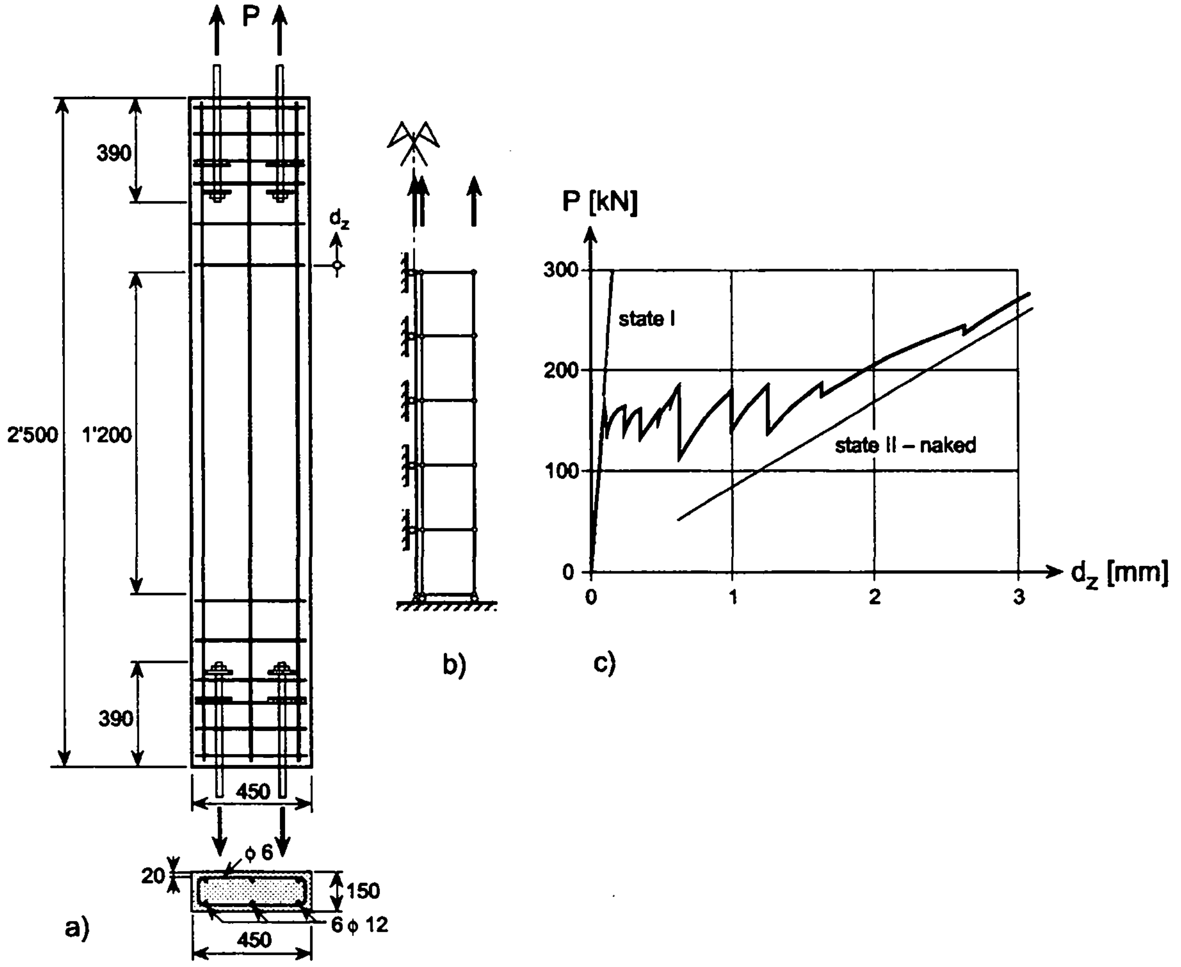

Figure 5.20: Tensile test in reinforced concrete: (a) setup, (b) mesh, (c) experimental response; (Jaccoud et al. 1984)

and compression and the concrete is only effective in compression. The difference between the experimental and the II-naked state response is due to the stiffness contribution of the concrete between the cracks known as the *tension stiffening effect* of concrete.

The purpose of this section is to study the capabilities of the numerical model to simulate the effect of the reinforcement in a concrete specimen subjected to an axial tensile force.

5.5.2 Prediction of the experimental results

The numerical simulation is performed with the mesh shown in figure 5.20(b) allowing to reproduce a uniaxial state of stress in the measured zone of the specimen. The mesh is composed of 5 quad-axi elements to simulate the concrete and 5 truss-axi elements for the reinforcement. A perfect bond between concrete and steel is assumed. The concrete characteristics are: E=35000 N/mm^2, ν=0.2, f_c=32.9 N/mm^2, f_t=2.35 N/mm^2, concrete flow rule with ψ_c=10^0, and G_f=470 N·m/m^2. The value of G_f is chosen to be five times larger than the experimental one in order to avoid snap-back behavior and to improve the numerical stability as large size finite elements are used. The steel characteristics are: E_s=210000 N/mm^2, f_y=540 N/mm^2, and H=10000 N/mm^2 (assumed). Two different simulations are performed in order to investigate the process of crack formation.

The first simulation is accomplished with a similar type of concrete in all the five elements (specimen with constant f_t). The response of this simulation is shown in figure 5.21 along with the experimental one. It can be observed that the state I, the peak load, and the state II-naked are reproduced by the numerical model. However, the process of crack formation observed experimentally (several cracks open at different load level) is different from the one predicted numerically (all the elements are cracked at the same time).

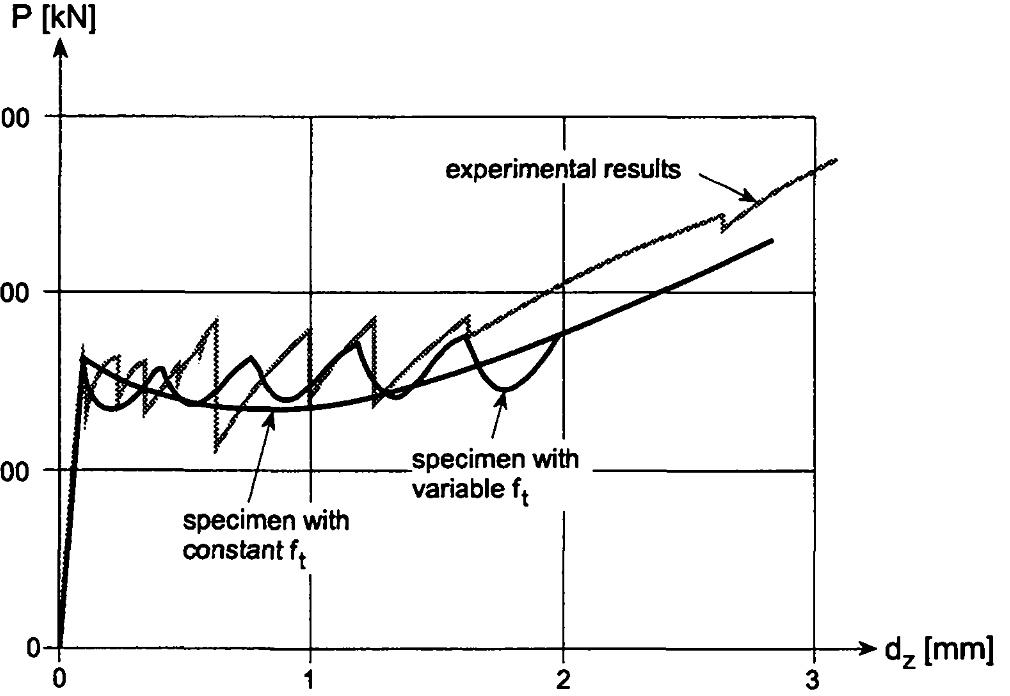

Figure 5.21: Experimental and numerical responses of the tensile test in reinforced concrete

In order to show that the numerical model is capable of reproducing the experimental cracking sequence, a second simulation is performed in which the tensile strength of the five concrete elements varies linearly (f_t=2.35, 2.45, 2.55, 2.65, 2.75 N/mm^2). By giving different values to the tensile strength, it is possible to observe the crack formation in one element at a time. This observation is achieved only if the trial stress is larger than the strength in the element where cracking is desired and lower than the strength in the other un-cracked elements. This condition is easily satisfied in this simulation because small increments of displacement are controlling the load steps. This approach is different from the one used in section 5.3.3 when analyzing the tensile test in plain concrete with different softening slopes in each element.

The response of this simulation is presented in figure 5.21 so that it can be compared to both, the previous simulation and the experimental one. Again, it can be observed that the state I, the peak load, and the state II-naked are reproduced numerically. In addition, the process of crack formation is comparable to the one observed experimentally, as once the first crack is formed, a softening branch is observed, followed by an increase of the load carrying capacity with a reduced stiffness up to the formation of an other crack and so on. This simulation illustrates that one way of improving the prediction of experimental results is to use non-uniform material characteristics so to reproduce material imperfections.

The simulation of the tensile test in reinforced concrete specimen can be further investigated. First, denser mesh can be used to examine the shear stress evolution as performed by Rots [120]. The influence of the fracture energy on the crack spacing can also be analyzed as performed by Li [76] and Barry [5]. The assumption of perfect bond does not entail the numerical prediction of this test, but this effect can be further studied as performed by Groot et al. [49]. These investigations are not accomplished here because, the purpose of this simulation is to establish that the numerical model is capable of reproducing the effect of the reinforcement when a concrete specimen is subjected to an axial tensile force, which is demonstrated.

5.6 Compressive test of reinforced concrete

5.6.1 Description of the test

The compressive test of spirally reinforced concrete columns is an other important practical example of reinforced concrete behavior. The numerical simulation of this test is interesting because of the strong mechanical interaction between the concrete and the steel as the spiral reinforcement causes the confinement pressure developing a triaxial state of stress in concrete. The experimental tests performed by Richart et al. [117] are considered as they illustrate the behavior of plain and spirally reinforced concrete columns loaded vertically up to failure. The columns are 1024 mm high and 254 mm in diameter and are surrounded by a spiral reinforcement. The test setup of column 12 is shown in figure 5.22(a). The response of two different columns, one without (column 02) and one with spiral reinforcement (column 12) are presented in figure 5.22(c) for comparison. It can be observed that the effects of the spiral reinforcement are to increase the ultimate load and the ductility. The purpose of this section is to investigate the capability of the numerical model to take into account this spiral reinforcement.

5.6.2 Prediction of the experimental results

The discretization of the entire column is a complicated task justifying the discretization of only one slice of concrete between the spiral reinforcement as shown in figure 5.22(b). The concrete is modeled with eight quad-axi elements and the bounding spiral reinforcement is modeled with 2 ring elements. The concrete characteristics are for columns 02 and 12 respectively: E=21600, 18300 N/mm^2, ν=0.2, f_c=17.5, 19.2 N/mm^2, f_t=2 N/mm^2 (assumed), concrete flow rule with ψ_c=40^0, and G_f=40 N·m/m^2 (assumed). The spiral reinforcement is made

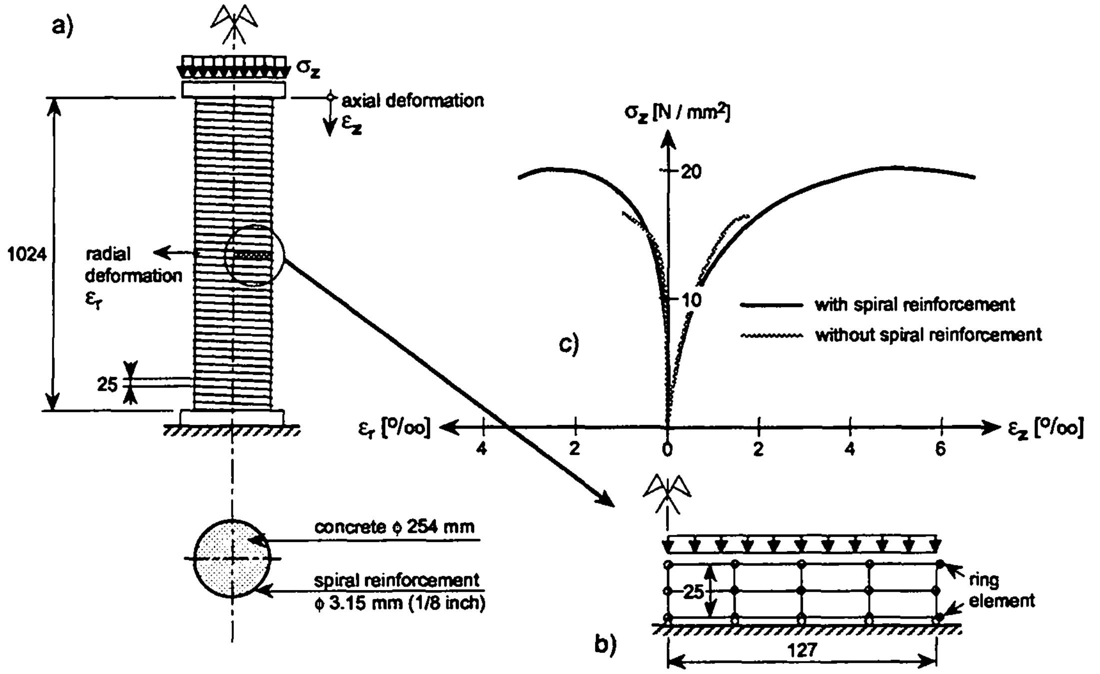

Figure 5.22: Compressive test in reinforced concrete: (a) setup, (b) mesh, (c) experimental responses; (Richard et al. 1929)

of 1/8 inch (ϕ=3.2 mm) steel characterized by: E=231000 N/mm^2, f_y=462 N/mm^2, and H=10000 N/mm^2 (assumed). A perfect bond between the concrete and steel is assumed. The responses obtained for the simulation of columns with and without spiral reinforcement are illustrated in figure 5.23.

From the response of the plain concrete column, it can be observed that the hardening behavior observed experimentally is not reproduced numerically. This is due to the fact that the hardening behavior of concrete is not included in the numerical model at the constitutive level as mentioned on page 54. The peak load predicted by the numerical model slightly overestimates the experimental one. This is due to some confusing value of the compressive strength given by Richard et al. as the cylindrical compressive strength for this column is 17.5 N/mm^2 (used in the numerical simulation) and the column failed experimentally at 15.7 N/mm^2. Another difference between the experimental and the numerical response is observed after the peak load as the numerical simulation predicts a softening branch which is not observed experimentally. This is due to the fact that the numerical simulation is performed under displacement control, allowing to capture softening response, whereas the experimental test is performed under load control, implying that softening cannot be captured.

From the response curve of the spirally reinforced concrete column, the same remarks as the ones presented for the simulation of the plain concrete column concerning the lack of hardening behavior, the overestimation of the peak load and the softening branch observed only with the numerical model are appropriate.

By comparing the response of the columns with spiral and without spiral reinforcement, it can be observed that the two dominant effects of the confinement reinforcement, that is increase of ultimate load and increase in ductility are well reproduced by the numerical model.

The perfect bond between concrete and steel assumed for the numerical simulation is not reported experimentally. This difference can further justify the stiffer response of the numerical simulation compared to the experimental one. Even though the experimental results are not perfectly reproduced with the numerical simulation, it is demonstrated that the numerical

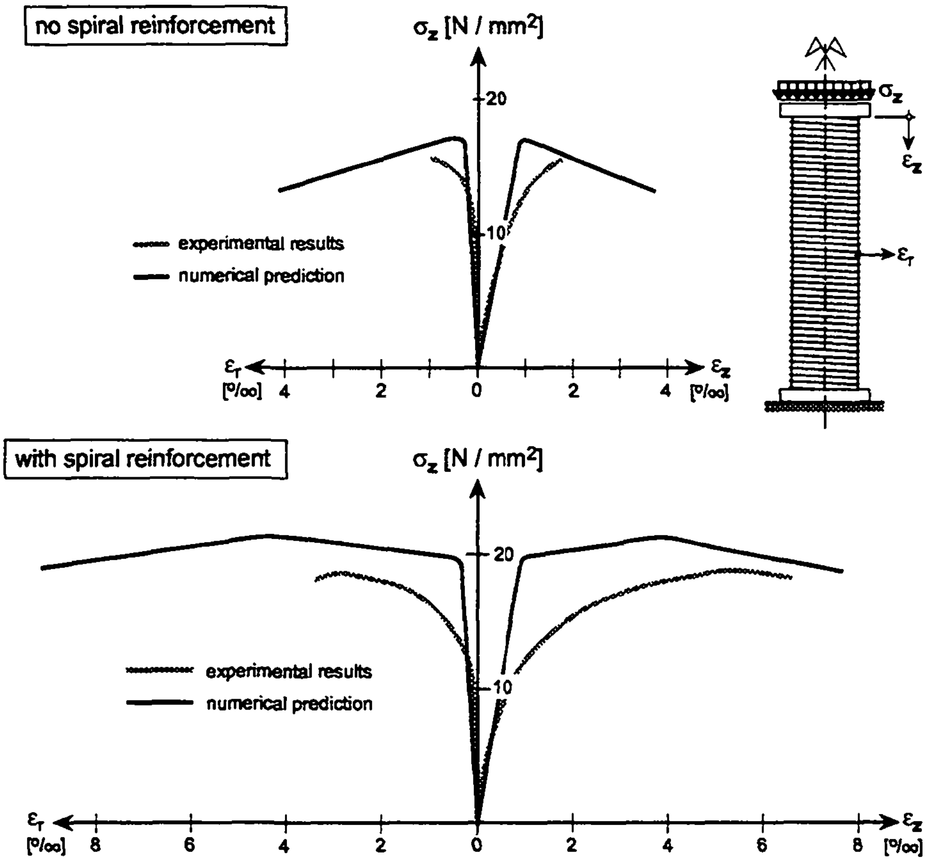

Figure 5.23: Experimental and numerical responses of a specimen under compression with and without spiral reinforcement

model takes into account the effect of confinement generated by the spiral reinforcement on a concrete column submitted to compression.

5.7 Consequences for punching failure simulation

The numerical simulation of these tests allow to establish the following consequences for the simulation of punching failure in reinforced concrete.

1. the flow rule: from the simulation of the footing it is shown that a deviatoric flow rule leads to a sharper failure mechanism. The simulation of the tensile test in plain concrete shows that the flow rule should follow the loading path for uniaxial traction. Therefore, it can be inferred that the developed concrete flow rule in section 3.5.3 is efficient for the concrete simulation. The adjustment of the dilatancy angle is based on the experimental results presented in figure 3.11 leading to $\psi_c = 10^0$.

2. the Newton-Raphson strategy: the investigation of strain localization for the tensile test reveals that the most powerful strategies are the 5 and 6 as described on page 68. Strategy number 6 is more general than number 5 because a number of iterations with the elastic stiffness is required as soon as divergence is observed and not only at the beginning of the load step. Therefore, as localization can occur during a load step this strategy is preferred and will be used in the following simulations.

3. stiffer behavior: by neglecting the hardening behavior at the constitutive level, the numerical prediction is too stiff, especially for high confinement. The perfect bond assumption also results in too stiff behavior.

The capabilities of the numerical model are demonstrated. Consequently, it can be used for the numerical simulation of punching failure in reinforced concrete structures.

Chapter 6

Numerical simulation of punching experiments

6.1 Introductory remarks

In this chapter, punching failure experiments are simulated using the numerical model developed in chapters 3 and 4 and tested in chapter 5. The purpose of these simulations is to examine the capabilities and limitations of the numerical model to reproduce punching failure in reinforced concrete structures.

Three slabs tested by Kinnunen and Nylander [68] are simulated because they cover different types of reinforcement with the same geometry allowing to preserve the finite element mesh. The first slab to be simulated is the slab made of ring reinforcement only. This slab was already analyzed numerically by Andrä [1] (described in chapter 1). The second slab to be analyzed is made of ring and radial reinforcement. This slab was already analyzed by Loseth et al. [78] (described in chapter 1). The last simulation investigates the behavior of slab made of orthogonal reinforcement for which the axially symmetric assumption is not satisfied.

For the following numerical simulations, the boundary conditions are presented only in the un-deformed finite element meshes as the figures obtained with the post-processor do not represent the boundary conditions.

6.2 Simulation of slab with ring reinforcement

6.2.1 Description of the simulation

The circular slab tested by Kinnunen and Nylander [68] and denoted by IB15a is simulated. This slab is considered first because of its perfect axially symmetric geometry as shown in figure 6.1 where only one fourth of the slab is plotted. It has a total diameter of 1840 mm and a thickness of 150 mm. Experimentally, the load is applied to the column (150 mm in diameter) by mean of a hydraulic jack and transferred to the floor by mean of 12 tie rods along a radius of 855 mm. The finite element mesh is developed so that the punching crack is aligned with the mesh without predefining the orientation of this crack. Furthermore, small elements are located at the corner slab-column as shown in figure 6.1. This mesh is composed of 288 quad-axi elements for concrete and 7 ring elements for steel. The load is applied by controlling the vertical displacement to capture an eventual softening response.

In the experiment, the concrete was made with standard Portland cement, water-cement ratio of 0.7, and aggregate from 0.125 mm to 32 mm. The only concrete characteristic which

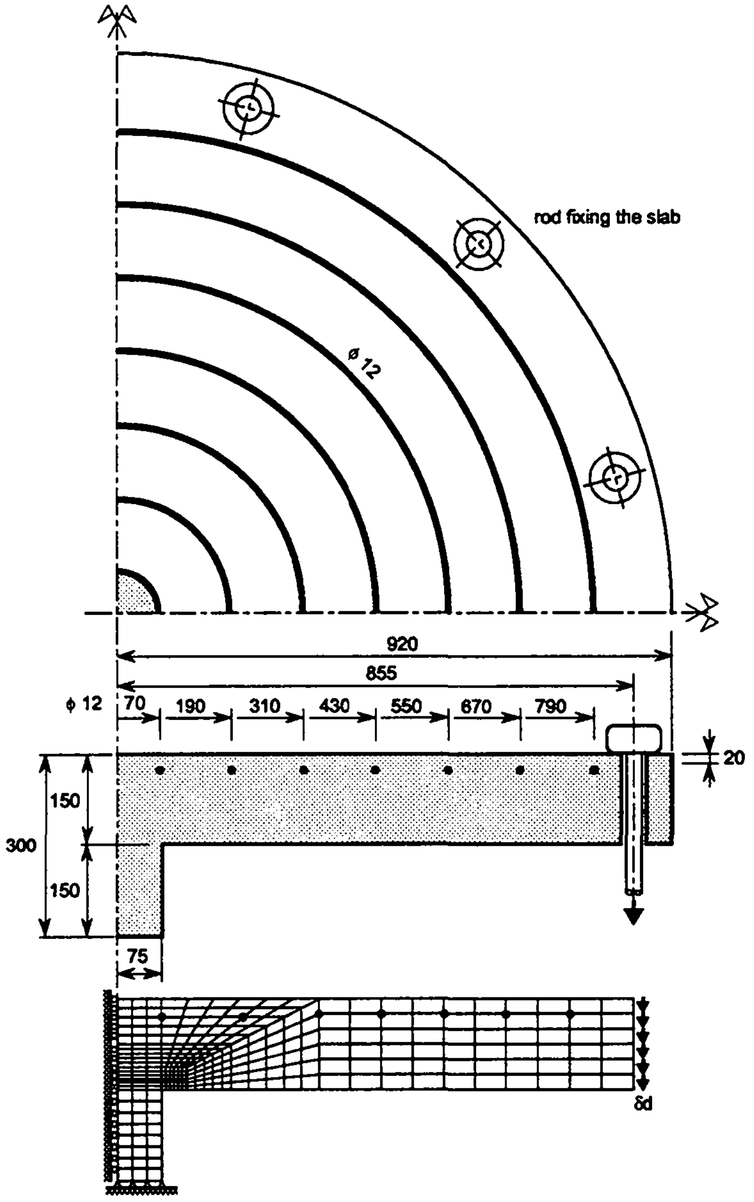

Figure 6.1: Overview, cross-section and mesh of slab with ring reinforcement

is reported is the uniaxial compressive strength on cube which is 324 and 330 kg/cm^2 for the two tested slabs. The mean compressive strength on cube is 33.3 N/mm^2. The compressive strength on cylinder is obtained by dividing the compressive strength on cube with the factor[1] 1.19 leading to f_c=28 N/mm^2.

The tensile attributes of concrete are important as this will be demonstrated in section 7.3.3. Therefore, the determination of these values are not assumed but are determined based on the CEB-FIP code model [25]. The tensile strength is obtained based on the following relation:

$$f_t = 0.33 f_c^{2/3}. \tag{6.1}$$

The resulting tensile strength is f_t=3 N/mm^2. The fracture energy is also determined based on the CEB-FIP code model [25]. It depends on the tensile strength and on the maximum aggregate size which is 32 mm. By linear interpolation the resulting fracture energy is G_f=120 N·m/m^2. Young's modulus is assumed to be E=25000 N/mm^2 and Poisson's ratio is assumed to be $\nu = 0.2$. The dilatancy angle at the ultimate uniaxial compressive strength characterizing the concrete flow rule is assumed to be $\psi_c = 10^0$.

The reinforcement is made of Swedish Kam steel ribbed bars of 12 mm in diameter which are characterized by an area of A=113 mm^2, Young's modulus of E=210000 N/mm^2, and a uniaxial yield strength of f_y=450 N/mm^2. The hardening modulus is assumed to be H=10000 N/mm^2. The positions of the ring elements are approached so that they are located at the nodes of the concrete finite element mesh as illustrated in figure 6.1. The bond between the steel and the concrete is assumed to be perfect.

6.2.2 Slab response

The response of the slab with ring reinforcement is shown in figure 6.2 where the load-displacement curve of the point located at the perimeter of the slab is presented. The experimental response and the one simulated numerically are superimposed for comparison. The experimental load-displacement curve is not given by Kinnunen and Nylander [68] as only the load-curvature curve is provided but it is based on a communication by Kinnunen [67]. From figure 6.2, it can be observed that the predicted punching load (202 kN) is bounded by the experimental failure loads (188 and 208 kN). The upper bound load is computed with the method proposed by Braestrup et al. [13] [14] (presented on page 4). The obtained upper bound load with the assumption that f_t=0, is 457 kN, which can be checked to be larger than the experimental and numerical results. Regarding the shape of the response curves, both are comparable as they both exhibit a linear behavior followed by a gradual development of non-linear response. However, the response predicted numerically is stiffer than the experimental one. At the punching load, the corresponding vertical displacement is 3.6 mm representing 40% of the experimental one. The difference between the experimental displacement and the one predicted numerically are explained mainly by four factors.

1. The experimental setup is assumed to be perfectly stiff.
2. The influence of large deformations is not considered in the model. Frey [43] limits the small rotations to 6^0. The elements along the punching crack are clearly exceeding this limit as shown in figure 6.3.
3. The hardening behavior is not implemented at the constitutive level.

---

[1] The relation between the concrete uniaxial compressive strength on cube and cylinder is given by the CEB-FIP code model [25] in table 2.1.1 for different values of the uniaxial compressive strength.

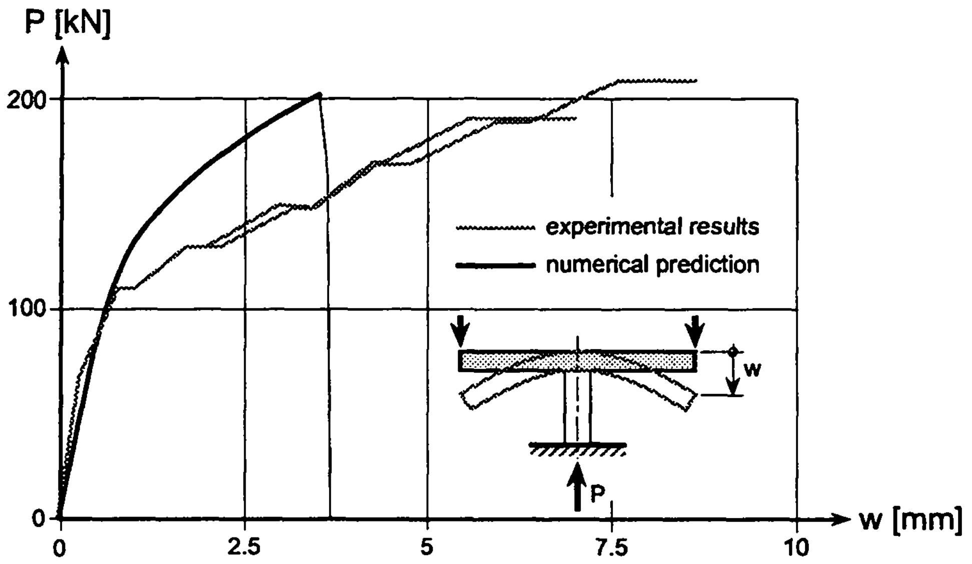

Figure 6.2: Responses of slab with ring reinforcement

4. A perfect bond between concrete and steel is assumed which prevents the slip of the reinforcement.

The numerical simulation is stopped because the denominator used to compute the plastic multiplier and the elastic-plastic constitutive matrix is too small so that the condition expressed in equation 3.99 is not satisfied.

Deformed meshes of the simulated slab are shown in figure 6.3 for three different types of response which correspond to the un-cracked state, the maximum load and after the occurrence of punching failure. The amplification of the deflection is different for the three meshes in order to visualize the deformed shape at the same magnification. At the un-cracked state, the deflection of the slab is characterized by a regular change of curvature along the radius. In the contrary, the deflections at the maximum load are concentrated in the elements located along the circumference of the column. This type of deformation is typical of a flexural cracked state and is due to an opened tangential flexural crack as shown in the following section. The last deformed mesh shown in figure 6.3 exhibits the punching failure mechanism where the deflections are concentrated in an inclined punching crack. These three deformed meshes reproduce the experimental observations characterizing punching failure.

The velocity field at the last load step is shown in figure 6.4. A jump of the velocity field is observed along the punching crack characterizing a strong discontinuity in the sense of the terminology distinguished by Willam et al. [150]. This strong discontinuity reveals a discrete failure process which illustrates that the numerical model can capture localized failure.

6.2.3 Cracking phenomenon

The cracking phenomenon is illustrated in figure 6.5 by exhibiting the radial and tangential cracks at five different load levels (controlled by the vertical displacement). The evolution of the cracking phenomenon is described as follows:

1. w=0.8 mm. A tangential flexural crack, which is initiated for the load step w=0.2 mm is located at the top of the slab just above the perimeter of the column. This crack is due to radial bending moment generated by the vertical force at the perimeter of the slab. At load step w=0.8 mm, radial cracks are observed around the column perimeter.

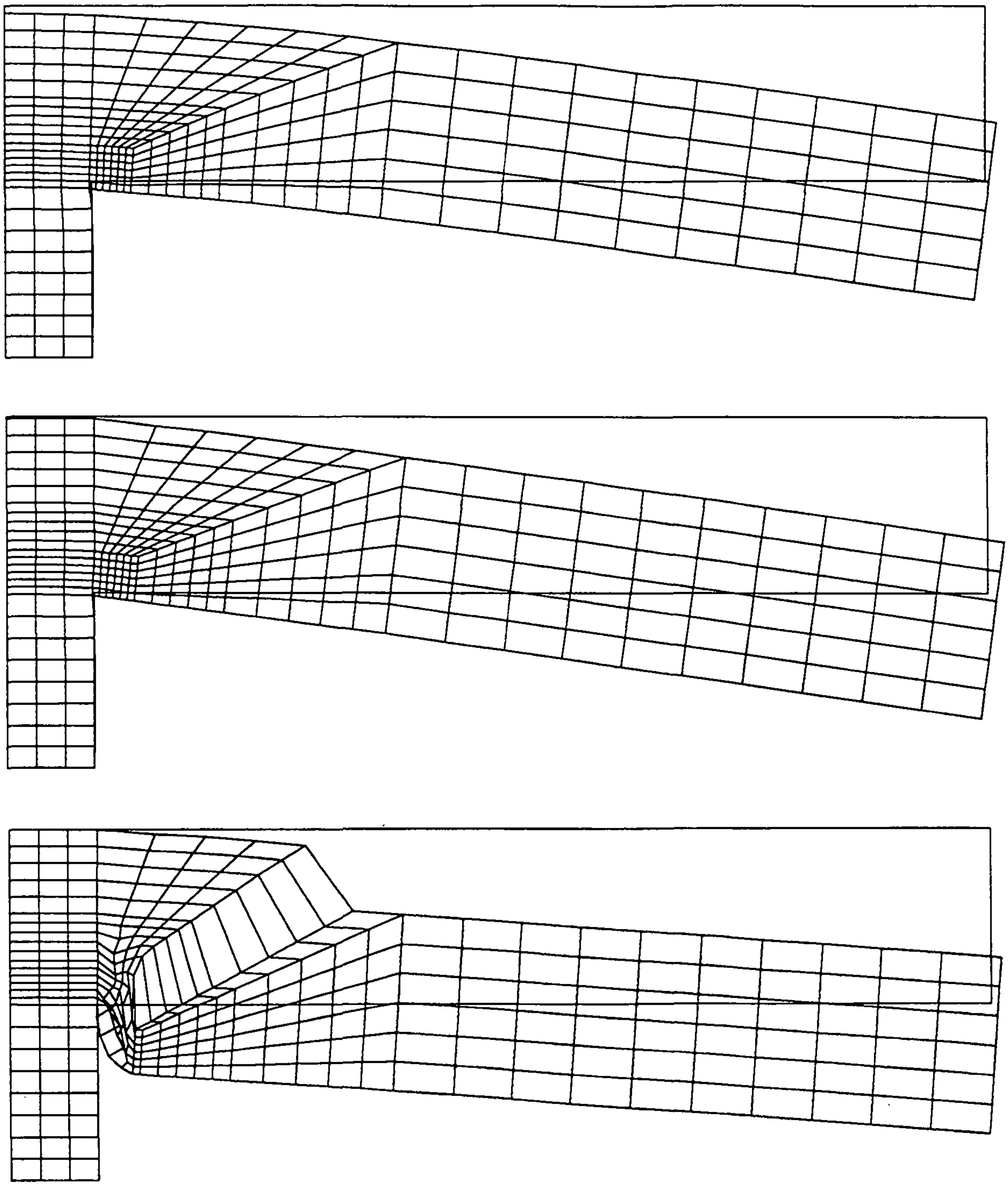

Figure 6.3: Deflections of slab with ring reinforcement: (a) un-cracked state (w=0.1 mm; amplification 1000), (b) maximum load (w=3.55 mm; amplification 30), (c) after punching failure (w=3.7 mm; amplification 30)

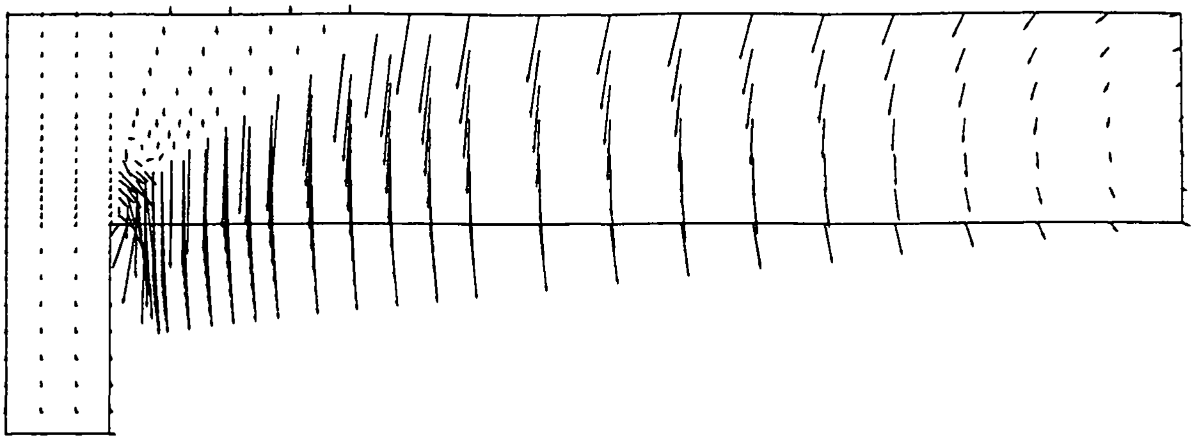

Figure 6.4: Velocity field of slab with ring reinforcement at the last load step

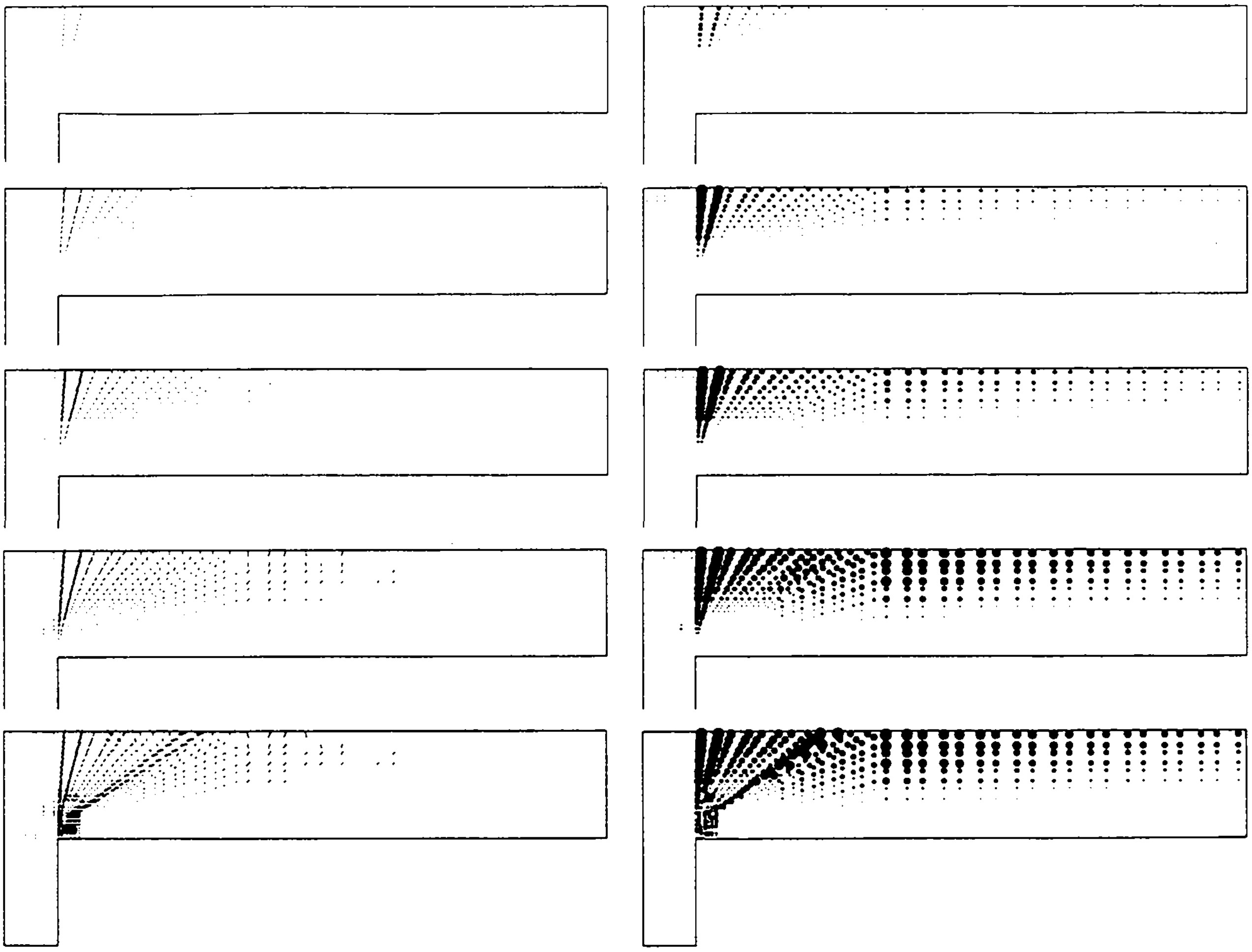

Figure 6.5: Tangential (left) and radial (right) cracks in slab with ring reinforcement for: (1) w=0.8 mm, (2) w=1.5 mm, (3) w=2.1 mm, (4) w=3.55 mm, and (5) w=3.7 mm

2. w=1.5 mm. The first stress-free crack is the tangential flexural crack which appeared just above the perimeter of the column. This crack is located at the exterior of the first ring reinforcement. Radial cracks expand almost up to the perimeter of the slab.

3. w=2.1 mm. The tangential flexural crack is opened through half the slab thickness. Radial cracks reach the perimeter of the slab. The first inclined cracks across the slab thickness arise even though no flexural cracks are reported at the top of the slab.

4. w=3.55 mm. This displacement corresponds to the maximal load. The tangential flexural crack is opened through 3/4 of the slab thickness. Radial cracks expand up to the perimeter of the slab and through half the slab depth. Inclined cracks are observed far from the column.

5. w=3.7 mm. This displacement corresponds to the last load step. The tangential flexural crack is opened through the complete slab thickness. Radial cracks are observed up to the perimeter of the slab and over more than 3/4 of the slab depth. The punching crack is inclined at 54^0 at the corner slab-column and 32^0 at the top of the slab.

The evolution of the cracking predicted by the numerical simulation reproduces the experimental observations as reported in chapter 2.

6.2.4 Observations related to strain and stress

The evolution of the concrete strain at the bottom of the slab at 100 mm from the axis of the column was reported by Kinnunen and Nylander [68]. The radial and tangential concrete strains obtained with the numerical prediction are compared to the experimental results as presented in figure 6.6. It can be observed that the numerical prediction of the evolution of the concrete strains at that particular point is only approaching the experimental results. The tangential strain predicted numerically is lower than the experimental one. The radial strain predicted numerically is larger than the experimental one and the numerical prediction does not reproduce the decreasing of the radial strain for high load level. It has to be noted that this

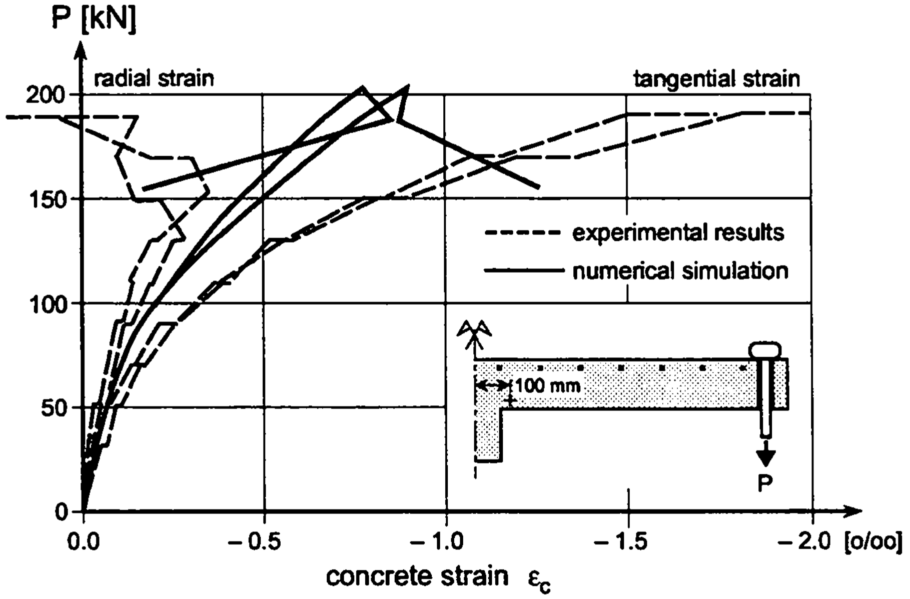

Figure 6.6: Radial and tangential strains in concrete for slab with ring reinforcement

decrease is observed at points which are closer to the corner slab-column. Once the maximum load is reached, the strain evolution follows in a more adequate way the experimental results as the tangential strain increases and the radial strain decreases very rapidly. It seems that the failure predicted numerically is more sudden than the one measured experimentally.

The material stability condition of Hill [51] stated in equation 3.45 is investigated. It is observed that for most of the Gauss points where yielding occur, the stability condition is not satisfied.

The acoustic tensor is analyzed at the corner slab-column. The scaled ratio of the determinant of the acoustic tensor is plotted versus the angle α (normal to the discontinuity) in figure 6.7 for two load steps: before failure and at failure. It is observed that before failure, the determinant of the acoustic tensor is minimal for two values of the inclination: α=80^0 and 152^0. This distribution is comparable to the one observed with the compressive test (figure 5.18). However, at failure, this distribution is characterized by a region 90^0 $\leq \alpha \leq$ 150^0 where the acoustic tensor is minimal. The average value of this region corresponds to α=120^0 which matches the inclination of the punching crack. At failure, the distribution of the acoustic tensor approaches the one observed for the tensile test (figure 5.12). Therefore, this indicates (not a rigorous proof) that the behavior at that particular point of the slab at failure is close to a tensile failure.

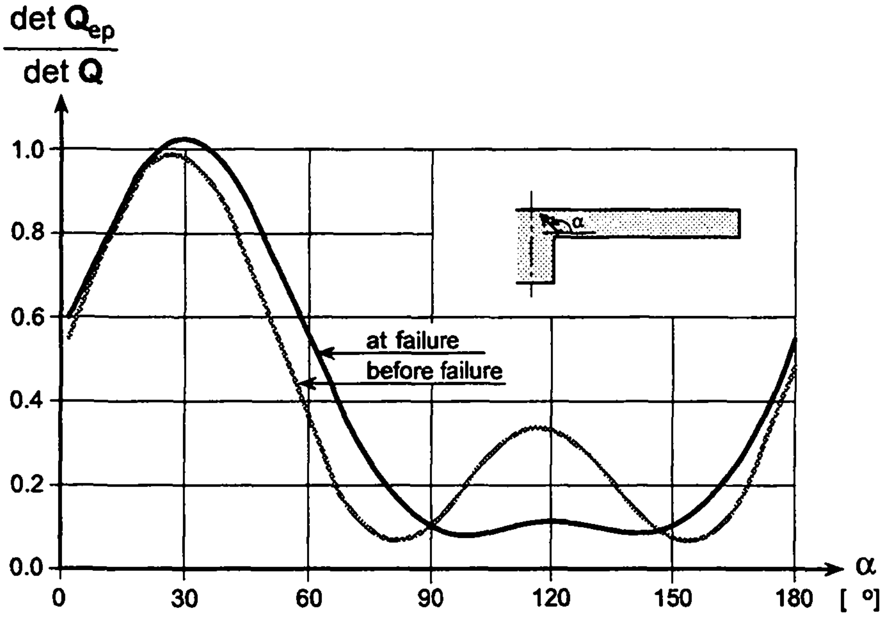

Figure 6.7: Evolution of the acoustic tensor at the corner slab-column for slab with ring reinforcement

The numerical prediction of the strains in the reinforcements are reproduced in figure 6.8 along with the experimental results. The same value of the displacement (w=3.5 mm) is considered which does not correspond to the same load level as the corresponding experimental load is 150 kN and the corresponding numerical load is 201 kN as presented in figure 6.2. It can be observed that the steel strains increase from the circumference of the column up to the punching pattern, where the extreme value of the steel strain is located. From that point the steel strains decrease for increasing radius. The numerical simulation predicts a variation of the steel strain along the radius which is slightly beneath the experimental one. It can be noted that the low value of the steel strain in the first ring reinforcement is due to the fact that this reinforcement is located above the column.

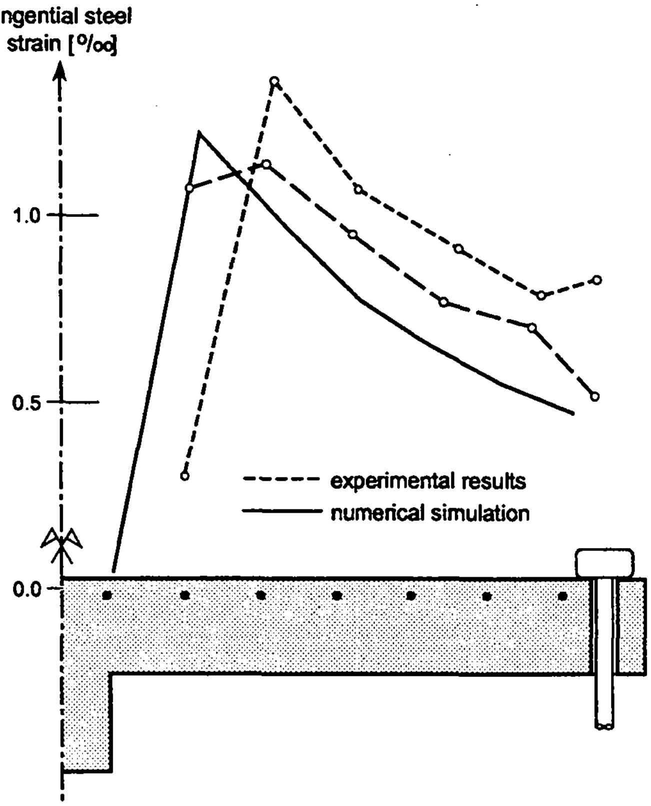

Figure 6.8: Tangential steel strains in slab with ring reinforcement

6.2.5 Influence of damage

The influence of the damage type is presented in figure 6.9 where the response curves of four slabs with different damage types are presented. It can be observed that the damage does not influence the initial response but modifies the response in the neighborhood of the failure load. The punching failure mechanism is observed for the slab with E-damage and shear damage. However, for the simulation without damage and the one with bulk damage, once the peak load is reached, the convergence cannot be obtained and elongated secondary branches are observed. It can be noted that slabs without damage and with bulk damage of concrete behave similarly. Analogous, slabs with shear damage and E-damage lead to comparable results. The relationship between these damage formulations is the zero diagonal terms generated only with the E-damage and shear damage as mentioned on page 60. This illustrates that these zero diagonal terms allow to capture the failure mechanism.

6.2.6 Influence of the mesh density

The punching simulation is performed with a dense mesh (800 quad-axi elements) in order to prove that the presented solution is independent of the mesh density. The response curve of the dense mesh simulation is presented in figure 6.10 along with the previous response curve. It can be observed that both response curves are close to one another and that the punching load is the same for both simulations. The ultimate displacement is the lowest for the dense mesh simulation. This is due to the formation of a more inclined punching crack for the dense mesh as shown in figure 6.11 compared to the one formed for the standard mesh simulation (shown in figure 6.3). The punching crack generated with the standard mesh simulation is located in a one-element band as shown in figure 6.5. For the dense mesh simulation, this band is divided into two bands, and the punching crack appears in the interior band explaining that

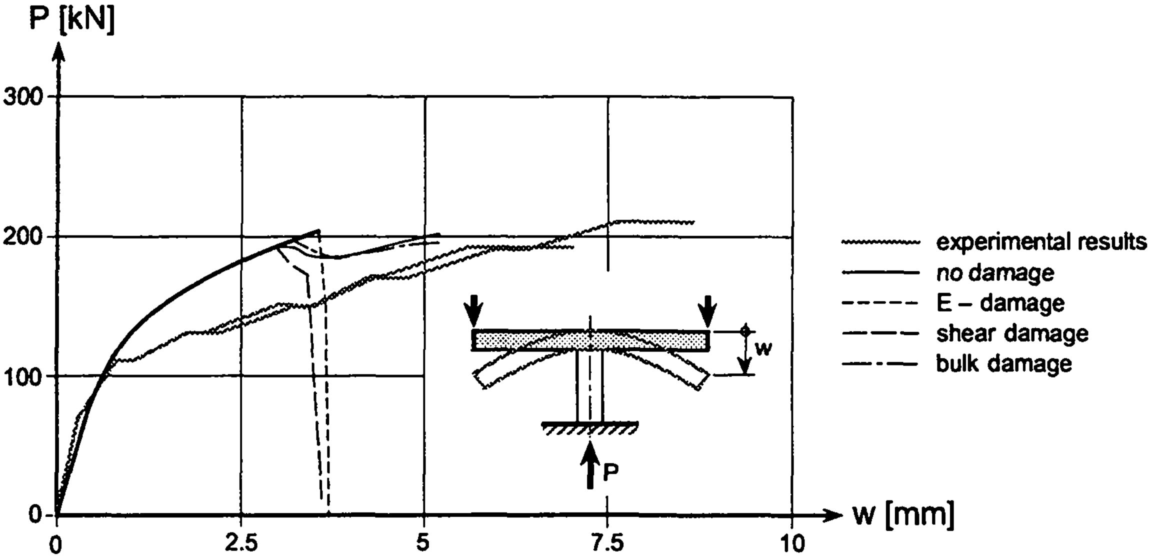

Figure 6.9: Influence of the damage type on the response of slab with ring reinforcement

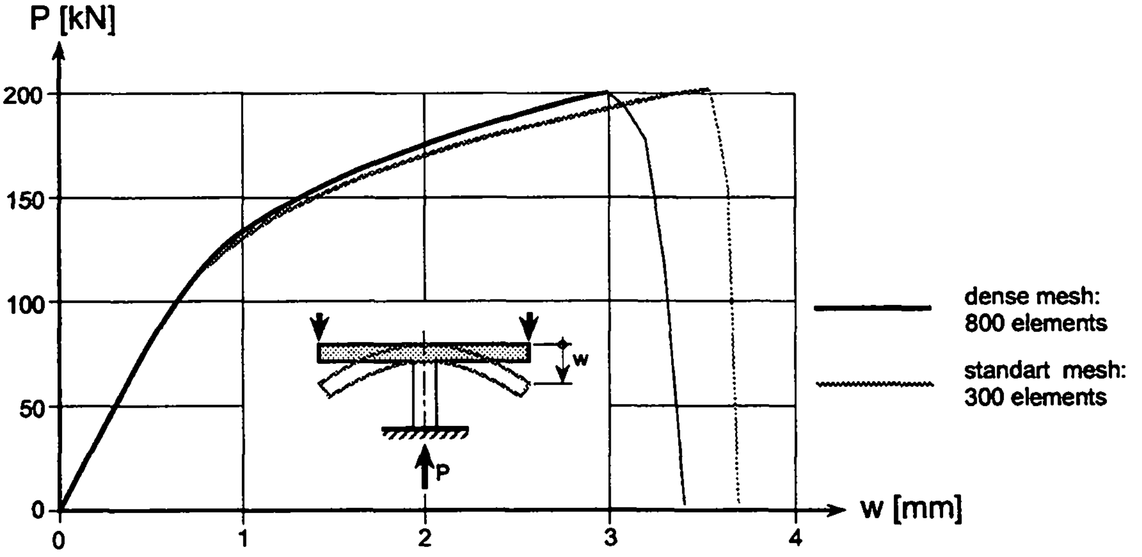

Figure 6.10: Influence of the mesh density on the response of slab with ring reinforcement

the inclination of the punching crack is different for the dense mesh compared to the one of the standard mesh simulation.

This dense mesh simulation presents a clear view of the cracking phenomenon in the vicinity of the column as illustrated in figure 6.11 for the four last load steps. For w=3.1 mm, the first inclined stress-free crack appears inside the slab thickness, just below the reinforcement. Increasing the vertical displacement of only 0.1 mm results in the growth of this inclined crack from the top of the slab to more than half the depth. For increasing displacement this crack grows toward the corner slab-column. At failure, the punching crack has reached the corner slab-column and the slab is separated into two parts. It can be observed that at the corner slab-column, the failure is not localized into only one band of element which is probably due to the mesh orientation. These plots illustrate that the punching crack results from cracks coalescence at the top of the slab. This cracks coalescence are further justified experimentally by the tests of Regan [113] (micro-cracks are formed across the slab thickness before failure occurs) or Moe [95] (formation of inclined cracks across the slab thickness) as described in chapter 2. Cracks coalescence is followed by a crack propagation at the bottom of the slab. Crack propagation phenomenon was suggested by the ACI committee [8]. However, the proposed direction of propagation is the contrary to the one observed here as the punching crack is propagating from the upper part of the slab to the bottom. It can be noted that the opened flexural tangential crack does not grow during the punching process.

At the top of the slab, the steel reinforcement controls the crack opening. The steel spreads the cracks so that many cracks are observed but none of them is a stress-free crack. Under the reinforcement, in the upper part of the slab, small inclined cracks are observed, but as no steel reinforcement is set in this region, some of these cracks can open, and others close, so that the deformation localizes into one inclined shear crack inducing the punching crack. This explains why inclined shear cracks form across the slab thickness. One conclusion of this observation is that a horizontal steel layer in the middle of the slab should increase the punching resistance by delaying the formation of inclined cracks.

The standard mesh simulation takes about ten hours on a Sun Sparc II computer. The dense mesh simulation is about four times longer. Therefore, the standard mesh simulation is preferred for the upcoming simulations.

6.3 Simulation of slab with ring and radial reinforcement

6.3.1 Description of the simulation

The second slab to be simulated is also a circular slab tested by Kinnunen and Nylander [68] but this one is slightly more complex than the previous one as it is composed of ring and radial reinforcements (slab IC15a). The geometry of this slab is shown in figure 6.12 where only one fourth of the slab is plotted. It has similar dimensions and boundary conditions than slab IB15a simulated before. The finite element mesh used for the simulation is shown in figure 6.12 which is composed of 288 quad-axi elements for concrete, 7 ring elements for tangential reinforcement, and 20 truss-axi elements for radial reinforcement.

The radial reinforcement is the only difference (except for the concrete characteristics) compared to the previous slab. For a slab with a constant number of radial bars, the percentage of reinforcement diminishes under increasing radius. But, truss-axi elements are characterized by their thickness as presented in section 4.4.3. Therefore, the thickness of the truss-axi elements must decrease under increasing radius to duplicate the radial reinforcement. This decrease is approximated by a step wise decreasing thickness, that is element by element. The

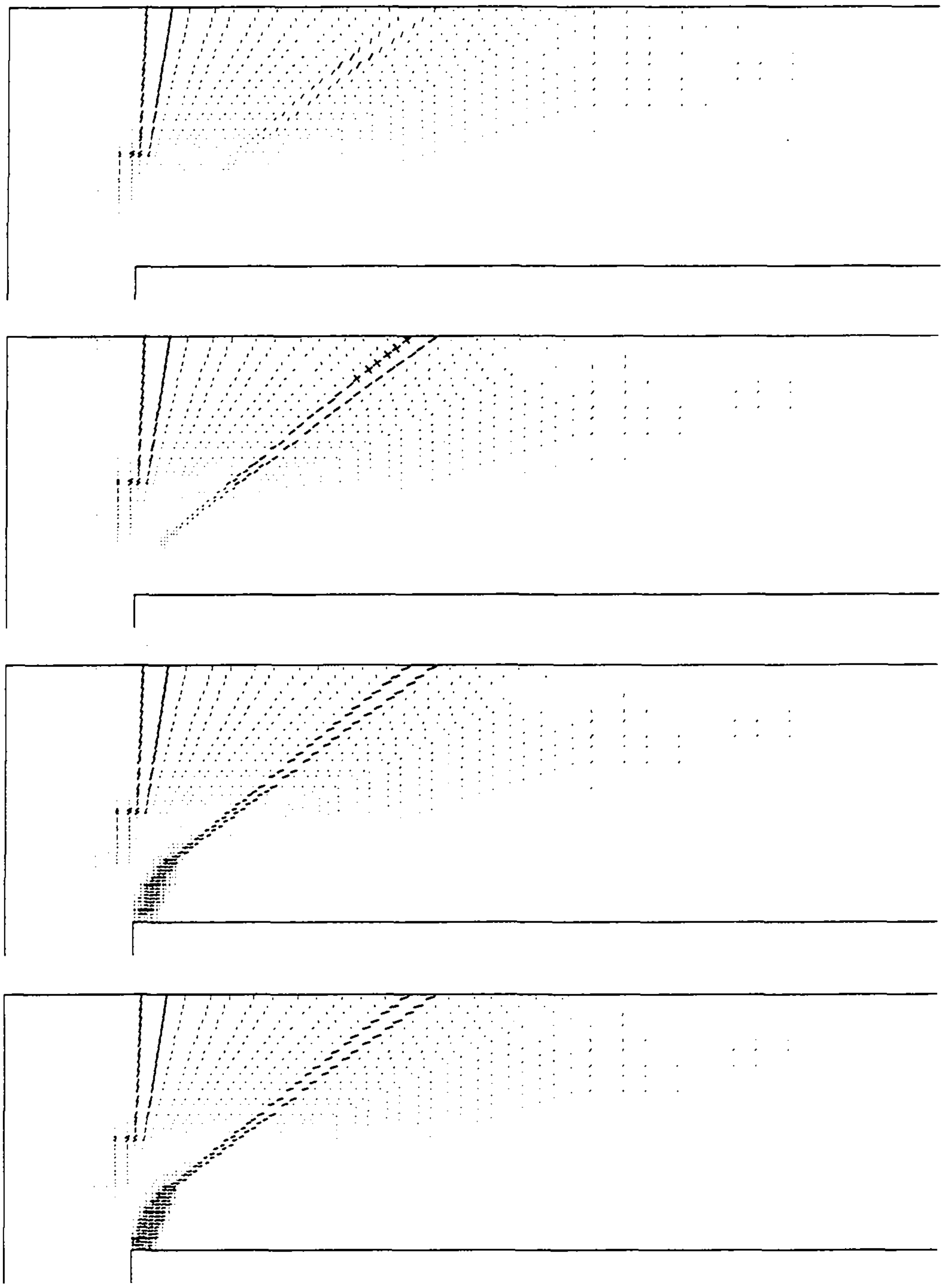

Figure 6.11: Tangential cracks at the four last load steps for slab with ring reinforcement (dense mesh): (1) w=3.1 mm, (2) w=3.2 mm, (3) w=3.3 mm, and (4) w=3.4 mm

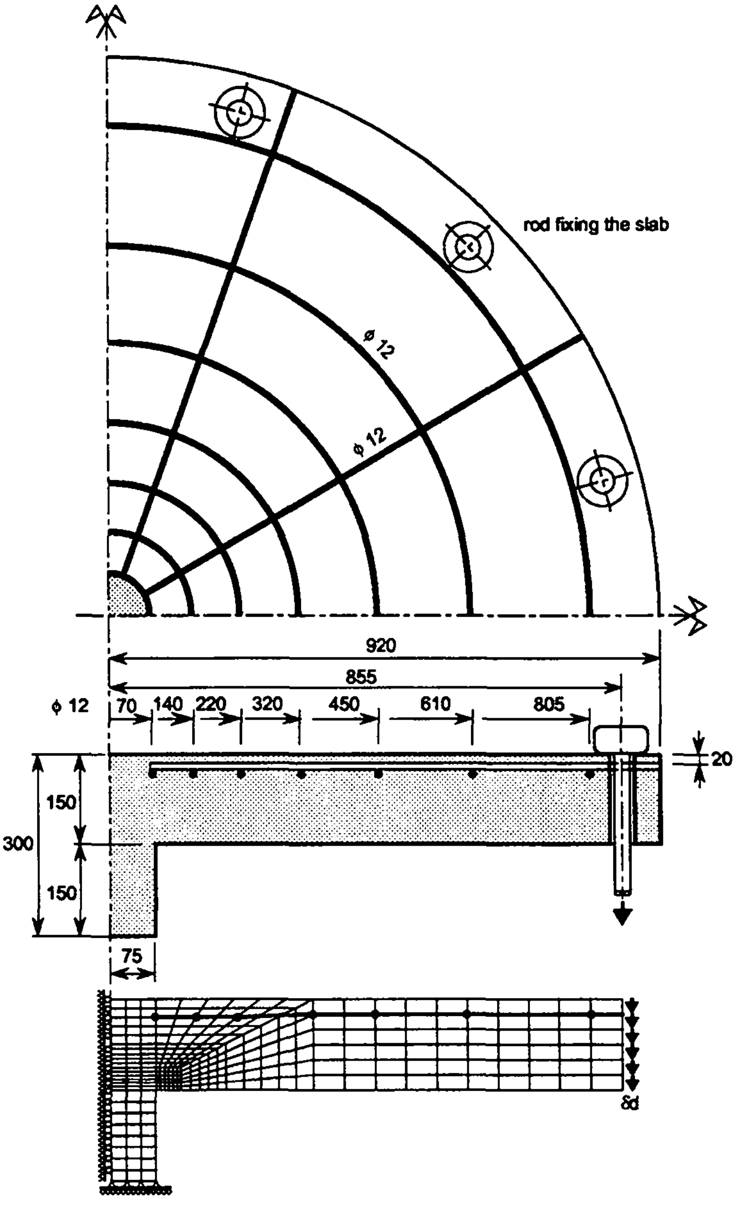

Figure 6.12: Overview, cross-section and mesh for slab with ring and radial reinforcement

positions of the ring elements are approached as shown in figure 6.12. A perfect bond between concrete and steel is assumed.

The concrete compressive strength on cube is 339 kg/cm^2=34.6 N/mm^2, which gives the compressive strength on cylinder of f_c=28.8 N/mm^2. The tensile strength is obtained based on equation 6.1 which gives f_t=3.1 N/mm^2. The fracture energy is assumed to be similar to the one of previous simulation, that is G_f=120 N·m/m^2. Young's modulus, Poisson's ratio, dilatancy angle, and steel characteristics are similar to the one used for slab IB15a.

6.3.2 Problems observed with the simulation

Two numerical simulations of this slab are performed, one with E-damage type of concrete and an other one without damage. The response of both simulations are shown in figure 6.13 where the load-displacement curve of the point located at the perimeter of the slab is presented. Both simulations lead to a comparable response up to the maximum load even though the response with E-damage is always beneath the one without damage. It can be observed that both simulations predict a maximum load which is close to the experimental one (203 kN) as the simulation with E-damage gives a maximum load of 210 kN and the simulation without damage gives a maximum load of 217 kN.

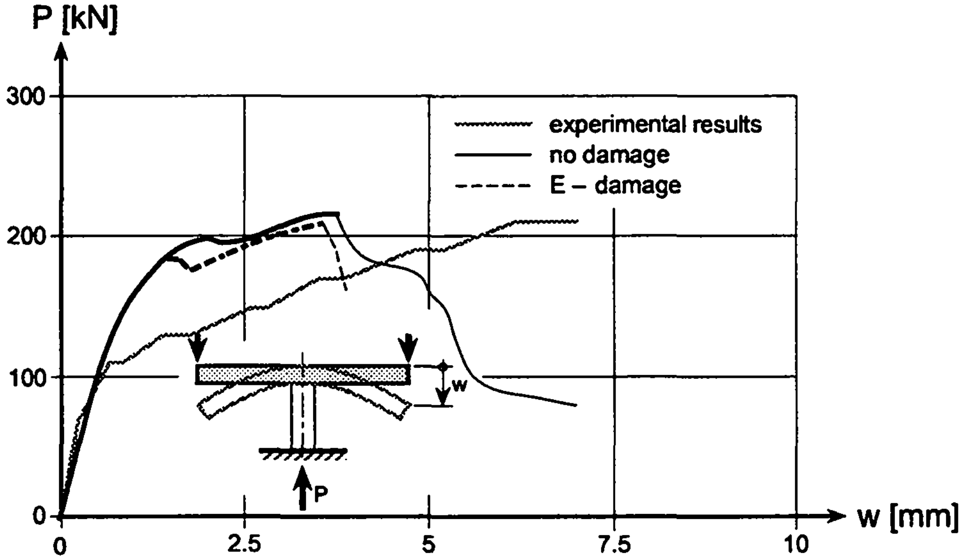

Figure 6.13: Responses of slab with ring and radial reinforcement for a concrete with E-damage and without damage

Once the maximum load is reached, the E-damage simulation predicts a sudden failure. The corresponding failure mechanism is a local mechanism where some nodes located at the upper part of the expected punching crack are moving upwards due to an amalgam of completely damaged elements. As an E-damage formulation is chosen, once an element is completely damaged, the stiffness matrix terms are zero. This implies that when an amalgam of damaged elements is formed, some nodes are not held any more resulting in an unstable structure.

The simulation without damage reveals no failure mechanism. However, after many unconverged load steps, a punching failure mechanism is generated. Based on these two simulations it can be concluded that:

- a simulation with E-damage leads to some local instabilities that circumvent the formation of the punching failure mechanism,

- a simulation without damage does not allow to observe a clear failure mechanism except along a secondary un-converged equilibrium path.

In order to generate the punching failure mechanism a simulation with E-damage in all the concrete elements is performed, except for the ones located in the area where local instabilities were observed. This approach is called partial-damage and is adopted in the following section.

6.3.3 Slab response

Using the partial-damage approach the simulation of the slab with ring and radial reinforcement is performed. The E-damage is implemented for all the elements except for the ones located in the upper part of the slab (superior third of slab thickness) from the axis of symmetry to the middle of the slab. The predicted response is shown in figure 6.14 where the load-displacement curve of the point located at the perimeter of the slab is exhibited. The experimental response and the one simulated numerically are superimposed for comparison. The punching load predicted numerically (214 kN) is close to the experimental failure load (204 kN). The shape of the numerical response curve is characterized by a descending branch which coincides with the appearance of the slightly inclined flexural tangential crack.

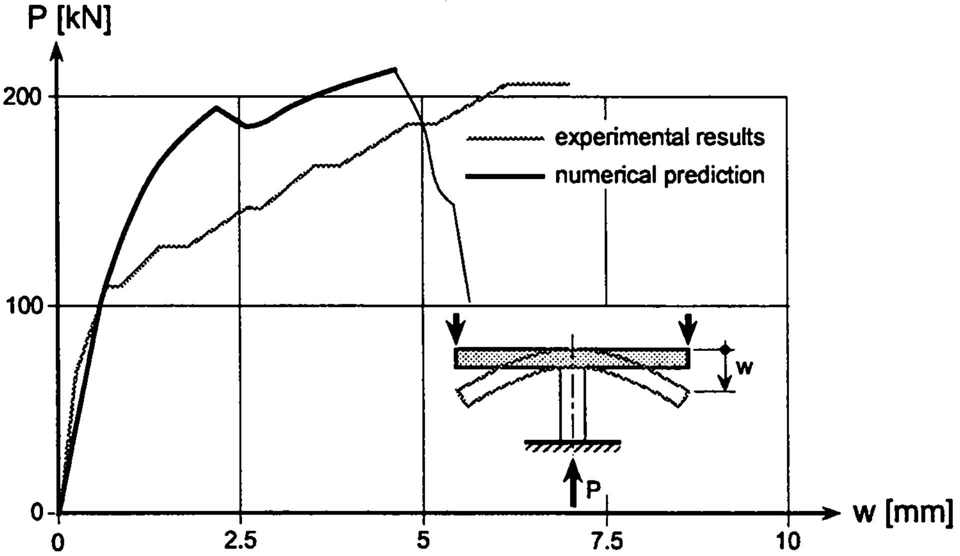

Figure 6.14: Responses of slab with ring and radial reinforcement

It can be observed that the response predicted numerically is stiffer than the experimental one. At the maximum load, the corresponding vertical displacement is 4.6 mm representing around 70% of the experimental one. The prediction of this slab deflection is improved, compared to the computation performed for the slab with ring reinforcement. This is probably due to the fact that the large-deformation effects are reduced due to the presence of the radial reinforcement. The numerical simulation is proceeded several load steps after the maximum load has been reached.

The deformed mesh shown in figure 6.15 exhibits the failure mechanism for w=5.6 mm which corresponds to the punching failure where the deflection is concentrated along two inclined opened bands of elements. One opened band corresponds to the slightly inclined tangential flexural crack. The second inclined band corresponds to the punching crack. This band is less inclined than the one observed in slab with ring reinforcement as shown in figure

6.3. The failure mechanism is also less visible than the one predicted for slab with only ring reinforcement.

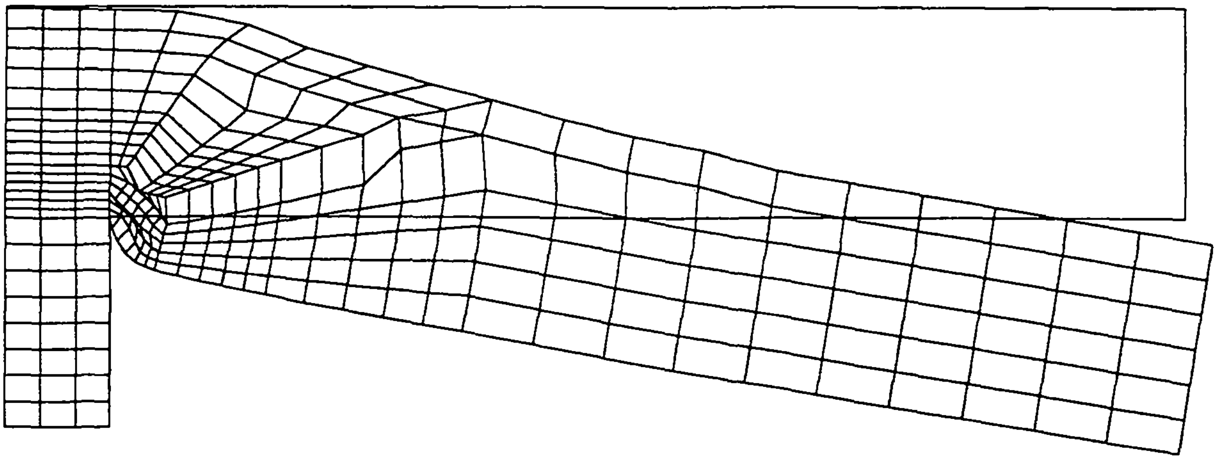

Figure 6.15: Deflections of slab with ring and radial reinforcement after punching failure

6.3.4 Cracking phenomenon

The cracking phenomenon is illustrated in figure 6.16 by exhibiting the radial and tangential cracks at five different load levels (controlled by the vertical displacement). The evolution of the cracking phenomenon is described as follows:

1. w=1.2 mm. The first stress-free crack is a tangential flexural crack which appears just above the perimeter of the column inside the slab without reaching the top of the slab. This crack is not vertical which is probably due to the high value of flexural reinforcement at the extremity of the column as ρ=1.73%. When this tangential flexural crack forms, the response curve exhibits a discontinuity which is not observed when the flexural crack is vertical as in slab with ring reinforcement. Inclined cracks across the slab thickness are observed. Radial cracks expand up to the perimeter of the slab.

2. w=1.3 mm. The flexural tangential crack expands toward the corner slab-column and does not reach the top of the slab. A horizontal stress-free crack forms under the radial reinforcement.

3. w=4.6 mm. This displacement corresponds to the maximal load. The tangential flexural crack is opened through 3/4 of the slab thickness but does not reach the top of the slab. The horizontal crack expands up to one third of the span and the extremity of this crack transforms into an inclined crack. Radial cracks expand up to the perimeter of the slab and through half the slab depth. Inclined cracks are observed far from the column.

4. w=5 mm. The depth of the stress-free tangential flexural crack is not modified. Inclined cracks are observed far from the column. The horizontal crack expands up to more than half the span of the slab.

5. w=5.6 mm. This displacement corresponds to the last load step. The tangential flexural crack is opened from the top to 3/4 of the slab depth. The tangential flexural crack and the punching crack are linked by a horizontal crack. Radial cracks are observed up to the perimeter of the slab and over more than 3/4 of the slab depth. The punching crack is inclined at 43^0 at the corner slab-column and 25^0 at the top of the slab.

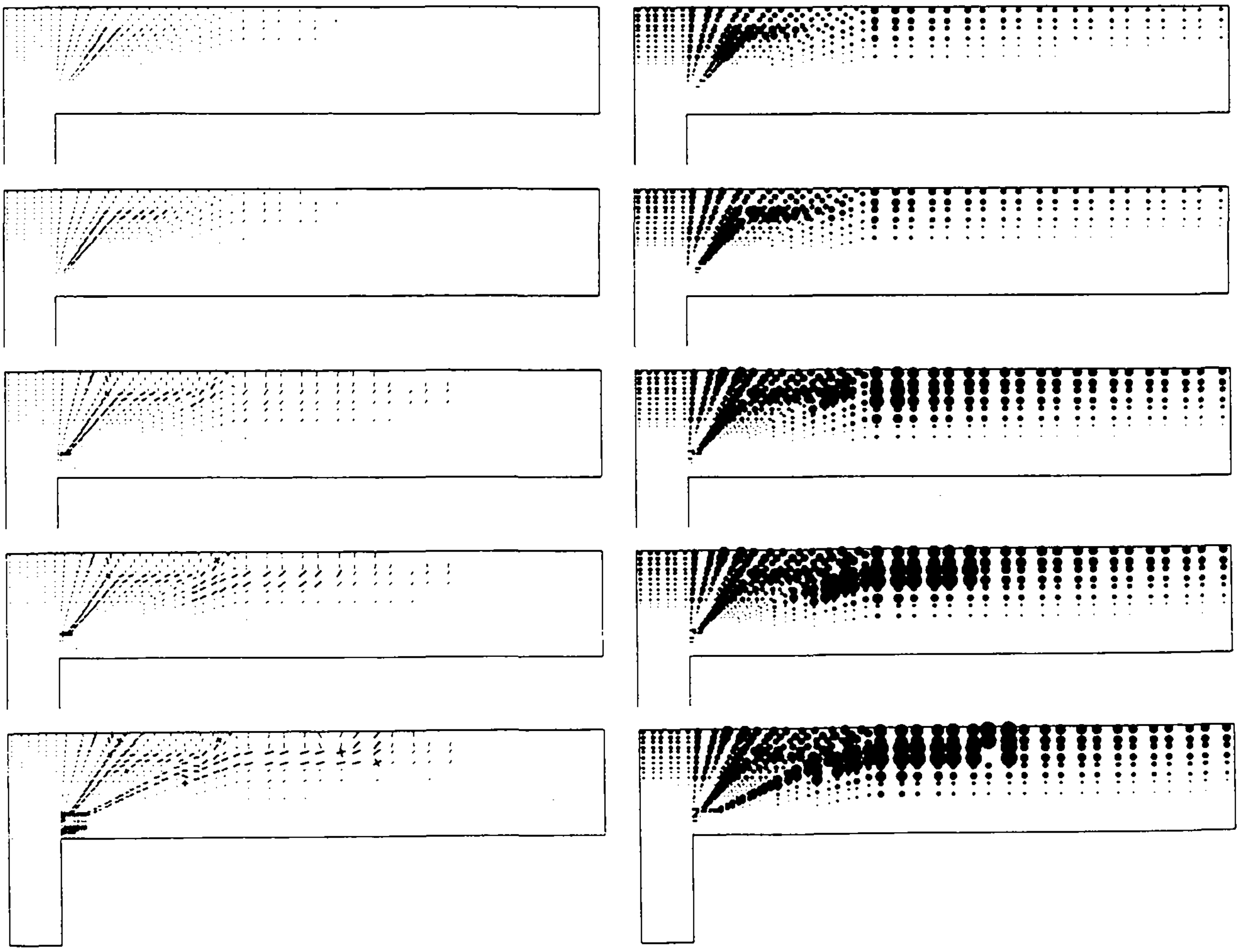

Figure 6.16: Tangential (left) and radial (right) cracks in slab with ring and radial reinforcement for: (1) w=1.2 mm, (2) w=1.3 mm, (3) w=4.6 mm, (4) w=5 mm, and (5) w=5.6 mm

The horizontal crack observed during this simulation, located under the radial reinforcement is due to the stress transfer from steel to concrete. This stress transfer is important due to the perfect bond assumption. Experimentally, horizontal cracks are also observed between the reinforcement layers as shown in figure 2.11.

6.4 Simulation of slab with orthogonal reinforcement

6.4.1 Description of the simulation

The third slab to be simulated is also a circular slab tested by Kinnunen and Nylander [68] but this time it is composed of orthogonal reinforcement (slab IA15a) which leads to a more complex simulation than the previous ones as the axisymmetric hypothesis is not verified.

The geometry of the slab is shown in figure 6.17 where only one fourth of the slab is plotted. It has similar dimensions and boundary conditions than slabs IB15a and IC15a. The finite element mesh used for the simulation is shown in figure 6.17. It is composed of 288 quad-axi elements for concrete, 7 ring elements for tangential reinforcement, and a variable number of truss-axi elements for radial reinforcement depending on the performed simulation.

The type of reinforcement is the only difference (except for the concrete characteristics) compared to the previous slabs. The percentage of orthogonal reinforcement is $\rho = 0.8\%$. For the axisymmetric numerical simulation only ring and truss-axi elements are available. The transformation of orthogonal reinforcement to ring and truss-axi elements is performed in assuming that the orthogonal reinforcement is equivalent to a thin plate of constant thickness. The equivalent thickness of this thin plate is computed based on the value of the percentage of reinforcement defined as the ratio of the steel and the concrete area

$$\rho = \frac{A_s}{A_c} = \frac{2\pi r t}{2\pi r d} = \frac{t}{d}. \tag{6.2}$$

The thickness of the equivalent thin steel plate is $t = \rho\, d = 0.8 \cdot 125 = 1$ mm. This equivalent thin steel plate is then replaced by ring and truss-axi elements. The ring elements have the same spacing than the one of the orthogonal reinforcement and an area which is function of this spacing s in the form: $A_s = t\ s$. The truss-axi elements are characterized by their thickness as presented in section 4.4.3 which is equal to the thickness of the equivalent thin steel plate. It should be noted that the method used to replace the orthogonal reinforcement by ring and truss-axi elements is correct only from the strength point of view. From the deformation point of view, this transformation leads to too stiff response. This phenomenon was illustrated in figure 2.6 as the deflection at failure for slab with axisymmetric reinforcement is lower than the one for slab with orthogonal reinforcement.

The positions of the ring elements are approached so that they are located at the nodes of the concrete finite element mesh as shown in figure 6.17. The two orthogonal reinforcement layers are assumed at the same depth.

The concrete compressive strength on cube is 335 kg/cm^2 and 328 kg/cm^2 leading to a mean value of 33.7 N/mm^2. The resulting compressive strength on cylinder is f_c=28.1 N/mm^2. The tensile strength is obtained based on equation 6.1 which gives f_t=3 N/mm^2. The fracture energy is assumed to be similar to the one of the previous simulation that is G_f=120 N·m/m^2. Young's modulus, Poisson's ratio, dilatancy angle, and steel characteristics are similar to the ones used for slabs IB15a and IC15a.

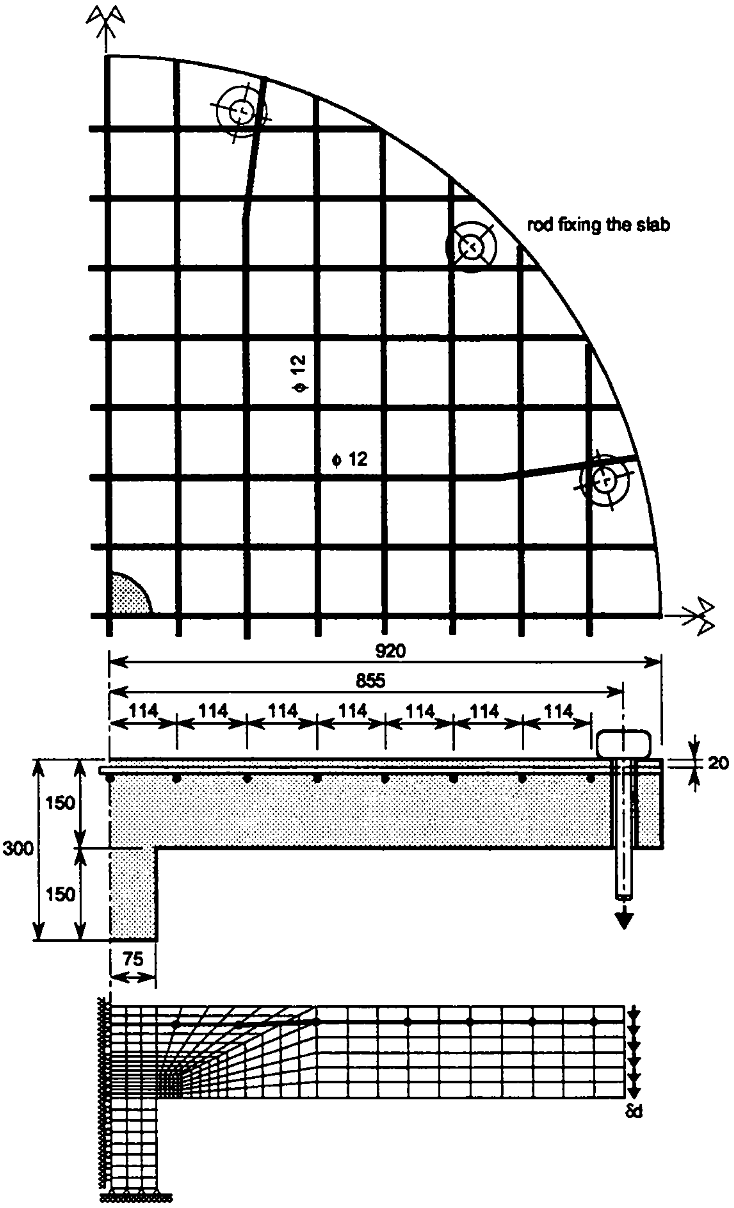

Figure 6.17: Overview, cross-section and mesh for slab with orthogonal reinforcement

6.4.2 Relaxing the perfect bond condition

Two numerical simulations of this slab are performed: one with E-damage and one without damage. Similar problems than the ones observed for the simulation of slab with ring and radial reinforcement were encountered. These problems result from the perfect bond assumption between concrete and steel. The perfect bond is responsible for the horizontal crack observed in the previous simulation (also observed for the simulation of the slab with orthogonal reinforcement) which is due to the high shear transfer between steel and concrete. Furthermore, a perfect bond simulation does not allow the cracks to open. For a perfect bond simulation, the steel reinforcement diffuses the forces along many cracked elements. The consequence of this restrain is that no localization of the deformation can be generated.

Consequently, the perfect bond condition between concrete and steel is relaxed. One way of reducing the perfect bond condition is by using bond elements between steel and concrete as originally proposed by Ngo and Scordelis [99] and reviewed by Groot et al. [49]. This method is not used here because of the complexity and the developments which are still in progress.

Another method which requires no transformation of the numerical model is developed here. The proposed method to relax the perfect bond between concrete and steel is to fasten rigidly the steel to the concrete only at the extremity of a fictitious fastening length l_F. This fictitious fastening length must allow a crack to grow. Consequently, this length is lower than the crack spacing of uniaxial traction. More rigorously, this length corresponds to twice the *transmission length*=l_T which is defined by Favre et al. [41] as the length over which slip between steel and concrete occurs. The empirical relation between the mean crack spacing and the transmission length is $l_T = 3/4\ s_{r,m}$. The fastening length should be larger than the finite element size. Consequently, this fastening length should be chosen as follows:

$$h^e < l_F < 2l_T = 1.5 s_{r,m}. \tag{6.3}$$

It should be mentioned that the fastening length is considered as a material characteristic. In order to determine the fastening length which should be applied for this slab simulation, the average final crack spacing is computed[2] as described by the Eurocode 2 [40] leading to $s_{r,m}$=110 mm. The fastening length must satisfy $l_F \leq 165$ mm.

6.4.3 Slab response

The numerical simulation of the slab with orthogonal reinforcement shown in figure 6.17 is performed by assuming a fastening length of around 75 mm. The fastening length is approximated due to the irregular finite element mesh. The response of this slab is shown in figure 6.18 where the load-displacement curve of the point located at the perimeter of the slab is exhibited. The experimental response and the one simulated numerically are superimposed for comparison. It can be observed that the response predicted numerically is stiffer than the experimental one. At the maximum load, the numerical vertical displacement is 3.3 mm representing around 30% of the experimental one. The stiffer prediction is already observed for low load level, which was not the case for the previous simulations as shown in figure 6.2 and 6.14. This justifies the affirmation that the too stiff prediction is due to the axisymmetric

---

[2] The Eurocode 2 [40] gives the following relation for the crack spacing:

$$s_{r,m} = 50 + 0.25 k_1 k_2 \frac{\phi}{\rho_r}$$

where $s_{r,m}$ is the average final crack spacing, $k_1 = 0.8$ for high bond steel, and $k_2 = 0.5$ for bending, ϕ is the bar diameter and $\rho_r = h/3$ is the effective reinforcement ratio.

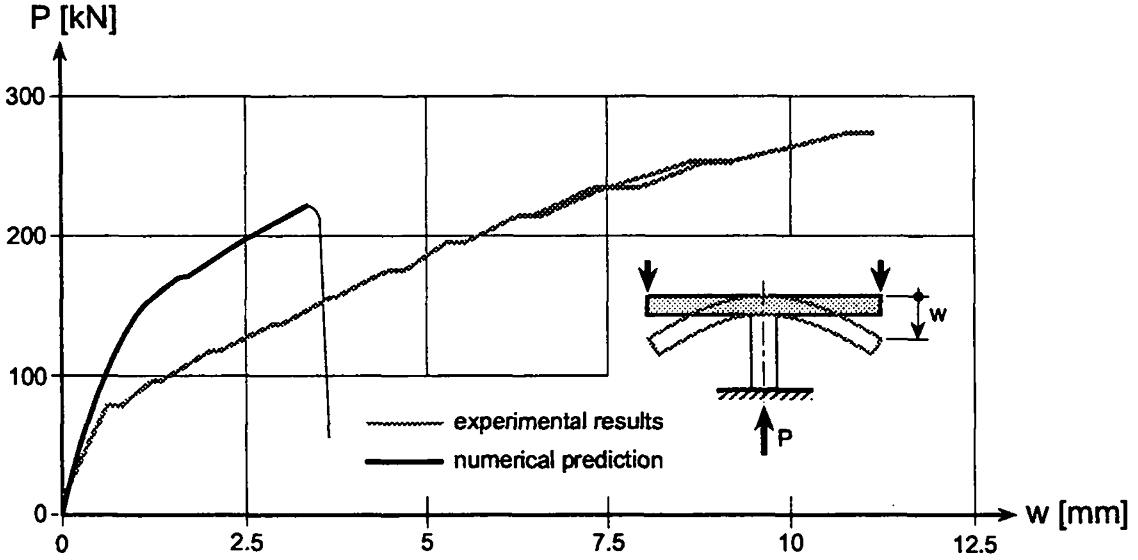

Figure 6.18: Responses of slab with orthogonal reinforcement

transformation of the orthogonal reinforcement. Axisymmetric reinforcement are stiffer than orthogonal reinforcement as already shown in figure 2.6 based on experimental results.

It can be observed that the punching load obtained numerically (222 kN) is lower than the experimental failure loads (255 kN and 274 kN) as it represents 84% of the mean experimental failure load. The higher value of the experimental failure load compared to the predicted one is due to the dowel action which is not considered in the numerical simulation. This dowel action is more important for orthogonal reinforcement than for axisymmetric reinforcement. The numerical simulation is stopped because the denominator used to compute the plastic multiplier is too small so that the condition expressed in equation 3.99 is not satisfied.

The deformed mesh shown in figure 6.19 exhibits the punching failure mechanism where the deflection is concentrated along two inclined opened bands of elements. One opened band corresponds to the tangential flexural crack. The second band corresponds to the punching crack. It can be observed that the radial reinforcement is not fixed at every nodes, allowing the flexural and the punching cracks to open.

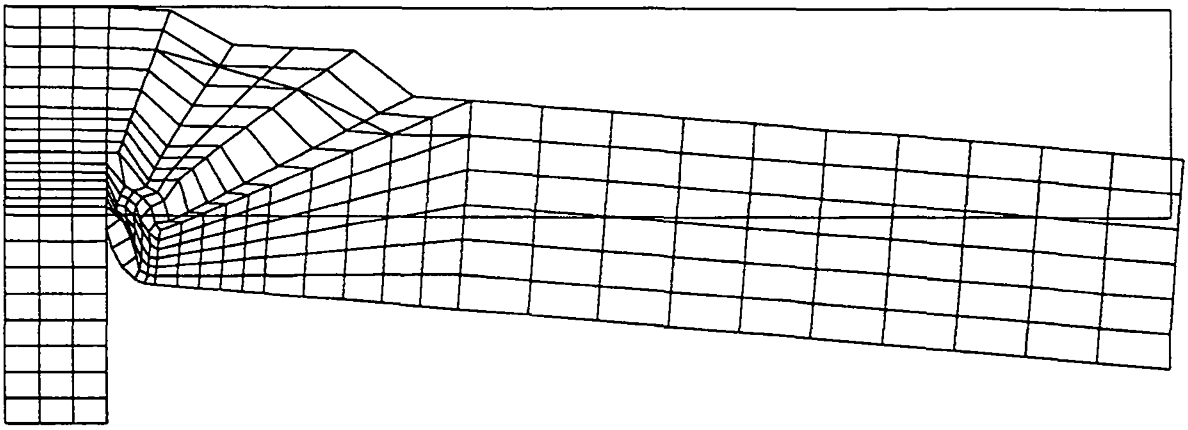

Figure 6.19: Deflections of slab with orthogonal reinforcement after punching failure

6.4.4 Cracking phenomenon

The cracking phenomenon is illustrated in figure 6.20 by exhibiting the radial and tangential cracks at five different load levels. The formation of inclined cracks is illustrated with the four ultimate crack patterns. The evolution of the cracking phenomenon is described as follows:

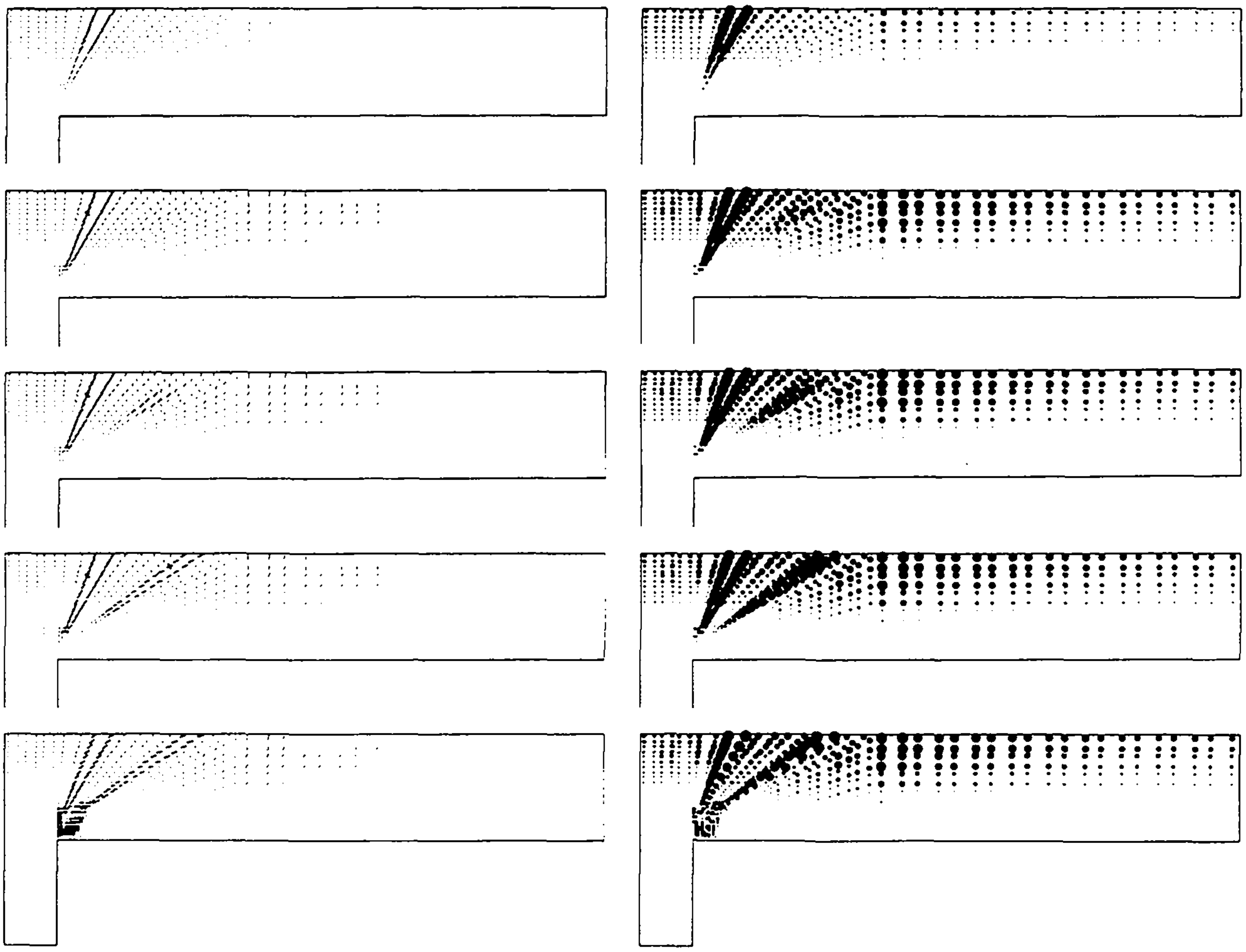

Figure 6.20: Tangential (left) and radial (right) cracks in slab with orthogonal reinforcement for: (1) w=1.8 mm, (2) w=3.3 mm, (3) w=3.4 mm, (4) w=3.5 mm, and (5) w=3.6 mm

1. w=1.8 mm. The first stress-free crack is a tangential flexural crack which appears just above the perimeter of the column. This crack is not vertical due to the position of the first ring reinforcement located at the exterior of the column perimeter. When this tangential flexural crack forms, the response exhibits a discontinuity as already observed for slab IC15a. Inclined cracks across the slab thickness are observed. Radial cracks expand up to the perimeter of the slab.

2. w=3.3 mm. This displacement corresponds to the maximal load. The tangential flexural crack is opened through more than 3/4 of the slab thickness. Radial cracks expand up to the perimeter of the slab and through half the slab depth. Inclined cracks are observed far from the column.

3. w=3.4 mm. An inclined stress-free crack appears across the slab thickness which illustrates the formation of the inclined shear crack across the slab thickness.
4. w=3.5 mm. The inclined stress-free crack growths in both directions reaching the top and the middle of the slab.
5. w=3.6 mm. This displacement corresponds to the last load step. The tangential flexural crack is opened through the complete slab thickness. Radial cracks are observed up to the perimeter of the slab and over more than 1/2 of the slab depth. The punching crack is inclined at 54^0 at the corner slab-column and 34^0 at the top of the slab.

The evolution of the cracking predicted by the numerical simulation reproduces the experimental results as described in chapter 2.

Chapter 7

Analysis of punching failure

7.1 Introductory remarks

The computational simulation tool developed in the previous chapters was demonstrated to be capable of simulating punching failure in reinforced concrete structures. Therefore, it is used to analyze the punching failure mechanism. The improvements which were made in the previous section concerning the treatment of bond between concrete and steel are considered.

The analysis of punching failure is performed on a—*reference slab*—which is similar to the one tested by Kinnunen and Nylander [68] denoted by IA15a and presented in section 6.4. The geometry of the slab is shown in figure 6.17 as well as the finite element mesh. The steel reinforcement is modeled as described in section 6.4.2 on page 122. The reference concrete characteristics are E=25000 N/mm^2, ν=0.2, f_c=28.1 N/mm^2, f_t=3 N/mm^2, G_f=120 N·mm/mm^2, and ψ_c=10^0. The reference steel characteristics are E=210000 N/mm^2, A=113 mm^2, f_y=450 N/mm^2, and H=10000 N/mm^2. The fastening length is l_F=75 mm.

The analysis of punching failure is initiated with the investigation of the requirement for a punching failure to be generated. Following, a parametric study is performed and the influence of the concrete characteristics, the steel reinforcement, and the geometry are examined.

7.2 Requirement for punching failure

7.2.1 Preliminaries

The purpose of this section is to determine the requirement for punching failure to occur. In table 2.1, the condition for punching failure to happen was expressed as: $P_{punch}/P_{flex} < 1$. This means that punching failure occurs if the flexural strength is high enough to satisfy this condition.

The requirement for punching failure is determined in simulating a plain concrete slab to have a flexural failure and a slab with ring reinforcement only inside the punching cone. Then, the determined condition is checked with an experimental test on micro-slabs.

7.2.2 Simulation of plain concrete slab

A plain concrete slab was very seldom tested in laboratory, certainly because of the difficulties to handle the tremendous influence of defects in the concrete material. This slab is simulated as described in section 7.1 and the response of the slab is shown in figure 7.1 where the load-displacement curve of the point located at the extremity of the slab is presented. The response curve exhibits a linear branch up to a vertical displacement of 0.25 mm which corresponds to

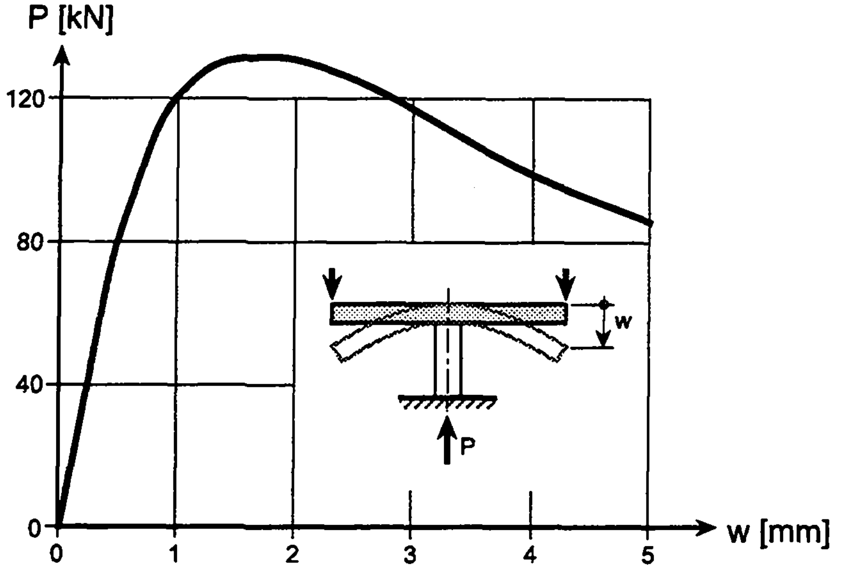

Figure 7.1: Response of plain concrete slab

the cracking load: P_{crack}=44 kN. The response is followed by a hardening regime up to the peak load which is observed at a vertical displacement of 1.5 mm corresponding to the ultimate flexural load: P_{flex}=132 kN. The peak point is followed by a stable softening branch which can be reproduced as the simulation is performed under displacement control.

The elastic vertical deflection of the slab obtained numerically is compared to the value given by the thin plate theory presented in appendix B.1. An exact matching between the two values is observed. The cracking load P_{crack}, which corresponds to the maximum load without any crack is computed analytically by disregarding the thin plate bending theory as described in appendix B.1. The cracking load computed with equation B.9 is 43.7 kN which is very close to the numerical prediction of 44 kN.

The evolution of the cracking phenomenon is described as follows:

1. The first crack is a tangential crack which appears at the top of the slab just above the perimeter of the column. This crack opens under increasing displacement to reach a stress-free crack during the descending branch of the response. The depth of this flexural crack increases with increasing displacement.

2. Radial cracks appear after the first tangential crack has been reported. For increasing load, they spread out toward the extremity of the slab. At the peak load, radial cracks reach the extremity of the slab.

This cracking phenomenon is similar to the one reported in the early stage of loading of slabs failing by punching. This illustrates that the punching failure is preceded by a flexural response phase as suggested in the phase decomposition presented in section 2.3.2 on page 21.

7.2.3 Simulation of slab with ring reinforcement only inside the punching cone

A slab similar to the plain concrete one, except for two ring reinforcements located only inside the punching cone is simulated. This slab is a modified version of slab IB15a (tested by Kinnunen and Nylander and already analyzed in section 6.2 and shown in figure 6.1) so that only the first two ring reinforcements are set. The slab characteristics are given in section 7.1.

The response of this simulation is presented in figure 7.2 where the load-displacement curve of the point located at the extremity of the slab is reported. It can be observed that the response is characterized by a linear branch, followed by a hardening regime. The hardening regime is characterized by an elongated branch where the maximum load of 136 kN is reached. A short softening branch is then observed which precedes the failure. The failure occurs suddenly as shown by the vertical branch of the response. The vertical branch is followed by a secondary converged branch which is doubtful as it succeeds to several un-converged equilibrium path. The consequence of the apparition of this secondary branch is that a clear separation of the slab cannot be obtained as was the case with the previous punching failure simulations.

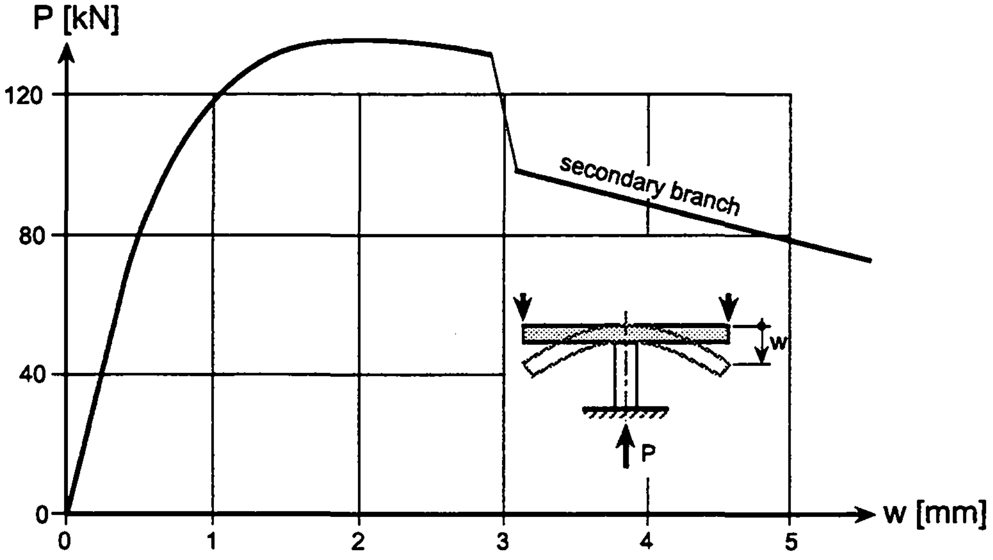

Figure 7.2: Response of slab with ring reinforcement only inside the punching cone

The adjunction of the two ring reinforcements in the plain concrete slab modifies slightly the value of the failure load (132 kN for the plain concrete slab and 136 kN for the slab with ring reinforcement only inside the punching cone). However, the type of failure between these two slabs is completely different, as for the plain concrete slab, a flexural failure is observed and for the slab with ring reinforcement inside the punching cone, a punching failure is generated. Therefore, the condition for punching failure to happen is determined which is: the punching failure occurs if flexural reinforcement is placed inside the punching cone, allowing the formation of this cone and preventing a flexural failure.

7.2.4 Experimental investigation

The requirement for punching failure is examined by testing two small slabs which are termed micro-slabs. These micro-slabs are scaled version (ratio 1/5) of the reference slab described in section 7.1. The purpose of this experimental investigation is to have an illustration of the requirement for punching failure.

The setup of these slabs is illustrated in figure 7.3. Both of these slabs are made of micro-concrete and both slabs are made of a wire netting of ϕ=0.5 mm, s=5 mm at the bottom and ϕ=0.5 mm, s=15 mm at the top of the slab. These wire netting were set to keep the different parts of the slab together after failure has occurred. The only difference between these two slabs is the reinforcement inside the punching cone as only one slab is made with two ring reinforcements inside the punching cone.

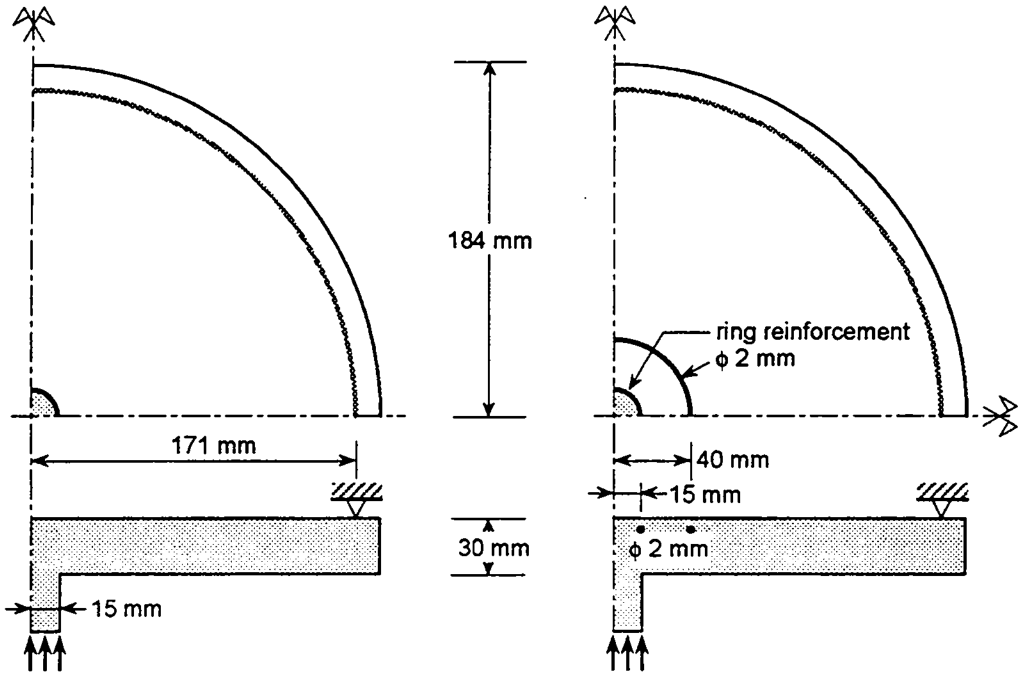

Figure 7.3: Test setup of the two micro-slabs

The experimental test is performed under displacement control. The failure load is 35 kN for slab without ring reinforcement and 38 kN for slab with ring reinforcement. The crack pattern at the top of the slab after failure is shown in figure 7.4. It can be observed that slab without ring reinforcement fails by formation of radial cracks, as shown on the left of figure 7.4, similarly to the yield-line pattern presented in figure B.3(a). However, slab with ring reinforcement, as shown at the right of figure 7.4, fails by punching. The top of the punching cone inclined at 45^0 can be distinguished.

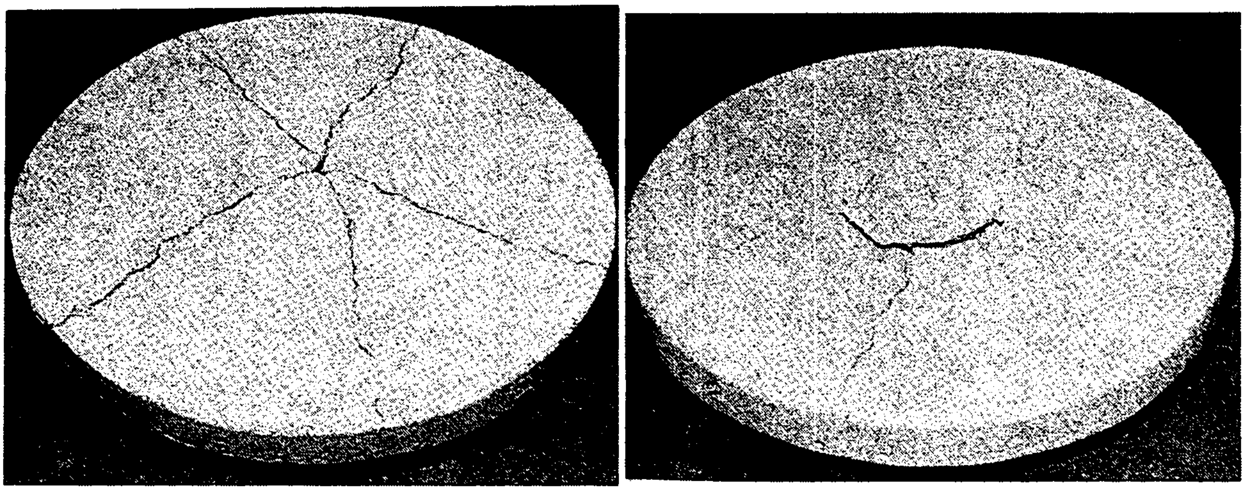

Figure 7.4: Overview of the top of the micro-slabs after failure: (left) slab without ring reinforcement; (right) slab with two ring reinforcements

This experimental investigation illustrates that the requirement for punching failure to occur is that flexural reinforcement is placed inside the punching cone, allowing the formation of this cone and preventing a flexural failure.

7.3 Influence of concrete characteristics

7.3.1 Preliminaries

The advantage of numerical simulations compared to experimental tests is that the concrete parameters can be modified independently in order to determine their influence. As an example, it is difficult to prepare in the laboratory a concrete with a constant compressive strength and a variable tensile strength. However, this can very well be captured with the numerical simulation. Even though it is unrealistic to modify the tensile strength without modifying the compressive one the consequences are important as the values of the uniaxial compressive and tensile strength are used independently.

This study of the influence of the concrete characteristics will allow to determine the sensitivity of each parameter characterizing concrete behavior in relation to punching failure. The slab presented in section 7.1 is used as reference slab.

7.3.2 Influence of elastic constants

Influence of Young's modulus

The influence of concrete Young's modulus is investigated with the simulation of three slabs with different Young's modulus (E=20000, 25000, 30000 N/mm^2). A similar punching failure mechanisms is observed for the three slabs. The response curves are presented in figure 7.5 where an affinity is observed between the three simulations. The punching load is very little influenced, as only a slight increase of the punching load is observed (218, 222, and 225 kN) with increasing value of Young's modulus.

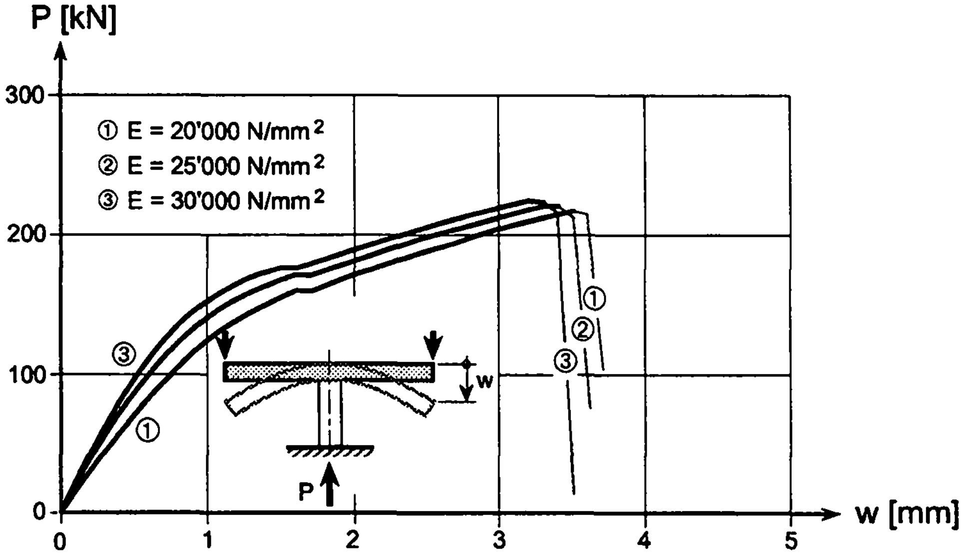

Figure 7.5: Influence of concrete Young's modulus on the response

Influence of Poisson's ratio

The influence of concrete Poisson's ratio is investigated with the simulation of three slabs with different Poisson's ratio (ν=0, 0.2, and 0.4). The value of ν=0.5 is not considered as this value is contrary to nature if the plastic flow rule is not deviatoric (the plastic deformation can be incompressible as already mentioned in section 5.2.3 and if this is the case, then the incompressibility of the elastic deformation is conceivable). For these three slab simulations, a similar punching failure mechanism is generated. The response curves are given in figure 7.6. It can be observed that Poisson's ratio slightly influences the response, as the ultimate value of the vertical displacement decreases with increasing value of Poisson's ratio. The failure load is little modified (229, 222, and 214 kN) for reducing value of Poisson's ratio.

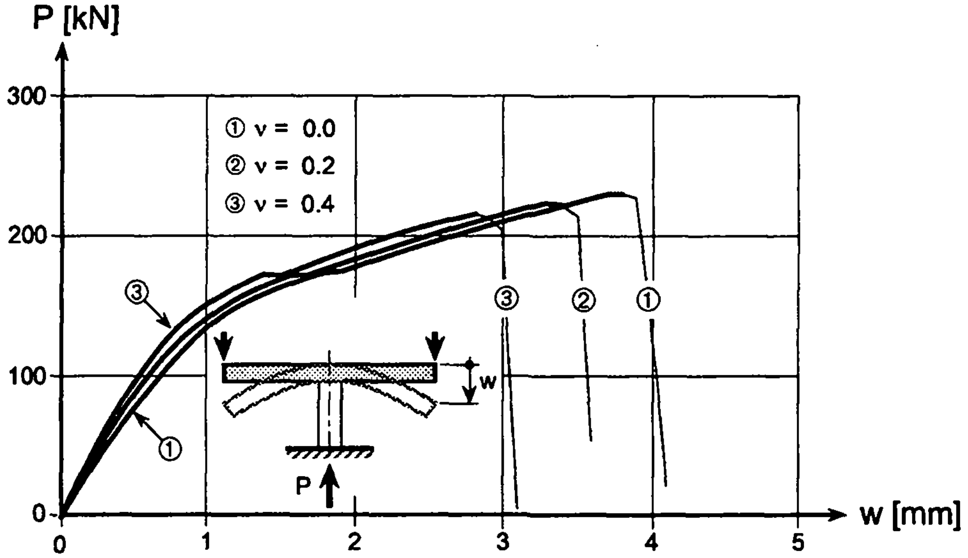

Figure 7.6: Influence of concrete Poisson's ratio on the response

7.3.3 Influence of the tensile attributes

Influence of the uniaxial tensile strength

The influence of the concrete uniaxial tensile strength is investigated in analyzing three slabs with different tensile strengths (f_t=2.1, 3, and 3.9 N/mm^2). A similar punching failure mechanism is observed for the three slabs. However, the response curves are influenced by the uniaxial tensile strength as shown in figure 7.7. After a similar elastic behavior, the response of the slabs during the flexural phase are different. A stiffer response is observed for the slab with a high value of tensile strength. The load at which the first stress-free tangential flexural crack appears (illustrated by a discontinuity of the response curves) increases with increasing value of the tensile strength. Once the tangential flexural crack has formed, the slope of the response is similar for all slabs. However, the failure occurs first for the slab with the lowest tensile strength. Consequently, the punching load and the ultimate displacement are influenced by the uniaxial tensile strength.

The influence of the uniaxial tensile strength on the punching load is clearly demonstrated. Therefore, it can be interesting to fit this influence with an analytical expression. The considered matching functions are power functions as they intersect the origin and are simple mathematical expressions. An illustration of this fitting is presented in figure 7.8. It can be observed that the best matching is obtained for[1]:

$$P_{punch} \propto f_t^{2/3}. \tag{7.1}$$

Using the relationship between the uniaxial tensile and compressive strength given by the

---

[1] The proportionality is indicated with the sign $\propto$.

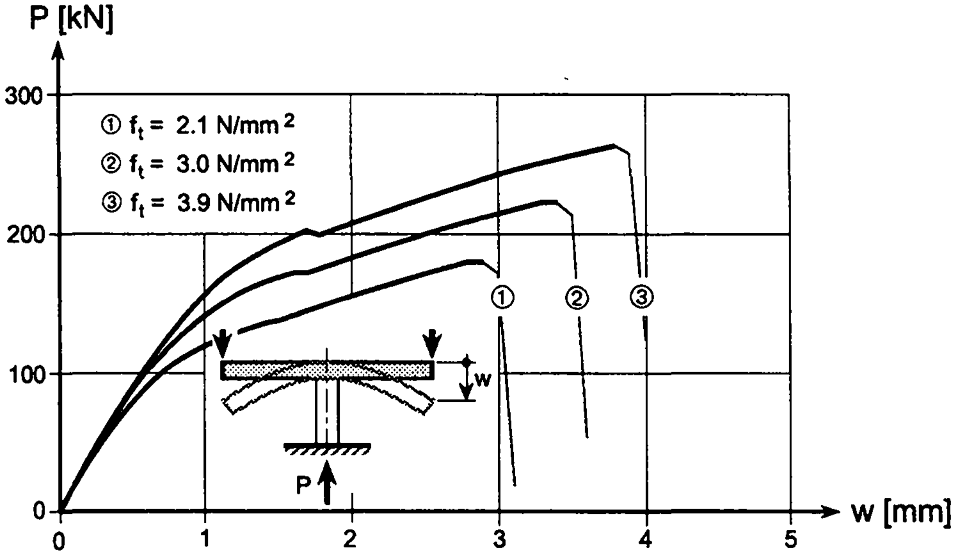

Figure 7.7: Influence of concrete uniaxial tensile strength on the response

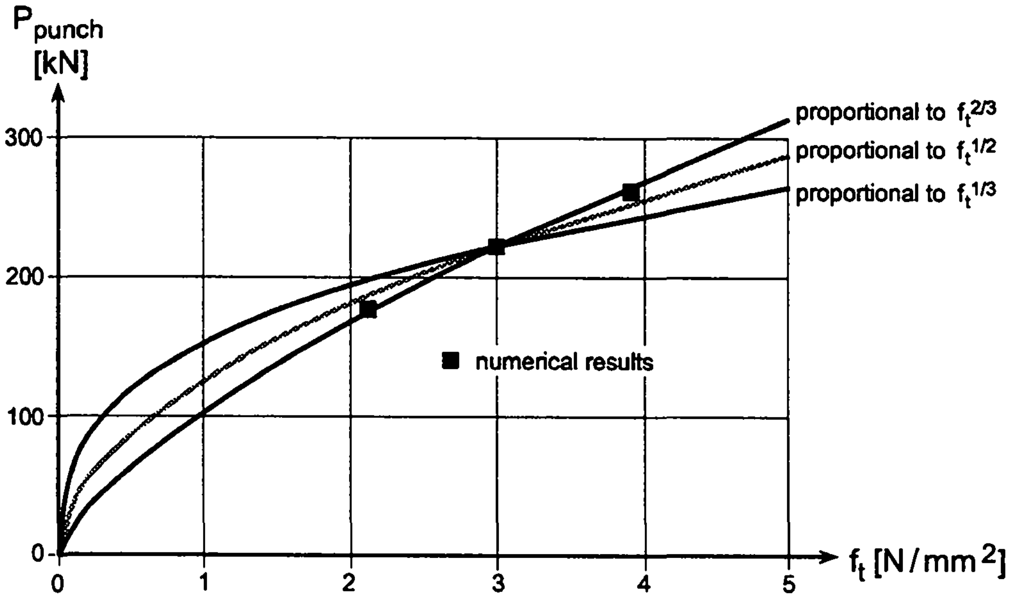

Figure 7.8: Relation between the concrete uniaxial tensile strength and the punching load

CEB-FIP code model [25]: $f_t \propto f_c^{2/3}$, this matching can be rewritten: $P_{punch} \propto f_c^{4/9}$. This expression is close to the experimental one reported by Regan [112]: $P_{punch} \propto f_c^{1/3}$.

The influence of the tensile stresses transmitted across the punching crack was demonstrated experimentally by Azad et al. [4]. An embedded flaw in the form of a conical insert at different angles was introduced in a slab. It is shown that for an inclination of this flaw of 30^0 (which corresponds to the inclination of the punching crack) the load carrying capacity is reduced by approximately one half. It can be concluded that the introduction of this artificial notches reduces the area where the tensile stresses develop.

Moe [95] mentioned that the punching failure is very often of a splitting type, and it is comparable to the type of failure observed in specimens under traction. Based on this observation, he expressed the fictitious shear strength in terms of a power function of the uniaxial compressive strength which matches the uniaxial tensile strength.

Influence of the fracture energy

The influence of the concrete fracture energy is investigated in analyzing three slabs with different values of the fracture energy (G_f=84, 120, and 156 N·m/m^2). A similar punching failure mechanism is observed for the three slabs. The corresponding response curves are shown in figure 7.9. It can be observed that the fracture energy does not influence the stiffness of the response but it influences the ductility as the maximum displacement is increased with increasing fracture energy. Furthermore, for increasing fracture energy, the punching load is increased (192, 222 to 249 kN).

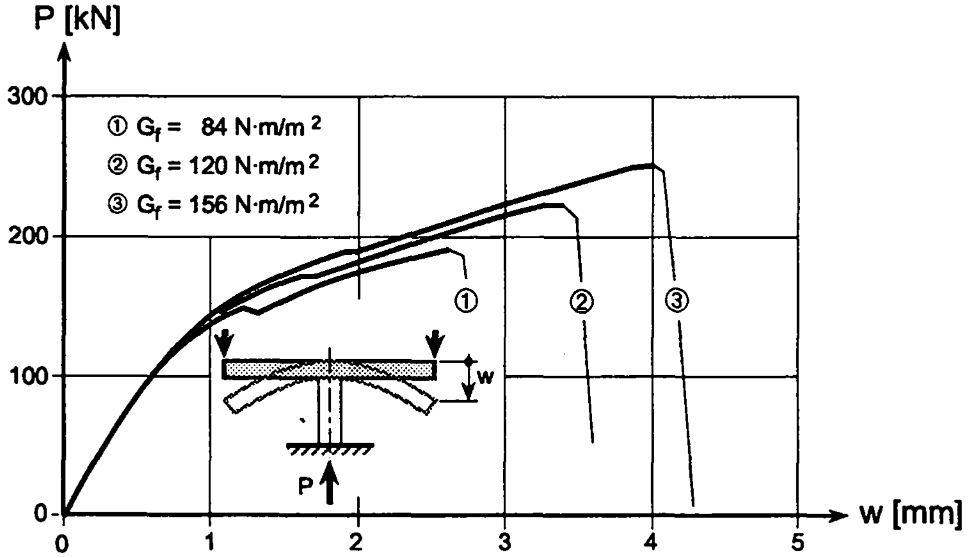

Figure 7.9: Influence of the concrete fracture energy on the response

7.3.4 Concrete parameters with little influence

Surprisingly, it is observed that the uniaxial concrete compressive strength does not influence the punching failure. This is shown by analyzing three slabs with different values of the uniaxial compressive strength: f_c=22.5, 28.1, and 33.7 N/mm^2. It is observed that for these three slabs, the same failure mechanism is generated and the responses are similar. Therefore, the uniaxial compressive strength does not influence the punching failure. This remark has to be related to the fact that the uniaxial compressive strength is proportional to the uniaxial tensile strength.

So, it can be concluded that the punching failure depends on the concrete quality and that the compressive part of the concrete strength does not influence the punching failure.

The influence of the number of cracks in uniaxial compression is investigated in analyzing three slabs with the values (b=5, 10, and 15). A similar punching failure mechanism is observed for these three slabs. The corresponding response curves are shown in figure 7.10. It can be observed that the number of cracks in uniaxial compression slightly influences the last part of the response curve. The sustainable displacements and the failure loads are hardly increased for increasing value of parameter b. The influence of this parameter is consequently not determinant.

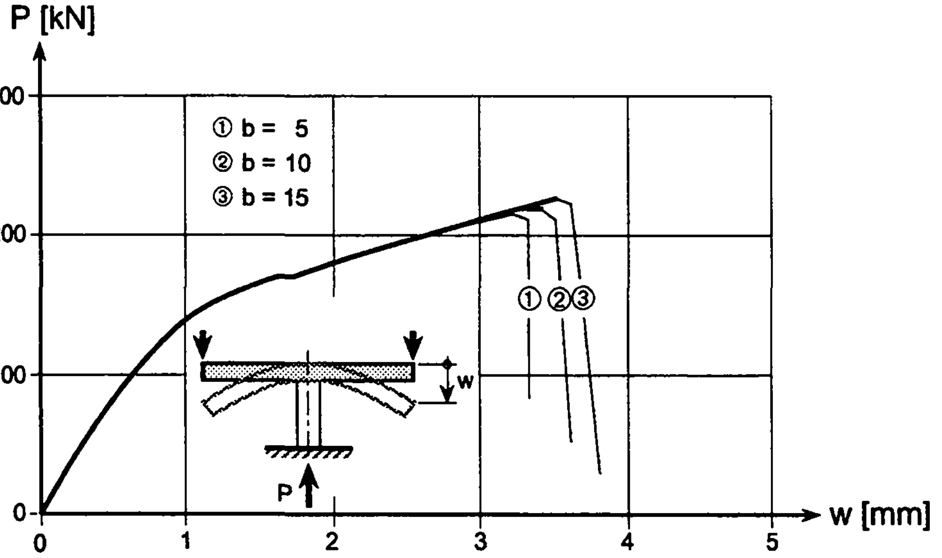

Figure 7.10: Influence of the number of cracks in compression on the response

Another parameter which has little influence on the punching failure is the out-of-roundness parameter (defined in section 3.5.2). This is shown in simulating three slabs with three different out-of-roundness parameters (e=0.52, 0.55, and 0.6). The considered values of this parameter are reasonable values for concrete as presented on page 43. The obtained failure mechanisms and responses of these three slabs are similar. As shown in figure 3.6, the out-of-roundness parameter influences the biaxial compressive strength and does not influence the compressive-tensile strength or the biaxial tensile strength. This further proves that the compressive part of the concrete strength does not influence the punching failure.

The influence of the flow rule is also investigated in simulating three slabs with different values of the dilatancy angle at the uniaxial ultimate compressive strength: $\psi_c=5^0$, 10^0, and 15^0. The failure mechanism and the responses of these three slabs are similar. Therefore, the dilatancy angle at the uniaxial ultimate compressive strength does not influence the punching failure.

7.4 Influence of the reinforcement

7.4.1 Influence of the percentage of reinforcement

The influence of the percentage of reinforcement is studied in simulating the behavior of similar slabs with a different percentages of reinforcement (the reference slab is presented in section 7.1). Orthogonal reinforcement is considered which is modeled with ring and truss-axi elements as described in section 6.4.2. Six different slabs are analyzed with a percentage of reinforcement ρ=0.2, 0.4, 0.8, 1.2, 1.6, and 2%. A similar punching failure mechanism is observed for all these slabs. The corresponding response curves are presented in figure 7.11 in addition to the response of the plain concrete slab simulation. It can be observed that after a similar initial elastic response, the behavior of the slabs varies tremendously depending on the percentage of reinforcement. With increasing the percentage of reinforcement, the value of the punching load is increased. The ductility is also influenced by the percentage of reinforcement as it decreases with increasing the percentage of reinforcement. The results of these simulations are comparable to the experimental results obtained by Elstner and Hognestad [37] and presented in figure 2.5(a) or the ones obtained by Criswell [27]. It should be mentioned that the influence of the dowel action is not considered here, and that increasing the percentage of reinforcement increases the contribution of the dowel action which increases the ductility of the failure.

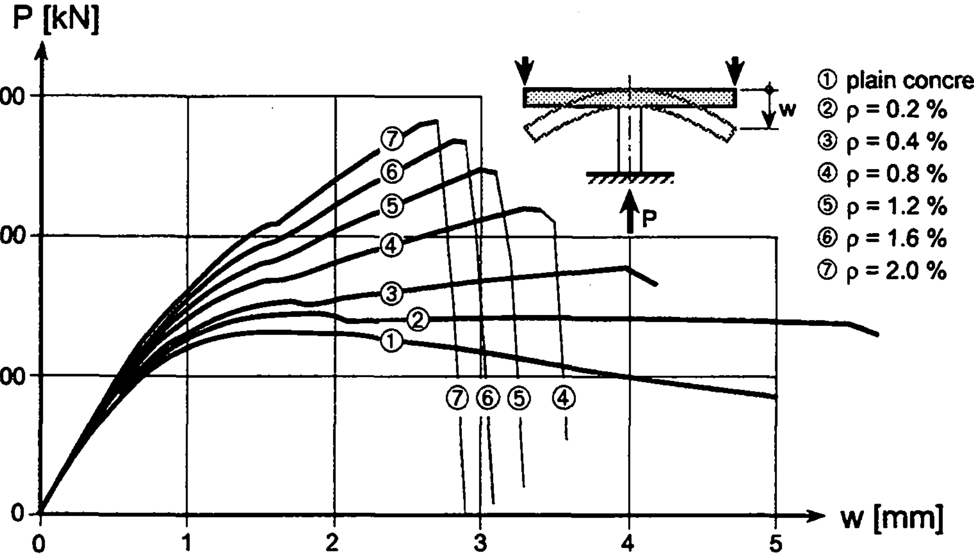

Figure 7.11: Influence of the percentage of reinforcement on the response

Yielding of the reinforcement is predicted numerically only in the slab with ρ=0.2% which has the most ductile response. Yielding occurs in the steel located just above the extremity of the column. However, a ductile type of response is predicted for slab with ρ=0.4%, even though no yielding of the reinforcement takes place. Yielding of the reinforcement is not strictly controlling the ductility of the response. This result is different from the one observed experimentally as presented by Elstner and Hognestad [37] and illustrated in figure 2.5(a) where yielding is measured in all the slabs. This difference is probably due to the bond modelling which does not reproduce the steel strain concentration in between a crack.

7.4.2 Influence of the fastening length

The influence of the steel fastening length is studied, because it was shown in section 6.4.2 that it influences the punching failure mechanism. This investigation is not rigorous as a constant value of the fastening length cannot be obtained on an irregular finite element mesh. However, this fastening length is approximated and the response curves for two values of the fastening length $l_F \approx 75, 100$ mm are presented in figure 7.12. The response curve of slab with a perfect bond is also given in figure 7.12 even though the failure is not due to punching but to local instabilities as described in section 6.4.2. It can be observed that the fastening length influences the response of the slab as the ultimate displacement is extended, and the failure

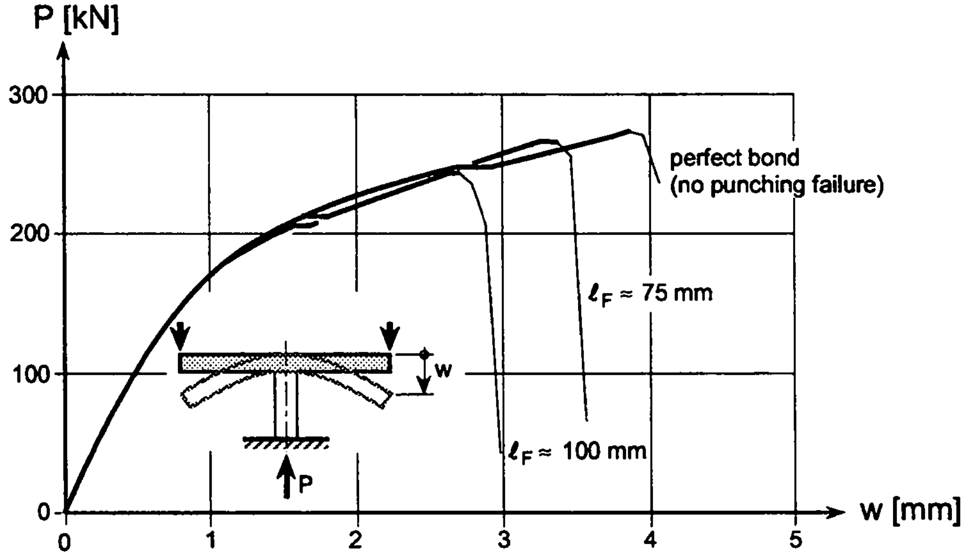

Figure 7.12: Influence of the fastening length on the response

load is consequently increased. It can be concluded that increasing the bond between steel and concrete increases the punching load and delays the punching failure. However, the influence of the fastening length should be further analyzed with bond elements for example.

7.5 Influence of the geometry

7.5.1 Influence of the size-effect

The size-effect is investigated in simulating three slabs of different sizes. These slabs are characterized by a similar scaling factor which applies to the concrete geometry (dimensions are given in table 7.1) and the steel area. Except for these dimensions, the slabs are similar: similar boundary conditions and similar concrete and steel characteristics. It can be noted that the concrete covering of the slab is also scaled as suggested by Bažant and Cao [10].

The finite element mesh is not similar for the three simulations. This is due to the fact that the softening slope is controlled by the finite element size h^e, as presented in section 3.5.4. For a constant mesh, by increasing the size of the structure, the finite element size is also increased so that the softening slope is steeper which can lead to unstable response. Therefore, a refinement of the mesh is required for the large structure so that the dense mesh used in section 6.2.6 is considered.

Another particularity of this investigation results from the steel fastening length, which should be constant from one slab to another as it is considered to be a material characteristic. This implies that the nodes at which the steel and the concrete are fixed are different depending on the size of the slab so as to approach a constant fastening length of 75 mm.

The response curves of these three slabs are presented in figure 7.13. It can be observed that the response curves are tremendously influenced by the size of the structure. However, no differences in the softening response are observed, which differs from the experimental results obtained by Bažant and Cao [10] as illustrated in figure 2.15. The main results of these simulations are summarized in table 7.1 along with the nominal shear stress computed based on equation 1.1. It can be observed that the size-effect influences the punching failure as the nominal shear stress decreases with increasing slab thickness. The size-effect law given

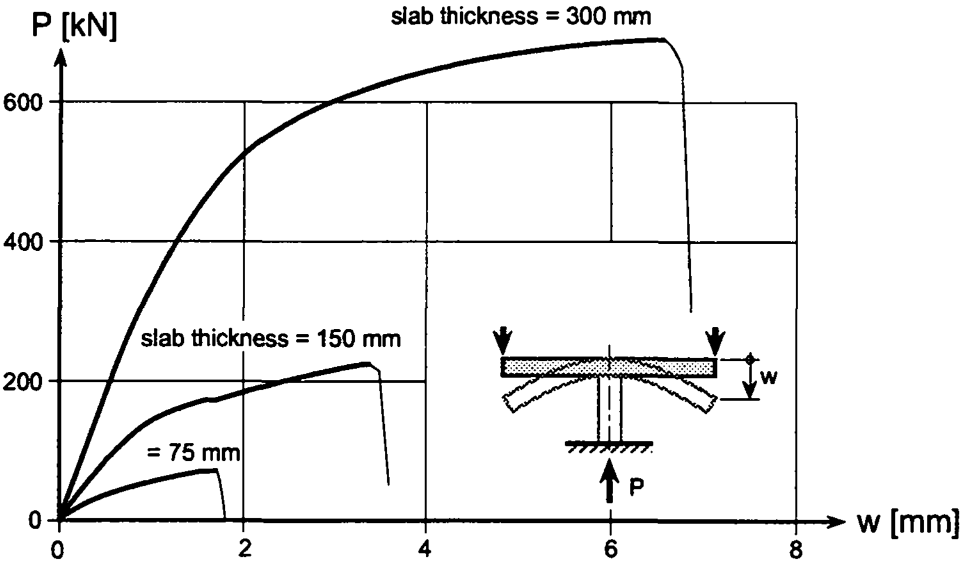

Figure 7.13: Influence of the size on the response

slab	h[mm]	ϕ column[mm]	ϕ slab[mm]	P_{punch} [kN]	τ_n [N/mm^2]
small	75	75	855	72	2.67
reference	150	150	1710	222	2.06
large	300	300	3420	689	1.69

Table 7.1: Influence of the size on the punching load and on the nominal shear stress

in equation 3.74 is approached, but more simulations should be performed to determine the constants of this law. The upper bound value of the nominal shear stress is computed as suggested by Braestrup et al. [14] [13] (presented on page 4). The resulting nominal shear stress is τ_n=5.83 N/mm^2 which can be checked to be larger than the values obtained numerically.

The tensile stress distribution along the punching crack just before the crack initiation is presented in figure 7.14 for the three simulated slabs. It can be clearly observed that the tensile stress distribution is not affine between the three slabs (an affine stress distribution would illustrate an insensitivity with regard to the size of the structure). For the small slab, the tensile stresses are high all along the punching crack. This is not the case for the large slab as a significant decrease of the tensile stress is observed from the bottom (2.1 N/mm^2) to the top of the slab (0.34 N/mm^2). Therefore, the modification of the tensile stress distribution along the punching crack reflects the size-effect.

The punching crack for the large slab is shown in figure 7.15. It can be compared to the one obtained with the reference simulation given in figure 6.20 on page 124. The inclination of the punching crack at the top of the large slab is 41^0 and it is 34^0 for the reference specimen. This increase of inclination with increasing the slab thickness was observed experimentally by Graf [48] as presented in section 2.2.1. However, the results obtained by Tolf [141] seems to show the opposite as the punching cracks in thicker slabs are either flatter than those in thinner slabs or at the same angle. This question should be further investigated keeping in mind that experimentally, the inclination of the punching crack is very sensitive as shown in figure 2.12.

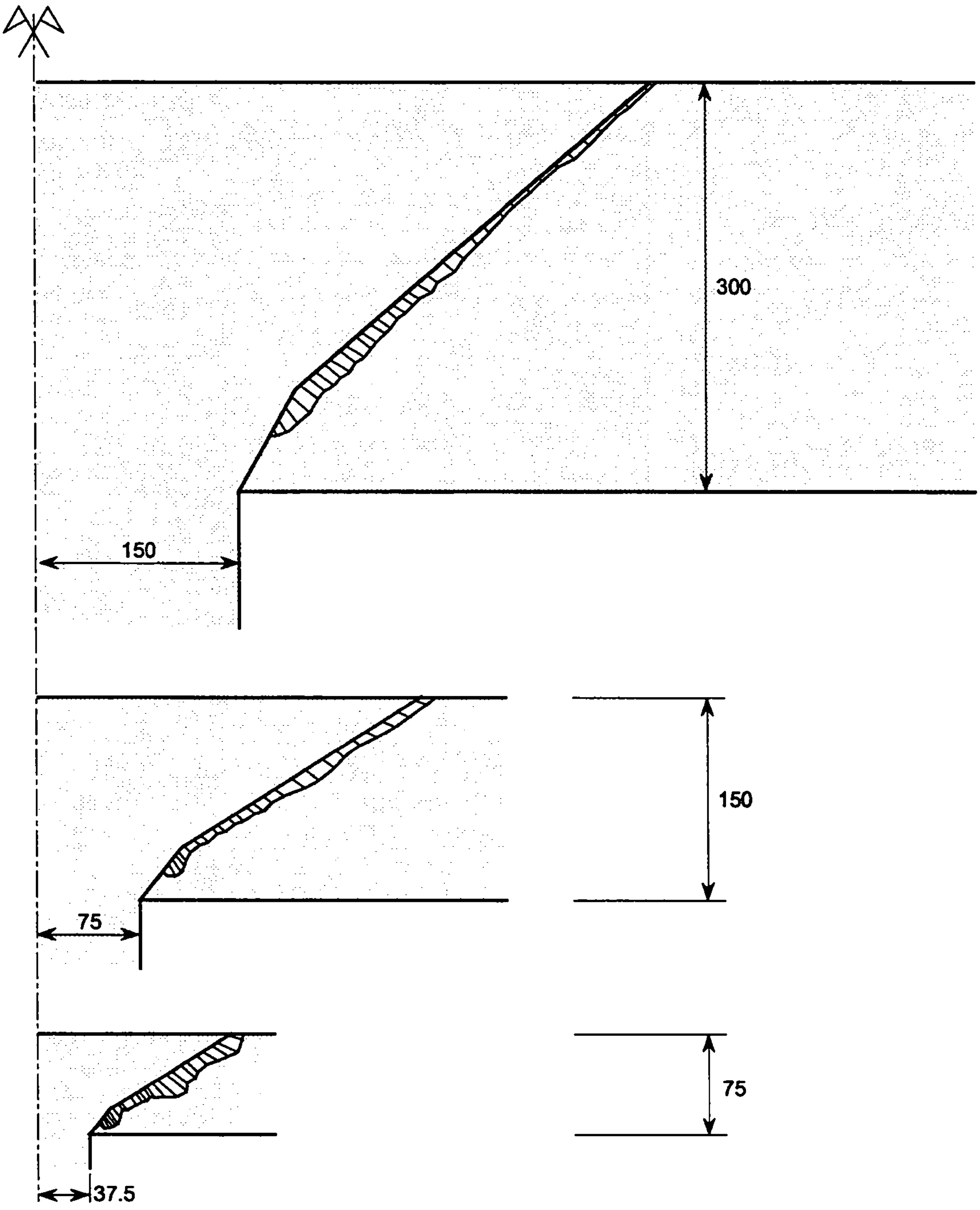

Figure 7.14: Influence of the size on the tensile stress distribution along the punching crack just before the failure initiation

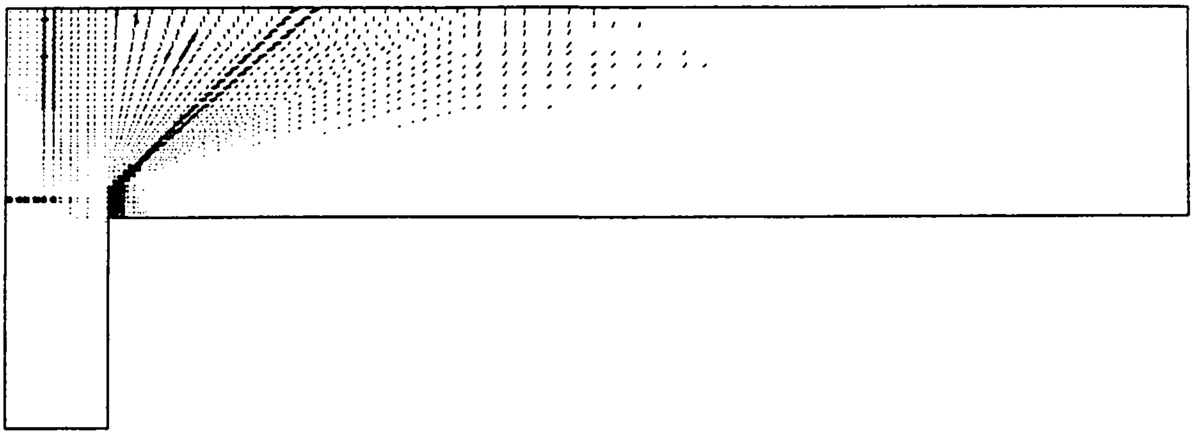

Figure 7.15: Tangential cracks at failure observed for the large slab (h=300 mm)

7.5.2 Influence of the radius

The influence of the radius of the slab is investigated in simulating three slabs with different radius (755, 855, and 955 mm). This value of the radius corresponds to the distance from the axis of the column to the load application point. A similar punching failure mechanism is observed for all these simulations. The corresponding response curves are presented in figure 7.16. It can be observed that the entire response is influenced by the radius of the slab.

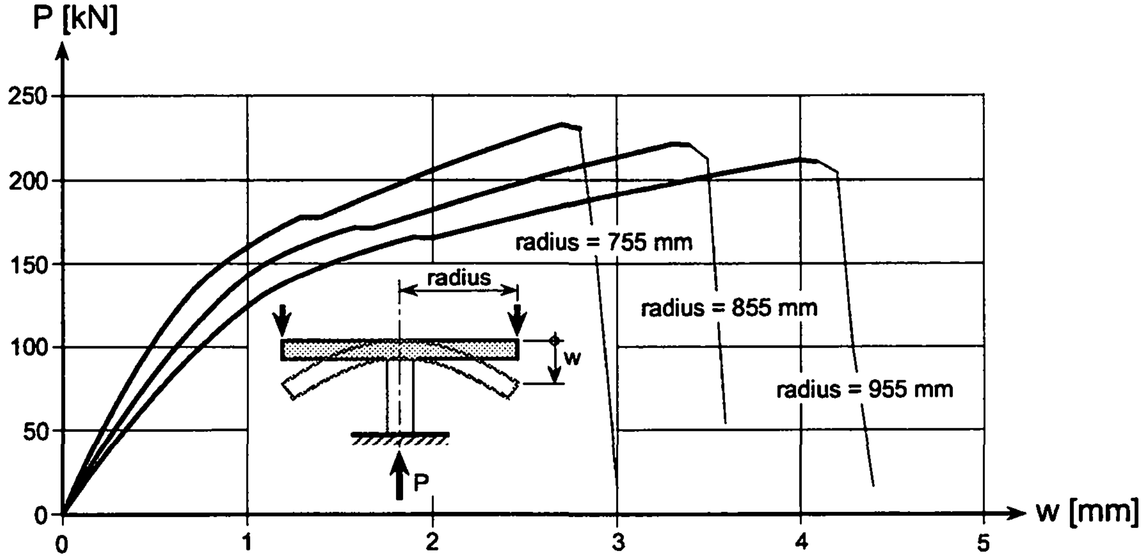

Figure 7.16: Influence of the radius on the response

However, the punching load is very little influenced by this radius (233, 222, and 212 kN). This reveals that in a circular slab, the applied bending moment—controlled by the radius—is not a determinant parameter for the value of the punching load.

Chapter 8

Conclusion

8.1 Recall of the framework

The purpose of this research is to analyze numerically the punching failure in reinforced concrete structures. The natural point of departure is the description of the failure phenomenon. The punching failure mechanism is introduced with four typical experiments and exploiting complementary results, a discussion of the failure phenomenon is presented. This discussion leads to the requirements that the numerical model should fulfill to predict the punching failure. They are: (1) general geometry and arbitrary boundary conditions, (2) treatment of multiple cracks, (3) interaction of shear and flexural effects, (4) reproduction of localized failure, (5) reproduction of size-effect, (6) treatment of the reinforcement. For a first approach, the assumption that the structure is axially symmetric is justified. It is also assumed that the bond between steel and concrete is perfect and that the dowel action (localized shear transfer mechanism between concrete and steel) is negligible.

8.2 Concluding remarks

8.2.1 The numerical model

The numerical model developed to analyze punching failure in reinforced concrete structures is based on the finite element method. The numerical model is implemented into a computer code applying the object-oriented programming concept. As it is the first time that this programming concept is applied to the non-linear finite element method, the algorithmic procedures required for non-linear analysis are carefully investigated to extract the object behavior and to extend the classes of a preexisting environment. It is shown that, due to the concept of non-anticipation of the state of the object, the sequence of the operations can easily be modified which results in a program that can be readily extended. It is also illustrated that the object-oriented concept leads to faster programming, because it re-uses existing classes. The reliability of this programming concept is also demonstrated by a reduction of data transfer as compared to procedural programming, leading to a reduction of programming errors. Consequently, the object-oriented programming method is suitable for non-linear finite element analysis and this concept should be preferred to procedural programming, especially for the development of numerical methods. The object-oriented implementation in C++ of the non-linear finite element method is described by Menétrey and Zimmermann [90]. In addition to the finite element code, a two-dimensional post-processor program for the interpretation of the numerical results is developed.

The numerical model reproduces the non-linear material behavior of reinforced concrete structures by decoupling the actions of steel reinforcement and concrete. The steel reinforcement is represented with uniaxial truss elements which follow a bi-linear stress-strain response. Concrete is modelled using continuum elements and is described within the framework of the flow theory of plasticity. The bond between concrete and steel reinforcement is assumed to be perfect.

The failure criterion is determinant for non-linear material description, and this justifies the development of an efficient failure criterion for concrete. This concrete failure criterion has the following characteristics: (1) three invariant formulation, (2) calibration in terms of the uniaxial tensile and uniaxial and biaxial compressive strength, (3) smooth and convex surface except for the vertex at equi-triaxial extension, (4) uncoupling of the cohesion and friction parameters for hardening/softening formulation, (5) modification of the deviatoric sections to a circular shape with increasing confinement. The validity of the triaxial failure criterion is demonstrated with both biaxial and triaxial concrete data. The concrete failure criterion and its generalization to include most standard failure criteria are described by Menétrey and Willam [89]. The influence of the failure criterion on the shear failure of footings, is demonstrated as it modifies tremendously the bearing stress and it can also alter the failure mechanism. The numerical analysis of the bearing capacity of circular footings is described by Menétrey and Zimmermann [91]. The failure criterion reproduces the uniaxial tensile and compressive strength of plain concrete experiments. The influence of the confinement pressure is also accurately reproduced as demonstrated with the simulation of the confined compressive test.

The flow rule developed for the concrete model is described with a plastic potential calibrated so that: (1) for the uniaxial tensile test, the plastic strain follows the loading path for uniaxial traction, (2) at the uniaxial ultimate compressive strength, the flow rule is given by the dilatancy angle (angle controlling the volume increase resulting from non-linear deformation). It is shown that this concrete flow rule reproduces the elastic unloading of the radial strain observed experimentally during a uniaxial tensile test in plain concrete. The influence of the flow rule is also investigated in analyzing the shear failure in a footing for different dilatancy angles. It is shown that the dilatancy angle does not only influence the ultimate bearing stress but also the type of failure mechanism.

The cracking is described by strain-softening which refers to a gradual decrease in tensile strength with additional deformation. The reduction of the tensile strength is controlled by the crack opening which is monitored by a constant fracture energy. The fracture energy is included in the model so that the size-effect is reproduced. This cracking model is implemented as an isotropic decohesion process of the failure criterion. In order to have a formulation which is mesh independent, the size of the finite element is included in the softening formulation so as to have a localization limiter. A fictitious number of cracks is introduced in the fracture model so that the amount of fracture energy which can be dissipated depends on the state of stress. The stiffness degradation due to cracking is simulated with an isotropic elastic damage model. It is checked that the developed cracking model predicts the softening in traction as well as confined compression for different confinement pressures. No hardening of the constitutive model is considered.

Different strategies of the modified Newton-Raphson algorithm are developed to capture localized failure. The localization capabilities of the numerical model are demonstrated with the simulation of the shear failure of a footing. Furthermore, strain localization of the deformation is also reproduced for plain and reinforced concrete tested in traction.

8.2.2 The simulation of punching failure

Once the numerical model is developed and tested, the simulation of punching failure is examined for three circular reinforced concrete slabs made of different types of reinforcement: ring, ring and radial, and orthogonal reinforcement. The comparison with the experimental results obtained by Kinnunen and Nylander [68] reveals that:

1. The punching failure mechanism, characterized by a localized inclined punching crack, is generated. However, in a slab with orthogonal reinforcement, in order to generate a punching failure, the perfect bond assumption between concrete and steel must be relaxed. The proposed method to relax this bond condition is to fasten rigidly the steel to the concrete only at the extremity of a fictitious fastening length. This fastening length is determined based on the crack spacing in uniaxial traction. This method demonstrates its efficiency by allowing the formation of the punching failure mechanism in slabs with orthogonal reinforcement.

2. The value of the punching load is accurately predicted for slabs with a perfect axially symmetric reinforcement. However, for the slab with orthogonal reinforcement, the punching load predicted numerically is lower than the experimental one. This difference is due to the dowel action which is neglected in the numerical model and is important for slabs with orthogonal reinforcement.

3. The predicted crack sequence is similar to the experimental one that is: (1) formation of a tangential flexural crack, (2) development of radial cracks which expand up to the support, (3) formation of inclined cracks through the slab thickness, (4) sudden failure by coalescence of inclined cracks into the punching crack and its propagation.

4. The predicted response is slightly stiffer than the experimental one, which is due to a combination of: (1) the experimental setup is assumed to be perfectly stiff, (2) the influence of large deformations is not considered by the model, (3) no hardening formulation is implemented at the constitutive level, (4) a perfect bond between steel and concrete is assumed. For slabs with orthogonal reinforcement, the numerical simulation is much too stiff compared to the experimental results even though the perfect bond condition is relaxed. This is due to the transformation of orthogonal reinforcement to axially symmetric reinforcement which overestimates the stiffness.

In summary, the numerical simulation of punching failure in reinforced concrete structures reproduces the experimental observations. Consequently, the developed computational simulation tool is used to investigate the punching failure mechanism. This investigation reveals that:

1. The punching crack results from a crack coalescence phenomenon at the top of the slab followed by a crack propagation at the bottom of the slab. The punching crack propagates from the upper part of the slab to the corner slab-column. In the upper part of the slab, under the reinforcement, some cracks open and others close, so that the deformation localizes into one inclined shear crack inducing the punching crack. But, at the top of the slab, the steel reinforcement controls the crack opening by spreading the cracks, explaining why inclined shear cracks form across the slab thickness. One conclusion of this observation is that a horizontal steel layer inside the slab should increase the punching resistance by delaying the formation of inclined cracks.

2. One requirement for punching failure to occur is determined. By simulating a plain concrete slab (flexural failure) and a slab with ring reinforcement inside the punching cone (punching failure) it is shown that punching failure occurs if flexural reinforcement is placed inside the punching cone, allowing the formation of this cone and preventing a flexural failure. This requirement is checked experimentally on micro-slabs.

3. The size-effect observed experimentally is reproduced numerically as the nominal shear stress decreases with increasing slab thickness. The modification of the tensile stress distribution along the upcoming punching crack reflects the size-effect.

4. The concrete parameters which control the punching failure are the uniaxial tensile stress and the fracture energy. Surprisingly, it is shown that the uniaxial compressive strength does not influence the punching failure process. This affirmation is in contradiction with the hypothesis of some analytical models which are based on the uniaxial compressive strength to predict the punching load. However, this contradiction is not absolute as the compressive strength of concrete depends physically on the tensile strength.

5. For an increase of the percentage of reinforcement the punching load increases, but the ductility diminishes.

6. The applied bending moment in a circular slab is not a determinant parameter for the value of the punching load.

The developed computational simulation tool gives a deep insight of the punching failure mechanisms. Therefore, numerical simulation should be recognized as a powerful tool to understand the complex behavior of reinforced concrete structures.

8.3 Suggestions for further work

During this research, unsolved or partially unsolved problems where encountered. These problems are presented here as suggestions for further work.

1. The punching failure in reinforced concrete should be analyzed with a three-dimensional numerical model, especially when orthogonal reinforcement is used. This three-dimensional version of the numerical model was developed in this research, but its capabilities were not investigated due to inadequate pre and post-processor facilities for three-dimensional visualization.

2. The punching failure is characterized by large deformations once failure occurs. The numerical model should therefore be extended to capture non-linear geometric effects due to large deformations.

3. The ductility of punching failure (ductile failure being preferred over brittle failure) is increased with shear reinforcement or prestressed tendons. The effect of this additional reinforcement should be examined numerically.

4. A perfect bond assumption between concrete and steel reinforcement prevents the numerical model from predicting the punching failure mechanism for slabs with orthogonal reinforcement. One simple but efficient method for relaxing the perfect bond assumption is proposed. However, the influence of bond between steel reinforcement and concrete should be investigated further with bond-elements for example.

5. The size-effect which influences the punching failure, should be further analyzed experimentally and numerically in order to examine its consequence on the punching crack inclination and on the softening response.

6. Inclined cracks inside the slab thickness observed experimentally are reproduced numerically. The formation of these inclined cracks could probably be delayed by setting a horizontal steel layer inside the slab. The effect of this horizontal layer should be further investigated experimentally and numerically.

7. The influence of the tensile strength of concrete on punching failure has been proven. Therefore, the application of new concrete with high tensile strength such as fiber reinforced concrete should be investigated experimentally.

8. The results of all these simulations could be used to develop an analytical model to predict the punching load.

A lot of work has still to be performed on the analysis of punching failure in reinforced concrete structures.

Bibliography

[1] H.-P. Andrä. Zum Tragverhalten des Auflagerbereichs von Flachdecken. Thesis, Universität Stuttgart, 1982.

[2] Committee ASCE-ACI. The shear strength of reinforced concrete members. *Journal of the Structural Division, Proceedings of the ASCE*, 99 and 100(ST 6):1091–1187 and 1543–1591, 1973 and 1974.

[3] AVS/Uniras. *FGL/Graphics*, 1993. Version 6v3b.

[4] A.K. Azad, M.H. Baluch, M.Y. Al-Mandil, A.M. Sharif, and K. Kareem. Loss of punching capacity of bridge deck slabs from crack damage. *ACI Structural Journal*, 90:37–41, 1993.

[5] A. Barry. Development of a stain-space damage and plasticity based numerical model for concrete. Thesis, Ecole Polytechnique Fédérale de Lausanne, 1994.

[6] K.J. Bathe. *Finite Element Procedures In Engineering Analysis.* Prentice-Hall, 1982.

[7] Z.P. Bažant. Size effect in blunt fracture: concrete, rock, metal. *Journal of Engineering Mechanics*, 110(4):518–535, 1984.

[8] Z.P. Bažant, editor. *Fracture mechanics of concrete structures: Part I, State-of-Art Report.* ACI Committee 446, Fracture Mechanics, 1992.

[9] Z.P. Bažant. Scaling laws in mechanics of failure. *Journal of Engineering Mechanics*, 119:1828–1844, 1993.

[10] Z.P. Bažant and Z. Cao. Size effect in punching shear failure of slabs. *ACI Structural Journal*, 84:44–53, 1987.

[11] R. De Borst and P. Nauta. Non-orthogonal cracks in a smeared finite element model. *Engineering computation*, 2:35–46, 1985.

[12] R. De Borst and P.A. Vermeer. Possibilities and limitations of finite elements for limit analysis. *Geotechnique 34*, 2:199–210, 1984.

[13] M.W. Braestrup. Punching shear in concrete slabs. In *Plasticity in reinforced concrete.* IABSE, Colloquium, Copenhagen, 1979.

[14] M.W. Braestrup, M.P. Nielsen, B.C. Jensen, and F. Bach. Axisymmetric punching of plain and reinforced concrete. Report 75, Structural research laboratory, Technical University of Denmark, 1976.

[15] J.T. Bromwich. On the roots of the characteristic equation of a linear substitution. *Acta mathematica*, 30, 1906.

[16] W. Burzynski. Uber die Anstrengungshypothesen. *Schweizerische Bauzeitung*, 94(21):259–262, 1929.

[17] Center Line. *ObjectCenter user's guide*, 1993. Version 2.

[18] W.F. Chen. *Limit analysis and soil plasticity*. Elsevier, 1975.

[19] W.F. Chen. *Plasticity in reinforced concrete*. McGraw-Hill, 1982.

[20] W.F. Chen and G.Y. Baladi. *Soil plasticity*. Elsevier, 1985.

[21] W.F. Chen and D.J. Han. *Plasticity for structural engineers*. Springer-Verlag, 1988.

[22] J. Chinn and R.M. Zimmerman. Behavior of plain concrete under various high triaxial compression loading conditions. Technical report WL TR 64-163, Air Force Weapons Laboratory, New Mexico, 1965.

[23] Comité Euro-International du Béton. *Concrete under multiaxial states of stress constitutive equations for practical design*, 1983. Bulletin d'information 156.

[24] Comité Euro-International du Béton. *Cracking and deformations*, 1985. Manual.

[25] Comité Euro-International du Béton. *CEB-FIP model code*, 1990. Bulletin d'information 195-196.

[26] A.D. Cox, G. Eason, and H.G. Hopkins. Axially symmetric plastic deformation in soils. *Philosophical transactions of the royal society of London*, 254:1–45, 1961.

[27] M.E. Crisweel. Static and dynamic response of reinforced concrete slab-column connections. *Publication SP-42, ACI*, 2, 1974.

[28] H. L. Davidson and W.F. Chen. Nonlinear response of drained clay to footings. *Computers and Structures*, 8:281–290, 1978.

[29] C.S. Desai and H.J. Siriwardane. *Constitutive laws for engineering materials*. Prentice-Hall, 1984.

[30] W.H. Dilger and A. Ghali. Shear reinforcement for concrete slabs. *Journal of the Structural Division, Proceedings of the ASCE*, 107(ST 12):2403-2420, 1981.

[31] J.W. Dougill. On stable progressively fracturing solids. *Journal of applied mathematics and physics*, 27:423–437, 1976.

[32] D.C. Drucker and W. Prager. Soil mechanics and plastic analysis or limit design. *Quarterly of Applied Mathematics*, 10:157–165, 1952.

[33] Y. Dubois-Pèlerin. Object-oriented finite element programming concepts and implementation. Thesis, Ecole Polytechnique Fédérale de Lausanne, 1992.

[34] Y. Dubois-Pèlerin and Th. Zimmermann. Object-oriented finite element programming. 3. A performant implementation in C++. *Computer Methods in Applied Mechanics and Engineering*, 103:165–183, 1993.

[35] Y. Dubois-Pèlerin, Th. Zimmermann, and P. Bomme. Object-oriented finite element programming. 2. A prototype program in Smalltalk. *Computer Methods in Applied Mechanics and Engineering*, 98(3):361–397, 1992.

[36] T. Dyngeland, K. Hoiseth, and E. Opheim. Nonlinear analyses of reinforced concrete members subjected to punching shear. In N. Bićanić H. Mang and R. De Borst, editors, *Computational modelling of concrete structures*, pages 865–873, Euro-C conference, Innsbruck, Austria, March 1994. Pineridge Press.

[37] R.C. Elstner and E. Hognestad. Shearing strength of reinforced concrete slabs. *Journal of the ACI*, 28(1):29–58, 1956.

[38] G. Etse. Theoretische und numerische Untersuchung zum diffusen und lokalisierten Versagen in Beton. Thesis, Universität Fridericiana zu Karlsruhe, 1992.

[39] G. Etse and K.J. Willam. A fracture energy-based constitutive formulation for inelastic behavior of plain concrete. *American Society of Civil Engineers, Journal of Engineering Mechanics*, 1994. In press.

[40] European Committee for Standardization, Central Secretariat: rue de Stassart 36, B-1050 Brussels. *Eurocode 2: Design of concrete structures Part 1: General rules and rules for buildings*, 1991.

[41] R. Favre, J.-P. Jaccoud, M. Koprona, and A. Radojicic. *Dimensionnement des structures en béton*, volume 8 of *Traité de Génie Civil.* Presses Polytechniques et Universitaires Romandes, 1990.

[42] C. Felippa. Nonlinear finite element methods. Class notes, University of Colorado at Boulder, 1991.

[43] F. Frey. Analyse non linéaire des structures. Notes de cours, Ecole Polytechnique Fédérale de Lausanne, 1986.

[44] Y.C. Fung. *Foundations of solid mechanics.* Prentice-Hall, 1965.

[45] H. Gesund and Y.P. Kaushik. Yield line analysis of punching failure in slabs. Publications 30-I, International Association for Bridges and Structural Engineering, 1970.

[46] G.H. Golub and C.F. Van Loan. *Matrix computations.* Johns Hopkins, second edition, 1991.

[47] F. González-Vidosa, M.D. Kotsovos, and M.N. Pavlović. Symmetrical punching of reinforced concrete slabs: an analytical investigation based on nonlinear finite element modeling. *ACI Structural Journal*, 85(3):241–250, 1988.

[48] O. Graf. Versuche über die Widerstandsfähigkeit von allseitig aufliegenden dicken Eisenbetonplatten unter Einzellasten. *Deutscher Ausschuss für Stahlbeton*, 1938. Heft 88.

[49] A.K. De Groot, G.M.A. Kusters, and Th. Monnier. Numerical modelling of bond-slip behavior. *Heron*, 26(1B), 1981.

[50] M. Hallgren and S. Kinnunen. Punching shear tests on circular high strength concrete slabs without shear reinforcement. *Nordic Concrete Research*, 10:37–47, 1991.

[51] R. Hill. A general theory of uniqueness and stability in elastic-plastic solids. *Journal of the Mechanics and Physics of Solids*, 6:236–249, 1958.

[52] R. Hill. Accelaration waves in solids. *Journal Mech. phys. solids*, 10:1–16, 1961.

[53] A. Hillerborg, M. Modeer, and P. E. Petersson. Analysis of crack formation and crack growth in concrete by means of fracture mechanics and finite element. *Cement and Concrete Research (US)*, 6:773–782, 1976.

[54] E. Hoek and E. T. Brown. Empirical strength criterion for rock masses. *Journal of the Geotechnical Engineering Division*, 106(GT9):1013–1035, 1980.

[55] E. Hognestad. Shearing strength of reinforced concrete column footings. *Journal of the ACI*, 50:189–208, 1953.

[56] E. Hognestad. Yield-line theory for the ultimate flexural strength of reinforced concrete slabs. *Journal of the ACI*, 24(7):637–656, 1953.

[57] C. Huet. An integrated approach of concrete micromechanics. In C. Huet, editor, *Micromechanics of concrete and cementitious composites*, pages 117–146. Presses Polytechniques et Universitaires Romandes, 1993.

[58] T.J.R. Hughes. Generalization of selective integration procedures to anisotropic and nonlinear media. *International Journal of Numerical Methods in Engineering*, 15:1413–1418, 1980.

[59] T.J.R. Hughes. *The Finite Element Method.* Prentice-Hall, 1987.

[60] T.J.R. Hughes. Nonlinear finite element analysis. A short course taught by T.J.R. Hughes and T.B. Belytschko, Munich, 1991.

[61] B.J. Hurlbut. Experimental and computation investigation of strain-softening in concrete. Master's thesis, University of Colorado at Boulder, 1983.

[62] J.-P. Jaccoud. Armature minimale pour le contrôle de la fissuration des structures en béton. Thesis, Ecole Polytechnique Fédérale de Lausanne, 1987.

[63] J.-P. Jaccoud, B. Francou, and J.-M. Camara. Armature minimale pour le contrôle de la fissuration. Rapport 82-13, Ecole Polytechnique Fédérale de Lausanne, 1984.

[64] K.W. Johansen. Yield-line theory. *Cement and concrete association*, 1962.

[65] B.W. Kernighan and D.M. Ritchie. *The C programming language.* Prentice-Hall, 1988.

[66] S. Kinnunen. Punching of concrete slabs with two-way reinforcement. *Transactions of the Royal Institute of Technology*, 198, 1963.

[67] S. Kinnunen. Determination of experimental load displacement curve. Private communication, 1994.

[68] S. Kinnunen and H. Nylander. Punching of concrete slabs without shear reinforcement. Transactions 158, Royal Institute of Technology, Stockholm, 1960.

[69] S. Kinnunen, H. Nylander, and P. Tolf. Plattjocklekens inverkan pa betongplattors hallfasthet vid genomstansning. Fősők med rektangulära plattor. Technical Report 137, Institutionen főr Byggnadsstatik Kungl Tekniska Hőgskolan, Stockholm, 1980.

[70] M. Klisinski. Degradation and plastic deformation of concrete. Iftr report 38, Polish Academy of Sciences, 1985.

[71] H. Kupfer. Das Verhaltern des Betons unter mehrachsiger Kurzzeitbelastung unter besonderer Berücksichtigung der zweiachsiger Beanspruchung. *Deutscher Ausschuss für Stahlbeton*, 1973. Heft 229.

[72] H. Kupfer, H.K. Hilsdorf, and H. Rusch. Behavior of concrete under biaxial stresses. *Journal of the ACI*, 66(52):656–666, 1969.

[73] T.W. Lambe and R.V. Whitman. *Soil mechanics*. John Wiley & Sons, 1969.

[74] J. Lemaitre and J.-L. Chaboche. Aspect phénoménologique de la rupture par endommagement. *Journal de mécanique appliquée*, 2:317–365, 1984.

[75] A. Leon. Uber die Scherfestigkeit des Betons. *Beton und Eisen*, 34:130–135, 1935.

[76] Y.-J. Li. Numerical simulation of crack propagation in concrete and rock. Thesis, Ecole Polytechnique Fédérale de Lausanne, 1994. In preparation.

[77] Y.-J. Li and Th. Zimmermann. An enhanced rotating crack model. In *Computational modelling of concrete structures*, Euro-C conference, Innsbruck, March 1994.

[78] S. Loseth, A. Slatto, and G. Syvertsen. Finite element analysis of punching shear failure of reinforced concrete slabs. *Nordic concrete research*, 82(1):18.1–18.17, 1982.

[79] J.S. Lovrovich and D.I. McLean. Punching shear behavior of slabs with varying span-depth ratios. *ACI Structural Journal*, 87(5):507–511, 1991.

[80] J. Lubliner. *Plasticity theory*. Macmillan, 1990.

[81] J. Lubliner, J. Oliver, S. Oller, and E. Onate. A plastic damage model for concrete. *International Journal of Solids Structures*, 25:299–326, 1989.

[82] L.E. Malvern. *Introduction to the mechanics of a continuous medium*. Prentice-Hall, 1969.

[83] G. Márkus. *Theorie und Berechnung rotationssymmetrischer Bauwerke*. Werner-Verlag, 1978.

[84] P. Marti, J. Pralong, and B. Thürlimann. Schubversuche an Stahlbeton-Platten. Bericht 7305-2, Institut für Baustatik und Konstruktion ETH Zürich, 1977.

[85] M. Matar and J. Salençon. Capacité portante des semelles filantes. *Revue française de géotechnique*, 9:51–76, 1979.

[86] D.I. McLean, L.T. Phan, H.S. Lew, and R.N. White. Punching shear behavior of lightweight concrete slabs and shells. *ACI Structural Journal*, 87(4):386–392, 1990.

[87] A. Mendelson. *Plasticity: theory and applications*. Macmillan, 1968.

[88] Ph. Menétrey. A three-dimensional model based on the finite element method and the plasticity theory to analyze plain concrete structures. Master's thesis, University of Colorado at Boulder, 1991.

[89] Ph. Menétrey and K.J. Willam. A triaxial failure criterion for concrete and its generalization. *ACI Structural Journal*, 1994. In press.

[90] Ph. Menétrey and Th. Zimmermann. Object-oriented non-linear finite element analysis: application to J2 plasticity. *Computers and Structures*, 49(5):767–777, 1993.

[91] Ph. Menétrey and Th. Zimmermann. On the numerical analysis of the bearing capacity of circular footing. Rapport interne IBAP 92.03.03, LSC 94.3, Ecole Polytechnique Fédérale de Lausanne, 1994.

[92] F.-X. Müller, A. Muttoni, and B. Thürlimann. Durchstanzversuche an Flachdecken mit Aussparungen. Bericht 7305-5, Institut für Baustatik und Konstruktion ETH Zürich, 1984.

[93] J.G.M. Van Mier. Strain-softening of concrete under multiaxial loading conditions. Thesis, Technische Hogeschool Eindhoven, 1984.

[94] L.L. Mills and R.M. Zimmerman. Compressive strength of plain concrete under multiaxial loading conditions. *ACI Journal*, 67(47):802–807, 1970.

[95] J. Moe. Shearing strength of reinforced concrete slabs and footings under concentrated loads. Bulletin D47, Portland Cement Association, 1961.

[96] A. Nadai. *Elastische Platten.* Springer-Verlag, 1925.

[97] A. Nadai. *Theory of flow and fracture of solids.* McGraw-Hill, 1950.

[98] J.C. Nagtegaal, D.M. Parks, and J.R. Rice. On numerically accurate finite element solutions in the fully plastic range. *Computer Methods in Applied Mechanics and Engineering*, 4:153–177, 1974.

[99] D. Ngo and A.C. Scordelis. Finite element analysis of reinforced concrete beams. *ACI Journal*, 64(3), 1967.

[100] L. Nilsson. Impact loading on concrete structures. Thesis, Chalmers University of Technology, Göteborg, 1979.

[101] R.W. Ogden. *Non-linear elastic deformations.* Ellis Horwood, 1984.

[102] M. Ortiz, Y. Leroy, and A. Needleman. A finite element method for localized failure analysis. *Computer Methods in Applied Mechanics and Engineering*, 61:189–214, 1987.

[103] M. Ortiz and E.P. Popov. Accuracy and stability of integration algorithms for elastoplastic constitutive relations. *International Journal of Numerical Methods in Engineering*, 21:1561–1576, 1985.

[104] M. Ortiz and J.C. Simo. An analysis of a new class of integration algorithms for elastoplastic constitutive relations. *International Journal of Numerical Methods in Engineering*, 23:353–366, 1986.

[105] St. Pietruszczak and Z. Mróz. Finite element analysis of deformation of strain-softening materials. *International Journal of Numerical Methods in Engineering*, 17, 1981.

[106] J. Pralong. Poinçonnement symétrique des planchers-dalles. Bericht 131, Institut für Baustatik und Konstruktion ETH Zürich, 1982.

[107] J. Pralong, W. Brändli, and B. Thürlimann. Durchstanzversuche an Stahlbeton und Spannbetonplatten. Bericht 7305-3, Institut für Baustatik und Konstruktion ETH Zürich, 1979.

[108] E. Pramono. *Numerical simulation of distributed and localized failure in concrete.* PhD thesis, University of Colorado at Boulder, 1988.

[109] J.H. Prevost and T.J.R. Hughes. Finite-element solution of elastic-plastic boundary-value problems. *Journal of applied mechanics*, 48:69–74, 1981.

[110] Pure software. *Purify, User's guide*, 1993. Release 2.1.

[111] B. Rebora, Th. Zimmermann, and J.P. Wolf. Dynamic rupture analysis of reinforced concrete shells. *Nuclear Engineering and Design*, 37:269–297, 1976.

[112] P.E. Regan. Behavior of reinforced concrete flat slab. Report 89, CIRIA, London, 1981.

[113] P.E. Regan. Punching shear in prestressed concrete slab bridges. Technical report, Engineering Structures Research Group, Polytechnic of Central London, 1983.

[114] P.E. Regan and M.W. Braestrup. *Punching shear in reinforced concrete.* Comité Euro-International du Béton, 1985. Bulletin d'information 168.

[115] J.R. Rice. The localization of plastic deformation. *Theoretical and applied mechanics*, pages 207–220, 1976.

[116] F.E. Richart. Reinforced concrete walls and column footings, part 1 and 2. *Journal of the ACI*, 20(2 and 3):97–127 and 237–260, 1948.

[117] F.E. Richart, A. Brandtzaeg, and R.L. Brown. The failure of plain and spirally reinforced concrete in compression. Bulletin 190, Engineering Experiment Station, University of Illinois, 1929.

[118] E. Rizzi. Localization analysis of damaged materials. Master's thesis, University of Colorado at Boulder, 1993.

[119] M. Romano. On Leon's criterion. *Meccanica*, pages 48–67, 1969.

[120] J.G. Rots. Computational modeling of concrete fracture. Thesis, Technische Hogeschool Delft, 1988.

[121] J.G. Rots, P. Nauta, G.M.A. Kusters, and J. Blaauwendraad. Smeared crack approach and fracture localization in concrete. *Heron*, 30(1), 1985.

[122] J.W. Rudnicki and J.R. Rice. Conditions for the localization of deformation in pressure-sensitive dilatant materials. *J. Mech. Phys. Solids*, 23:371–394, 1975.

[123] J. Salençon and M. Matar. Capacité portante des fondations superficielles circulaires. *Journal de mécanique théorique et appliquée*, 1(2), 1982.

[124] M.A. Save and C.E. Massonnet. *Plastic analyses and design of plates, shells and disks.* North-Holland, 1972.

[125] F. Schleicher. Der Spannungszustand an der Fliessgrenze (Plastizitätsbedingung). *Zeitschrift für Angewandte Mathematik und Mechanik*, 6(3):199–216, 1926.

[126] L.A. Segel. *Mathematics applied to continuum mechanics.* Dover, 1987.

[127] J.C. Simo and T.J.R. Hughes. General return mapping algorithms for rate independent plasticity. In C.S. Desai, E. Krempl, P.D. Kionsis, and T. Kundu, editors, *Constitutive laws for engineering materials theory and applications*, pages 221–231, 1987.

[128] J.C. Simo and J.W. Ju. Strain and stress based continuum damage models, i. formulation, ii. computational aspects. *International Journal of Solids Structures*, 23(7):821–840 and 841–869, 1987.

[129] J.C. Simo and R.L. Taylor. Consistent tangent operators for rate-independent elastoplasticity. *Computer Methods in Applied Mechanics and Engineering*, 48:101–118, 1985.

[130] S.H. Smith. On fundamental aspects of concrete behavior. Master's thesis, University of Colorado at Boulder, 1987.

[131] Société suisse des ingénieurs et des architectes. *Constructions en béton*, 1989. Norme 162.

[132] B. Stroustrup. *The C++ Programming Language*. Addison-Wesley, 1987.

[133] SunPro. *SPARCompiler C++*, 1993. Version 4.0.

[134] SunPro. *SPARCompiler C*, 1993. Version 3.0.

[135] A.N. Talbot. Reinforced concrete wall footings and column footings. Bulletin 67, Engineering Experiment Station, University of Illinois, 1913.

[136] R. Taylor and B. Hayes. Some tests on the effect of edge restraint on punching shear in reinforced concrete slabs. *Magazine of Concrete Research*, 17(50):39–44, 1965.

[137] R.L. Taylor, P.J. Beresford, and E.L. Wilson. A non-conforming element for stress analysis. *International Journal of Numerical Methods in Engineering*, 10:1211–1219, 1976.

[138] K. Terzaghi. *Theoretical soil mechanics*. Chapman and Hall, 1946.

[139] S.P. Timoshenko and J.N. Goodier. *Theory of elasticity*. McGraw-Hill, 1970.

[140] S.P. Timoshenko and S. Woinowsky-Krieger. *Theory of plates and shells*. McGraw-Hill, 1959.

[141] P. Tolf. Plattjocklekens inverkan pa betongplattors hallfasthet vid genomstansning. Főrsők med cirkulära plattor. Technical Report 146, Institutionen főr Byggnadsstatik Kungl Tekniska Hőgskolan, Stockholm, 1988.

[142] A.S. Vesić. *Foundation engineering handbook*, chapter 3, Bearing capacity of shallow foundations, pages 121–147. Van Nostrand Reinhold, 1975.

[143] R. Walther and M. Miehlbradt. *Dimensionnement des structures en béton*, volume 8 of *Traité de Génie Civil*. Presses Polytechniques et Universitaires Romandes, 1990.

[144] R. Walther, D. Weber, and Ph. Menétrey. Durchstanzversuche an Stahlbetondecken mit der Stützenkopfverstärkung Tobler-WALM. Schlussbericht, Ecole Polytechnique Fédérale de Lausanne, 1994. In preparation.

[145] S. Weihe. Implicit integration schemes for multi-surface yield criteria subjected to hardening/softening behavior. Master's thesis, University of Colorado at Boulder, 1989.

[146] M.L. Wilkins. Calculations of elastic-plastic flow. In M. Rotenberg: Academic Press B. Alder, S. Fernbach, editor, *Methods in computational physics: Volume 3: Fundamental methods in hydrodynamics*, pages 211–263, 1964.

[147] K.J. Willam, N. Bićanić, and S. Sture. Constitutive and computational aspects of strain-softening and localization in solids. In *Symposium on constitutive equations : micro, macro and computational aspects*, New Orleans, 1984.

[148] K.J. Willam and G. Etse. Failure assessment of the extended Leon model for plain concrete. Sci-c-Conference 1990: Zell am See, Austria, 1990.

[149] K.J. Willam, B. Hurlbut, and S. Sture. Experimental, constitutive and computational aspects of concrete failure. In *Finite Element Analysis of Reinforced Concrete Structures*, University of Tokyo, May 1985. ASCE, US-Japan joint seminar.

[150] K.J. Willam, Th. Münz, G. Etse, and Ph. Menétrey. Failure conditions and localization in concrete. In *Computational modelling of concrete structures*, Euro-C conference, Innsbruck, Austria, March 1994.

[151] K.J. Willam and E.P. Warnke. Constitutive model for triaxial behavior of concrete. In *Concrete structures subjected to triaxial stresses*, Bergamo, Italy, May 1974. International Association for Bridges and Structural Engineering.

[152] Zace Services Ltd. *User's guide: ZSOIL, version 2.1*, 1993.

[153] O.C. Zienkiewicz and R.L. Taylor. *The finite element method*, volume 1-2. McGraw-Hill, fourth edition, 1989 and 1991.

[154] Th. Zimmermann, Y. Dubois-Pèlerin, and P. Bomme. Object-oriented finite element programming. 1. Governing principles. *Computer Methods in Applied Mechanics and Engineering*, 98(2):291–303, 1992.

[155] Th. Zimmermann and C. Rodriguez. Nonlinear analysis of a reactor building for airplane impact loadings. In *6th international conference on structural mechanics in reactor technology*, Paris, 1981.

Appendix A

Mathematical definitions

The mathematical notations are presented here in a compact form. Further developments can be found in the book of Segel [126]. The cartesian coordinate system (x, y, z) is adopted where the axis are denoted: x_1, x_2, x_3 and the unit vectors are: (e_1, e_2, e_3). The coordinates of a point are defined as (x_1, x_2, x_3). A vector (bold-face symbol) $\boldsymbol{u}$ have the components (u_1, u_2, u_3) or u_i. The subscript $_i$ is an index ranging from 1 to 3. The summation convention applies on the index, that is the symbol $\sum_i$ is omitted if the index $_i$ appears twice in a term of a sum. The Kronecker delta is defined as

$$\delta_{ij} = \begin{cases} 1 & \text{if} \quad i = j \\ 0 & \text{if} \quad i \neq j. \end{cases} \tag{A.1}$$

The permutation tensor is defined as

$$e_{ijk} = \begin{cases} 1 & \text{if } ijk = 123, 231, 312 \\ -1 & \text{if } ijk = 321, 213, 132 \\ 0 & \text{otherwise.} \end{cases} \tag{A.2}$$

The decomposition of a vector is expressed as $\boldsymbol{u} = u_i e_i$. The scalar product between two vectors is $\boldsymbol{u} \cdot \boldsymbol{v} = u_i e_i \cdot e_j v_j = u_i v_i$. The projection of a vector is denoted as $e_i \cdot \boldsymbol{u} = u_i$. The cross product between two vectors is $\boldsymbol{u} \times \boldsymbol{v} = e_i e_{ijk} u_j v_k$.

A tensor of rank n is a linear operator so that:

- In a cartesian coordinate system, there is a rule for associating the tensor $\boldsymbol{\Theta}$ (bold-face symbols) with a unique ordered set of 3^n quantities $\Theta_{i_1 \dots i_n}$ called the components.
- If $\Theta_{i_1 \dots i_n}$ and $\Theta'_{i_1 \dots i_n}$ are the components of $\boldsymbol{\Theta}$ in two different Cartesian coordinate systems. Defining T_{ij} the cosine of the angle between the x_i and x_j axis, then: $\Theta_{i_1 \dots i_n} = T_{i_1 j_1} \dots T_{i_n j_n} \Theta'_{i_1 \dots i_n}$. For a second order tensor, this can be written as: $\Theta_{pq} = T_{pm} T_{qn} \Theta'_{mn}$.

A tensor $\boldsymbol{\Theta}$ of rank two, whose components with respect to the basis e are Θ_{ij} satisfies the equation: $\boldsymbol{\Theta} = \Theta_{ij} e \otimes e$ where $\otimes$ is the tensorial product without contraction. For tensorial operation, the symbol "$\cdot$" signifies single contracted tensor product, whereas ":" signifies double contracted tensor product. The second order identity tensor is $\mathbf{1} = \delta_{ij} e_i \otimes e_j$ and the symmetric fourth order identity tensor is $\mathbf{I} = 1/2(\delta_{ik}\delta_{jl} + \delta_{il}\delta_{jk}) e_i \otimes e_j \otimes e_k \otimes e_l$.

Total differentiation is denoted by d, whereas the partial differentiation is denoted by ∂ and the abbreviation: $_{,i} = \partial / \partial x_i$. The gradient operator is denoted ∇ and operating over a scalar field ϕ leads to: $\nabla \phi = \text{grad } \phi = e \phi_{,i}$, and over a vector field $\boldsymbol{v}$ leads to: $\nabla \boldsymbol{v} = v_{i,j} e \otimes e$. The divergence operator is denoted by $\nabla \cdot$ and operating on the vector field $\boldsymbol{v}$ leads to: $div \boldsymbol{v} = \nabla \cdot \boldsymbol{v} = v_{i,i}$. The curl of vector field is denoted as curl $\boldsymbol{v} = \nabla \times \boldsymbol{v} = e e_{ijk} v_{k,j}$

The divergence theorem also called the Gauss theorem is expressed as

$$\int_S v_i n_i dS = \int_V \frac{\partial v_i}{\partial x_i} dV, \tag{A.3}$$

stating that the integral of the outer normal component of a vector n_i over a closed surface S is equal to the integral of the divergence of the vector v over the volume V bounded by the closed surface.

Appendix B

Flexural analysis of circular slabs

B.1 Linear elastic analysis

The derivation of the elastic theory of circular slabs is given by Timoshenko, Goodier and Woinowsky [140] [139] and the main ingredients are presented here for circular slabs. The thin plates theory with small deflection is considered which is based on the following assumptions:

- no deformation of the middle plane,
- the cross sections remain plane during bending, so that they undergo only a rotation with respect to their neutral axis,
- the normal stresses are disregarded.

The vertical displacement of the slab is denoted by w. The curvature in the radial and tangential direction are:

$$\frac{1}{r_r} = -\frac{d^2w}{dr^2} \tag{B.1}$$

$$\frac{1}{r_\varphi} = -\frac{1}{r}\frac{dw}{dr}. \tag{B.2}$$

The bending moments are assumed to be similar to the pure bending moments[1] so that:

$$m_r = -D\left(\frac{d^2w}{dr^2} + \frac{\nu}{r}\frac{dw}{dr}\right) \tag{B.3}$$

$$m_\varphi = -D\left(\frac{1}{r}\frac{dw}{dr} + \nu\frac{d^2w}{dr^2}\right), \tag{B.4}$$

where m_r and m_φ denote the bending moment per unit length and D is the flexural rigidity of the plate which is given by:

$$D = \frac{Eh^3}{12(1-\nu^2)}. \tag{B.5}$$

---

[1] The effect on deflections of shearing stresses acting on normal sections of the slab perpendicular to meridians, such as the section cut by the conical surface, is neglected as suggested by Timoshenko and Woinowsky [140] footnote 1 p. 52.

Applying the equilibrium equations, the fourth order differential equation governing the response of an elastic circular slab is obtained:

$$\frac{1}{r}\frac{d}{dr}\left\{r\frac{d}{dr}\left[\frac{1}{r}\frac{d}{dr}\left(r\frac{dw}{dr}\right)\right]\right\}=\frac{p}{D}. \tag{B.6}$$

This equation can be integrated if the intensity of the load p is given as a function of the radius. This task was performed for a large number of different circular slabs by Màrkus [83]. The slab which is closer to most of the experimental tested slab is a simply supported slab loaded uniformly along a circle of radius r_s. The bending moments of this slab are shown in figure B.1.

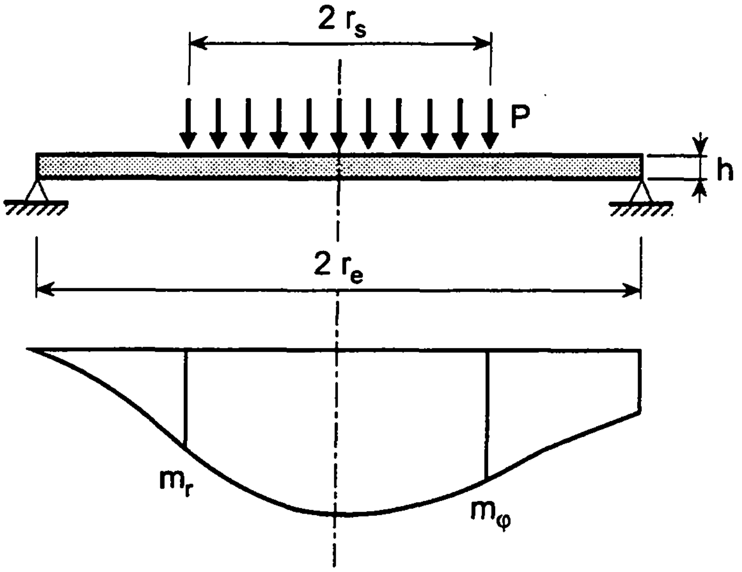

Figure B.1: Elastic bending moments of a simply supported circular slab loaded uniformly over a circular region

The moments at the center are:

$$m_r = m_\varphi = \frac{p\,r_e^2}{16}c_2,\quad c_2=(c_1-4(1+\nu)\ln\beta)\beta^2,\quad c_1=4-(1-\nu)\beta^2, \tag{B.7}$$

and the vertical deflection is:

$$w=\frac{p\,r_s^2 r_e^2}{64D(1+\nu)}c_3,\quad c_3=4(3+\nu)-(7+3\nu)\beta^2+4(1+\nu)\beta^2\ln\beta, \tag{B.8}$$

where $\beta = r_s/r_e$ and ν is Poisson's ratio.

The shear stress through the slab thickness satisfies a parabolic distribution which is zero at the top and bottom of the slab and maximum at the middle. It must be noted that in all the derivations presented here, the effect of shearing stresses and normal pressures has not been taken into account.

The stress distribution close to the column can be obtained only if the thin plate bending assumptions are disregarded. The bending theory of thin plate is assumed to be valid only at a certain distance b from the extremity of the load application. The problem of stress distribution near the center of the plate is reduced to the problem of an axisymmetric stress distribution in a circular cylinder of height h and radius b loaded by a total load P distributed over a small circle of radius r_s and by bending reactions along the lateral boundary. The integration of this problem is presented by Nádai [96]. The resulting stress distribution through the slab thickness is non-linear. The compressive stresses is many times larger than the tensile stresses. However, for brittle material the compressive strength is higher than the traction strength implying that the tensile stress is determinant for the load carrying capacity. The load for which the first cracking is observed is determined based on this derivation which gives:

$$P_{crack} = \frac{f_t h^2}{(1+\nu)\left(0.485 \log \frac{r_c}{h} + 0.52\right) + 0.48}. \tag{B.9}$$

Once the first cracking has occurred, the flexural behavior of slab can be analyzed based on the plasticity theory as described in the following section.

B.2 Plastic analysis

The behavior of reinforced concrete slabs is characterized by cracking which influences the distribution of bending moments. For a circular slab clammed into a circular column, the tangential moments at the column are zero if the column is perfectly rigid. Once tangential cracking occurs, the tangential moments develop and they generate the formation of radial cracks. The radial moments diminishes, except at the column face. This moment evolution is shown in figure B.2 as suggested by Regan [112].

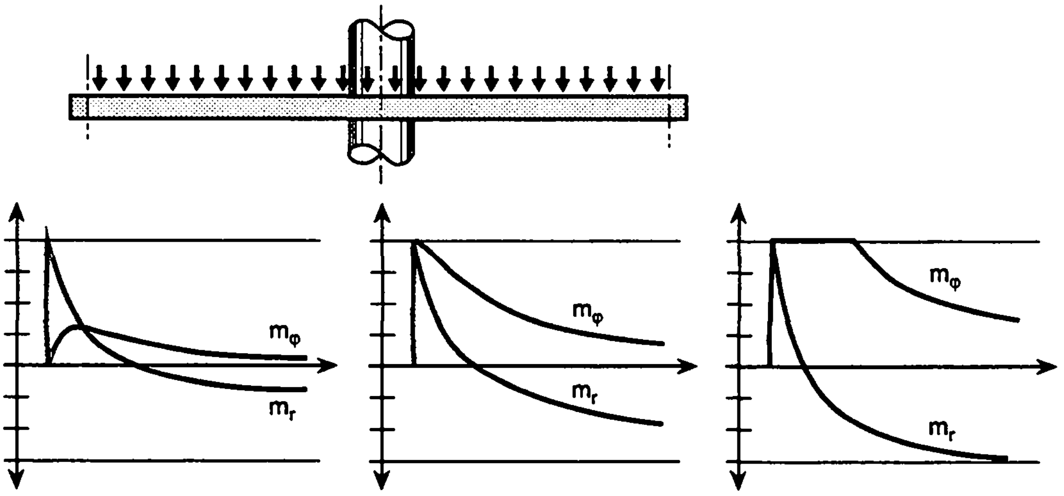

Figure B.2: Plastic evolution of the bending moments of a circular slab; (Regan 1981)

Such a moment evolution was shown by Rebora et al. [111] to be possible to model with non-linear finite element analysis. For a circular clamped slab they showed that the moment growth starts from the elastic state to a state which is close to the plastic cracking state.

In accordance to the experimental results the collapse mechanism is due to the formation of yield-lines[2]. The ultimate load obtained with the yield-line theory is slightly different from the experimental one because the membrane and others non-flexural actions of the slab are not considered.

---

[2] Yield lines are lines about which adjacent parts of the plate experience exclusively a relative rotation. The yield-line method allow to determine the limit load which is defined as the plastic collapse load of an idealized structure for which the plastic deformation can increase without limit under a constant load. Two basic assumptions are made: perfectly plastic material response, small deformation of the structure. The yield-line method is an upper bound method underestimating the limit load. Further detail of this method are given by Johansen [64] and Hognestad [56].

Considering a circular slab of radius r_e and of constant thickness, loaded vertically over a small circle of radius r_s, two mechanisms are examined which differs by the presence of cracking beneath the load as shown in figure B.3. The value of this ultimate flexural load is given by Gesund and Kaushik [45] or Save and Massonnet [124]. For mechanism (a), the ultimate load is given by:

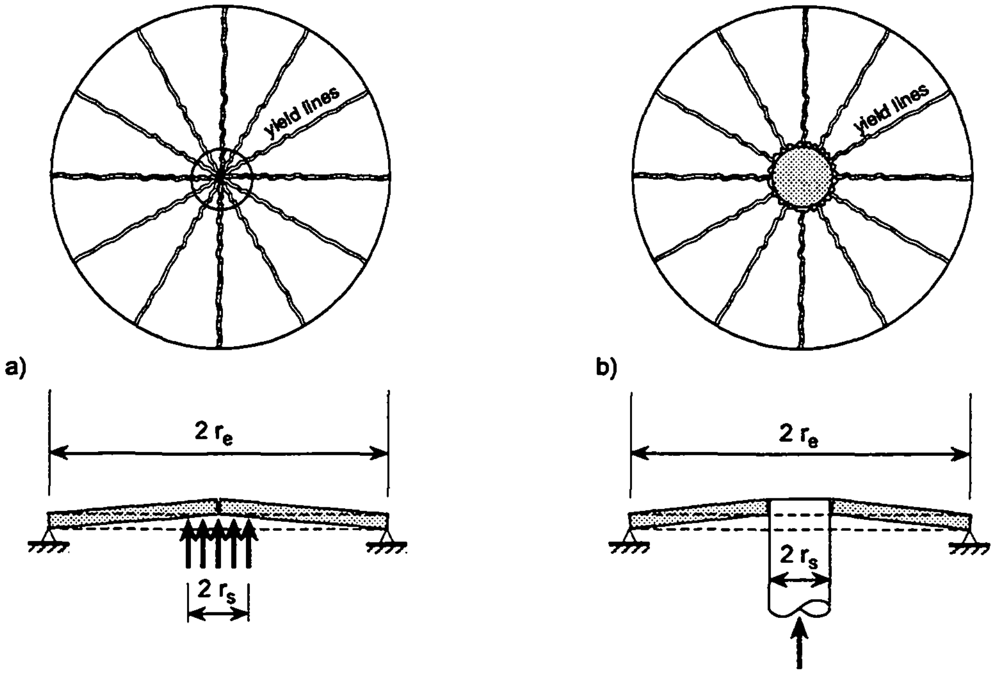

Figure B.3: Yield line pattern for a circular slab loaded at the center; (a) with, (b) without cracking beneath the load

$$P_{flex} = \frac{2\pi m_R}{1 - \frac{2r_s}{3r_e}}. \tag{B.10}$$

For mechanism (b), the ultimate load is given by:

$$P_{flex} = \frac{2\pi m_R}{1 - \frac{r_s}{r_e}}. \tag{B.11}$$

The resistant bending moment m_R is determined as described by Walther and Miehlbradt [143].

Appendix C

Gradients of the concrete model

C.1 Gradients of the failure criterion

The generalized failure criterion developed in section 3.54 is expressed as:

$$f(\xi,\rho,\theta,\phi,c) = [A_f\rho]^2 + \phi\,[B_f\rho r(\theta,e) + C_f\xi] - c. \tag{C.1}$$

The partial derivative of the failure criterion with respect to the hydrostatic, deviatoric stress invariants and deviatoric polar angle are expressed as:

$$\begin{aligned} \frac{\partial f}{\partial \xi} &= \phi C_f & \text{(C.2)} \\ \frac{\partial f}{\partial \rho} &= 2A_f^2\rho + \phi B_f r(\theta,e) & \text{(C.3)} \\ \frac{\partial f}{\partial \theta} &= \frac{\partial f}{\partial r(\theta,e)}\frac{\partial r(\theta,e)}{\partial \theta}. & \text{(C.4)} \end{aligned}$$

The partial derivative of the yield criterion with respect to the elliptic function is:

$$\frac{\partial f}{\partial r(\theta,e)} = \phi B_f\rho. \tag{C.5}$$

The derivative of the yield criterion with respect to the softening internal variable is:

$$\frac{\partial f}{\partial q} = \frac{\partial f}{\partial c}\frac{\partial c}{\partial w}\frac{\partial w}{\partial q}, \tag{C.6}$$

where the gradients are:

$$\begin{aligned} \frac{\partial f}{\partial c} &= -1 & \text{(C.7)} \\ \frac{\partial c}{\partial w} &= -\frac{a}{w_r}\exp\left\{-a\frac{w}{w_r}\right\} & \text{(C.8)} \\ \frac{\partial w}{\partial q} &= h^e\frac{1}{N}. & \text{(C.9)} \end{aligned}$$

C.2 Derivative of the elliptic function

The elliptic function $r(\theta,e)$ expressed in equation 3.49 is:

$$r(\theta,e) = \frac{4\,(1-e^2)\cos^2\theta + (2e-1)^2}{2\,(1-e^2)\cos\theta + (2e-1)\,[4\,(1-e^2)\cos^2\theta + 5e^2 - 4e]^{1/2}}. \tag{C.10}$$

The derivative of the elliptic function leads to a complex expression, which is computed using the definition of the derivative of a fraction as follows:

$$\frac{\partial r(\theta, e)}{\partial \theta} = \frac{\partial}{\partial \theta}\left(\frac{U}{V}\right) = \frac{V\ U' \ -\ U\ V'}{V^2}, \tag{C.11}$$

where prime stands for derivative with respect to θ and the different terms are:

$$\begin{aligned}
U &= 4\left(1-e^2\right)\cos^2\theta + (2e-1)^2 \\
V &= 2\left(1-e^2\right)\cos\theta + (2e-1)\left[4\left(1-e^2\right)\cos^2\theta + 5e^2 - 4e\right]^{1/2} \\
U' &= -8(1-e^2)\cos\theta\sin\theta \\
V' &= -2(1-e^2)\sin\theta - 4(2e-1)(1-e^2)U^{-\frac{1}{2}}\cos\theta\sin\theta.
\end{aligned}$$

These expressions are always defined for $0.5 < e \leq 1$ and $0 \leq \theta \leq \pi/3$.

C.3 Gradients of the plastic potential

The plastic potential developed in section 3.5.3 is expressed as:

$$g(\rho,\xi) = (A_g\rho)^2 + B_g\rho + C_g\xi. \tag{C.12}$$

The partial derivative of the plastic potential with respect to the hydrostatic and deviatoric stress invariants are:

$$\frac{\partial g}{\partial \xi} = C_g \tag{C.13}$$

$$\frac{\partial g}{\partial \rho} = 2A_g^2\rho + B_g. \tag{C.14}$$

C.4 Derivative of the invariants of the stress tensor

The derivative of the stress invariants I_1, J_2 and J_3 with respect to the stress tensor are:

$$\frac{\partial I_1}{\partial \sigma_{ij}} = \delta_{ij} \tag{C.15}$$

$$\frac{\partial J_2}{\partial \sigma_{ij}} = s_{ij} \tag{C.16}$$

$$\frac{\partial J_3}{\partial \sigma_{ij}} = s_{ik}s_{kj} - \frac{2}{3}J_2\delta_{ij}. \tag{C.17}$$

The derivative of the hydrostatic stress invariant ξ with respect to the stress tensor is:

$$\frac{\partial \xi}{\partial \sigma_{ij}} = \frac{1}{\sqrt{3}}\delta_{ij}. \tag{C.18}$$

The derivative of the deviatoric stress invariant ρ with respect to the stress tensor is:

$$\frac{\partial \rho}{\partial \sigma_{ij}} = \frac{1}{\rho}s_{ij}. \tag{C.19}$$

The similitude angle θ can be expressed as:

$$\theta = \frac{1}{3}\arccos\left(\frac{3\sqrt{3}}{2}\frac{J_3}{J_2^{\frac{3}{2}}}\right) = \frac{1}{3}\arccos r. \tag{C.20}$$

The derivative of the similitude angle θ with respect to the stress tensor can be decomposed as follows:

$$\frac{\partial\theta}{\partial\sigma_{ij}} = \frac{\partial\theta}{\partial r}\left(\frac{\partial r}{\partial J_2}\frac{\partial J_2}{\partial\sigma_{ij}} + \frac{\partial r}{\partial J_3}\frac{\partial J_3}{\partial\sigma_{ij}}\right), \tag{C.21}$$

where:

$$\begin{aligned}
\frac{\partial\theta}{\partial r} &= -\frac{1}{3}\frac{1}{\sqrt{1-r^2}} \text{ with } r \neq 0 \\
\frac{\partial r}{\partial J_2} &= -\frac{9}{4}\sqrt{3}\frac{J_3}{J_2^{\frac{5}{2}}} \text{ with } J_2 \neq 0 \\
\frac{\partial r}{\partial J_3} &= 1.5\sqrt{3}\frac{1}{J_2^{\frac{3}{2}}} \text{ with } J_2 \neq 0.
\end{aligned}$$

Appendix D

The numerical model for soil

D.1 Drucker-Prager material model

The Drucker-Prager [32] yield condition is expressed as

$$f(\rho, \xi) = \rho + \sqrt{6} a_\phi \xi - \sqrt{2} k, \tag{D.1}$$

where the value of a_ϕ and k are material characteristics. This yield condition is represented by a conical surface in the principal stress space. A graphical representation of this surface in the meridian and deviatoric planes is shown in figure D.1. The plastic potential is expressed similarly by a conical surface characterized by the angle ψ so that

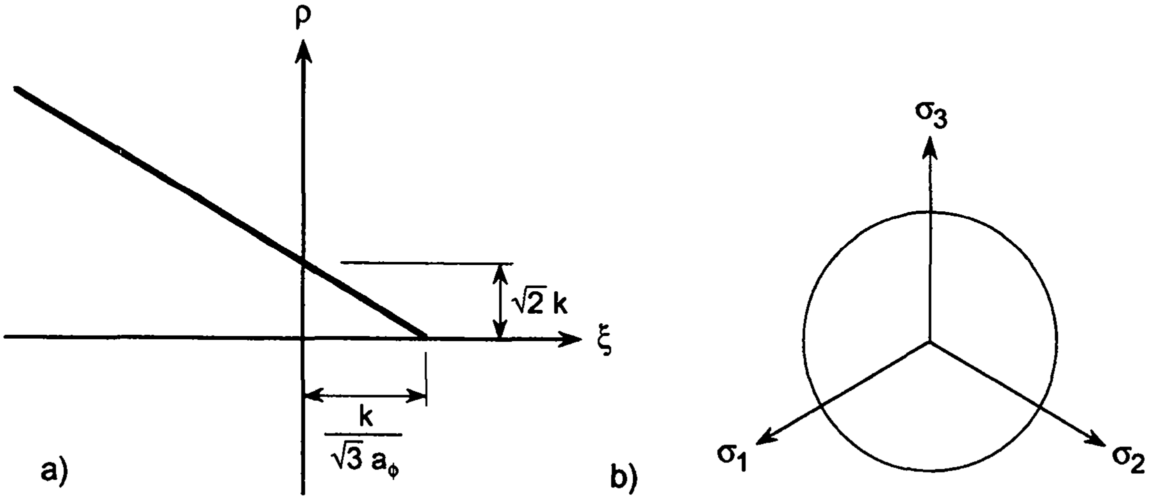

Figure D.1: Drucker-Prager yield surface in the: (a) meridian, and (b) deviatoric planes

$$g(\sigma) = \rho + \sqrt{6} a_\psi \xi, \tag{D.2}$$

where a_ψ is also a material characteristic. The plastic flow direction is consequently expressed as

$$m = \frac{1}{\rho} s + \sqrt{2} a_\psi \mathbf{1}. \tag{D.3}$$

Based on the definition of the yield condition and the plastic flow direction, the plastic multiplier given in equation 3.40 can be expressed in a closed form

$$\Delta\gamma = \frac{f^{trial}}{9K a_\phi a_\psi + G}, \tag{D.4}$$

where K is the bulk modulus and G is the shear modulus. The elastic-plastic constitutive operator given in equation 3.44 can also be expanded in an explicit matrix form so that

$$Dep_{ijkl} = \frac{9K^2 a_\phi a_\psi \delta_{ij}\delta_{kl} + \frac{3KG}{\sqrt{J_2}}[a_\phi \delta_{kl} s_{ij} + a_\psi \delta_{ij} s_{kl}] + \frac{G^2}{J_2} s_{ij} s_{kl}}{9K a_\phi a_\psi + G}. \tag{D.5}$$

The yield surface has an apex located at

$$\sigma_{apex} = \frac{k}{\sqrt{3}a_\phi}\mathbf{1}. \tag{D.6}$$

If the trial stress is in the vertex region defined by

$$\xi > \sqrt{6}a_\psi \rho + \frac{k}{\sqrt{3}a_\phi}, \tag{D.7}$$

then the stress point returns to the apex. The Drucker-Prager material model leads to a perfectly explicit formulation, simplifying its numerical implementation in computer codes.

D.2 A smooth Mohr-Coulomb material model

A smooth version of the original Mohr-Coulomb criterion is considered. This smooth formulation is preferred over the original formulation as the treatment of the corners in the deviatoric plane is avoided. This smooth Mohr-Coulomb condition is derived from the general yield condition given in equation 3.54 and proposed by Menétrey and Willam [89]

$$f = \frac{1}{2}(3 - \sin\phi_{mc})\rho r(\theta, e) + \sqrt{2}\sin\phi_{mc}\xi - \sqrt{6}c\cos\phi_{mc}. \tag{D.8}$$

The function $r(\theta, e)$ is the elliptic function proposed by Willam and Warnke [151] given in equation 3.49. The out-of-roundness parameter e is recalled from table 3.3.

$$e = \frac{3 - \sin(\phi_{mc})}{3 + \sin(\phi_{mc})}. \tag{D.9}$$

It can be noted that for $\phi_{mc} = 0^0$, $e = 1$ and for $\phi_{mc} = 90^0$, $e = 0.5$. This yield surface is illustrated in the deviatoric plane in figure D.2. Two different values of friction angle are considered to illustrate that the smooth Mohr-Coulomb surface is close to the original surface for large friction angle.

The adopted plastic potential is the same surface as the one considered for the Drucker-Prager material model given in equation D.2. The corresponding stress return algorithm in the deviatoric plane is analogous to the radial return algorithm proposed by Wilkins [146]. This expression of the plastic potential is mainly justified by its simplicity. However, the resulting flow rule is non-associated as the yield surface is elliptic in the deviatoric plane and the plastic potential is circular. The elastic-plastic constitutive matrix is given in equation 3.44.

The yield surface is characterized by an apex located at

$$\sigma_{apex} = \frac{\sqrt{3}c}{\tan\phi_{mc}}\mathbf{1}. \tag{D.10}$$

If the trial stress is in the vertex region defined by

$$\xi > \sqrt{6}a_\psi \rho + \frac{\sqrt{3}c}{\tan\phi_{mc}}, \tag{D.11}$$

then the stress is returned to the top of the apex.

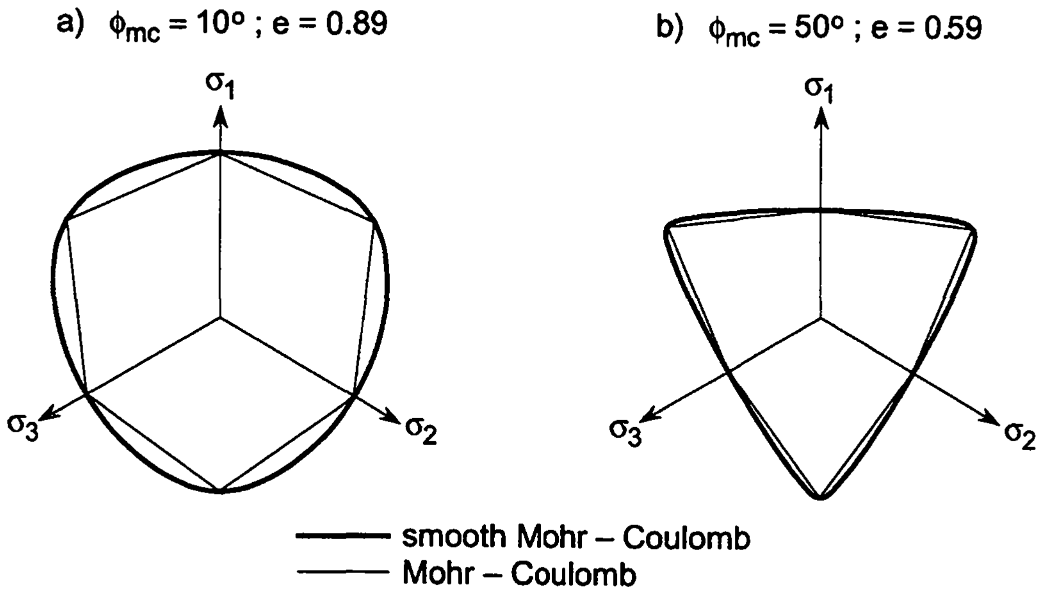

Figure D.2: Deviatoric sections of the smooth Mohr-Coulomb yield surface: (a) $\phi_{mc} = 10^0$, (b) $\phi_{mc} = 50^0$.

D.3 Calibration of the soil characteristics

The yield conditions of soils are usually characterized by the friction angle ϕ_{mc} and the cohesion c_{mc}. The Mohr-Coulomb yield surface is expressed in terms of these two parameters allowing a direct calibration. However, the Drucker-Prager yield surface is not expressed in terms of these two parameters and a calibration with the Mohr-Coulomb yield surface is performed. Triaxial calibration of the Drucker-Prager yield surface with the Mohr-Coulomb one leads to

$$a_\phi = \frac{2\sin\phi_{mc}}{\sqrt{3}(3 \pm \sin\phi_{mc})} \qquad \text{(D.12)}$$

$$k = \frac{6\, c_{mc}\cos\phi_{mc}}{\sqrt{3}(3 \pm \sin\phi_{mc})}, \qquad \text{(D.13)}$$

where + and − signs express respectively a calibration along the tensile (internal) and compressive (external) meridians. In the following, a Drucker-Prager condition calibrated to the internal (external) Mohr-Coulomb meridians is called internal (external) Drucker-Prager material model.

The Drucker-Prager yield surface is a conical surface in the stress space which is characterized by its opening angle α. For a zero value of the cohesion, the apex of the cone is located at the origin of the stress space. Up to a limiting opening angle, this cone is entirely located in the compression region. To determine this angle, the limiting cone shown in figure D.3 is considered. The limiting angle can be obtained in taking the scalar product of two limiting vectors: one defined by the hydrostatic axis $P = (1,1,1)$ and one by the bisecting line of the $X1$ and $X2$ axis defined as $V = (1,1,0)$ so that

$$P \cdot V = P_1V_1 + P_2V_2 + P_3V_3 = 2 = \|P\|\|V\|\cos\alpha. \qquad \text{(D.14)}$$

This leads to the limiting value $\cos\alpha = \sqrt{\frac{2}{3}}$ that is $\alpha \cong 35.26^0$. This limiting angle is expressed in the principal stress space and can be transformed in the meridian plane given by (ξ, ρ) as

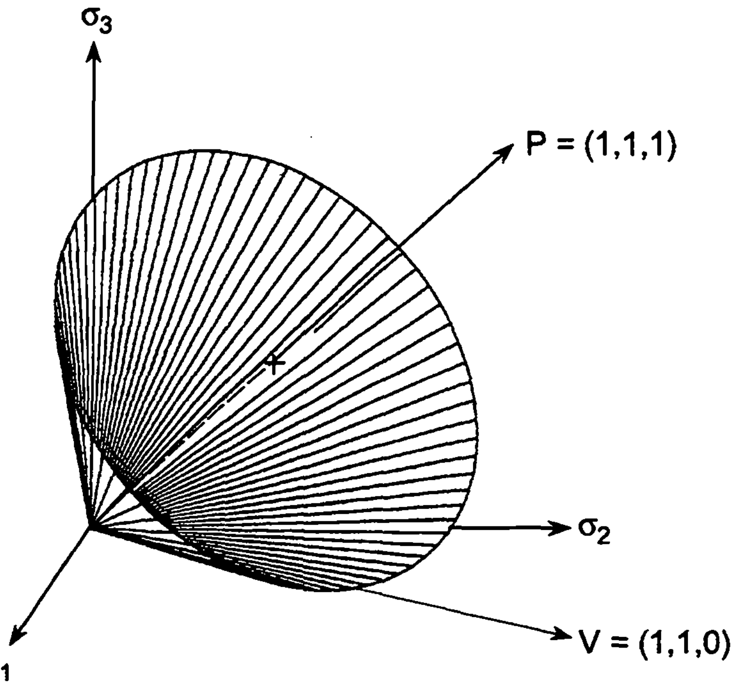

Figure D.3: Limiting Drucker-Prager cone in the stress space.

follows. Considering the slope of the Drucker-Prager surface in the meridian plane as shown in figure D.1(a) and equalling to the tangent of the cone opening leads to

$$\frac{\sqrt{3}a_\phi}{\frac{1}{\sqrt{2}}} = \sqrt{6}a_\phi = \tan\alpha. \tag{D.15}$$

This gives the limiting value $a_\phi = \frac{1}{\sqrt{12}}$. Therefore, $a_\phi \leq \frac{1}{\sqrt{12}}$, implies that the Drucker-Prager yield surface is located in the compressive region and $a_\phi > \frac{1}{\sqrt{12}}$, implies that some parts of the surface are in the tensile region. This limiting value can be further expressed in terms of the friction angle using equation D.12. For the internal Mohr-Coulomb adjustment it implies a friction angle of $\phi_{mc} \leq 90^0$. However, for the external Mohr-Coulomb calibration the limiting friction angle is $\phi_{mc} \leq 36.8^0$. The importance of this limitation for the footing problem will be investigated in section 5.2.2.

The analysis of the above results suggests that the calibration of the Drucker-Prager surface is best when using a mean value between the internal and external Mohr-Coulomb adjustment such as

$$a_\phi = \frac{2\sqrt{3}\sin\phi_{mc}}{9-\sin^2\phi_{mc}} \tag{D.16}$$

$$k = \frac{6\sqrt{3}\,c_{mc}\cos\phi_{mc}}{9-\sin^2\phi_{mc}}. \tag{D.17}$$

This calibration will lead to results which are closer to the ones obtained with the Mohr-Coulomb criterion, especially for axisymmetric computations. It can be noted that this calibration is characterized by a limiting friction angle $\phi_{mc} = 45.1^0$ for which the load carrying capacity tends to infinity. This adjustment covers most of the friction angles observed in soil.

Appendix E

Implementation of the numerical model

E.1 Introductory remarks

The computational simulation tool developed in chapters 3 and 4 is implemented into a computer code in applying the object-oriented programming concept. As it is the first time that this programming concept is applied to the non-linear finite element method, this implementation is presented in this appendix. A special format of the input file is required which is described for people who will have the opportunity to use or further develop this program. The results obtained with the numerical computation are also described. The post-processing treatment is presented in order to explain how the figures presented in this research were generated.

E.2 Object-oriented implementation

E.2.1 Preliminary

In recent articles and reports Th. Zimmermann, Y. Dubois-Pèlerin and P. Bomme [33], [34], [35], [154] proposed an object-oriented approach to finite element programming and demonstrated the effectiveness of the new approach by analyzing truss and two-dimensional structures in the linear static and dynamic range. In the framework of this research, this approach is extended and it is shown how object-oriented programming can be applied to non-linear finite element analysis particularly for J_2 plasticity[1].

E.2.2 Implementation for J_2 plasticity material

This section presents a summary of the conclusion of the object oriented non-linear finite element implementation of J_2 plasticity as presented by Menétrey and Zimmermann [90]. The objects as defined and classified for linear finite element analysis were extended in order to handle non-linear analysis. The algorithmic procedures required for non-linear analysis have been investigated to extract the object behavior and to extend the classes of the preexisting environment. In fact, non-linear analysis relies more heavily than linear analysis on algorithmic procedures and it is not obvious whether it can be properly integrated into an object-oriented approach without a significant loss of efficiency.

---

[1] J_2 plasticity is similar to the Huber-Mises criterion expressed in equation 3.56.

It is shown that the extended classes were capable of modelling the algorithmic procedures, illustrating that the object-oriented programming approach can be used for non-linear analysis. Furthermore, due to the concept of non-anticipation of the state of the object, the sequence of the operations can be easily modified. This results in a program that can be readily extended. It is also illustrated that the object-oriented concept leads to faster programming, because it re-uses existing classes. The extension of the class hierarchy for non-linear analysis required only two new classes and the extension of only eight classes out of the original 40 ones. This facilitated debugging since potential programming errors had to be located inside the extended classes. The reliability of object-oriented programming is also demonstrated by a reduction of data transfer as compared to procedural programming, again reducing possible programming errors.

E.2.3 Proposed class hierarchy

The object hierarchy presented in table E.1 is an extended version based on the research done by Dubois-Pèlerin [33] for linear elastic-dynamic analysis and the one performed by Menétrey and Zimmermann [90] for non-linear material behavior. The class names (an object is an instance of a class) are printed in typewriter characters for clarity. The class hierarchy presented in table E.1 is not complete as many other classes such as the utility classes, as for example the `FloatMatrix`, `FloatArray`, `Dictionary` are not described.

`Domain`			
`FEMComponent`	`Element`	`Quad`	`Quad2D`
			`QuadAxi`
		`Truss`	`Truss2D`
			`TrussAxi`
		`Ring`	
	`Load`	`BoundaryCondition`	
		`NodalLoad`	
	`LoadTimeFunction`	`ConstantFunction`	
		`PieceWiseLinearFunction`	
	`Material`	`ElasLin`	
		`UElaPla`	
		`J2Plasticity`	
		`Soil`	
		`Concrete`	
	`Node`		
	`TimeStep`		
`Dof`			
`GaussPoint`			
`LinearSystem`			

Table E.1: Class hierarchy

E.2.4 Description of the main classes

The class `Domain` groups all the information and tasks depicting a given problem where a specific problem is an instance of class `Domain`. The class `Node` manages its position and degrees of freedom `Dof`, computes and assembles its load vector, and updates its data. A `Dof` (degree of freedom) is an attribute of `Node`. Its tasks are managing the unknowns, numbering the equation, checking the boundary condition, and updating its data. The class `Element` encapsulates all the information concerning the differential equations to be solved. The class `Element` is the father class of the five different classes of element: `Quad2D`, `QuadAxi`, `Truss2D`, `TrussAxi`, and `Ring`. The class `GaussPoint` manages its coordinates, its weight and the value of the stress, strain and internal variable vectors as well as the constitutive matrix. The class `Material` is the father class of the five different classes of material: `ElasLin`, `UElaPla`, `J2Plasticitity`, `Soil`, and `Concrete`. An abstract father class: `FEMComponent`, implements the access to the class `Domain`, the numbering of the components and the file read-write procedures. The classes `Dof` and `GaussPoint` are not derived from `FEMComponent` because they are attributes of `Node` and `Element` respectively.

E.2.5 Technical information

The numerical model was programmed with the C++ language (see Stroustrup [132]) on a Sun Sparc 2 work-station with the Sun C++ [133] compiler. The ObjectCenter [17] platform is used to develop the code. The Purify [110] program is employed to check the memory allocation.

E.3 Input format

The structure to be analyzed is described in an input file which is characterized by a special input format described in this section. This input format is subdivided into eight groups of data: "PrintResults", `TimeStep`, "Algorithm", `Material`, `Load`, `LoadTimeFunction`, `Node`, and `Element`. Each of these groups should respect a prescribed format presented in the following, but no order in the sequence of declaration of each group is required. A group of data is ended with **. In the following description, "i", "j", "k", "l", "m" are integers and "x", "y", "z" are doubles even though the distinction is not necessary.

The keyword "PrintResults" controls the desired output and is used with the following format.

```
1 PrintResults
1 out i pel j pno k loc l *
```

Only one keyword "PrintResults" is read per input file. The keyword "out" controls the generation of the output file so that for "i"=0, no output file is generated, for "i"=1, an output file with convergence results and nodal values is created, and for "i"=2, a complete output file is produced. The keyword "pel" and "pno" control the creation of the plot files for the plot of `Element` and `Node` values respectively (the value "j" or "k"=0 implies no respective plot file creation whether "j" or "k"=1 implies the generation of plot files). The keyword "loc" indicates the number "l" of `GaussPoint` where the localization analysis should be performed. At the beginning of the simulation, the description of the Gauss point is requested and for each Gauss point a different file is created with the results of the acoustic tensor computation.

The class `TimeStep` implements a time step in the load history of the problem. For static analysis, the time step is equivalent to the load step. The number and size of each time step increment is indicated in the following format.

```
TimeStep i
j dt x *
```

The number of desired time steps is given by "i". The current number of time step is "j" and "x" is the increment of time. The number of time step "j" must be incremented from 1 to "i".

The keyword "Algorithm" controls the algorithm that should be used with the following format.

```
Algorithm 1
1 MaxIt i Tolerance x ModNR j NbItKel k NbConItKel l StopIfNotCon m *
```

Only one keyword "Algorithm" is considered per input file. The keyword "MaxIt" is the maximum number of iterations "i" that should be performed during one time step. The keyword "ModNR" (modified Newton-Raphson), "NbItKel" (number of iterations with the elastic stiffness matrix), and "NbConItKel" (number of converging iterations with the elastic stiffness matrix) control the type of algorithm which is desired as indicated in table E.2. These strategies are described in section 4.3.4. The keyword "StopIfNotCon" (stop if not converged) controls the progression of the computation if the convergence is not reached at the maximum number of iteration. For "StopIfNotCon"=0, the choice is given to stop or continue the computation once the "MaxIt" have been reached, if "StopIfNotCon"=1, the computation is aborted, and if "StopIfNotCon"=-1, the computation is proceeded.

#	Strategies	ModNR	NbItKel	NbConItKel
1	Initial load method	0	0	0
2	Stiffness of previous converged step	MaxIt	0	0
3	Newton-Raphson (update every j iterations)	j	0	0
4	***Kel*** for the first "l" iterations	j	1	0
5	***Kel*** for the first "l" converging iterations	j	0	1
6	***Kel*** for f(l) converging iterations at the beginning and if divergence is observed	j	0	-1

Table E.2: Generation of the modified Newton-Raphson algorithm, different strategies

The class `Material` describes the different type of material in the following form:

```
Material i
j class "name of the class" "material characteristics" *
```

The number of objects `Material` is given by "i". The current number of material is "j". Different type of `Material` are available and for each of them, the required material characteristics are given as follows:

- `ElasLin` is the elastic linear material class characterized by: E≡ Young's modulus, n≡ Poisson's ratio, A≡ area, d≡ density, and t≡ thickness as described in section 3.4.
- `J2Plasticity` is the J_2 plasticity material class characterized by: E≡ Young's modulus, n≡ Poisson's ratio, A≡ area, Y≡ yield stress, K≡ hardening modulus, d≡ density, and t≡ thickness.
- `UElaPla` is the uniaxial bilinear material class characterized by: E≡ Young's modulus, A≡ area, Y≡ yield stress, K≡ hardening modulus, d≡ density, and t≡ thickness.
- `Soil` is the Drucker-Prager material class characterized by: E≡ Young's modulus, n≡ Poisson's ratio, k≡ cohesive parameter, F=a_ϕ ≡ frictional parameter, p= a_ψ ≡ dilatancy parameter, d≡ density, and t≡ thickness as described in appendix D.1.

- `Concrete` is the concrete material class characterized by: E≡ Young's modulus, n≡ Poisson's ratio, fc≡ compressive strength, ft≡ tensile strength, Af, Bf, Cf≡ adjustment of the failure criterion, e≡ out-of-roundness parameter of the failure criterion, phif≡ frictional parameter of the failure criterion, Ag, Bg, Cg≡ adjustment of the flow rule, eg≡ out-of-roundness parameter of the flow rule, phig≡ frictional parameter of the flow rule, wr≡ crack rupture opening, a, b≡ softening parameters, d≡ density, and t≡ thickness as described in section 3.5.

The class `Load` describes the different types of load and boundary conditions in the form:

```
Load i
j class BoundaryCondition loadTimeFunction k displacement: D x d y *
j class NodalLoad loadTimeFunction m components n y1 ... yn *
```

The number of objects `Load` is given by “i”. The `BoundaryCondition` is controlled by the load time function “k” and by a value of displacement “x”. This type of `BoundaryCondition` can be used either for fixed or for displacement control boundary conditions where “d” stands for total displacement and “D” for increment of displacement. The `NodalLoad` is controlled by the load time function “m”. The number of components of the nodal value are given by “n” and the values of the load by “y1 ... yn”.

The class `LoadTimeFunction` describes the different load time function in the following form:

```
LoadTimeFunction i
j class ConstantFunction f(t) x *
j class PiecewiseLinFunction nPoints n t x1 ... xn f(t) y1 ... yn *
```

The number of objects `LoadTimeFunction` is given by “i”. Two different functions are commonly used: the `ConstantFunction` and the `PiecewiseLinearFunction`. The value of the constant one is given by “x”. The evolution of the piece wise linear function is controlled by “n” points determined by the time values “x1 ... xn” and the corresponding values of the function “y1 ... yn”.

The class `Node` describes the nodal coordinates of the finite element mesh in the form:

```
Node i
j numberOfDofs k coord k x1 ... xk bcOnDofl m loads n l1 ... ln *
```

The number of objects `Node` is given by “i”. For the corresponding “j” node the number of degree of freedom and the number of coordinate (these values are equal to 2 for the considered `Element`) are given by “k”. The corresponding coordinates are given by “x1 ... xk”. The boundary condition is controlled by the keyword “bcOnDof” and the number of `Dof` on which the boundary condition is applied is “l”. The considered `BoundaryCondition` is given by its number “m”. The applied `Load` is given by the keyword “loads” and corresponds to “l” different `Load` objects of number l1 ... ln.

The class `Element` describes the elements that are used in the form:

```
Element i
j class Quad2D material k integ l nodes n1 n2 n3 n4 *
j class QuadAxi material k integ l nodes n1 n2 n3 n4 *
j class Truss2D material k nodes n1 n2 *
j class TrussAxi material k nodes n1 n2 *
j class Ring material k nodes n1 *
```

The number of objects `Element` is given by "i". The five different types of `Element` available are given with the "j" number. The `Material` number is given by "k". For the `Quad2D` and `QuadAxi` different integration are possible which are controlled by the keyword "integ". For standard integration, "integ"=0 and for $\overline{\boldsymbol{B}}$ integration "integ"=-2. The node list is given after the keyword "nodes".

E.4 Results and post-processing

Once the input file has been created and the numerical simulation performed, the results are given in four different files. The standard file is the output file which includes information concerning the performed `TimeStep`, the `Node` and the `Element`.

The visualization of the behavior of the structure often called post-processing is determinant for the understanding of the response of the structures. The post-processing treatment is based on a computer code written in C (see Kernighan and Ritchie [65]) and compiled with the Sun C compiler [134] with the UNIRAS [3] graphical library. Two files had to be generated to be used for graphical representations of the structure. One of this file stores the `Node` values and the other the `Element` ones.

The values at the `Node` allow to plot the displacement and velocity field of the structure at a given amplification and for a special zooming section. The velocity is obtained at a given time step by subtracting to the current displacement the one obtained at the previous time step. The plot of the displacement is mainly used to check the deflection of the structure, boundary conditions, and the eventual mechanism. The velocity plot is mainly used to detect localization characterized by a discontinuous velocity field.

The values at the `Element` allow the following plots:

- The plot of the principal stresses: the principal stresses in the plane are obtained based on the following equation:

$$\left.\begin{array}{c}\sigma_1\\ \sigma_2\end{array}\right\} = \frac{1}{2}(\sigma_{11}+\sigma_{22}) \pm \sqrt{\left(\frac{\sigma_{11}-\sigma_{22}}{2}\right)^2 + \sigma_{12}^2}. \tag{E.1}$$

  The value of the inclination of the principal stress is given by:

$$\tan\alpha_i = \frac{\sigma_i - \sigma_{11}}{\sigma_{12}}. \tag{E.2}$$

- The plot of the tensile stresses is obtained similarly to the plot of the principal stresses, but in plotting only the positive stresses.

- The plot of the tangential cracks: the tangential cracks are plotted if the principal deformation is bigger than the rupture deformation in uniaxial traction: ϵ_1 and $\epsilon_2 > \epsilon_r = f_t/E$. The tangential cracks are symbolized with a straight line for which the length is computed based on the cohesion parameter and the size of the element such that:

$$\text{crack length} = \frac{1}{3}(1-c)h^e. \tag{E.3}$$

  The crack orientation is similar to the principal strains orientation. A stress-free crack is symbolized with a thicker straight line and is represented if $c < 0.01$.

- The plot of the radial cracks: the radial cracks are plotted if the out-of-plane deformation is bigger than the rupture deformation in uniaxial traction: $\epsilon_3 > \epsilon_r = f_t/E$. The radial cracks are depicted with a circle for which the radius is computed based on the cohesion parameter and the size of the element such that:

  $$\text{radius of the radial crack} = \frac{1}{3}(1-c)h^e. \tag{E.4}$$

  No special treatment is performed to distinguish a radial stress-free crack.

It has to be noted that the plot of the cracks is considered only if the analysis is performed with the `Concrete` material.

Curriculum vitae

Philippe Gérald Menétrey
Born on June 21, 1963.

Education:

1979	"Diplôme d'études secondaires", math-sciences.
1984	"Maturité féderale", type C.
1989	Diploma of Civil Engineer, "Ecole polytechnique féderale de Lausanne" (EPFL).
1991	Master of Science in Civil Engineering, University of Colorado, Boulder.

Employment Experience:

Each summer time from 1983 to 1986; Guex SA, Jongny.

Trainee in a contractor firm.

During summer time in 1987 and 1988; Junior Entreprise-EPFL, Lausanne.

Project manager
Developed User's Manuals for computer programs applied to civil engineering.

February 1989 to June 1990; Walther, Mory & Maier AG, Bâle.

Civil Engineer in a consulting office.
Designed industrial buildings in reinforced and prestressed concrete and steel. Designed a continuous post-tensioned box girder railway bridge. Designed different pile foundations, earth-retaining walls, and sheet pile walls. Contributed to the competition for a cable stayed bridge.

September 1991 to present; IBAP-EPFL, Lausanne.

Assistant under the guidance of Professor R. Walther.
Investigated the numerical analysis of punching failure in reinforced concrete structures. Worked out student exercises for the design of reinforced and prestressed concrete structures. Directed final diploma projects. Collaborated to punching tests in laboratory. Contributed to technical documents on cable stayed-bridges and shell structures.

Distinction:

Awarded the "Prix Stucky EPFL" in 1989 for an outstanding diploma project.